

# **Electrochemically Deposited Ceria Structures for Advanced Solid Oxide Fuel Cells**

Thesis by

Evan C. Brown

In Partial Fulfillment of the Requirements

For the Degree of

Doctor of Philosophy



California Institute of Technology

Pasadena, California

2011

(Defended May 20, 2011)

© 2011

Evan C. Brown

All Rights Reserved

# Acknowledgements

Foremost, I would like to dedicate this work to the One who loved me first. Truly, there is no greater love than one who lays down his life for another.

I would like to thank my wife for giving me such support and encouragement. Those words are easily written, but they were never given lightly by her. As for the rest of my family, I would not have accomplished much without all of their love and their crazy; especially my parents, who inspire me and have always reminded me who I am.

I also want to thank Sossina Haile for being my advisor and my advocate—without her help, this manuscript would be 100 times longer with half as much insight. She has shown me how compassion and strength can blend together in true leadership. And I want to thank my labmates and science friends for the community and fellowship we have shared. Particularly, I want to thank Dr. William Chueh for too many things to count (but specifically for analysis, measurements, and insights pertaining to Chapter 4), Dr. Yong Hao (Chapter 4, microfabrication), Dr. David Boyd for his analytical expertise, and Stephen Wilke (Chapter 2, fabrication and SEM assistance). Also, to Taesik Oh, Aron Varga, Mary Louie, Carol Garland (TEM), Jane Liu (FIB), Aminy Ostfeld, and Sylvia Sullivan for invaluable discussions and technical assistance. I would also like to acknowledge the Global Climate and Energy Program in conjunction with Stanford University for funding.

# Abstract

As the pursuit towards emissions reduction intensifies with growing interest and nascent technologies, solid oxide fuel cells (SOFCs) remain an illustrious candidate for achieving our goals. Despite myriad advantages, SOFCs are still too costly for widespread deployment, even as unprecedented materials developments have recently emerged. This suggests that, in addition to informed materials selection, the necessary power output—and, thereby, cost-savings—gains must come from the fuel cell architecture. The work presented in this manuscript primarily investigates cathodic electrochemical deposition (CELD) as a scalable micro-/nanoscale fabrication tool for engineering ceria-based components in a SOFC assembly. Also, polymer sphere lithography was utilized to deposit fully connected, yet fully porous anti-dot metal films on yttria-stabilized zirconia (YSZ) with specific and knowable geometries, useful for mechanistic studies. Particular attention was given to anode structures, for which anti-dot metal films on YSZ served as composite substrates for subsequent CELD of doped ceria. By tuning the applied potential, a wide range of microstructures from high surface area coatings to planar, thin films was possible. In addition, definitive deposition was shown to occur on the electronically insulating YSZ surfaces, producing quality YSZ|ceria interfaces. These CELD ceria deposits exhibited promising electrochemical activity, as probed by A.C. Impedance Spectroscopy. In an effort to extend its usefulness as a SOFC fabrication tool, the CELD of ceria directly onto common SOFC cathode materials without a metallic phase was developed, as well as templated deposition schemes producing ceria nanowires and inverse opals.

# Table of Contents

<b>Acknowledgements.....</b>	<b>iii</b>
<b>Abstract.....</b>	<b>iv</b>
<b>Table of Contents.....</b>	<b>v</b>
<b>List of Figures.....</b>	<b>x</b>
<b>List of Tables.....</b>	<b>xvi</b>
<b>List of Symbols and Notations.....</b>	<b>xviii</b>
<b>1 Introduction and Background.....</b>	<b>1</b>
1.1 A Global Perspective.....	1
1.2 SOFC Introduction.....	3
1.2.1 SOFC Basics.....	3
1.2.2 Materials Selection: Samaria-Doped Ceria (SDC).....	7
1.2.3 Cell Architecture.....	10
1.3 Anti-Dot Substrates: A New Design Framework.....	12
1.4 Three-Dimensional Structures and Their Fabrication by CELD.....	14
1.4.1 SOFC Fabrication Method/Morphology Non-Negotiables.....	14
1.4.2 Cathodic Electrochemical Deposition (CELDD).....	16
<b>2 Anti-Dot Substrates.....</b>	<b>19</b>

2.1 Polymer Sphere Lithography Background and Summary.....	19
2.2 Experimental Details.....	23
2.2.1 Substrate Preparation.....	23
2.2.2 Nanosphere Deposition.....	23
2.2.3 Microsphere Deposition.....	23
2.2.4 Metal Deposition.....	24
2.2.5 Microstructure Analysis.....	24
2.2.6 High Temperature Stability.....	25
2.3 Results and Discussion.....	25
2.3.1 Nanosphere Lithography Results.....	25
2.3.2 Microsphere Lithography Results.....	26
2.3.3 Microstructure Fidelity.....	31
2.3.4 Thermal Stability.....	36
<b>3 Cathodic Electrochemical Deposition of Undoped and Doped Ceria.....</b>	<b>38</b>
3.1 Introduction.....	38
3.2 Experimental Details.....	40
3.2.1 Substrate Definition.....	40
3.2.2 Experimental Setup.....	42
3.2.3 Characterization Details.....	45
3.3 Results.....	46
3.3.1 Bulk.....	46
3.3.2 High Surface Area (HSA) Coatings.....	52
3.3.3 Thin Films.....	58

3.4 Discussion.....	64
3.4.1 General Deposition Overview.....	64
3.4.2 The Physical Deposition Picture.....	69
3.4.3 Deposition on Non-Conducting Parts of the Substrate.....	71
3.4.4 HSA and Thin Film Transients.....	79
<b>4 The Electrochemical Activity of CELD Ceria Structures.....</b>	<b>84</b>
4.1 Introduction, Methods, and Background.....	84
4.1.1 A.C. Impedance Spectroscopy (ACIS) Introduction.....	84
4.1.2 Experimental Approach.....	87
4.1.3 System Precedence.....	90
4.2 Arc Identification: PLD Films vs. CELD Coatings.....	91
4.2.1 Representative Spectra.....	91
4.2.2 Origin of the Single Arc in the Metal-Sandwich Configuration.....	94
4.2.3 Origin of the HF Arc in Embedded Metal Configurations.....	97
4.2.4 Origin of the LF Arc in Embedded Metal Configurations.....	102
4.3 The SDC Gas Interface Arc: A Closer Look.....	104
4.3.1 Platinum Strips.....	104
4.3.2 Nickel Anti-Dot Films.....	115
<b>5 Sundry Specialized CELD Microstructures.....</b>	<b>121</b>
5.1 Anodic Aluminum Oxide (AAO) Templated Nanowires.....	121
5.1.1 AAO Template Formation Mechanism and Background.....	121
5.1.2 AAO Fabrication Experimental Details.....	124

5.1.3	AAO Template Results.....	126
5.1.4	Ceria Nanowire Growth.....	133
5.2	Inverse Opals.....	135
5.2.1	Inverse Opal Definition and Background.....	135
5.2.2	Inverse Opal Fabrication Details.....	136
5.2.3	Inverse Opal Results.....	136
5.3	Oxidation Protection Coatings.....	138
5.3.1	Experimental Details.....	138
5.3.2	Results.....	139
5.4	CELD Ceria Grown Directly on MIEC SOFC Cathode Substrates.....	140
5.4.1	Substrate Preparation Details.....	141
5.4.2	CELD Results and Discussion.....	143
<b>6</b>	<b>Summary and Conclusions.....</b>	<b>150</b>
	<b>Appendix A: ImageJ Analysis Details.....</b>	<b>152</b>
	<b>Appendix B: Additional Images.....</b>	<b>155</b>
B.1	Additional CELD Images.....	155
B.2	Additional AAO Images.....	158
B.3	Additional Inverse Opal Images.....	160
B.4	Additional MIEC Substrate Images.....	160
B.5	Additional Oxidation Protection Coating Images.....	161
	<b>Appendix C: Alternate SOFC Microstructure Fabrication Routes.....</b>	<b>162</b>

C.1	Solution Impregnation into AAO Templates.....	162
C.2	Copper Nanowire Synthesis.....	165
	<b>References.....</b>	<b>169</b>

# List of Figures

1.1	SOFC schematic.....	4
1.2	SOFC polarization curve.....	6
1.3	Electrolyte materials' ionic conductivity comparison.....	8
1.4	3PB and 2PB in powder-processed electrodes schematics.....	10
1.5	Anti-dot film and templated electrode microstructure schematics.....	15
2.1	SEM images of the polymer sphere lithography process.....	20
2.2	Representative anti-dot film SEM images.....	22
2.3	SEM images of nanosphere short- and long-range coverage.....	26
2.4	SEM images of nanosphere coverage for 500, 680, and 790 nm spheres.....	27
2.5	SEM images of multilayers and void regions from microsphere deposition.....	28
2.6	Optical photographs of multilayers and void regions.....	28
2.7	Optical photographs of the water wash method.....	30
2.8	Optical and SEM images of one spin coat with the water wash method.....	30
2.9	SEM images of microsphere coverage for 2 and 3.2 $\mu$ m spheres.....	31
2.10	Pore diameter histograms of Cu anti-dot films.....	33
2.11	2PB area fraction histograms of Cu anti-dot films.....	33
2.12	SEM and AFM images of Ni anti-dot films before and after thermal treatment.....	37
3.1	Pourbaix diagram for the Ce-H <sub>2</sub> O-H <sub>2</sub> O <sub>2</sub> system from ref [86].....	40
3.2	SEM images of porous metal network on YSZ substrates used for CELD...	41

<b>3.3</b>	CELD setup schematic with corresponding potential electrode values.....	44
<b>3.4</b>	XRD and EDS analyses of undoped and doped bulk CELD ceria.....	47
<b>3.5</b>	Raman analyses of undoped and doped bulk CELD ceria.....	48
<b>3.6</b>	FT-IR analyses of undoped and doped bulk CELD ceria.....	51
<b>3.7</b>	TGA analyses of undoped and doped bulk CELD ceria.....	51
<b>3.8</b>	SEM images of undoped HSA ceria on YSZ/Pt strips.....	53
<b>3.9</b>	SEM images of doped HSA ceria on various substrates.....	54
<b>3.10</b>	SEM images of HSA ceria deposited from the doped + H <sub>2</sub> O <sub>2</sub> electrolyte....	55
<b>3.11</b>	SEM images of the HSA microstructure's thermal stability.....	56
<b>3.12</b>	SEM images of a crack-free HSA structure after annealing.....	57
<b>3.13</b>	SEM images of as-deposited thin film morphologies.....	58
<b>3.14</b>	AFM scans of as-deposited thin films from the doped and doped + H <sub>2</sub> O <sub>2</sub> electrolytes.....	59
<b>3.15</b>	SEM cross-sectional images of thin film morphologies.....	60
<b>3.16</b>	SEM images of the deposits from the doped + acetic electrolyte.....	62
<b>3.17</b>	SEM images showing the thermal stability of thin films on YSZ/Pt strips...	63
<b>3.18</b>	CV scan for the doped and doped + H <sub>2</sub> O <sub>2</sub> electrolytes.....	68
<b>3.19</b>	SEM images of as-deposited HSA CELD ceria growth on exposed YSZ surfaces.....	73
<b>3.20</b>	SEM images of as-deposited planar CELD ceria growth on exposed YSZ surfaces.....	75
<b>3.21</b>	SEM images of equivalent HSA growth on YSZ and Pt strip regions.....	76
<b>3.22</b>	SEM images of as-deposited planar growth on the 3PB region of a	

	YSZ/Pt strips substrate.....	78
<b>3.23</b>	TEM and HRTEM images of HSA CELD ceria.....	78
<b>3.24</b>	HSA voltage transients and corresponding chronological SEM images.....	80
<b>3.25</b>	Thin film current transients.....	82
<b>4.1</b>	Representative Nyquist plot for a PLD/Pt strips exposed configuration.....	85
<b>4.2</b>	Schematics showing 2PB reaction pathways for lithographically defined substrates, metal-embedded and metal-sandwich configurations for PLD and CELD samples for ACIS studies.....	89
<b>4.3</b>	SEM images of PLD and CELD metal-embedded samples.....	90
<b>4.4</b>	Representative Nyquist plots for PLD and CELD metal-embedded samples.....	92
<b>4.5</b>	Nyquist plots with hydrogen and water partial pressure dependencies for a representative CELD/Ni anti-dot-embedded sample.....	93
<b>4.6</b>	Representative Nyquist plots for metal-sandwich configurations.....	94
<b>4.7</b>	Hydrogen partial pressure dependence of the single arc from metal-exposed and metal-sandwich configurations.....	95
<b>4.8</b>	SEM images of the deleterious phenomena associated with CELD/metal-sandwich samples.....	96
<b>4.9</b>	Hydrogen partial pressure dependence of the HF arc from metal-embedded configurations.....	98
<b>4.10</b>	Hydrogen and water partial pressure dependence, as well as 3PB and metal spacing dependencies, of the HF arc for large pattern sized PLD samples...99	99

<b>4.11</b>	TEM images showing voids in the HSA CELD deposit near the exposed metal surfaces.....	101
<b>4.12</b>	Hydrogen partial pressure dependence of the LF arc from metal-embedded and the single arc from metal-exposed configurations.....	103
<b>4.13</b>	Pt pattern size effect on the SDC gas interfacial ASR partial pressure dependencies.....	106
<b>4.14</b>	SEM images of undoped CELD ceria on 5-5 $\mu\text{m}$ and 20-20 $\mu\text{m}$ Pt patterns on YSZ.....	106
<b>4.15</b>	Undoped CELD deposition time effect on the SDC gas interfacial ASR partial pressure dependencies.....	108
<b>4.16</b>	SEM images of undoped CELD ceria samples deposited for 5 and 10 minutes.....	108
<b>4.17</b>	Doped CELD deposition time effect on the SDC gas interfacial ASR partial pressure dependencies.....	109
<b>4.18</b>	SEM images of doped CELD ceria samples deposited for 5, 10, and 20 minutes.....	109
<b>4.19</b>	Doping effect for 5 minute deposits on the SDC gas interfacial ASR partial pressure dependencies.....	110
<b>4.20</b>	SEM images of doped and undoped CELD ceria samples deposited for 5 minutes.....	111
<b>4.21</b>	Doping effect for 10 minute deposits on the SDC gas interfacial ASR partial pressure dependencies.....	111

<b>4.22</b>	SEM images of doped and undoped CELD ceria samples deposited for 10 minutes.....	111
<b>4.23</b>	Consecutive depositions effect on the SDC gas interfacial ASR partial pressure dependencies.....	113
<b>4.24</b>	SEM images of consecutive depositions following thermal treatment.....	114
<b>4.25</b>	SEM image comparison of doped CELD/Ni anti-dot-embedded samples deposited for 5, 10, and 20 minutes.....	117
<b>4.26</b>	Deposition time effect for doped CELD/Ni anti-dot-embedded samples on the SDC gas interfacial ASR partial pressure dependencies.....	118
<b>4.27</b>	SEM image comparison of two doped CELD HSA samples and one doped CELD planar sample.....	119
<b>4.28</b>	SDC gas interfacial ASR partial pressure dependencies comparison between two HSA and one planar doped CELD samples.....	120
<b>5.1</b>	AAO structure schematic.....	122
<b>5.2</b>	SEM images of AAO templates grown from Al foil.....	127
<b>5.3</b>	SEM image comparison of phosphoric acid pore diameter etching times.....	128
<b>5.4</b>	SEM images of AAO templates grown from sputtered Al thin films.....	129
<b>5.5</b>	Current transients for AAO templates grown from various Al thin film samples, whose optical photographs are also shown.....	130
<b>5.6</b>	SEM images of the barrier layer from AAO templates grown from Al foil	

	and sputtered Al thin films.....	132
<b>5.7</b>	SEM images of as-deposited CELD ceria nanowires in the pores of AAO..	134
<b>5.8</b>	SEM images of AAO ceria nanowires after thermal treatments.....	134
<b>5.9</b>	SEM images of ceria inverse opal structures on YSZ/Pt strips and Ni anti-dot substrates grown via CELD.....	137
<b>5.10</b>	SEM images of difficulties encountered during the inverse opal fabrication process.....	138
<b>5.11</b>	SEM images of the oxidative protection coating activity of CELD ceria coatings on Ni anti-dot films.....	140
<b>5.12</b>	SEM images of the depositing surface of porous BSCF substrates that has been planarized via abrasive paper.....	143
<b>5.13</b>	SEM images of as-deposited undoped CELD ceria grown on dense BSCF..	144
<b>5.14</b>	SEM images of as-deposited doped CELD ceria grown on porous BSCF...	145
<b>5.15</b>	CV scan comparison between Ni and BSCF substrates for the doped electrolyte.....	145
<b>5.16</b>	SEM images of thin films of CELD ceria grown on porous BSCF at non-standard and open working potentials.....	147
<b>5.17</b>	SEM images of various CELD ceria structures deposited near the meniscus area of a dense BSCF sample.....	149
<b>A.1</b>	The ImageJ analysis process.....	154
<b>B.1</b>	Additional CELD HSA SEM images.....	155

<b>B.2</b>	Additional CELD thin film cracking SEM images.....	156
<b>B.3</b>	Additional CELD TEM images.....	157
<b>B.4</b>	Additional optical and SEM images of AAO templates.....	158
<b>B.5</b>	Additional CELD ceria nanowires SEM images.....	159
<b>B.6</b>	Additional CELD inverse opal SEM images.....	160
<b>B.7</b>	Additional CELD on MIEC substrate SEM images.....	160
<b>B.8</b>	Additional oxidation protection coating SEM images.....	161
<b>C.1</b>	SEM images of unaided solution phase impregnated ceria nanowires.....	163
<b>C.2</b>	SEM images of sonicated-assisted impregnated ceria nanowires.....	163
<b>C.3</b>	SEM images of stirring-assisted impregnated ceria nanowires.....	163
<b>C.4</b>	SEM images of sonicated- and stirring-assisted impregnated ceria nanowires.....	164
<b>C.5</b>	SEM image of an un-etchable AAO template after thermal treatment.....	164
<b>C.6</b>	SEM images of CuO nanowires thermally grown from Cu foil.....	166
<b>C.7</b>	SEM images of CuO nanowires thermally grown from thin films of Cu on SDC and porous Cu films after harsh hydrogen plasma treatment.....	167
<b>C.8</b>	SEM images of Cu nanowires resulting from reduction via a hydrogen plasma at moderate power densities.....	168

## List of Tables

<b>2.1</b>	Comparison of theoretical and experimental 3PB length areal density and percent 2PB exposure for different initial PS sphere diameters.....	34
------------	--	----

**3.1** CELD liquid electrolyte compositions..... 43

# List of Symbols and Notations

$n$	number of electrons
$F$	Faraday's constant
$E_N$	Nernstian voltage
$\delta$	oxygen non-stoichiometry
$\text{Ce}^{3+/4+}$	dissociated aqueous cerium ions of a particular cerium valence
$\text{Ce(III/IV)}$	precipitated/solid cerium species of a particular cerium valence
$\rho_{3PB}^{theo}$	theoretical 3PB areal density
$\rho_{3PB}^{exp}$	experimental 3PB areal density
$f_{2PB}^{theo}$	theoretical 2PB area fraction
$f_{2PB}^{exp}$	experimental 2PB area fraction
$\phi_i$	initial PS sphere diameter
$\phi_f$	final PS sphere diameter
$D$	crystallite size
$\lambda$	XRD x-ray wavelength
$\beta$	adjusted full-width half max
$\theta$	XRD diffracting angle
$Z$	complex impedance
$R$	resistance
$C$	capacitance
$\omega$	frequency
$j$	$\sqrt{-1}$

$\tilde{Z}$	complex impedance normalized by total deposited area
$\tilde{R}$	resistance associated with a Nyquist arc normalized by total deposited area
$\tilde{Z}^*$	complex impedance normalized by the projected area of the exposed SDC surface
$\tilde{R}^*$	resistance associated with a Nyquist arc normalized by the projected area of the exposed SDC surface

### Abbreviations

SOFC	solid oxide fuel cell
CELD	cathodic electrochemical deposition
YSZ	yttria-stabilized zirconia
OCV	open circuit voltage
SDC	samaria-doped ceria
GDC	gadolinia-doped ceria
MIEC	mixed ionic-electronic conductor
3PB	three-phase boundary
2PB	two-phase boundary
PLD	pulsed-laser deposition
CVD	chemical vapor deposition
AELD	anodic electrochemical deposition
PS	polystyrene
SEM	scanning electron microscopy
AFM	atomic-force microscopy

HSA	high surface area
SCE	standard calomel electrode
XRD	x-ray diffraction
FT-IR	Fourier transform infrared
CV	cyclic voltammetry
EDS	x-ray energy dispersive spectroscopy
TEM	transmission electron microscopy
ACIS	A.C. impedance spectroscopy
ASR	area-specific resistance
LF	low frequency
HF	high frequency
AAO	anodic aluminum oxide
BSCF	$\text{Ba}_{0.5}\text{Sr}_{0.5}\text{Co}_{0.8}\text{Fe}_{0.2}\text{O}_{3-\delta}$
SCN	$\text{Sr}_x\text{Co}_y\text{Nb}_z\text{O}_{3-\delta}$

# Chapter 1

## Introduction and Background

### 1.1 A Global Perspective

Eventually, the world will run out of fossil fuels, period. This simple fact necessarily motivates an intensive search for alternatives. As if to underscore the immediacy of such a quest, geopolitical tensions and complications have again and again proven to disrupt what people love most about fossil fuels—they are consistently available, relatively easy to use, and, above all else, cost little to do so. Finding a (host of) suitable replacement candidate(s) is difficult, owing to the plethora of pros to using fossil fuels. Indeed, societies worldwide have in many cases developed around their day-to-day use, making widespread adoption of anything else a nearly overwhelming task: humans are loathe to radically change. Nevertheless, the pioneer views this picture as ripe with opportunity, and science has historically cast itself as a trail blazer of progress.

There is a finite amount of energy that is available for power generation, in any form. And since thermodynamics dictates that energy cannot be created or destroyed, we are limited to options such as solar, wind, nuclear, hydroelectric, tidal, biomass, and geothermal forms of energy. Of these, solar energy is far and away the most abundant, and, therefore, the most practical to develop. Even as all of the so-called “renewable energy” technologies are considered, two of the most attractive, solar and wind, suffer from intermittency issues—the sun only shines during the day, and inclement weather can be prohibitive; wind is notoriously temperamental. Energy storage media are necessary to complement a system that relies solely on these renewable energy

technologies for power generation. Energy that is converted from solar or wind could be used at a later time, for instance, when the electricity demand exceeds the supply ability, like at night or when the wind isn't blowing. Chemical bonds remain the most efficient energy storage method, although significant gains have been made in batteries and supercapacitors [1-4]. But once a fuel is made, there is the question of how one extracts the stored energy. Humans have almost entirely relied upon combustion of fossil fuels to do so, but the by-products invariably add to the growing amount of greenhouse gases in the earth's atmosphere. With the daunting prospect of global climate change, a better fuel (and way of extracting its stored energy) is desperately needed.

Fuel cells have tremendous promise to address these concerns. A fuel cell is an energy conversion device that relies upon electrochemical driving forces to extract energy from a fuel as electricity, rather than the familiar, but Carnot-restricted combustion cycles. This allows more of the chemical potential in a fuel to be converted into useful work, with calculated efficiencies in excess of 80% for combined heat and power systems [5]. Fuel cells operating at higher temperatures can run off of a wide range of fuels, from standard, already-in-use fossil fuels to pure hydrogen. This flexibility is a pragmatic necessity for bridging the current addiction to greenhouse-gas-producing fuel to a "clean", carbon-free source. A number of future scenarios can be imagined, but a particularly compelling vision for the power generation of the future is to utilize solar energy to split water into hydrogen and oxygen, where the hydrogen is stored until power is needed. The hydrogen could then be utilized as the fuel in a fuel cell, producing electricity. The by-product of such a process is water, which can be fed back to the original input stream.

Challenges undoubtedly remain. Chief among those are economic—fuel cells are ~10-100 times too expensive to be competitive [5-6]. To ameliorate this issue, better performing and cheaper materials/fabrication processes need to be developed.

This manuscript concentrates on combining modern, high-performance materials with advanced architectural designs of solid oxide fuel cells (SOFCs), all to achieve the ultimate goal of dramatically increasing their power output. Two fairly well-established fabrication methods with little to no prior demonstration of actual application in a fuel cell are utilized here for SOFCs, namely, polymer sphere lithography [7-8] for substrate preparation and cathodic electrochemical deposition [9-10] for oxide material deposition. Extensive modifications and further development was needed to appropriately adapt them, which are the subjects of Chapters 2 and 3. Chapter 4 details activity analyses of various SOFC components made with these fabrication methods, and Chapter 5 involves the fabrication of specialized microstructures. First, however, a broad introduction to SOFC operational basics is presented in Section 1.2, and the necessary linkage of, applicability towards, and motivation for utilizing polymer sphere lithography and cathodic electrochemical deposition in SOFC fabrication is subsequently established in sections 1.3 and 1.4, respectively.

## **1.2 SOFC Introduction**

### *1.2.1 SOFC Basics*

A fuel cell consists of three main components: an electrolyte sandwiched between two electrodes, the anode and cathode. The electrolyte is an ionically conducting material, allowing ions, but not electrons, to migrate through it. Fuel cells are typically categorized

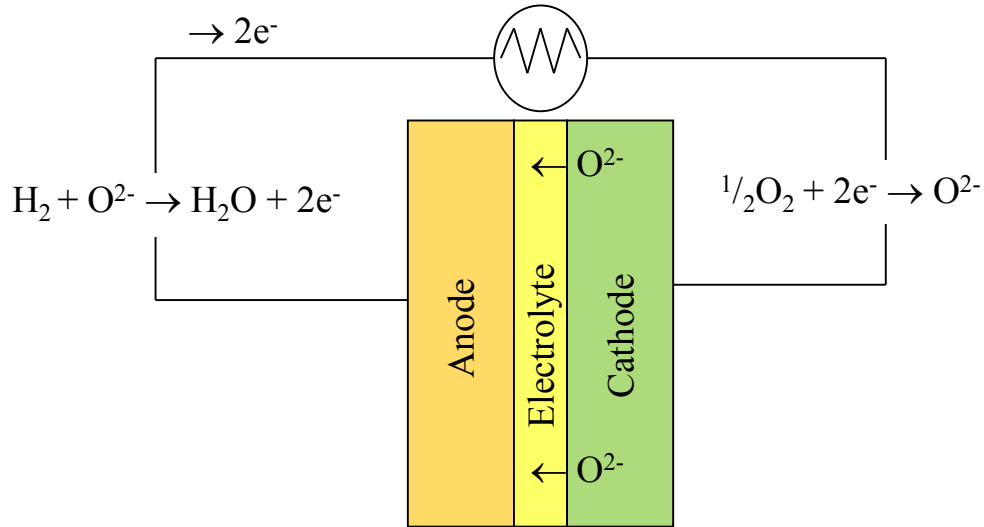


**Fig. 1.1.** A schematic of a generalized SOFC, showing each electrode's half-reactions and the migration directions of each mobile species.

by their mobile ionic species and temperature of operation. In this manuscript, solid oxide fuel cells are the focus. They are solid-state devices (meaning no liquid electrolytes) and typically conduct oxygen ions through metal oxide constituents, although some proton-conducting SOFCs exist [11-12]. Each electrode is responsible for facilitating transport of electrons, oxygen ions, and gaseous reactants to surface reaction sites, where the appropriate half-cell reaction occurs. A schematic of a generalized SOFC is shown in Fig. 1.1. On the anode side, fuel is introduced, where it reacts with oxygen ions supplied from the cathode that have migrated through the solid electrolyte, producing water vapor and electrons, according to the half-reaction in Eqn. 1.1.

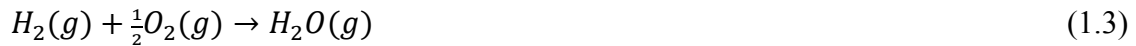


Driven by the need to maintain overall charge neutrality, the negatively charged electrons travel through an externally connected circuit to the cathode, effectively offsetting the dearth of negative charge left by migrating oxygen ions. These incoming

electrons then react with atmospheric oxygen, producing oxygen ions according to the half-reaction:



The two electrode half-reactions combine to yield the overall reaction given in Eqn 1.3, from which the  $\Delta G_{rxn}$  can be calculated and then converted to a Nernstian voltage (Eqn. 1.4), measured as the open circuit potential (OCV), where  $n$  is the number of participating electrons and  $F$  is Faraday's constant. This is the potential at which no net current is flowing through the cell. For the high temperatures of SOFCs and pure oxygen/hydrogen atmospheres, typical OCVs are  $\sim 1.1$  V.



$$E_N = \frac{\Delta G_{rxn}}{nF} \quad (1.4)$$

Various deleterious phenomena decrease the operating voltage from the theoretical Nernstian value, as depicted in the polarization curve of Fig. 1.2. A cell's power output is defined as the operating voltage multiplied by the drawn current, meaning that these processes lower SOFCs' power output. At open circuit conditions, leaks in the sealing that separate the anodic and cathodic compartments, as well as holes in the solid electrolyte, can allow fuel cross-over, which immediately lowers the operating voltage. Also, non-zero electronic conductivity in the solid electrolyte has the same effect. Once current is drawn from the cell, three so-called overpotentials further decrease the operating voltage. Activation overpotentials are related to the finite-rate electrode reaction kinetics, and typically dominate the voltage losses. Ohmic overpotentials originate from conductivity resistances encountered when charged species

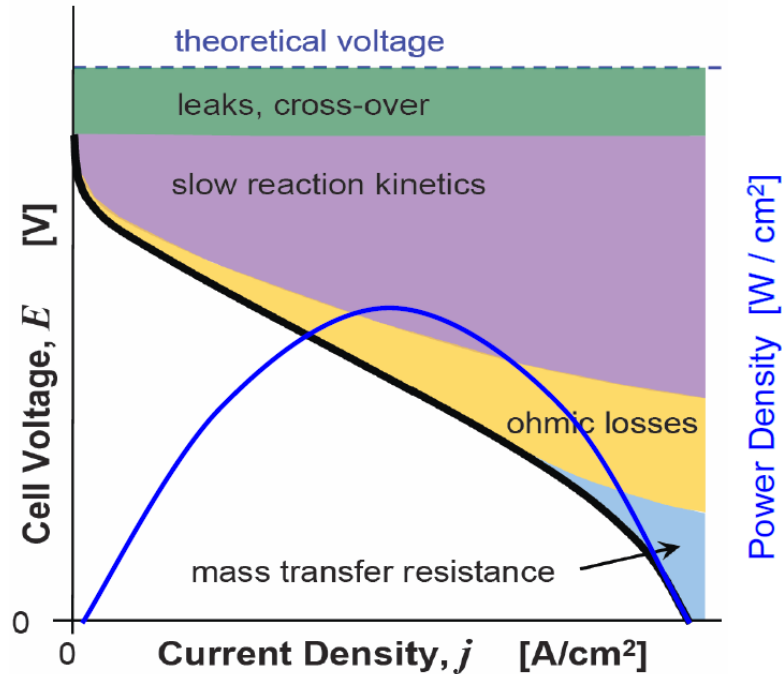


**Fig. 1.2.** A visualization of the overpotential losses typically encountered in SOFCs and the associated power density output of such a cell.

migrate throughout the cell. Concentration overpotentials arise when not enough reactants are supplied to the half-reaction sites, most often caused by mass transfer limitations in the gas phase, but these effects are only seen at very high current densities beyond practical operating conditions.

Species' transport through the crystal structure of metal oxides is generally thermally activated, and electrode kinetics are enhanced as temperature increases; therefore, high temperatures are desirable as they increase conductivity and reaction rates. Standard SOFC operating temperatures are anywhere from 700 – 1000 °C [5-6]. These high temperatures enforce strict requirements for component materials, even making choice of the interconnect material, which conducts the electrons to and from the respective electrodes, a complicated matter. In fact, the lack of cheap, viable options for

high temperature interconnects has largely motivated the move toward intermediate operating temperatures, i.e., 500-650 °C. This is the point at which stainless steel and its derivatives can resist prohibitive oxidation, and could therefore conceivably be used for interconnects [13]. Furthermore, thermal cycling can lead to significant wear and tear due to differences in thermal coefficients of expansion, although it is less severe at lower temperatures.

Manufacturing scalability and its cost is a perpetual concern. Low-throughput, expensive fabrication processes cannot be a part of the final solution, although they can be useful toward more fundamental understanding. Similarly, catalytic materials can be used to impact and define sluggish reaction kinetic pathways, but they often consist of expensive, rare precious metals such as platinum or palladium [14]. Even though much lower operating temperatures can be achieved, this strategy is not viable on a large scale.

With so many aspects to SOFC technology, a methodical approach is needed to gain fundamental insights and elucidate the rate-limiting steps, eventually contributing to an informed, optimized design. From the brief overview above, two design focal points emerge—materials selection and cell architecture.

### 1.2.2 *Materials Selection: Samaria-Doped Ceria (SDC)*

Cerium(IV) oxide (or, ceria— $\text{CeO}_{2-\delta}$ ) has a cubic fluorite structure, capable of large oxygen non-stoichiometry ( $\delta$ ) via oxygen vacancies. In the moderate oxygen partial pressure atmospheres experienced by the SOFC electrolyte (known as the electrolytic regime), the oxygen vacancy concentration in ceria is extrinsically pinned down by a

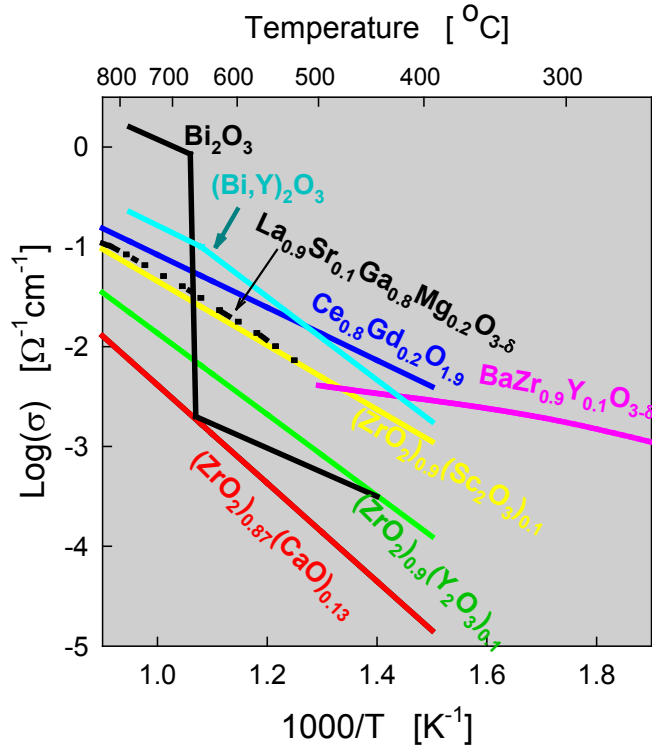
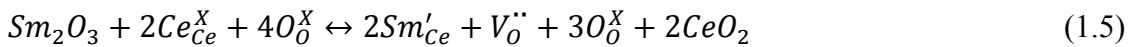


**Fig. 1.3.** A through-plane ionic conductivity comparison for common electrolyte materials taken from [13].

strictly 3+ cation dopant, such as samarium (SDC) or gadolinium (GDC). A samarium doping example is written here in Kröger-Vink notation:



This induces significant ionic conductivity at intermediate temperatures, garnering much interest for doped ceria as the SOFC electrolyte component [15-17]. Fig. 1.3 shows a conductivity comparison between common SOFC electrolyte materials, including the traditional favorite, yttria-stabilized zirconia (YSZ)[14]. A generally accepted benchmark for electrolyte conductivity is  $\sim 0.01 \text{ S cm}^{-1}$ , above which a candidate is deemed suitable. According to this metric, ceria-based electrolytes could potentially operate from 500 – 650 °C, without sacrificing performance, as would be the case with YSZ.

Additionally, under the high temperature reducing conditions typically seen in a SOFC anode, intrinsic oxygen vacancies form spontaneously via the oxidation of lattice oxygen, according to [1]:



These vacancies are charge compensated by electrons, which subsequently cause the cerium cations to change valence from nominally all 4+ to mixed 4+/3+. This gives rise to a non-trivial electronic conductivity via polaron hopping, making ceria a so-called mixed ionic-electronic conductor (MIEC). Although MIEC perovskite-type metal oxides are commonly employed as cathodes [18-20], there are few that are stable under the anode's high temperature reducing conditions, and those that are have low conduction and/or slow hydrogen electrooxidation kinetics [21-23].

Due to the lack of available MIECs, a traditional SOFC anode is typically composed of a random, three-dimensional amalgamation of an electronically conducting phase, e.g., nickel, an ionically conducting phase, e.g., YSZ, and a gas-permeable "phase," e.g., a network of pores [24-25]. The intersection of these three phases is termed the three phase boundary (3PB), shown schematically in Fig. 1.4a. The 3PB density (Fig. 1.4b) defines the number of reaction sites per projected electrolyte area, as the anode half-reactions can only take place at this intersection. This is in stark contrast to a MIEC, where electrochemical reactions can theoretically take place at nearly any point along its exposed surface, or the two phase boundary (2PB), as in Fig. 1.4c. There has been a significant effort to establish and quantify the anodic electrochemical activity of ceria-based 2PBs, even in the absence of a closely-adjacent, purely electronically conducting phase [26-32]. Therein, it is definitively shown that the surface of doped ceria alone is,

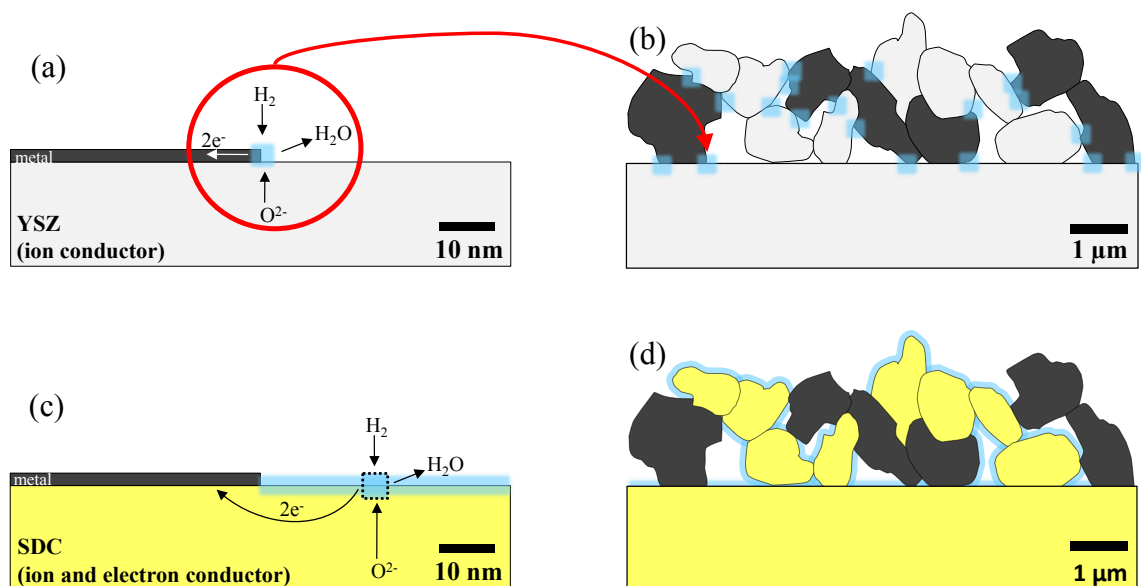


**Fig. 1.4.** Schematic diagrams of (a) the three-phase boundary (3PB) region where gas, metal, and yttria-stabilized zirconia (YSZ) phases intersect; (b) the 3PB density for a powder-processed anode; (c) the two-phase boundary (2PB) region of a mixed ionic-electronic conductor like samaria-doped ceria (SDC); and (d) the 2PB density for the same anode as in (b), but with SDC instead of YSZ. Light blue areas indicate electrochemically active regions.

itself, electrocatalytically active, and its bulk electronic conductivity is sufficient to place a current collector up to several microns away from a reaction site. Comparing the visualized anodes in Fig. 1.4b and d, it can be seen that a simple materials switch from YSZ to SDC affords a much greater reaction site density, owing to 2PB dominance over 3PB. In this way, materials selection paves the way for an architectural design paradigm, one where 2PB microstructures, rather than more restrictive 3PB microstructures, are possible.

### 1.2.3 Cell Architecture

Returning to the polarization curve of Fig. 1.2, there are three general design guidelines related to the three overpotentials outlined above. First, to reduce ohmic losses, all conduction pathways should be kept as short as possible. The primary culprit of ohmic

loss is oxygen ion transport through the solid electrolyte—the conclusion here is simple: make the electrolyte layer thin ( $\mu\text{m}$  scale). Second, for a given electrode reaction rate, maximizing the number of active reaction sites will increase the current density, on the basis of the projected area of the cell. For a MIEC anode like SDC, this effectively translates into maximizing the active surface area (nm scale). Third, one must ensure easy gas phase access by highly porous, non-tortuous electrodes, although this is less of a concern than the previous two ( $\mu\text{m}$  and perhaps nm scale).

The ideal cell design must balance  $\mu\text{m}$  and nm length scales, which also means that new fabrication approaches must accommodate both. As SOFCs are high temperature devices, care should be taken to ensure stability of any as-fabricated nanometer-sized features. Despite the obvious need for feature size reduction, a general hierarchical structure is desirable for aspects like electronic current collection—electrons cannot be expected to only travel through nanometer-sized metal films or multiple-micron-lengths of SDC without incurring severe resistance penalties.

State-of-the-art powder processing methods that produce Ni/YSZ cermet anodes (as in Fig. 1.4b) are cheap and scalable, but offer limited structural tunability and little fundamental insight into the details of SOFC operation [25]. This is primarily due to the randomized nature of the electrode geometry—key features like 3PB (or 2PB in the case of a MIEC), pore size, conduction pathway lengths, and so on are all ill-defined. Even if these parameters are determined post production (and probably using a destructive method), the sample-to-sample variation is relatively high for randomized structures [33]. On the other hand, cell architectures with specifically engineered and well-defined geometries offer dual advantages of physically-correlated diagnostic analyses and the

subsequent ability to alter the design in accordance with the results. For instance, knowing the relationship between a SDC anode's 2PB and its impedance spectra (c.f. Chapter 4) could lend valuable insight into which design knob to turn, and how much.

In summary, most operational voltage loss mechanisms in today's SOFCs inform an overall feature size reduction of every component of the cell architecture. This move should be done intelligently, so as not to incidentally incur other penalties, e.g., gas diffusion limitations and bulk transport resistances, while at the same time maintaining manufacturability, scalability, and the ability to produce large total footprint cells. Furthermore, trending towards defined, as opposed to randomized, geometries can help link performance to tunable features.

As such, there is tremendous need and potential for entirely new SOFC design schemata, as well as complimentary fabrication techniques.

### **1.3 Anti-Dot Substrates: A New Design Framework**

In recognition of the need to examine geometrically well-defined structures, some recent mechanistic studies have employed two-dimensional electrodes patterned onto the electrolyte of interest [18, 34-36]. This approach has begun to bear fruit and mechanistic models have begun to be developed [37-38]; however, challenges in understanding 'real' fuel cells remain because the two-dimensional patterns have a substantially lower areal density of 3PBs (defined as the 3PB length per unit of projected electrolyte area) than the systems they represent. Specifically, conventional photolithographic techniques with a minimum feature size of about 5  $\mu\text{m}$  can attain a maximum areal 3PB density of 2,000  $\text{cm cm}^{-2}$  [34]. In contrast, typical fuel cell electrodes boast values as high as 800,000  $\text{cm cm}^{-2}$

$\text{cm}^{-2}$  [33]. Such significant microstructural differences can plausibly induce differences in reaction pathways. Accordingly, there is a pressing need to obtain geometrically defined electrode structures with tunable feature sizes that are more relevant to SOFC electrocatalysis.

Demonstrated below is a facile fabrication strategy, known as polymer sphere lithography, in which monodisperse polymer spheres serve as sacrificial templates to construct anti-dot metal films (see Fig. 1.5a), permitting access to 3PB areal densities over an enormous range, from 2,000 to 43,500  $\text{cm}^{-2}$ . Though not previously explored in the fuel cell context, the anti-dot structure is ideal for advancing the aforementioned fundamental studies for this reason.

When these porous, metal films are overlaid onto an electrolyte substrate such as YSZ or SDC, the fraction of exposed electrolyte area and the 3PB are concurrently and specifically known, true for all two-dimensional lithographic processes. This enables electrocatalysis studies for the underlying electrolyte material, particularly as it pertains to 3PBs (and 2PBs for MIECs). The accessible 3PB regime here is previously untouched by conventional lithography, moving much closer to actually-in-use 3PB densities. Use in conjunction with diagnostic tools such as A.C. Impedance Spectroscopy (ACIS) allows definitive relationships between 3PBs/2PBs and various electrochemical activity-related materials characterization parameters to be established, e.g. rate limiting processes' resistances, capacitances, etc. And when combined with traditional lithography techniques, an extremely wide range of 3PBs can be sampled. Although tempting, such a geometry as-is, however, is not actually a suitable electrode candidate because of issues like high electronic resistance through the relatively thin anti-dot metal film.

An even higher number of reaction sites can be achieved by moving from a planar to a three-dimensional structure, and these anti-dot films are a good starting point to get a variety of well-defined three-dimensional electrode structures.

Chapters 2 and 5 present the fabrication of the anti-dot structure and its derivatives, and Chapter 4 discusses the performance of its related SOFC electrodes.

## **1.4 Three-Dimensional Structures and Their Fabrication by CELD**

Using the anti-dot structure as a starting point for the fabrication of high surface area three-dimensional structures, several specific, more optimized architectures can be considered, as in Fig. 1.5. Cathodic electrochemical deposition (CELD) is an ideal candidate to produce template-free high surface area structures, as well as templated frameworks like inverse opals (Fig. 1.5c and d) and nanowires/tubes (Fig. 1.5e). As a testimony to their flexibility, anti-dot based substrates can also accommodate new and old approaches such as screen printing [39], pulsed-laser deposition (PLD) [40], chemical vapor deposition (CVD) [41], and CELD (c.f. Chapter 3).

### *1.4.1 SOFC Fabrication Method/Morphology Non-Negotiables*

Up to this point, only general SOFC materials/architectural design guidelines have been discussed, without reference to a particular method to produce such schemes. This section is devoted to the assessment of new fabrication techniques and their associated as-produced morphologies, to aid in their development.

Before any new fabrication method/morphology is adopted for SOFCs, a few non-negotiable requirements must be met. First, the fabrication method must be able to

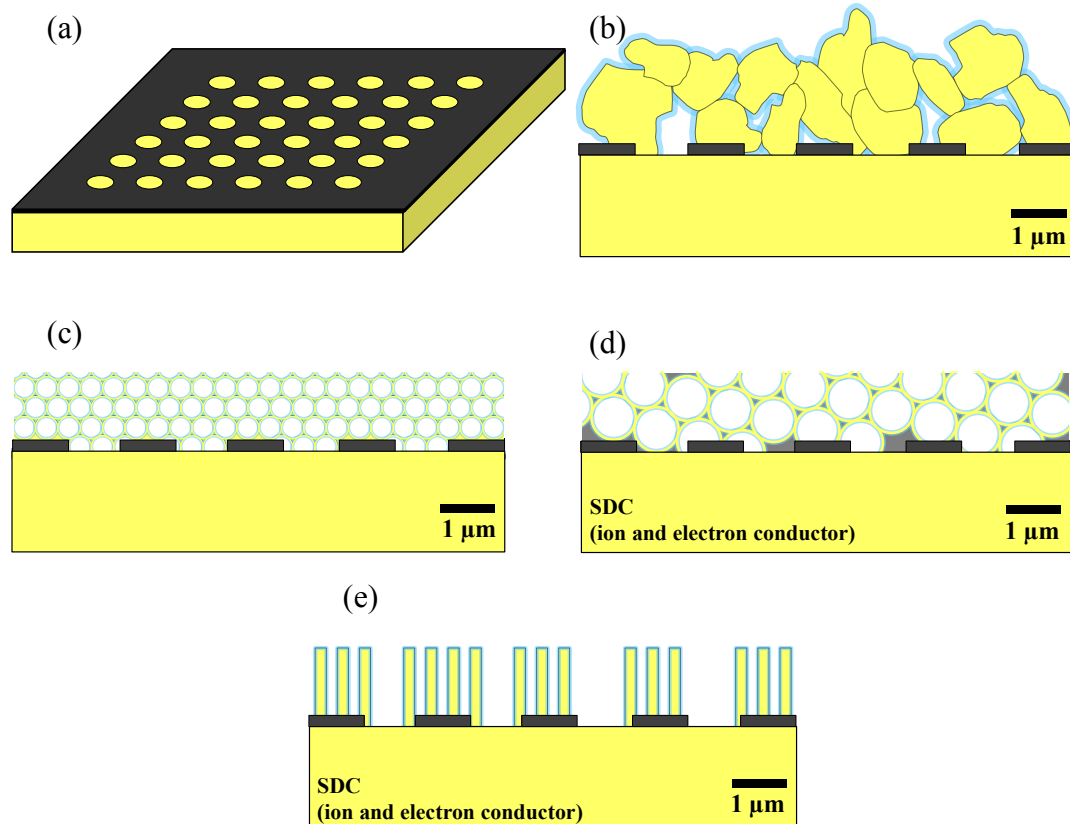


**Fig. 1.5.** (a) A schematic of a metal anti-dot network; (b) a cross-sectional depiction of the anti-dot film in (a) replacing metal powder as a current collector and thereby increasing the 2PB density; and examples of potential templated electrodes with tunable geometries like inverse opals (c) and (d), and nanowires (e).

consistently produce the desired materials composition. Keeping large-scale manufacturability in mind, basic repeatability is absolutely necessary. Second, the as-deposited morphology/microstructure cannot be adversely affected by SOFC operating conditions, e.g., high temperatures, oxidizing/reducing atmospheres, etc. This includes, for instance, cracking in electrolytes and agglomeration of small features in electrodes. Third, continuous and accessible migration pathways to and from surface reaction sites must exist in the electrodes. Of course, low resistance pathways are desirable, rather than only connected ones.

In this manuscript, cathodic electrochemical deposition is evaluated as a components fabrication tool for a SDC-based, intermediate temperature SOFC.

#### 1.4.2 *Cathodic Electrochemical Deposition (CELD)*

CELD is a liquid-based, low temperature fabrication technique that is able to produce ubiquitous and conformal metal oxide/hydroxide coatings of tunable surface area at low capital and operational costs [42-43]. The experimental setup is straightforward (see Fig. 3.2): three electrodes are immersed in a liquid electrolyte—electrons flow out of the anode and into the cathode through the external circuit, and the reference electrode measures the cell potential but does not allow any current to flow through it. A working potential is applied, and the appropriate electrochemical reactions occur.

Being liquid-based makes CELD scalable as a batch process, and allows easy control of large substrates, even if irregularly shaped: appropriate operating configurations ensure uniform deposition on protruding and porous substrates alike. Furthermore, cation doping in liquid systems is simple [44-47], while the low operating temperatures diminishes the incorporation of undesirable impurities. Low temperatures and open, ambient conditions also reduce the experimental complexity, especially in regard to otherwise stringent substrate requirements. Other common metal oxide fabrication methods, such as CVD and PLD, typically involve *in situ* high temperatures with a background atmosphere of oxygen—prime conditions for unwanted oxidation of metallic substrate components, and risky due to the potential for impurity incorporation into the oxide phase. CELD is also favorable as a manufacturing process as deposition times are on the order of minutes, rather than hours or days. In addition to being explored

for general SOFC applications [48-52], CELD ceria has been previously studied for corrosion protective coatings [46, 53-56], superconductor buffer layers [44], powder synthesis for increased sinterability [57], and nanowire/tube fabrication [49, 58-59]. Aside from ceria, other SOFC-relevant materials have been produced using this method, such as BaTiO<sub>3</sub>, Nb<sub>2</sub>O<sub>5</sub>, ZrO<sub>2</sub>, LaMnO<sub>3</sub> [42], and Y<sub>2</sub>O<sub>3</sub> [60].

There are two general categories of oxide/hydroxide electrochemical deposition, defined by which electrode experiences the desired deposition, known as the working electrode. Anodic electrochemical deposition (AELD) directly oxidizes Ce<sup>3+</sup>(aq) ions to insoluble Ce(IV) [54, 61-62]. A stabilizing ligand must be added to the electrolyte solution to ensure that Ce(III) species do not precipitate prematurely. A fundamental limitation of this technique is that Ce<sup>3+</sup> ions must contact a surface that can conduct electrons away; as CeO<sub>2</sub> is generally insulating, AELD should only be able to deposit extremely thin films, on the order of tens of nanometers.

Cathodic electrochemical deposition, on the other hand, proceeds by a two-step process. First, the electrolyte solution becomes progressively basic as electrochemical reduction reactions of various electrolytic species occur due to the applied cathodic potential at the cathode|electrolyte interface. This is widely referred to as electrogeneration of base. Second, the newly-formed base induces chemical precipitation of Ce(III/IV) species, e.g. Ce(OH)<sub>3</sub> or hydrated CeO<sub>2</sub>, which are finally oxidized to the desired fluorite CeO<sub>2</sub> phase. It is somewhat surprising that a Ce(IV) deposit on the cathode could result from a nominally Ce<sup>3+</sup> electrolyte—this is a testament to the purely chemical nature of the deposition step. Restated, the nucleation and growth process here is non-Faradaic. One example reaction each from the electrogeneration of base and

precipitation steps is given in Eqns. (1.7) and (1.8), respectively, although a myriad of possibilities exist (see Chapter 3 for an in-depth discussion).



Detailed investigation of and results from the CELD of ceria microstructures are presented in Chapters 3 and 5. Performance analyses of CELD ceria-based SOFC anode structures are presented in Chapter 4.

## Chapter 2

# Anti-Dot Substrates

### 2.1 Polymer Sphere Lithography Background and Summary

Polymer sphere lithography and, in particular, nanosphere lithography have gained recent attention for a wide range of applications ranging from novel nanofabrication techniques and photonic crystals to superhydrophobic surfaces [8, 63-64]. Most often, because the polymer spheres are typically not treated prior to metal deposition, the resulting patterned film is limited to isolated locations corresponding to the interstices between the template beads [7, 65-66]. With control of the fabrication process, however, the film may form a fully interconnected, yet fully porous network, acquiring what has been termed an ‘anti-dot’ configuration [67-68]. Specifically, an ordered layer of monodisperse polystyrene (PS) spheres is first applied to the surface of a SOFC electrolyte material; afterwards, the spheres are radially etched in an oxygen plasma, so as to create vias between them. Metal is deposited using a line-of-sight deposition method that enables the still-round PS to serve as a lithographic mask. Upon removal of the polymer template, the desired anti-dot porous structure is obtained. This process is illustrated stepwise in Fig. 2.1.

The periodicity provided by polymer sphere self-assembly is not critically important for SOFC studies; however, sufficient knowledge of microstructural parameters is required, as is high temperature stability. Accordingly, both factors are evaluated below.

Essential to the success of the polymer sphere lithographic technique is achieving a single layer of the polymer spheres across the entirety of the substrate. Several

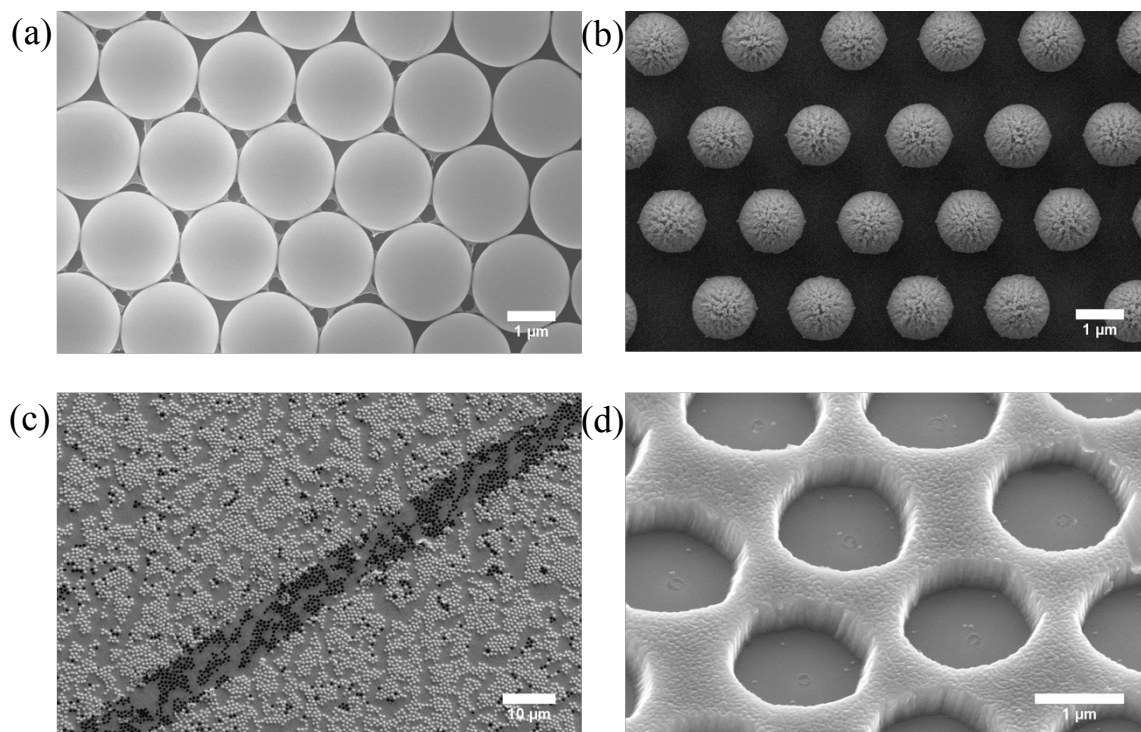


**Fig 2.1.** The polymer lithography process, all on YSZ: (a) a monolayer of 500 nm polystyrene (PS) spheres; (b) diameter of spheres reduced *via* oxygen plasma etching; (c) metal (Cu) deposited by thermal evaporation; (d) PS spheres removed.

approaches for monolayer deposition have been pursued in the literature, with varying degrees of complexity and experimental constraints. The most common methods are combined sedimentation plus evaporation [69-70]; spin-coating plus evaporation [71]; and controlled evaporation in combination with gradual substrate withdrawal from the solution (dip-coating) [72]. More exotic methods include electrophoretic assembly (suitable only to conducting substrates), and high pressure infusion in combination with ultrasonication [73-75]. While sedimentation, dip-coating, and spin-coating are relatively straightforward methods that produce structures with regularity sufficient for electrocatalysis studies, they suffer from the tendency of the processes to yield regions with multiple layers and others entirely devoid of the polymer spheres. Furthermore,

achieving adequate control of the evaporation step for the former two can require excessive processing times. With the exception of a dip-coating setup encased to provide strict humidity control [72], these methods have difficulty spanning the nanosphere-microsphere range; that is, any given polymer sphere deposition method works with either nanospheres or microspheres, but not both (note: PS spheres less than 1  $\mu\text{m}$  in diameter are herein referred to as nanospheres, whereas spheres greater than 1  $\mu\text{m}$  are referred to as microspheres).

Here, spin coating is employed as a facile means of obtaining the desired monolayers on YSZ and SDC substrates, where a slight variation of the standard spinning approach is necessary for microspheres. Utilization of electronically insulating substrates precludes electrodeposition as a means of subsequent growth of the metallic film, motivating the two-step process pursued here of bead etching and vapor phase metal deposition. For the plasma-etched spheres to serve as effective templates, it is necessary for film growth to be limited to line-of-sight methods that avoid deposition in the void space on the underside of the round beads. Thermal evaporation has been employed in this work for conventional metals (copper, nickel, titanium, titanium/gold, aluminum), whereas electron-beam evaporation has been used for platinum (due to its high melt temperature), with equal effectiveness in all cases. A representative selection of the types of anti-dot electrode structures obtained in this work is presented in Fig. 2.2. The ability to fabricate anti-dot structures from a range of metals on multiple electrolyte materials is essential for ultimate fundamental electrochemical studies.

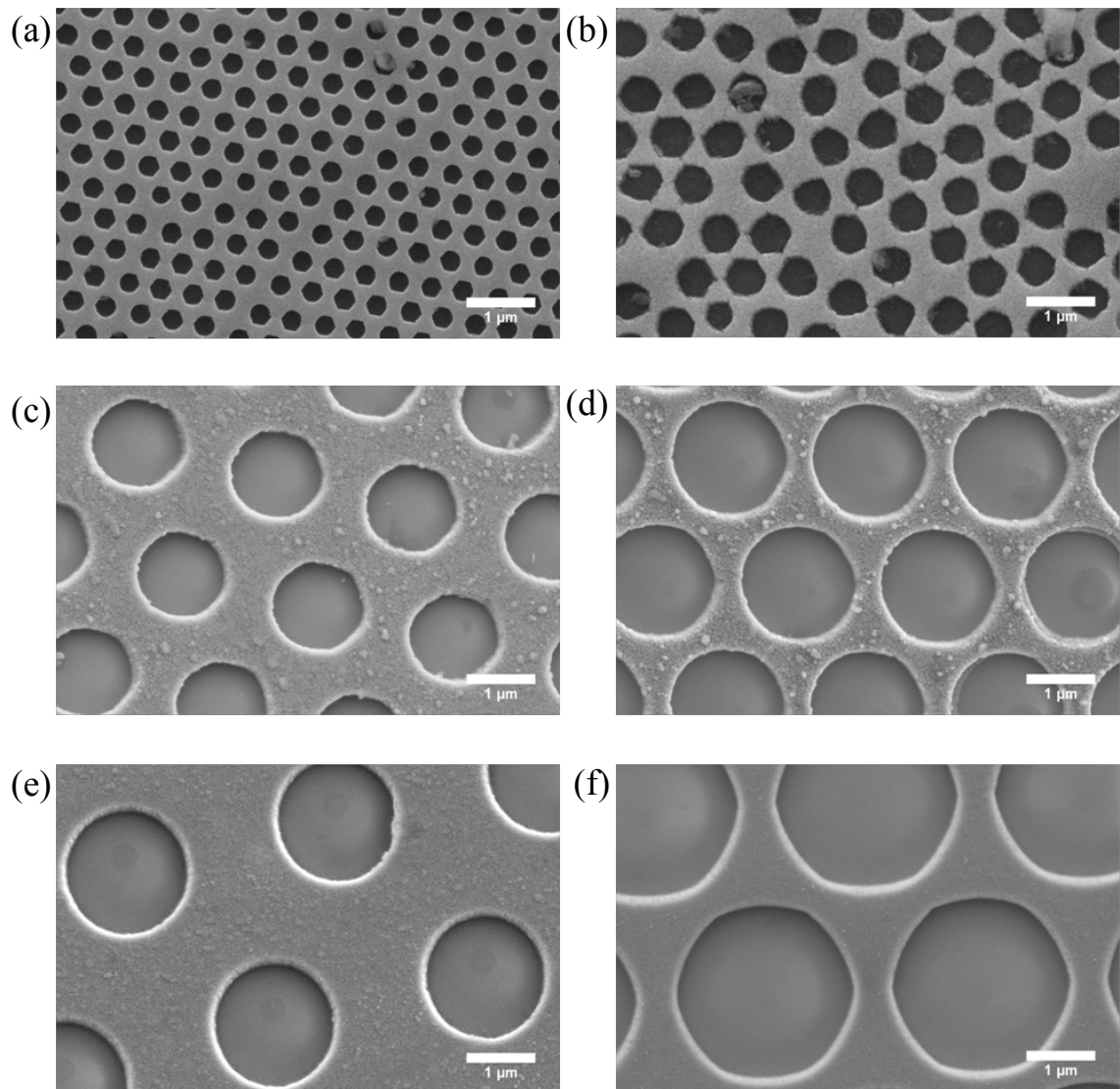


**Fig 2.2.** Selection of representative copper anti-dot metal films on YSZ showing a range of feature sizes achieved using polymer sphere lithography: (a) 500 nm initial bead size; (b) 790 nm initial bead size; (c) 2 μm initial bead size, heavily etched; (d) 2 μm initial bead size, lightly etched; (e) 3.2 μm initial bead size, heavily etched; and (f) 3.2 μm initial bead size, lightly etched.

## 2.2 Experimental Details

### 2.2.1 *Substrate Preparation*

The YSZ substrates (MTI Corporation) used are (100) single-crystals, and the SDC substrates are epitaxially deposited thin films on single-crystal YSZ via pulsed laser deposition [32]. For subsequent use for nanosphere deposition, the substrates were exposed to an oxygen plasma for 5 minutes at 75 W and 250 mTorr (Technics Planar Etch II) to enhance hydrophilicity. In contrast, as-purchased or as-fabricated substrates were directly used for microsphere deposition.

### 2.2.2 *Nanosphere Deposition*

Monolayers were spun using a Laurell, WS-400B-6NPP/LITE spin coater, with a 10 wt% suspension of PS nanospheres, surface functionalized with carboxyl groups (Bangs Laboratories, Inc.<sup>TM</sup>). Before spin coating on the substrate, the as-received PS suspension is sonicated to ensure the beads are homogeneously dispersed. Exactly 35  $\mu\text{L}$  of the suspension was manually spread over the entire 1 cm x 1 cm substrate before spinning. The final RPM of the spin coater was 3000 RPM, with varying accelerations depending on the starting PS diameter. The PS monolayer was radially etched in the same oxygen plasma system, but at elevated powers (75 – 200 W). In this step, the beads do not move from their original positions. Typical etching times were anywhere from 5 – 20 minutes.

### 2.2.3 *Microsphere Deposition*

Non-functionalized PS beads were used for the larger diameters (Thermo Scientific), as 10 wt %. 35  $\mu\text{L}$  of the PS suspension was manually spread over the entire substrate and

spun as before. The spin coater was spun at 4000 RPM. A standard laboratory spray bottle was used to employ the water-wash method, described in detail in Section 2.3.2. If the spin-wash-dry cycle was repeated too many times, immovable multilayers would form. For the 2  $\mu\text{m}$  spheres, the cycle was repeated 3 times; for the 3.2  $\mu\text{m}$  spheres, the cycle was repeated 6 times.

#### 2.2.4 *Metal Deposition*

An in-house constructed thermal evaporation system was used to deposit copper, nickel, titanium, titanium/gold, or aluminum (Alfa Aesar, 99.98+%) at  $10^{-5}$  Torr. Platinum networks were evaporated using an electron beam evaporator (re-manufactured CHA MK-40). The now covered PS beads were removed with an acetone-soaked cotton swab; regardless of the metal deposited, the surface became lustrous after wiping repeatedly, indicating the PS was gone.

#### 2.2.5 *Microstructure Analysis*

Optical photos were taken using a Nikon SMZ1500 stereomicroscope. Electron micrographs were taken on an LEO 1550VP Field Emission SEM. Atomic force microscopy (AFM) images were collected using a Park Systems XE-70 AFM. Image analyses were performed using ImageJ 1.41o freeware. Statistical data pertaining to anti-dot structural features was collected from a series of SEM photos that captured a little over 1% of the total substrate area, constituting 100-400 photos, depending on the magnification used. The number of pores evaluated per sample was 60,000-650,000: the

pore areas were assumed to be perfectly circular, and the diameters were calculated from the individual pore areas.

### 2.2.6 *High Temperature Stability*

Nickel networks 200 nm thick were brought to 600 °C under flowing 98.7% H<sub>2</sub> and 1.3% H<sub>2</sub>O and held there for 50 hours.

## 2.3 **Results and Discussion**

### 2.3.1 *Nanosphere Lithography Results*

Monolayers of as-purchased, carboxyl-functionalized polystyrene spheres with diameters less than 1 μm (specifically, 500, 680, and 790 nm) were prepared by spin-coating onto a hydrophilic surface (Fig. 2.3), where the optimal spin acceleration, ultimate spin rate, and dwell time were each found to depend on the sphere diameter. Non-functionalized beads displayed insufficient attraction to one another and, consequently, spin-coating resulted in large areas devoid of the template, despite exhaustive attempts at optimizing the spinning conditions. The next step, etching of polystyrene by oxygen plasma treatment, is well-known and was readily applied here [68]. It was observed that short treatments generate contacts between the spheres, presumably as a consequence of softening of the polymer. This undesirable ‘necking’ was avoided by longer treatments that remove at least ¼ of the original sphere diameter. Finally, in order to ensure the removal of the template without damage to the desired pattern, the film thickness is limited to approximately ½ the diameter of the etched spheres, with the further constraint that a minimum thickness of about 150 nm is required in order to attain acceptable electron transport properties in

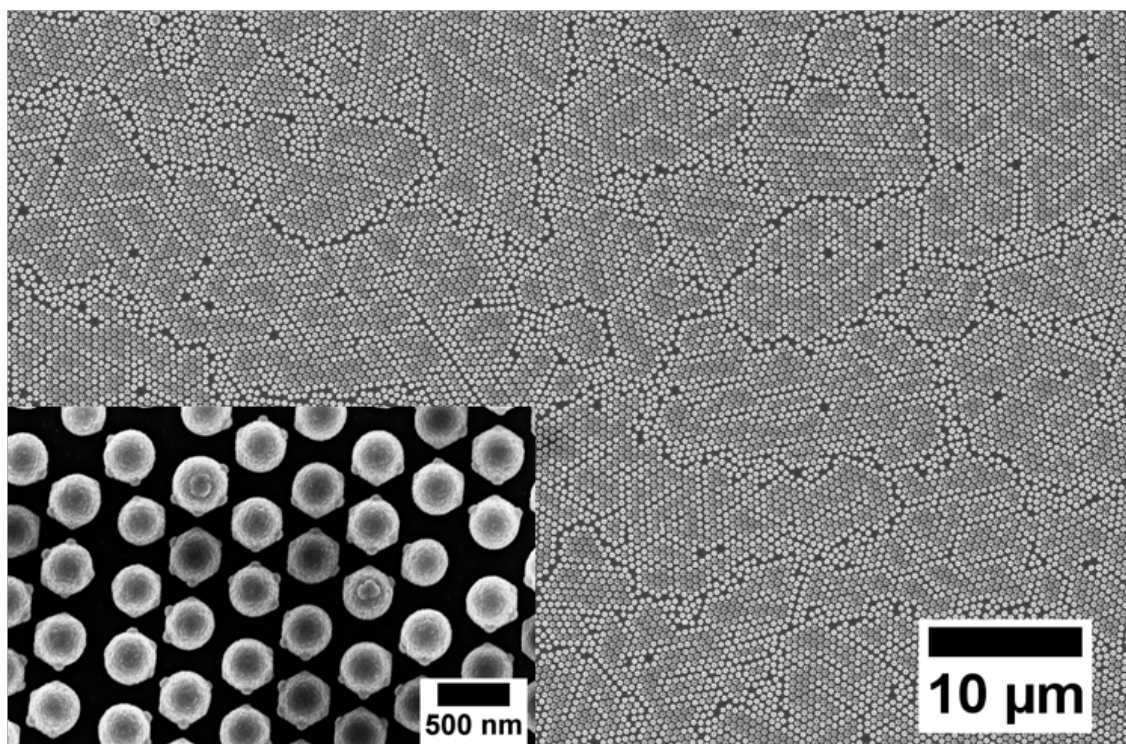


**Fig 2.3.** SEM images of etched PS beads of 500 nm initial diameter covering large areas of the substrate from a single spin coat step.

the porous film. These considerations preclude fabrication of useful anti-dot electrodes with PS spheres of less than 500 nm in diameter. Fig. 2.4 shows that qualitatively similar coverage is achievable with a variety of different PS sphere diameters.

### 2.3.2 *Microsphere Lithography Results*

In contrast to the deposition of nanospheres, no set of conditions could be identified for the preparation of a comprehensive monolayer of PS microspheres using a single spin-coating step. Under all accessible spinning conditions, functionalized PS microspheres assembled into irreversible multilayers (see SEM images in Fig. 2.5) that could not be modified for further use due to the line-of-sight nature of the metal deposition step. If metal deposition was pursued regardless of the presence of multilayers, unacceptable

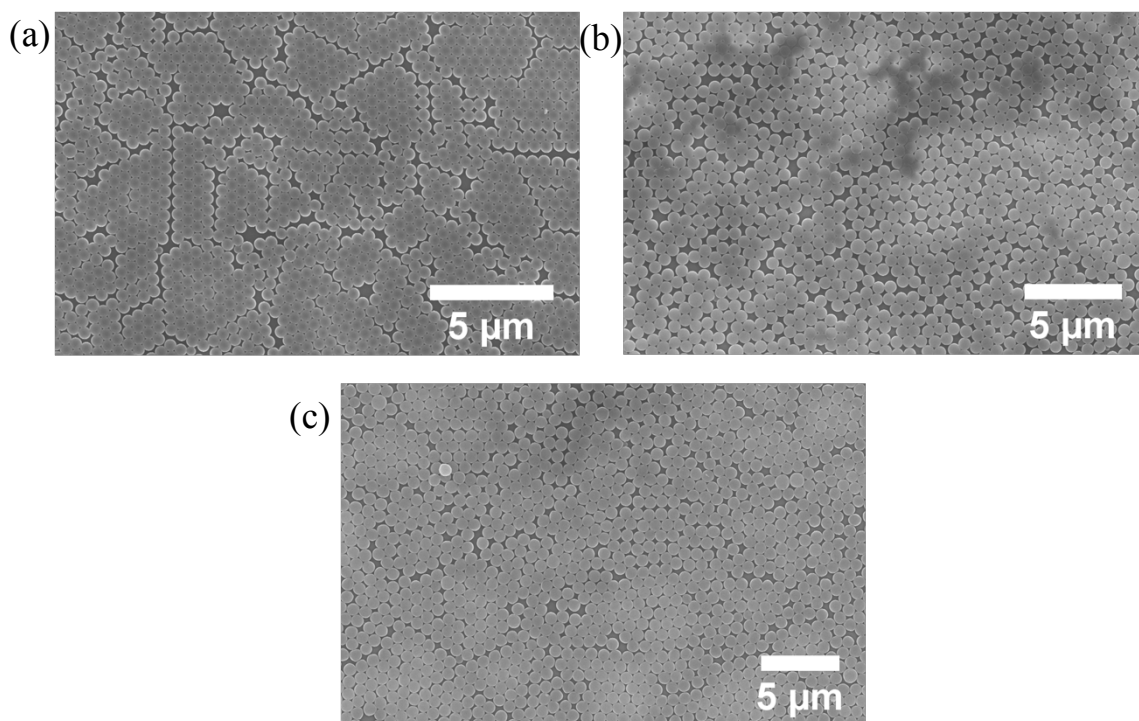


**Fig 2.4.** Substrate coverage via a single spin-coat for polystyrene nanospheres on YSZ: (a) 500 nm diameter; (b) 680 nm diameter; and (c) 790 nm diameter. Each image contains ~1200 beads.

levels of irregularity in the anti-dot films resulted, as in Fig. 2.5b. In contrast, at high spinning rates, non-functionalized PS microspheres formed monolayers, but with only partial coverage (see Fig. 2.5c), whereas at lower spinning rates multilayer regions emerged (particularly towards the edge of substrate), without elimination of the void areas. A low magnification optical image of such a dilemma is shown in Fig. 2.6, where multilayer regions (white portions) mark the border of the substrate, as well as covering a little less than half of the remaining interior; and void regions (dark areas, more easily seen in Fig. 2.6b) litter the entirety of the interior. The thick multilayer border region is of particular concern, as it can constitute up to 10% of the total substrate.

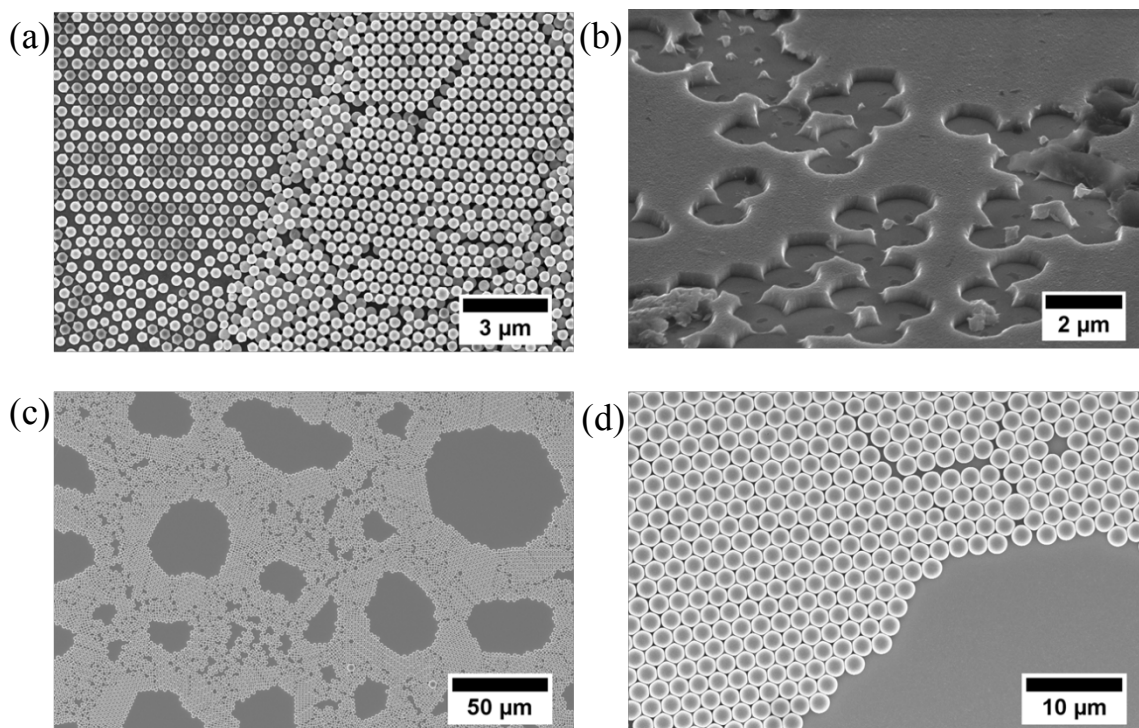


**Fig 2.5.** (a) Irreversible multilayers formed after a single spin coat of functionalized PS microspheres; (b) the resulting metal film porosity suffers from such multilayers; and (c) and (d) a single spin coat of non-functionalized PS microspheres formed monolayers on most parts of the substrate, but with a significant number of voids.

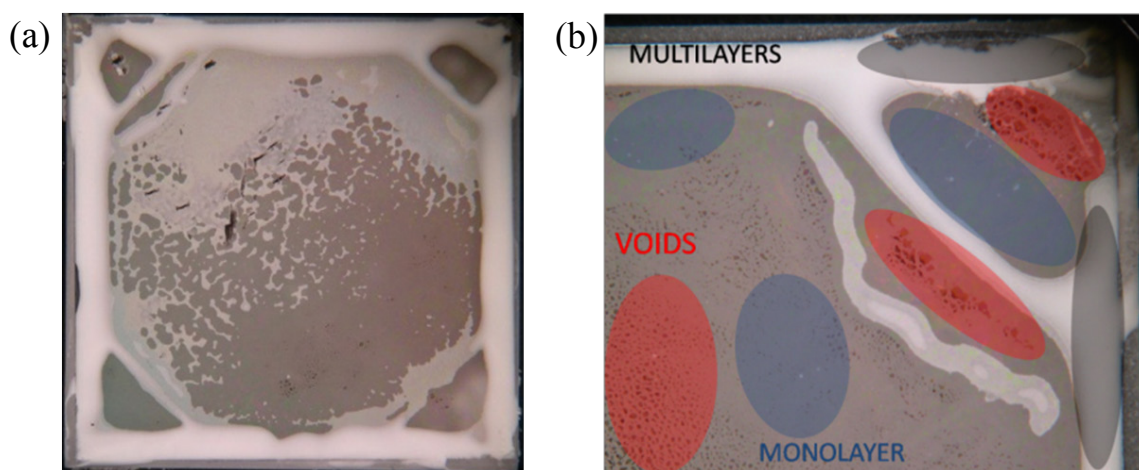


**Fig 2.6.** Optical photographs of the entire 1 x 1 cm YSZ substrate (a) and a zoomed in view of one corner (b) with a single spin coating of PS microspheres. The white regions are multilayers, the light gray regions are monolayers, and the dark regions are voids.

As an alternative to a single-step monolayer deposition procedure, a process was

developed employing multiple spin-coating steps of the non-functionalized PS beads, depicted in Fig. 2.7. Specifically, a substrate for which the first deposition has yielded a mixture of void regions, monolayer regions and multilayer regions is gently rinsed with water to remove the excess layers in the multilayer regions and the spin-coating is repeated to induce deposition in the void regions. The process is repeated multiple times until the void regions constitute less than about 10% of the substrate area, beyond which multilayer regions cannot be removed by a gentle rinse with water. In a final step, a small amount of the PS suspension is directly applied to the substrate and allowed to dry, eliminating the remaining void regions but with unordered sphere arrangement, as opposed to the relatively periodic arrangement produced by spin coating. For this reason, the spin coating step is repeated as many times as possible before this last step is applied, as disorder in the PS monolayer undoubtedly affects the 3PB/2PB densities. Fig. 2.8 exhibits the most extreme case of utilizing only one spin coat run, resulting in a large portion of the substrate being disordered.

Somewhat fortuitously, the build-up of multilayers causes the otherwise bleakly opaque PS monolayer regions to have a progressively whiter hue—this enables trouble areas to be identified on-the-spot and water-washed more thoroughly, allowing the majority of the void areas to be replaced by an orderly arranged PS monolayer via spin-coating. As will be explicitly shown in Section 2.3.3, the water-wash method produces sufficient coverage and ordering so as to give confidence in the predictability of the theoretical values of 3PB density and 2PB area fraction. As a consequence of these adaptations, microsphere anti-dot substrate preparation is easily repeatable with a high degree of accuracy.

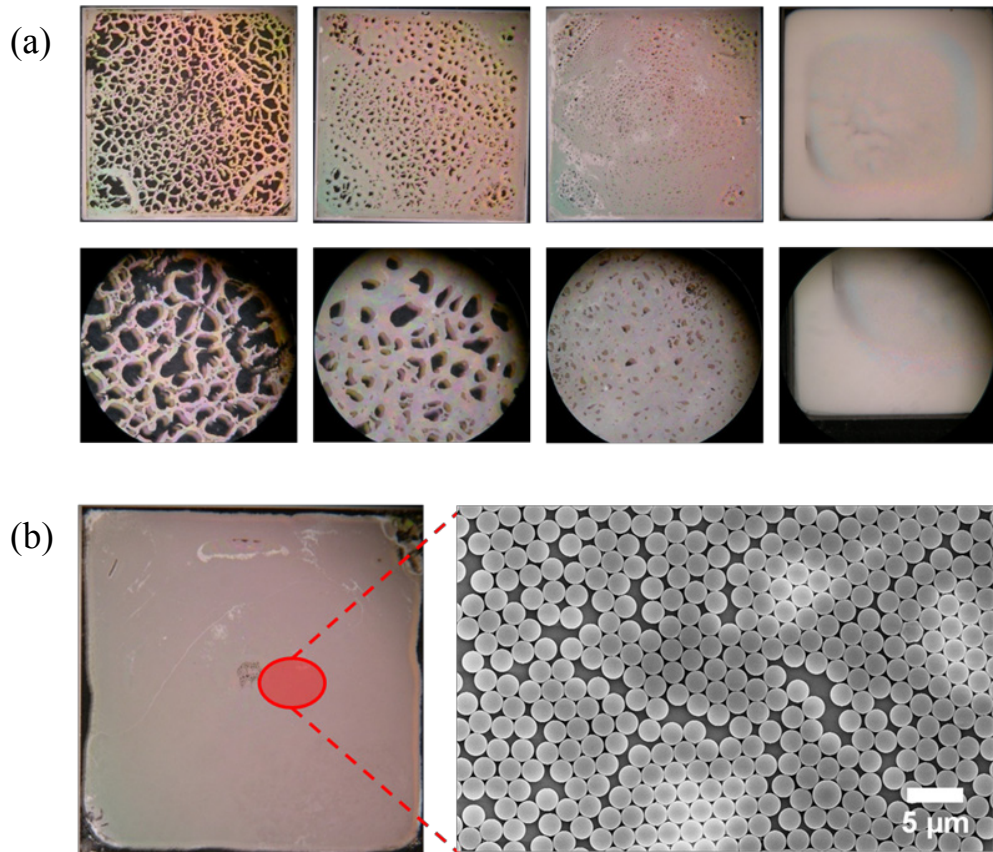


**Fig 2.7.** (a) The water-wash method utilizes sequential spin coats with water-washing in-between steps. 2  $\mu\text{m}$  beads shown here on a standard 1 x 1 cm YSZ substrate; (b) an optical photograph showing comprehensive monolayer coverage over the entirety of the substrate after the final multilayers are washed off, and a magnified SEM image of a monolayer of 2  $\mu\text{m}$  beads.

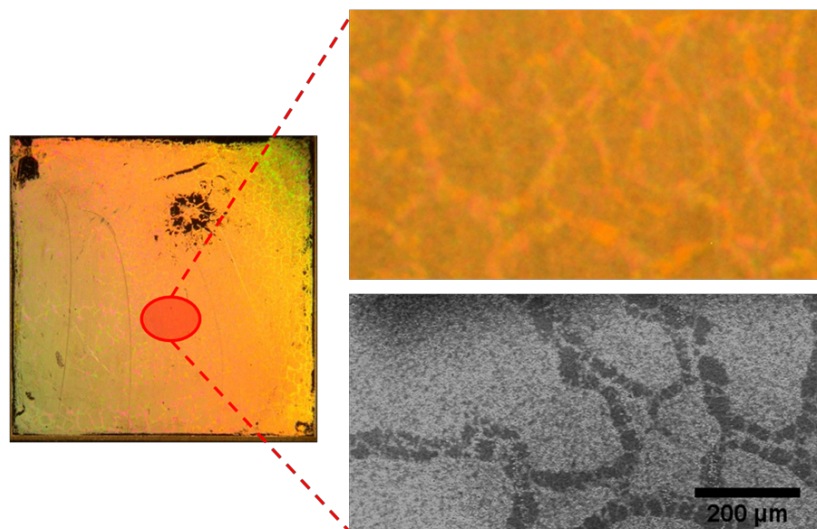


**Fig 2.8.** Optical and SEM images showing the result of utilizing only one spin coat step in the water-wash method. The darker regions in the SEM image correspond to relatively ordered arrangements of PS beads from the spin coat step; alternatively, the lighter regions correspond to unordered arrangements from the final evaporation step. The substrate shown here is 1 x 1 cm YSZ with gold metal.

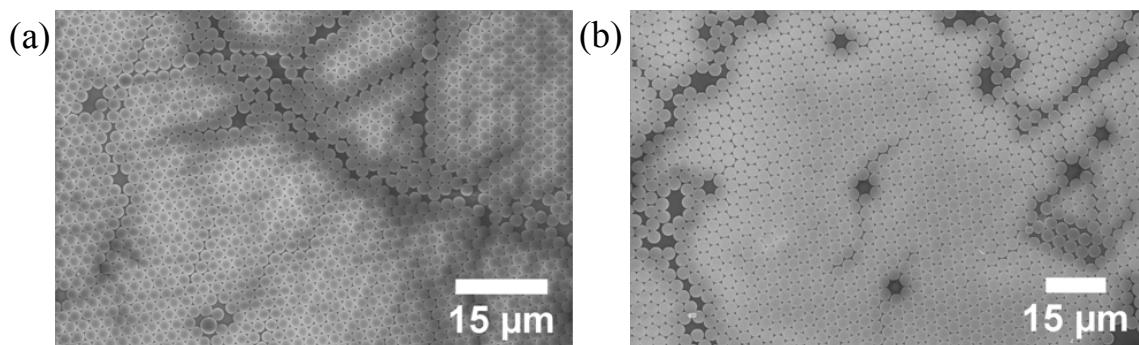


**Fig 2.9.** Monolayer substrate coverage via multiple spin and wash cycles of polystyrene microspheres on YSZ: (a) 2  $\mu\text{m}$ , and (b) 3.2  $\mu\text{m}$ . Both images contain  $\sim 1200$  beads.

By this method, it was possible to prepare comprehensive monolayers of PS beads up to 3.2  $\mu\text{m}$  in diameter with the same coverage quality as the nanospheres (compare the nanosphere coverage of Fig. 2.4 to the microsphere coverage of Fig. 2.9). After the microsphere monolayer deposition is complete, the subsequent plasma treatment, metal deposition and template removal steps then proceed as described for the nanosphere lithography, where, again, a minimum of  $\frac{1}{4}$  of the bead diameter must be removed in order to prevent necking during oxygen plasma treatment.

### 2.3.3 *Microstructural Fidelity*

Given the importance of three-phase boundaries for SOFC electrocatalysis, the 3PB areal density is a key parameter describing the microstructural features of these or any fuel cell electrode. A further important parameter in the case of the two-dimensional electrodes prepared here is the metal coverage, or inversely, the fraction of exposed electrolyte area, i.e., the 2PB areal density. With knowledge of these two parameters and an ability to tune them over a wide range, it becomes possible to achieve the goal of deconvoluting microstructural and compositional influences on electrocatalysis rates.

For a perfect micro-/nanosphere lithographic process in which the template beads display ideal periodicity over the entirety of the substrate, both the 3PB areal density,  $\rho_{3PB}$ , and the 2PB area fraction,  $f_{2PB}$ , can be computed from knowledge of the starting bead size and the extent of size reduction induced upon plasma etching. The theoretical values of these two quantities are given in equations 2.1 and 2.2, respectively, as functions of the initial ( $\phi_i$ ) and final ( $\phi_f$ ) diameters of the PS beads.

$$\rho_{3PB}^{theo} = \frac{2\pi}{\sqrt{3}} \left( \frac{\phi_f}{\phi_i} \right) \frac{1}{\phi_i} \quad (2.1)$$

$$f_{2PB}^{theo} = \frac{\pi}{2\sqrt{3}} \left( \frac{\phi_f}{\phi_i} \right)^2 \quad (2.2)$$

For an imperfect fabrication process, many kinds of defects exist—disordered regions of PS beads, multilayer and void areas (areal defects); grain boundaries between ordered regions (line defects); and singly missing PS beads within an ordered region (point defects). To assess the influence of these random structural elements, a continuous string of scanning electron microscopy (SEM) images (typically numbering from 100-400 images per sample) was collected from border to border for four representative films. From each image the following parameters were determined: the number and diameter of the pores, the metal|substrate interface length, i.e., 3PB length, and the exposed electrolyte area fraction, i.e., 2PB area fraction. The film characteristics and measured results are summarized below in Table 2.1 and Figures 2.10 and 2.11.

The distribution of pore diameters (Fig. 2.10) in the films was found to be rather narrow, with a Gaussian peak width that is  $\sim 2\%$  of the mean diameter. This distribution largely reflects the size distribution in the as-purchased PS beads, also about 2%, as oxygen plasma treatment was observed to remove material from the beads in a spatially uniform fashion, both radially and from bead to bead (Fig. 2.1b) [76]. In addition to the

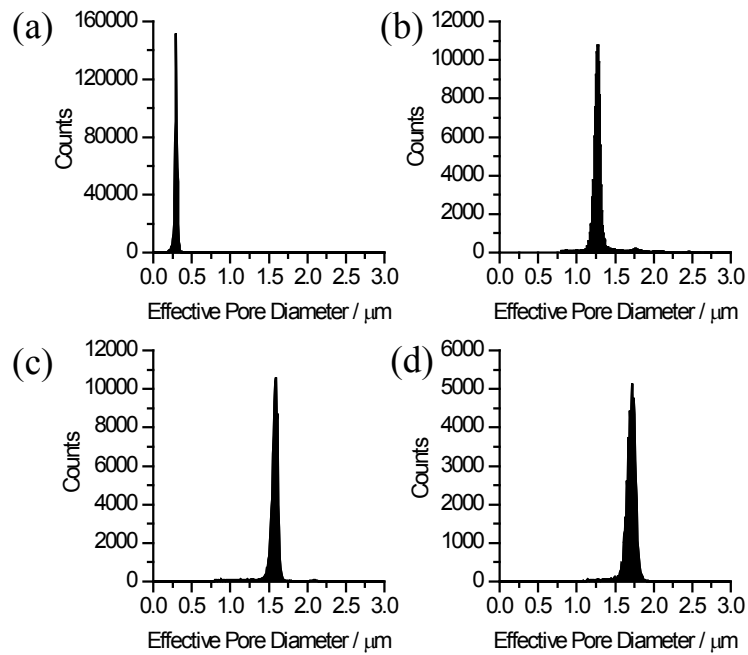


**Fig 2.10.** Pore diameter histograms of copper networks on YSZ, reflecting the different starting PS bead sizes: (a) 500 nm etched to 300 nm; (b) 2  $\mu\text{m}$  etched to 1.29  $\mu\text{m}$ ; (c) 2  $\mu\text{m}$  etched to 1.58  $\mu\text{m}$ ; (d) 3.2  $\mu\text{m}$  etched to 1.72  $\mu\text{m}$ .

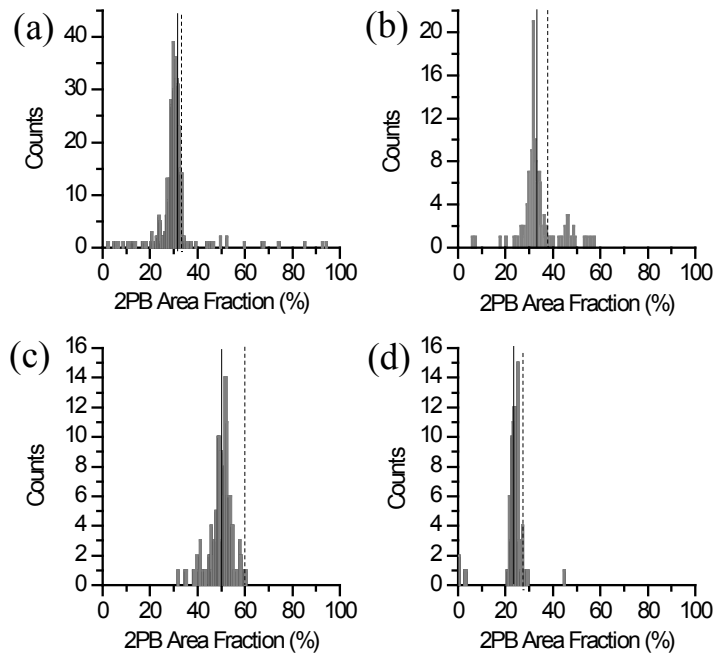


**Fig 2.11.** 2PB area fraction histograms of copper networks on YSZ, reflecting different starting PS bead sizes: (a) 500 nm etched to 300 nm; (b) 2  $\mu\text{m}$  etched to 1.29  $\mu\text{m}$ ; (c) 2  $\mu\text{m}$  etched to 1.58  $\mu\text{m}$ ; (d) 3.2  $\mu\text{m}$  etched to 1.72  $\mu\text{m}$ . Solid and dashed lines indicate the average and theoretical values, respectively.

pores represented in the histograms of Figure 2.10, a small number of pores with large diameters,  $> 3 \mu\text{m}$ , was also observed. These are taken to reflect regions in which multilayers of PS beads occurred, which prevents metal deposition over larger areas (c.f. Fig. 2.5b). For the PS with an initial diameter of  $2 \mu\text{m}$ , the number of these multilayer-induced pores is less than 1% of the total; for the  $3.2 \mu\text{m}$  initial diameter spheres, the number is less than 0.5%; and for the  $500 \text{ nm}$  spheres, the number is less than 0.1%. Aside from their statistical insignificance, the contribution of these large diameter pores to the overall  $\rho_{3PB}$  is confirmed to be small, as indicated by the good agreement between the theoretical and experimental values of this parameter, Table 2.1, and they are omitted from the plotted range for clarity.

The image-to-image variation in the 2PB area fraction (Fig. 2.11) shows that the variability in  $f_{2PB}$  is more significant than the pore diameter variability. The widest distribution in  $f_{2PB}$  is evident for the film prepared using  $500 \text{ nm}$  PS beads, where the standard deviation is 12% of the substrate area (i.e.,  $f_{2PB}$  is  $31.5 \pm 12.0\%$ ). Moreover, in all cases, the observed 2PB area was lower than that computed from the initial and final

**Table 2.1.** Comparison of theoretical and experimental 3PB length areal density and percent 2PB exposure for different initial PS bead diameters.

Initial bead diameter, $\phi_i/\mu\text{m}$	Final pore diameter, $\phi_f/\mu\text{m}$	Pore diameter Gaussian width/ $\mu\text{m}$	Theoretical 3PB length density/ $\text{m cm}^{-2}$	Experimental 3PB length density/ $\text{m cm}^{-2}$	Theoretical percent 2PB exposure	Experimental percent 2PB exposure	2PB exposure standard deviation
0.5	0.3	0.06	435	406	32.6%	31.5%	12.02
2	1.29	0.07	117	112.8	37.7%	33.4%	6.70
2	1.58	0.08	143	137.3	56.6%	49.7%	4.69
3.2	1.72	0.10	61	57.6	26.2%	23.5%	3.60

PS sphere sizes. This can be attributed to the occurrence of point and line defects in the PS two-dimensional crystals, as well as the presence of disordered regions in the monolayer. The statistics surrounding the two films prepared using PS beads with an initial diameter of 2  $\mu\text{m}$  suggest that line and point defects become increasingly important as the extent of etching is minimized. In the case of the film obtained from lightly etched PS beads ( $\phi_f = 1.58 \mu\text{m}$ ) there is a large difference between  $f_{2PB}^{theo}$  and  $f_{2PB}^{exp}$  (56.6 vs. 49.7 %). When the beads are more heavily etched ( $\phi_f = 1.29 \mu\text{m}$ ), the difference decreases, whereas the difference between  $\rho_{3PB}^{theo}$  and  $\rho_{3PB}^{exp}$  and the distribution of pore sizes for the two films are essentially the same. This behavior can be understood as follows. In the case of the lightly etched film, isolated missing beads (both point defects and dislocations behave as isolated, absent beads in a two-dimensional crystal) become a significant portion of the open area available for metal deposition, and, in this manner, such defects increasing in number dominate the coverage features.

The histograms of 2PB area display significant numbers of occurrences outside of what is roughly the main peak. As already indicated, regions with 2PB area below the mean occur as a consequence of defects in the two-dimensional crystals, i.e., voids in the PS bead array, whereas regions with higher fractions of 2PB area occur because multilayers form during the PS bead deposition process, i.e., excessive coverage of the substrate with PS beads. The 500 nm diameter nanospheres generate films in which slightly less than 10% of the regions display significant PS bead void areas, whereas 4% display multi-layered areas. In contrast, for both sizes of microspheres (2 and 3.2  $\mu\text{m}$ ) the regions affected by voids in the PS bead array are less than 5%, indicating that the multiple deposition process has more comprehensively filled the monolayer. The

occurrence of multilayer regions for the 2  $\mu\text{m}$  microspheres accounts for 11% of the regions imaged, whereas for the 3.2  $\mu\text{m}$  it is only 1%, suggesting that multi-layer removal becomes facile as the bead size increases.

Overall, despite the imperfection of the monolayer deposition process, the theoretical and experimental values, respectively, of  $f_{2PB}$  and of  $\rho_{3PB}$  agree quite well with one another, indicating that the fabrication is, in fact, rather controlled. Indeed, all of the experimental  $\rho_{3PB}$  values are within 93% of the theoretical, and this was found to hold irrespective of substrate employed or metal deposited. Accordingly, the geometric features of any sample prepared by the methodology presented here can, within a reasonable degree of certainty, be predicted from knowledge of  $\phi_i$  and  $\phi_f$ .

#### 2.3.4 *Thermal Stability*

An additional important characteristic of model fuel cell electrodes is thermal stability. That is, the 3PB length and 2PB area must not change during the course of a high-temperature electrochemical measurement. To evaluate thermal stability, nickel anti-dot networks were annealed at 600  $^{\circ}\text{C}$  for over 48 hours under humidified hydrogen, typical operating conditions for the anode of an intermediate temperature SOFC. SEM images reveal no discernable microstructural evolution as a consequence of the heat treatment (Fig. 2.12ab), whereas slight changes are visible in the atomic force microscopy (AFM) images (Fig. 2.12cd). Specifically, the nickel surface roughens, from a root mean square roughness of approximately 8 to 14 nm, and the grains undergo slight growth, in a direction limited largely to the surface normal. No other metal networks were subjected to high temperatures.

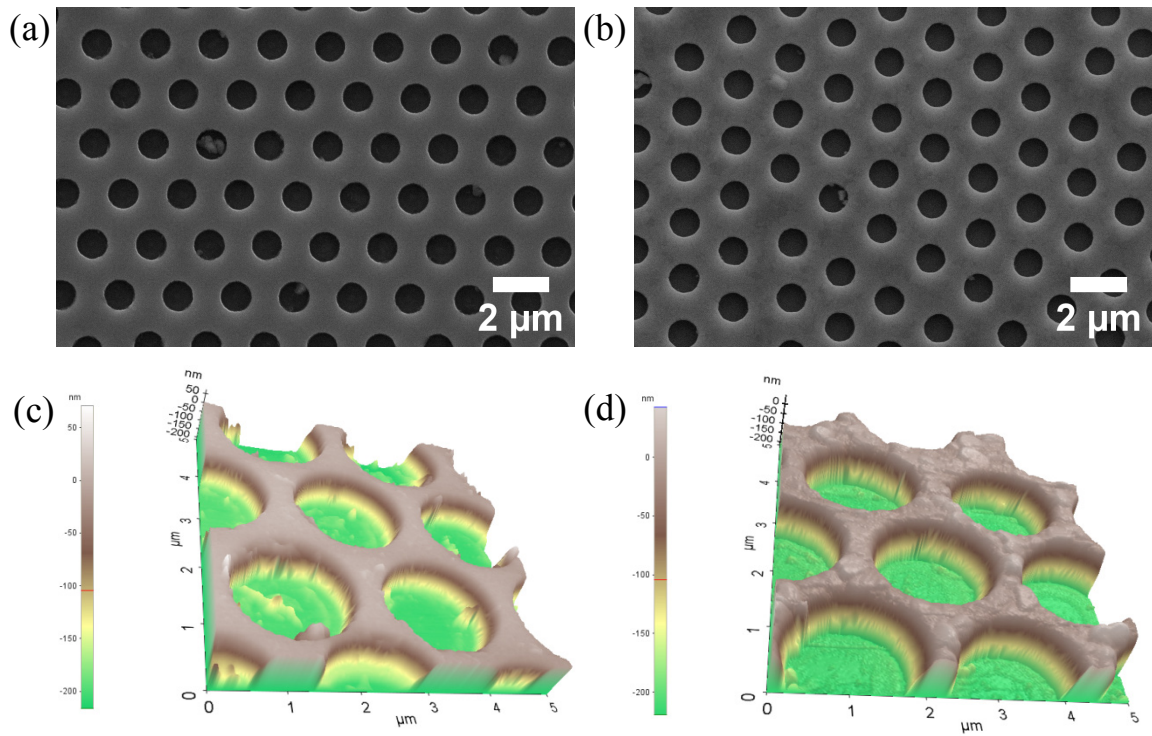


**Fig 2.12.** Images of an anti-dot porous nickel network (a) and (c) before thermal treatment at 600 °C under hydrogen ( $p_{H_2} = 0.1$  atm); and (b) and (d) after thermal treatment. (a) and (b) are top-down SEM images; (c) and (d) are AFM images.

# Chapter 3

## Cathodic Electrochemical Deposition of Undoped and Doped Ceria

### 3.1 Introduction

There are numerous reports in the literature regarding the CELD of ceria [45-46, 53, 55, 57, 77-83], including a handful that generally list SOFCs as potential applications, but with limited demonstration [48-52]. In addition, the contribution of electrogeneration of base to CELD is well-documented [42-43]. However, insight related to the crucial SOFC design criteria outlined in Section 1.4.1 is incomplete as most reports focus on as-deposited composition and characterization, which is a broad area of study by itself due to the large parameter space. Aside from grain growth evolution and brief mention in a few studies, high temperature data are largely missing [49-51, 78, 80, 83]. Perhaps most importantly, the vast majority of reports utilize non-porous, purely metallic substrates, which violate the continuous pathway for ionic species requirement. To the best of the author's knowledge, a composite conducting/non-conducting substrate is mentioned only once as a part of a larger study, in which the CELD of ceria was performed on a nickel/yttria-stabilized zirconia cermet, but was not explored in detail [45]. Therefore, this study assesses CELD according to (1) its compositional control, (2) the high temperature behavior of its coatings, (3) its ability to meet minimum SOFC configurational requirements, and (4) its potential for wide-ranging microstructural optimization. In so doing, the electrogeneration of base/chemical precipitation mechanism is validated with the assistance of others' previous works [55, 82, 84-86], and

new insights are gained regarding the roles of the working potential and the depositing species to the resulting microstructure, allowing a predictive, instead of haphazard, approach to future CELD work.

In order to explore the flexibility of CELD as a fabrication tool, a range of deposition conditions were examined, and a correspondingly wide range of reproducible morphologies were obtained. Rather than describe the entirety of those results, two primary types of morphologies are reported here—high surface area (HSA) coatings and thin, planar films. These two microstructures are evaluated in the context of the HSA coatings' ability to be used as electrode components and the thin, planar films' ability to be used as electrolyte components.

As a visual aid to understand the general deposition mechanism and to distinguish between the two experimental conditions probed in this chapter, a Ce-H<sub>2</sub>O-H<sub>2</sub>O<sub>2</sub> Pourbaix diagram is shown in Fig. 3.1, adopted from reference [85]. Pourbaix diagrams are pictorial representations of thermodynamic stabilities in the potential-pH parameter space, although they do not contain any kinetics information. Initially, with no applied potential, the pH sits in the range 2.5 – 4 (note that this diagram was constructed versus the natural hydrogen electrode (NHE), whereas the working potentials in this manuscript are referenced versus the standard calomel electrode (SCE), or +0.25 V vs. NHE). Once a working potential is applied, the state of the system moves along a straight horizontal line to the right, indicating that the electrolyte is becoming more basic. The black arrow on the right-hand side vertical axis of Fig. 3.1 shows the working cathodic potential for the HSA coating and the gray arrow indicates the working potential for thin films. The

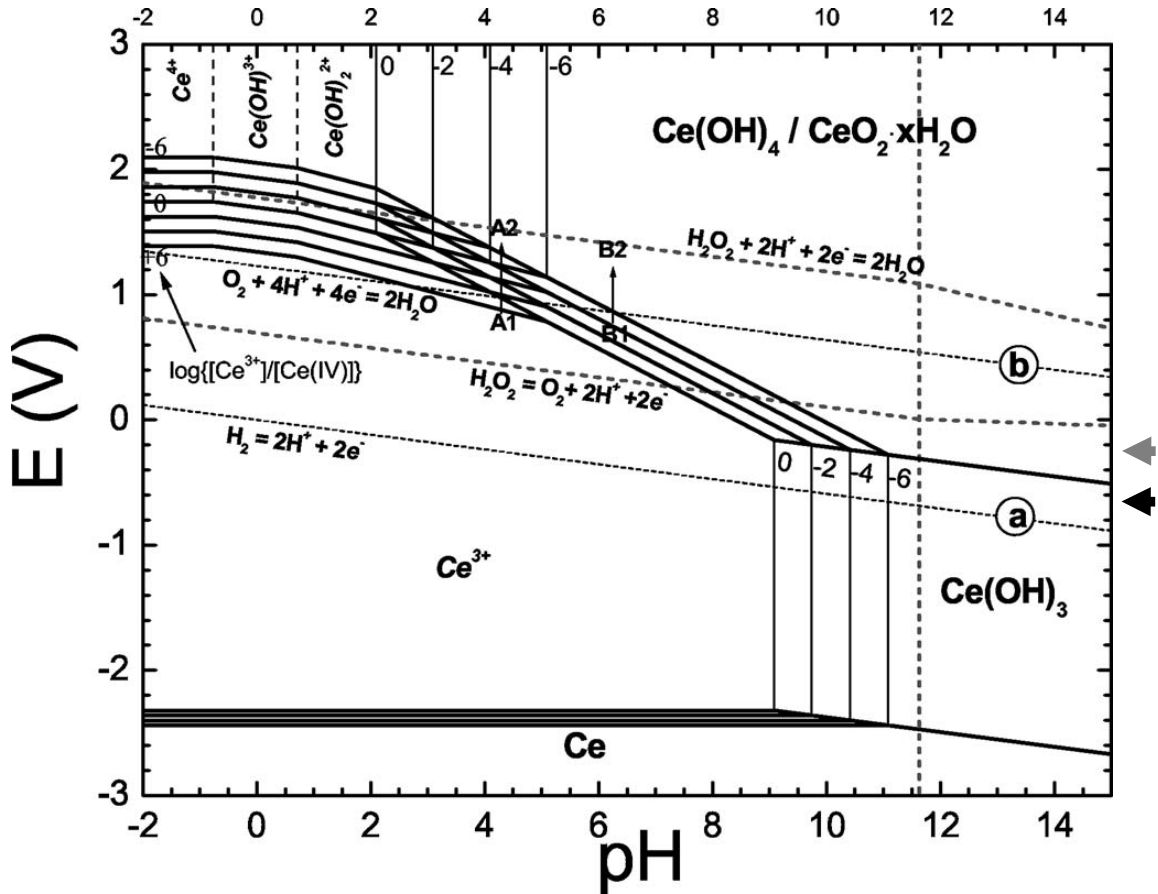


**Fig. 3.1.** Pourbaix diagram for the Ce-H<sub>2</sub>O-H<sub>2</sub>O<sub>2</sub> system, reprinted with permission from [86]. The black arrow on the right-hand side, vertical axis represents a typical HSA depositing potential (-0.8 V vs. SCE); the gray arrow represents the thin films' depositing potential (-0.55 V vs. SCE). Final interfacial pH values are ~10.5.

applied potentials are used for the two morphologies, regardless of the composition of the electrolyte solution.

## 3.2 Experimental Details

### 3.2.1 Substrate Definition

The primary type of substrates used was a composite substrate, comprised of a supporting YSZ base, on top of which various kinds of porous metal networks are overlaid. The

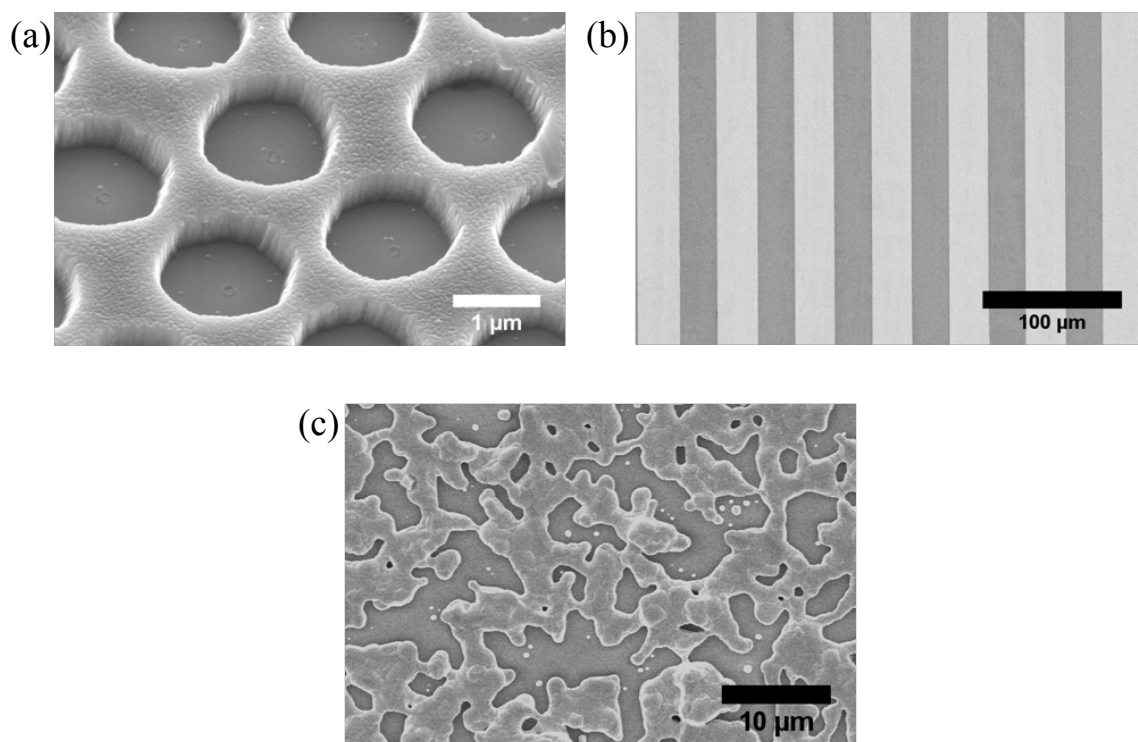


**Fig. 3.2.** Interconnected nickel anti-dot network (a), photolithographically defined platinum strip network (b), and platinum paste network (c) on single-crystal YSZ supporting substrates. The darker regions of each image are the exposed YSZ.

pores in the metal films are necessary to allow for oxygen ion flux, and connectedness in the metal networks is necessary to provide electronic conduction.

All reagents obtained were research grade. YSZ single-crystals (MTI Corp.), 1 cm x 1 cm x 0.5 mm, oriented (100) are used as the supporting substrates. On the surface of the YSZ, two primary porous metal network configurations are used. One, 400 nm thick nickel anti-dot films are made via polymer sphere lithography (Fig. 3.2a), the details of which are described in Chapter 2 of this manuscript. Two, 200 nm thick parallel platinum strips are made via conventional photolithography (Fig. 3.2b), obtained from Dr. Yong Hao, whose work is described in detail elsewhere [31]. The strips are electrically connected to one another by a platinum border near the edge of the YSZ substrate. Here, the widths of the platinum strips are made identical to each other and to the open spacing

between them, denoted by the shorthand 5-5 $\mu\text{m}$  and 10-10 $\mu\text{m}$ , indicating that the widths are 5 and 10  $\mu\text{m}$ , respectively. It should be mentioned that these lithographic networks allow both the metal and exposed YSZ surface areas to be specifically known, to a high degree of accuracy.

One additional, thicker metal network configuration is used, but only to test the high temperature annealing behavior of the deposits (Fig. 3.2c). Platinum paste (Engelhard 6082) is spread across the entire YSZ surface and allowed to dry for two hours, and then heat treated at 400  $^{\circ}\text{C}$  for 1 hour and 900  $^{\circ}\text{C}$  for 2 hours at 1  $^{\circ}\text{C min}^{-1}$  to remove residual organics and sinter the platinum particles together. This results in a spider-web-like network of platinum with feature sizes on the order of microns, necessary to prevent metal coarsening at higher temperatures from damaging the deposits.

To obtain large amounts of the deposits for bulk studies, 0.25 mm thick nickel foil substrates are used with depositions performed at 0.8  $\text{mA cm}^{-2}$  for 1-2 hours. The powdery deposits are subsequently scraped off of the nickel foil and gathered for analysis. Also, in order to image cross-sections of the thin film deposits, 350 – 400 nm thick nickel films are thermally evaporated onto 1 x 1 cm silicon substrates.

### 3.2.2 *Experimental Setup*

A traditional three-electrode cell, like the one schematically shown in Fig. 3.3a, is used with a standard calomel electrode (SCE) for a reference electrode, and a carbon rod for the counter (anodic) electrode, using a Solartron 1286 Electrochemical Interface for potentio/galvanostatic control.

Four different liquid electrolyte solution compositions are used, but they are all nitrate-based, with a total cation concentration held constant at 0.05 M. The first electrolyte solution contains undoped ceria with no additional additives, where the cerium nitrate concentration is 0.05 M—referred to as “undoped.” The second is samarium doped with no additional additives, where  $[\text{Sm}^{3+}] + [\text{Ce}^{3+}] = 0.05 \text{ M}$ , and the relative samarium content ranges from 4 to 50% of the cerium content—referred to as “Sm-doped.” The third is samarium doped, but also contains 0.025 M hydrogen peroxide as an additive—referred to as “Sm-doped +  $\text{H}_2\text{O}_2$ .” Hydrogen peroxide is reported to help with adhesion and promote Ce(IV) precipitation over Ce(III) [45, 48]. The fourth is samarium doped, but also contains 0.05 M acetic acid as an additive—referred to as “Sm-doped + acetic.” Acetic acid is most commonly employed in AELD as a stabilizing ligand, which helps prevent unwanted Ce(III)-based precipitation [54]. In the CELD case, the stabilizing ligand action of acetic acid has been previously utilized to simply retard the overall deposition rate, with the hypothesis that slower deposition rates would lead to denser, more adherent coatings [46]. This electrolyte solution is only briefly investigated, primarily in Section 3.3.3. The electrolyte solution compositions are summarized in Table 3.1.

**Table 3.1.** CELD liquid electrolyte compositions.

<b>Electrolyte Solution Name</b>	<b>[Ce(NO<sub>3</sub>)<sub>3</sub>]</b>	<b>[Sm(NO<sub>3</sub>)<sub>3</sub>]</b>	<b>[Additive]</b>
<b>Undoped</b>	0.05 M	0 M	n/a
<b>Sm-doped</b>	0.0498 M	0.002 M	n/a
<b>Sm-doped + H<sub>2</sub>O<sub>2</sub></b>	0.0498 M	0.002 M	0.025 M H <sub>2</sub> O <sub>2</sub>
<b>Sm-doped + acetic acid</b>	0.0498 M	0.002 M	0.05 M acetic acid

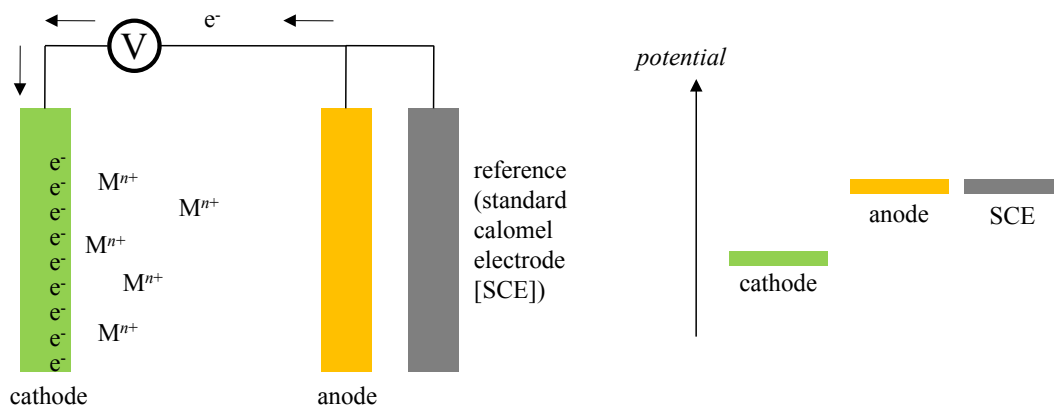


**Fig. 3.3.** Schematic representation (a) of the standard three-electrode liquid electrochemical cell used for CELD; and (b) the corresponding relative potential values.

The unadjusted, initial pH of the undoped and Sm-doped electrolyte solutions is around 4, whereas the Sm-doped +  $H_2O_2$  electrolyte solution is 2.5 – 3, and the Sm-doped + acetic electrolyte solution is 2.5. All electrolyte solutions are allowed to naturally aerate before each deposition, ensuring that an adequate measure of dissolved oxygen is incorporated. The depositions are conducted at room temperature, and over a metal surface area roughly equal to  $0.5 \text{ cm}^2$ .

First, high surface area (HSA) coatings are obtained in galvanostatic mode, at  $0.8 - 2 \text{ mA cm}^{-2}$ , deposited for 1 – 60 minutes, which corresponds to  $0.5 - 20 \text{ }\mu\text{m}$  thick coatings. The effective operating voltages for the HSA coatings are approximately  $-0.7$  to  $-1.0 \text{ V vs. SCE}$ . Second, thin, planar films are obtained in potentiostatic mode, at  $-0.5$  to  $-0.55 \text{ V vs. SCE}$ , deposited for 0.2 – 60 minutes, which corresponds to  $30 - 300 \text{ nm}$  thick films.

### 3.2.3 *Characterization Details*

Both as-deposited and annealed deposits are analyzed, with typical annealing temperatures ranging from 650 – 1000 °C for 10 – 24 hours, in 0.1% H<sub>2</sub> in Ar, or in ambient air. “Bulk” characterization results from deposits that are scraped off of nickel foil substrates (not patterns), to eliminate convolution of substrate effects. These coatings are deposited for relatively longer periods at the HSA working potential, but are identical in every other way to their thinner counterparts. X-ray diffraction patterns (XRD) are obtained using a Phillips X’Pert Pro powder x-ray diffractometer using Cu K $\alpha$  radiation (45 kV, 40 mA). Raman spectra are obtained with a Renishaw Ramascope (532 nm diode pumped laser) equipped with a Leica DMLM microscope, and FT-IR spectra are obtained using a Durascope Nicolet ATR system (KBr beam splitter). Thermogravimetric analysis is performed with a Netzsch STA 449 C. The electrolyte solutions are characterized using cyclic voltammetry (CV) at 50 mV s<sup>-1</sup> from 0 to -1.25 V vs. SCE, using the same Solartron 1286. The morphology of the coatings are imaged using scanning electron microscopy (SEM), with two different systems, a Zeiss 1550VP FE SEM equipped with an Oxford INCA x-ray energy dispersive spectrometer (EDS) and a Hitachi S-4100 FE SEM. Atomic-force microscopy (AFM) is used to measure the thin, planar films’ roughness with a Park Systems XE-70. Transmission electron microscopy (TEM) is performed on a FEI Tecnai F30UT operated at 300 kV, with the lift-out performed on an Omniprobe Autoprobe 200 (the lift-out procedural details are summarized elsewhere) [87-88].

### 3.3 Results

#### 3.3.1 Bulk

Fig. 3.4 shows the as-deposited and annealed XRD patterns for typical CELD ceria deposits, both for the undoped and Sm-doped electrolyte solutions. These particular deposits were obtained at  $0.8 \text{ mA cm}^{-2}$ , approximately corresponding to  $-0.8 \text{ V vs. SCE}$  (the Sm-doped, Sm-doped +  $\text{H}_2\text{O}_2$ , and Sm-doped + acetic electrolyte solutions give qualitatively identical XRD patterns). In all cases, both the as-deposited and annealed deposit patterns show a cubic fluorite structure, indicating that  $\text{CeO}_{2-\delta}$  is the primary phase at this working potential, regardless of the temperature history or annealing atmosphere. Similar behavior has been observed in the literature [53, 77]. The as-deposited patterns are shifted to slightly lower diffracting angles, indicating some level of Ce(III) content that is afterwards oxidized to Ce(IV) upon annealing. The lattice constants of the doped films post-annealing can be used to determine how much samarium is incorporated into the ceria structure. The measured samarium doping levels in the deposits are compared to the nominal samarium doping levels in the electrolyte solution, and are plotted in the inset of Fig. 3.4. Also shown are the EDS compositional analyses. It is evident that the concentration of samarium in the films is greater than the concentration of samarium in the electrolyte solutions. From these results, a solution samarium relative concentration of 4.6% is chosen in order to obtain a target deposit composition of  $\sim 12\%$ , which is a desirable doping level in terms of optimal oxygen ion conductivity.

Some ambiguity in the literature exists with regard to the as-deposited crystal structure, as both crystalline  $\text{Ce}_2\text{O}_3$  and  $\text{Ce}(\text{OH})_3$  are possibilities, although some of the

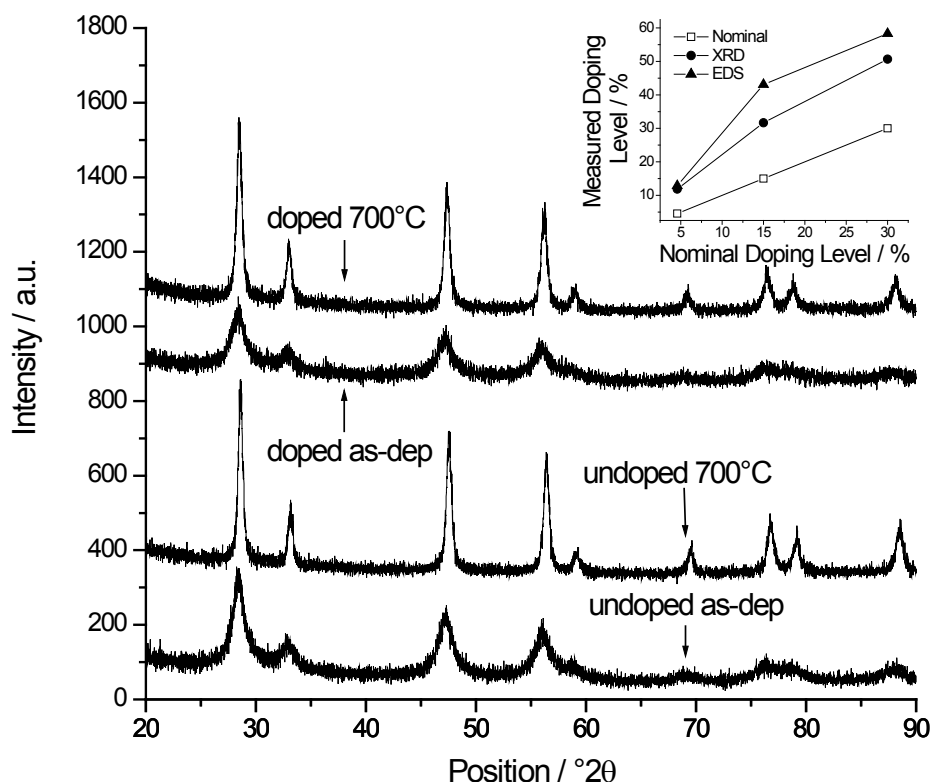


**Fig. 3.4.** As-deposited and annealed XRD patterns for the undoped and doped electrolytes, deposited at  $0.8 \text{ mA cm}^{-2}$  ( $\sim -0.8 \text{ V vs. SCE}$ ). The annealed patterns are identical in both  $0.1\% \text{ H}_2$  in Ar and ambient air annealing atmospheres. Also shown is the doping level measured in the coatings by XRD and EDS vs. the doping level in the liquid electrolyte (inset).

variance can be explained by differing operational parameters that greatly affect the precipitating species.  $\text{Ce}_2\text{O}_3$  has distinct XRD peaks from  $\text{CeO}_2$ , and it is clear that those peaks are absent here, in contrast to a report where traces were detected [59]. On the other hand,  $\text{Ce}(\text{OH})_3$  shares some large-intensity peak positions with  $\text{CeO}_2$ , differing by less than one degree of each other, which convolutes shifting that is solely due to mixed valency in the  $\text{CeO}_2$  phase. However, among other missing peaks, a particularly highly-diffracting  $\text{Ce}(\text{OH})_3$  peak at  $\sim 39.5^\circ$  is missing in all of the as-deposited patterns, strongly suggesting that  $\text{Ce}(\text{OH})_3$  is not the diffracting phase. Furthermore, the fact that the

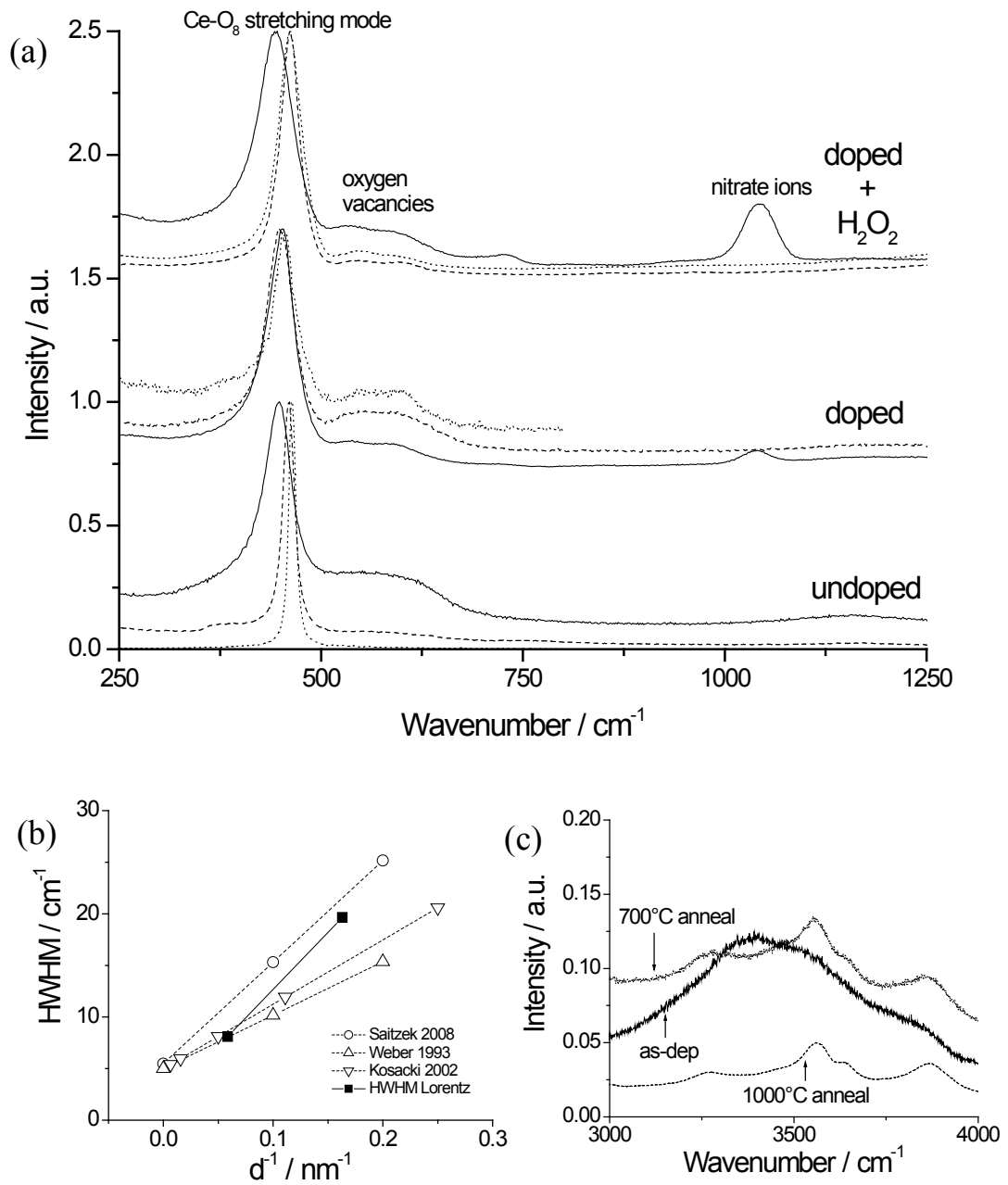


**Fig. 3.5.** Raman spectra (a). Top group: doped +  $\text{H}_2\text{O}_2$  electrolyte; solid line is as-deposited, dashed line is 700 °C annealed, dotted line is 1000 °C annealed. Middle group: doped electrolyte; solid line is as-deposited, dashed line is 700 °C annealed, dotted line is doped ceria reference powder. Bottom group: undoped electrolyte; solid line is as-deposited, dashed line is 700 °C annealed, dotted line is undoped ceria reference powder. (b) HWHM vs. crystallite size for the undoped electrolyte with literature comparison. (c) Hydration peaks for the doped electrolyte—the relative intensity decreases after annealing. All annealing is under ambient air conditions.

annealed patterns are simply shifted versions of their as-deposited counterparts reinforces this notion.

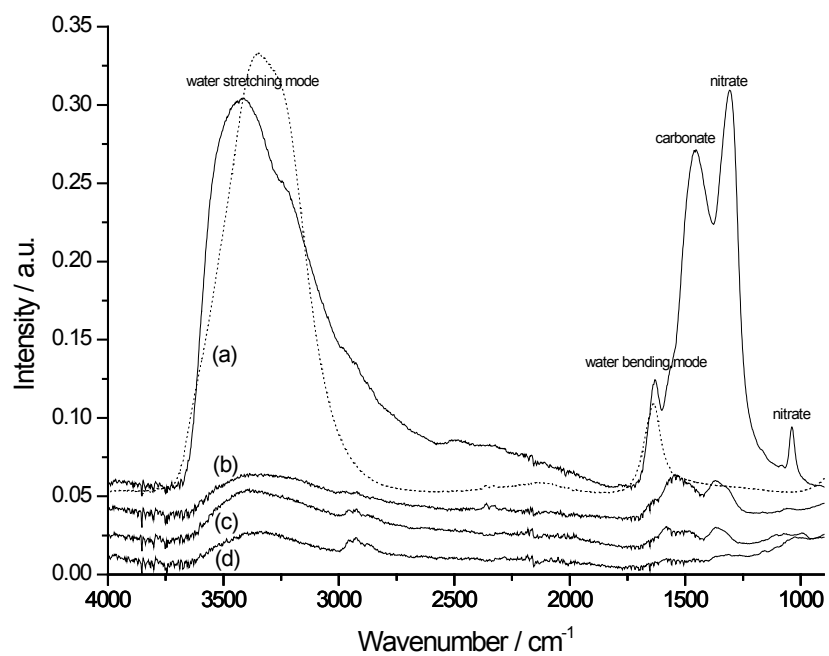
The as-deposited peaks are broader than the annealed peaks in every case, indicating grain growth at high temperatures. Using the general Scherrer equation ( $D = 0.9\lambda/\beta\cos\theta$ ), where  $D$  is the crystallite size,  $\lambda$  is the x-ray wavelength,  $\beta$  is the adjusted full-width half max of the peak at position  $2\theta$ , the as-deposited crystallite size is determined to be approximately 6 nm, which increases to 15 – 20 nm after annealing at 700 °C for 10 hours in either reducing or oxidizing atmospheres. This is in good agreement with others' CELD of ceria findings [78, 83]. The undoped results are summarized in Fig. 3.5b, where the half-width at half-max of the Raman peak at  $\sim 466\text{ cm}^{-1}$  is plotted against the inverse of the crystallite size. The sizes obtained in this work even correspond well with undoped ceria obtained by other fabrication means [89-91].

Fig. 3.5a shows the Raman spectra obtained for all three electrolyte solutions as-deposited and annealed at 700 °C, as well as undoped and Sm-doped reference spectra, and one scan of a Sm-doped + H<sub>2</sub>O<sub>2</sub> sample annealed at 1000 °C. All of the spectra share a main Ce-O stretching mode peak centered at  $\sim 466\text{ cm}^{-1}$  [89-91], which shifts upon samarium doping [46, 50]. As can be seen, the annealed undoped and Sm-doped main peaks agree well with their respective references. This band can also reportedly shift up to  $\sim 10$  wavenumbers due to nanoscale crystallite size effects [58, 91-92], which could partly explain why the Sm-doped and Sm-doped + H<sub>2</sub>O<sub>2</sub> as-deposited peaks are shifted from one another. The exact doping level in the deposits could also be slightly different for these two electrolyte solutions. A band at  $\sim 600\text{ cm}^{-1}$  indicates oxygen vacancies in the ceria lattice [46], which is seen in all of the Sm-doped and Sm-doped + H<sub>2</sub>O<sub>2</sub> scans, as

well as the as-deposited undoped sample. The origin of this peak is the samarium doping in the Sm-doped electrolyte solutions' cases, and partial Ce(III) content in the as-deposited undoped case, whose peak disappears upon annealing. These data agree well with the XRD results. Also, oxygen vacancies have been known to shift the main Ce-O peak, perhaps explaining the lack of movement from as-deposited to annealed samples with the Sm-doped electrolyte solution. The bands centered at  $\sim 740$  and  $1049\text{ cm}^{-1}$  are attributed to nitrate ions [53], and they disappear upon annealing, as expected.

In the  $3000 - 4000\text{ cm}^{-1}$  range, a broad multi-peak exists for all of the electrolyte solutions' as-deposited samples, depicted for the Sm-doped electrolyte solution in Fig. 3.5c. A peak in this range indicates some O-H inclusion in the deposit, either as  $\text{H}_2\text{O}$  or hydroxides. The distinction between the two, particularly for  $x\text{H}_2\text{O}\cdot\text{CeO}_2$  and  $\text{Ce}(\text{OH})_4$  is subtle [56, 92], and unimportant for the ultimate aim of this work. What this peak does indicate, however, is that there is some hydrated content in the as-deposited samples, even though the XRD patterns exhibit the cubic fluorite structure. After annealing to  $700^\circ\text{C}$ , these Raman peaks decrease in relative intensity and appear to reach a steady-state, possibly indicating some grain boundary and/or unavoidable powder surface hydration.

Selected FT-IR spectra are shown in Fig. 3.6. All depositions give qualitatively identical spectra, so only the Sm-doped case is shown. These results show further evidence of hydration of the as-deposited material. The as-deposited scan (Fig. 3.6a) exhibits two peaks attributed to OH stretching ( $\sim 3600\text{ cm}^{-1}$ , broad) and bending ( $\sim 1640\text{ cm}^{-1}$ , sharp) modes, that are shared with liquid water, shown for reference in Fig. 3.6 as the dotted line. Additionally, carbonate ( $\sim 1450\text{ cm}^{-1}$ ) and nitrate ( $\sim 1300$  and  $1040\text{ cm}^{-1}$ ) peaks are identified [53]. Fig. 3.6c and 3.6d are spectra from Sm-doped deposits annealed



**Fig. 3.6.** FT-IR spectra for the doped electrolyte. (a) As-deposited (solid line) and liquid water droplet (dotted line) overlaid; (b) doped ceria powder reference; (c) 700 °C annealed; and (d) 1000 °C annealed.

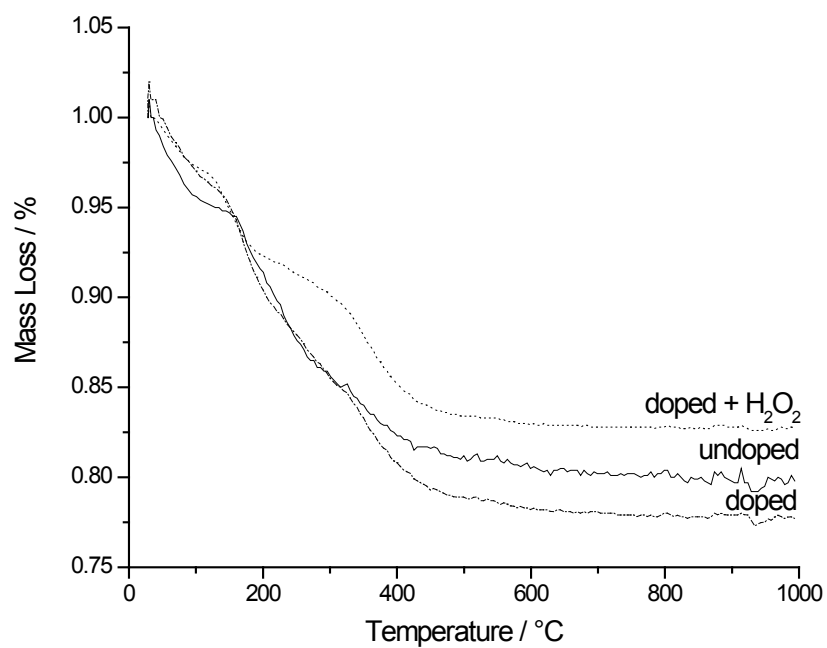


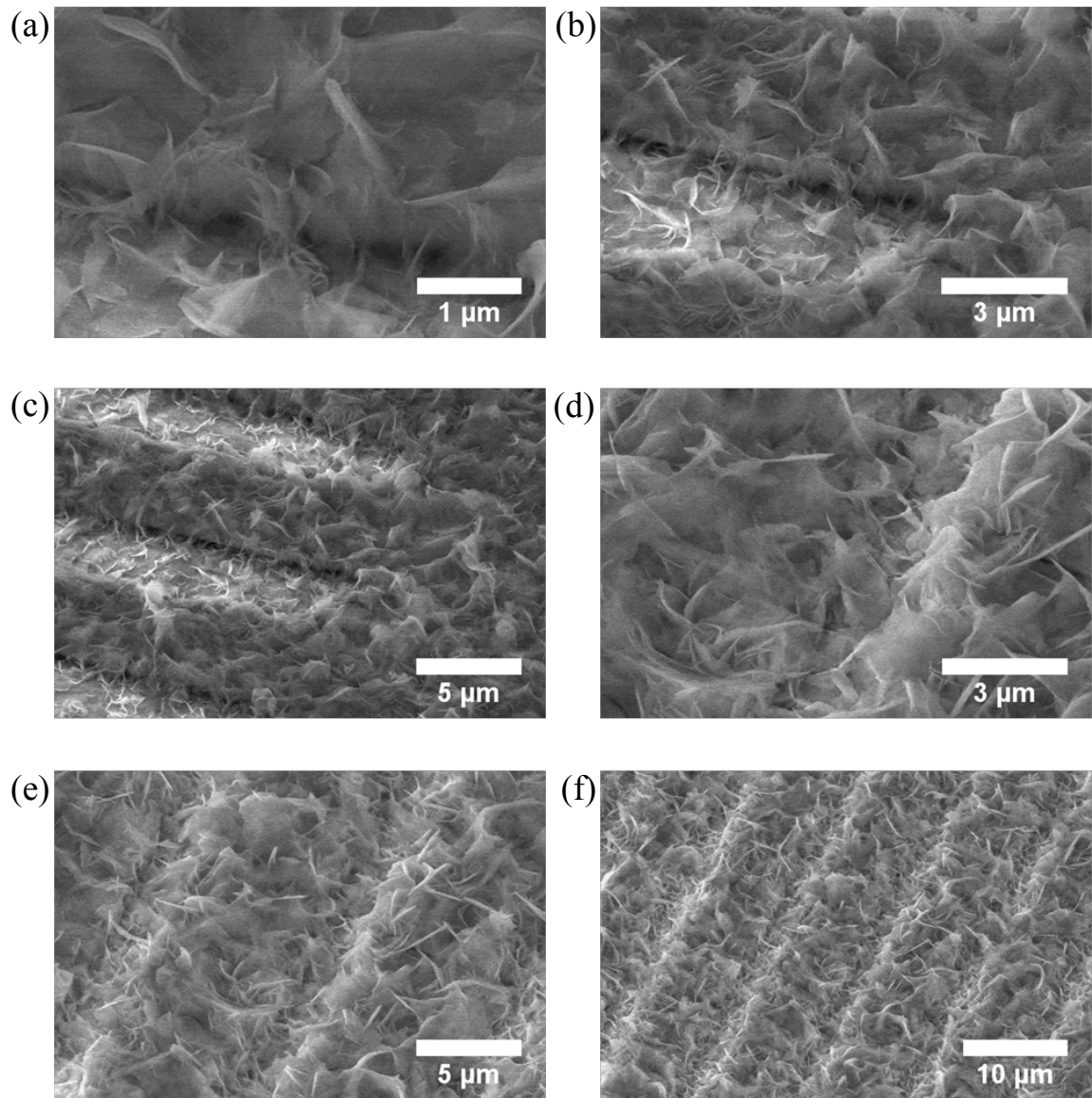
**Fig. 3.7.** TGA weight loss for three electrolytes. Final weight loss ranges from 13-21%.

at 700 and 1000 °C, respectively, showing all peaks dramatically losing intensity, consistent with the XRD and Raman results. The spectra from the annealed deposits correlate well with a SDC reference spectrum (Fig. 3.6b). TGA measurements underscore these data, showing significant weight loss (~13-21%) upon heating (Fig. 3.7) [48, 78]. From the previous results, this is probably due to a combination of hydration, nitrate, and carbonate removal.

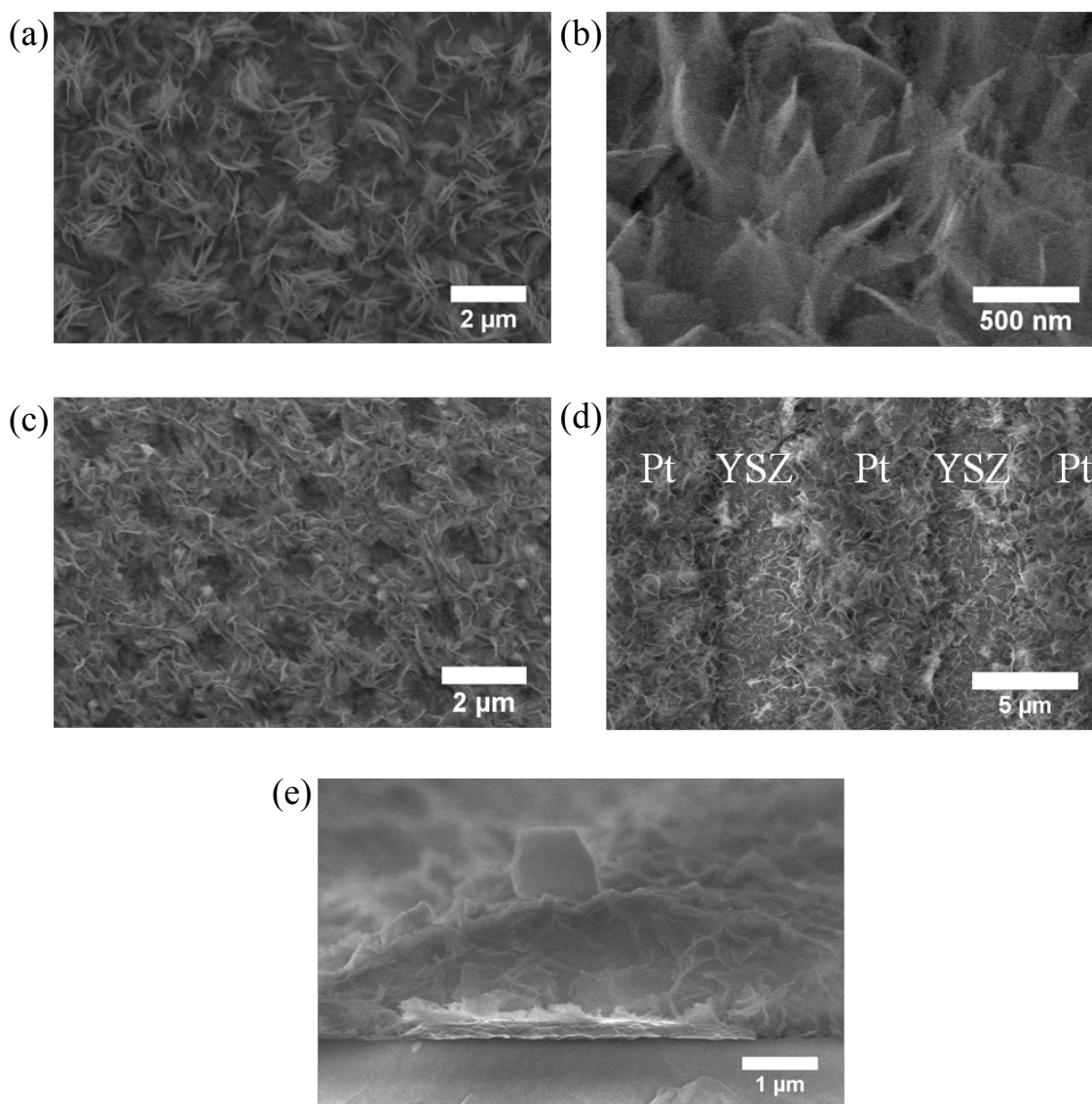
### 3.3.2 High Surface Area (HSA) Coatings

Fig. 3.8 and Fig. 3.9 show representative SEM images of a HSA coating deposited at 0.8 mA cm<sup>-2</sup> on various substrates with the undoped and Sm-doped electrolyte solutions, respectively. The microstructure appears to consist of an overlapping, intersecting combination of needle-like and nano-sheet growth emerging from the substrate base, with widths varying from 10 – 50+ nm. Similar microstructures have been reported in refs [46, 53, 77, 80]. There is a slight morphological change between the undoped and Sm-doped electrolyte solutions, as can be seen by comparing Figures 3.8 and 3.9, but is minimal compared to the difference toggled by changing the depositing potential. The coating thickness depends on the deposition time, but typically ranges from slightly less than 1 μm up to tens of microns.

The operational current density was found to alter the overall morphology and, particularly, the sizes of the finer features, with 0.8 mA cm<sup>-2</sup> being the most ideal current density because of its large-scale deposition uniformity and its nanoscale features. Extensive SEM analysis of the deposits obtained from a variety of experimental conditions revealed that smaller current densities tend toward lower surface area,



**Fig. 3.8.** SEM images of the as-deposited HSA microstructure deposited on YSZ/5-5 μm platinum pattern substrates at  $0.8 \text{ mA cm}^{-2}$  with the undoped electrolyte for 5 minutes (a), (b), and (c); and 10 minutes (d), (e), and (f).



**Fig. 3.9.** SEM images of the as-deposited HSA microstructure deposited at  $0.8 \text{ mA cm}^{-2}$  with the doped electrolyte. Nickel-only substrates used in (a) and (b) with a 5 minute deposition; a nickel anti-dot network on a YSZ substrate used in (c) with a 5 minute deposition; and a 5-5  $\mu\text{m}$  platinum strip network on YSZ used in (d, top-down view) and (e, cross-section) with a 10 minute total time deposition. A platinum strip is seen in (e) directed out of the page.

featureless coatings, and larger current densities tend to encourage different growth rates in different depositing areas, producing bush-like regions at the expense of less developed regions.  $0.8 \text{ mA cm}^{-2}$  approximately corresponds to  $-0.8 \text{ V vs. SCE}$ ; alternatively, these microstructures can be fabricated potentiostatically, but galvanostatic mode is more consistent run-to-run for the HSA morphology. Despite the fairly randomized nanoscale features, the deposition is ubiquitous and uniform, even up to several  $\text{cm}^2$ . The morphology evolves from nicely adherent to largely cracked as the deposition time and, hence, coating thickness increase. The HSA microstructure is maintained, even when metal network substrates are used (c.f. Fig. 3.8, 3.9c, d, and e).

An analogous, but not identical HSA morphology can be obtained using the Sm-

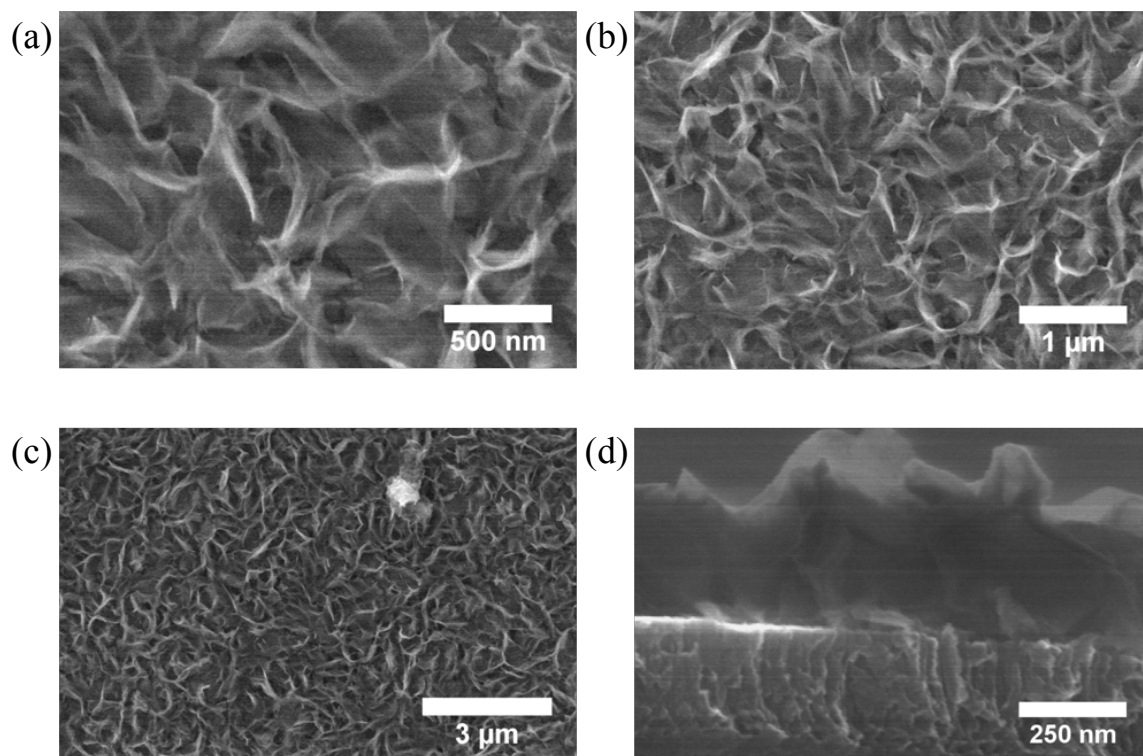


**Fig. 3.10.** SEM images of the as-deposited HSA microstructure obtained with the doped  $+ \text{H}_2\text{O}_2$  electrolyte at  $0.8 \text{ mA cm}^{-2}$ .

doped + H<sub>2</sub>O<sub>2</sub> electrolyte solution, shown in Fig. 3.10, but the finer features are larger in size and fewer in number than the Sm-doped electrolyte solution and thereby less ideal for surface area enhancement. The HSA structure was not attempted for the Sm-doped + acetic electrolyte solution, as the acetic acid addition is intended for dense, thin film growth.

To probe the high temperature stability of the HSA microstructure, HSA deposition was performed on platinum paste substrates (c.f. Fig. 3.2c), and subsequently annealed at temperatures of 800, 1000, and 1100 °C (Fig. 3.11a, b, and c, respectively) for 10 hours in ambient air. As can be seen, the nanoscale features stay intact up to 800 °C, at which temperature some coarsening begins and then worsens as the temperature

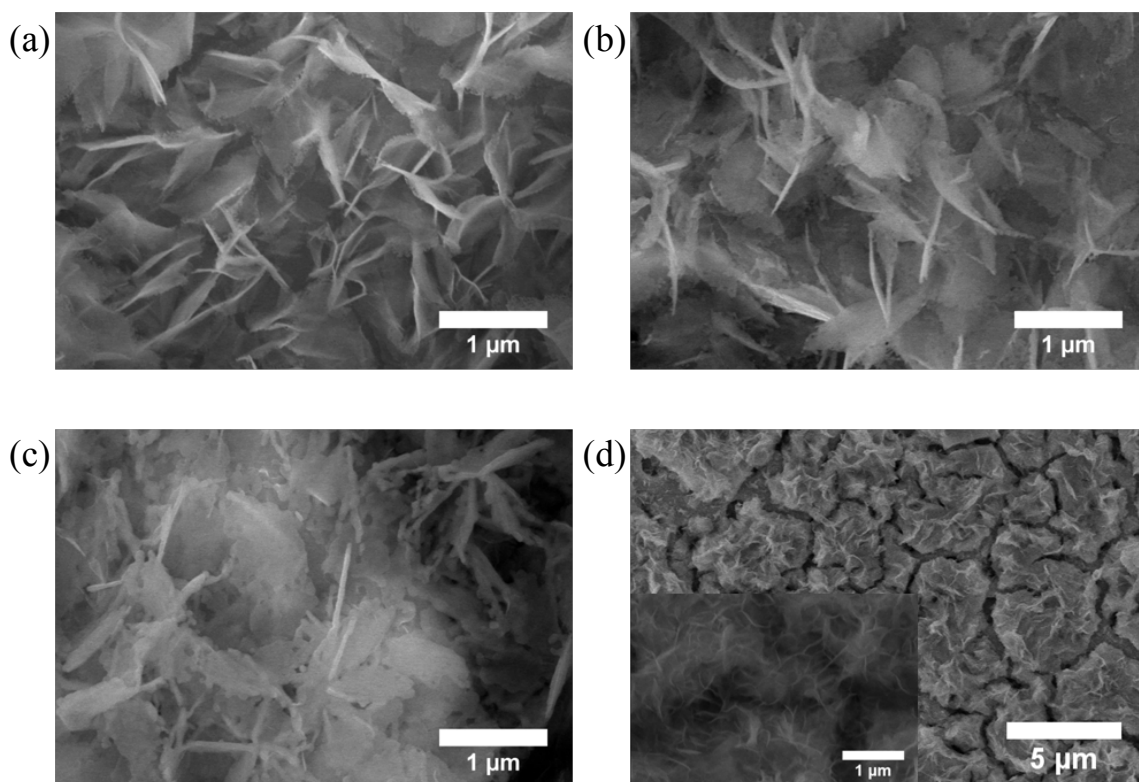


**Fig. 3.11.** Doped electrolyte HSA morphology high temperature stability with platinum paste networks on YSZ substrates: (a) annealed for 10 hours in ambient air at 800 °C; (b) 1000 °C; and (c) 1100 °C. Also, cracks can form after annealing, shown in (d) for the doped electrolyte on a YSZ/nickel anti-dot substrate, but are healed by a subsequent deposition (d, inset).

increases up to 1100 °C, at which point the finer features have nearly coarsened away. This coarsening behavior is reasonable, considering the melting temperature of ceria is ~2400 °C. Although not always the case, some microscale shrinkage that leads to significant cracking can occur even after lower temperature annealing, i.e., 650 – 700 °C (Fig. 3.11d). This problem is particularly pronounced for thicker coatings. However, subsequent depositions can heal cracks that have formed, at least as far as the SEM can image, as shown in the inset of Figure 3.11d. Additionally, for relatively thick coatings, the microstructure can emerge from the electrolyte solution cracked as-deposited, even before any heat treatment—without exception, previous studies on the HSA microstructure only report cracked as-deposited coatings [46, 53, 77, 80]. It is unclear whether this cracking is due to drying, or the deposition process itself. For both the deposition-related and annealing-related cracking issues, the comparatively thinner, more conformal depositions on porous metal networks on YSZ are more resistant to cracking than metal-only substrates. The in-plane degrees of freedom of the porous metal networks could provide an avenue to relieve the two crack-inducing driving forces. In fact, it is entirely possible to produce crack-free, annealed HSA coatings, as can be seen in Fig. 3.12.

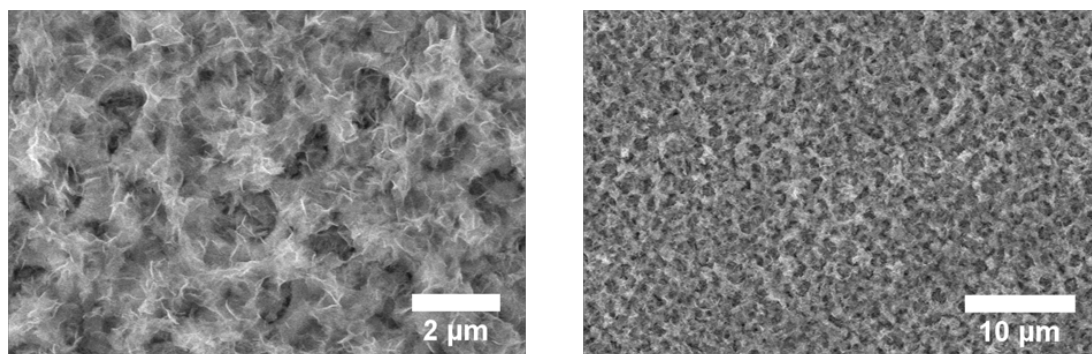


**Fig. 3.12.** As-annealed, crack-free HSA morphology deposited from a Sm-doped electrolyte solution at 0.8 mA cm<sup>-2</sup> for 5 minutes onto a YSZ/Ni anti-dot substrate and thermally treated at 600 °C in 0.1% H<sub>2</sub> in Ar for 10 hours.

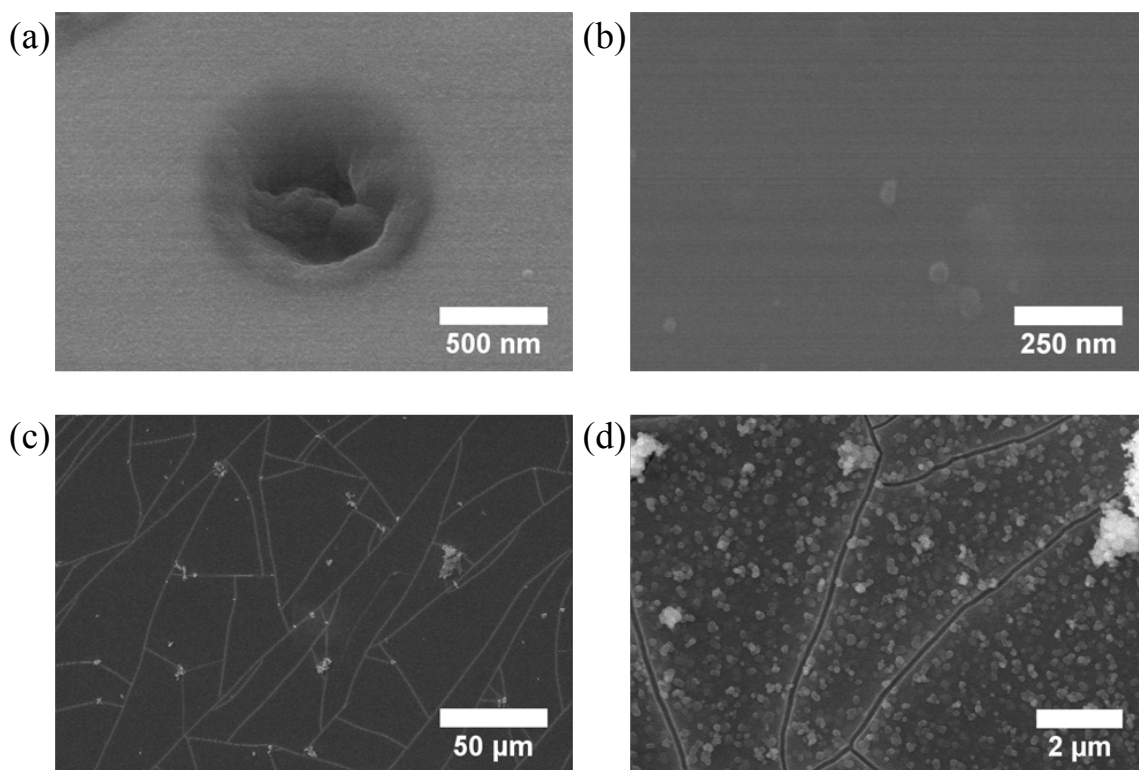


**Fig. 3.13.** As-deposited thin film morphologies. (a) Doped electrolyte (deposited at  $-0.525$  V vs. SCE), highly magnified view of the thin film deposit closing a pore of the nickel anti-dot network; (b) top-down view of the characteristically featureless doped +  $\text{H}_2\text{O}_2$  electrolyte thin film; (c) cracks form at thicknesses above  $200$  nm with the doped +  $\text{H}_2\text{O}_2$  electrolyte; (d) globular, three-dimensional growth occurs at thicknesses above  $250$  nm with the doped +  $\text{H}_2\text{O}_2$  electrolyte. The samples in (b) – (d) are deposited at an applied potential of  $-0.55$  V vs. SCE.

### 3.3.3 Thin Films

Planar, thin films were obtained potentiostatically at operating voltages from  $-0.5$  to  $-0.55$  V vs. SCE. These films are practically featureless, as in Fig. 3.13b, and nearly atomically smooth—even after annealing at  $650$  °C for 24 hours in  $0.1\%$   $\text{H}_2$  in Ar, the average surface roughness measured by AFM is  $1.6$  nm for the Sm-doped electrolyte solution and  $1.3$  nm for the Sm-doped +  $\text{H}_2\text{O}_2$  electrolyte solution (Fig. 3.14). For all four electrolyte solutions, crack-free, planar growth occurs up to a point, when undesirable three-

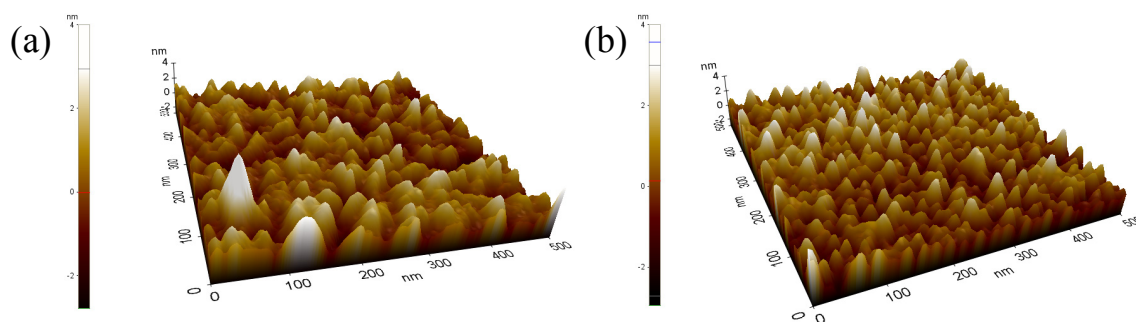


**Fig. 3.14.** AFM roughness scans for thin film morphologies from the doped and doped +  $\text{H}_2\text{O}_2$  electrolytes with 1.6 and 1.3 nm roughness values, respectively. Both samples are deposited on thin film nickel on silicon substrates and subsequently annealed at  $650\text{ }^\circ\text{C}$  for 24 hours in 0.1%  $\text{H}_2$  in Ar. (a) is deposited at  $-0.525\text{ V}$  vs. SCE for 30 minutes and (b) is deposited at  $-0.55\text{ V}$  vs. SCE for 0.5 minutes.

dimensional growth and cracking begin. It might be possible to utilize multiple sequential depositions to increase the thickness range for crack-free growth as in ref [48].

For the Sm-doped electrolyte solution, planar growth occurs up to  $\sim 50\text{ nm}$  (Fig. 3.15a), after which three-dimensional growth predominates; although, unlike the HSA microstructure, its sharp features are not on the nanoscale. If deposition is continued, cracking occurs when the planar plus three-dimensional growth thickness reaches about  $1\text{ }\mu\text{m}$ . Light-brown coloration can be seen overlaying the lustrous metallic regions of the substrate. This thin film growth is enough to begin to close the pores of the nickel anti-dot network, as in Fig. 3.13a.

For the Sm-doped +  $\text{H}_2\text{O}_2$  electrolyte solution, planar growth occurs up to  $\sim 250\text{ nm}$  (Fig. 3.15b), after which three-dimensional growth predominates. Unlike the Sm-doped electrolyte solution, cracking occurs before the three-dimensional growth period, at thicknesses around  $200\text{ nm}$  (Fig. 3.13c). This electrolyte solution's three-dimensional growth is clustered and also lacking finer features (Fig. 3.13d). Resembling the Sm-doped electrolyte solution, a light-brown coloration is observed for films  $50\text{ -- }100\text{ nm}$  thick, and deep blue-green and red-orange colors occur for thicker films.

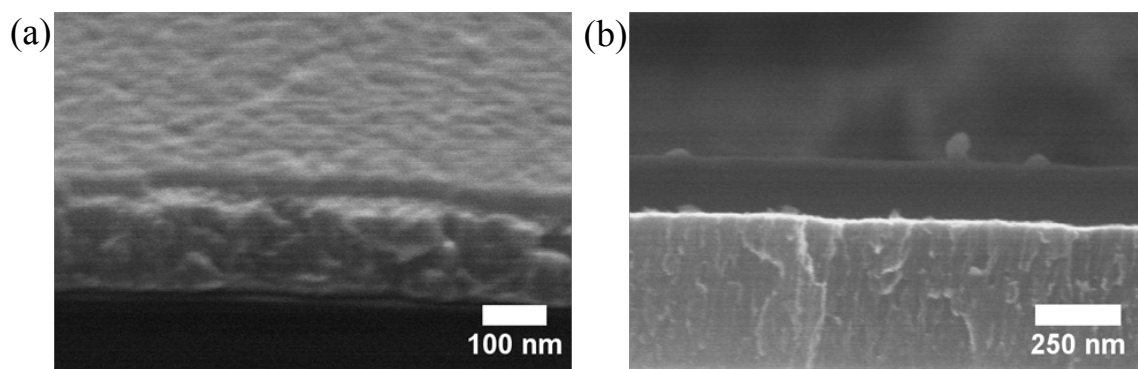


**Fig. 3.15.** SEM images of as-deposited thin film cross sections deposited on thin film nickel on silicon substrates from (a) the doped electrolyte at  $-0.5$  V vs. SCE for 1 hour, with a thickness of  $\sim 40$  nm (image taken at a  $75^\circ$  angle); and (b) the doped +  $\text{H}_2\text{O}_2$  electrolyte at  $-0.55$  V vs. SCE for 5 minutes, with a thickness of  $\sim 200$  nm (image taken at a  $90^\circ$  angle).

The Sm-doped + acetic electrolyte solution yields deposits very similar to the Sm-doped electrolyte solution (see Fig. 3.16ab). This electrolyte solution poses some difficulty in maintaining uniform two-dimensional growth across the entirety of the substrate, however. As an example, Fig. 3.16c is shown, which is an image taken from the same sample as in Fig. 3.16a and b. Although limited to a few trials, adjusting the initial pH by NaOH addition significantly alters the deposited morphology, as can be seen in Fig. 3.16d, e, and f for an initial pH adjusted from 2.5 to 5. With higher pH, rounded, gumbdrop-like islands nucleate and grow, although it is unclear if they are completely connected, and there are uncontrollable sections of three-dimensional growth.

Sm-doped +  $\text{H}_2\text{O}_2$  ceria-coated platinum strips are shown as-deposited (Fig. 3.17a) and annealed in 0.1%  $\text{H}_2$  in Ar (Fig. 3.17b). Practically no distinction can be made via SEM before and after annealing. Fig. 3.17c shows two platinum strips after annealing, where the left strip is coated and the right is uncoated. Significant surface roughness differences can be seen between the two, noting that the exposed platinum has begun to coarsen, whereas the coated platinum appears to be physically prevented from doing so. That neither the as-deposited nor the annealed films are cracked is consistent with a

report that defined a critical crystallite size of 28 nm, via XRD determination, only above which cracking in thin ceria films occur, albeit for anodic depositions [93]. From the XRD analysis above, the as-deposited and annealed crystallite sizes in this work are below this critical value.

To summarize the CELD findings thus far, depositing conditions were identified that produced both HSA and thin, planar film morphologies, across a variety of electrolyte solution compositions. It appears as though an additive-free electrolyte solution maximizes the apparent surface area for the HSA deposits. Also, hydrogen peroxide allows thicker films to be deposited, as compared to the additive-free Sm-doped electrolyte solution. In all cases and for each morphology, there is no discernable microstructural evolution at fuel cell operating temperatures. Desirable levels of samarium doping have also been incorporated into the deposits.

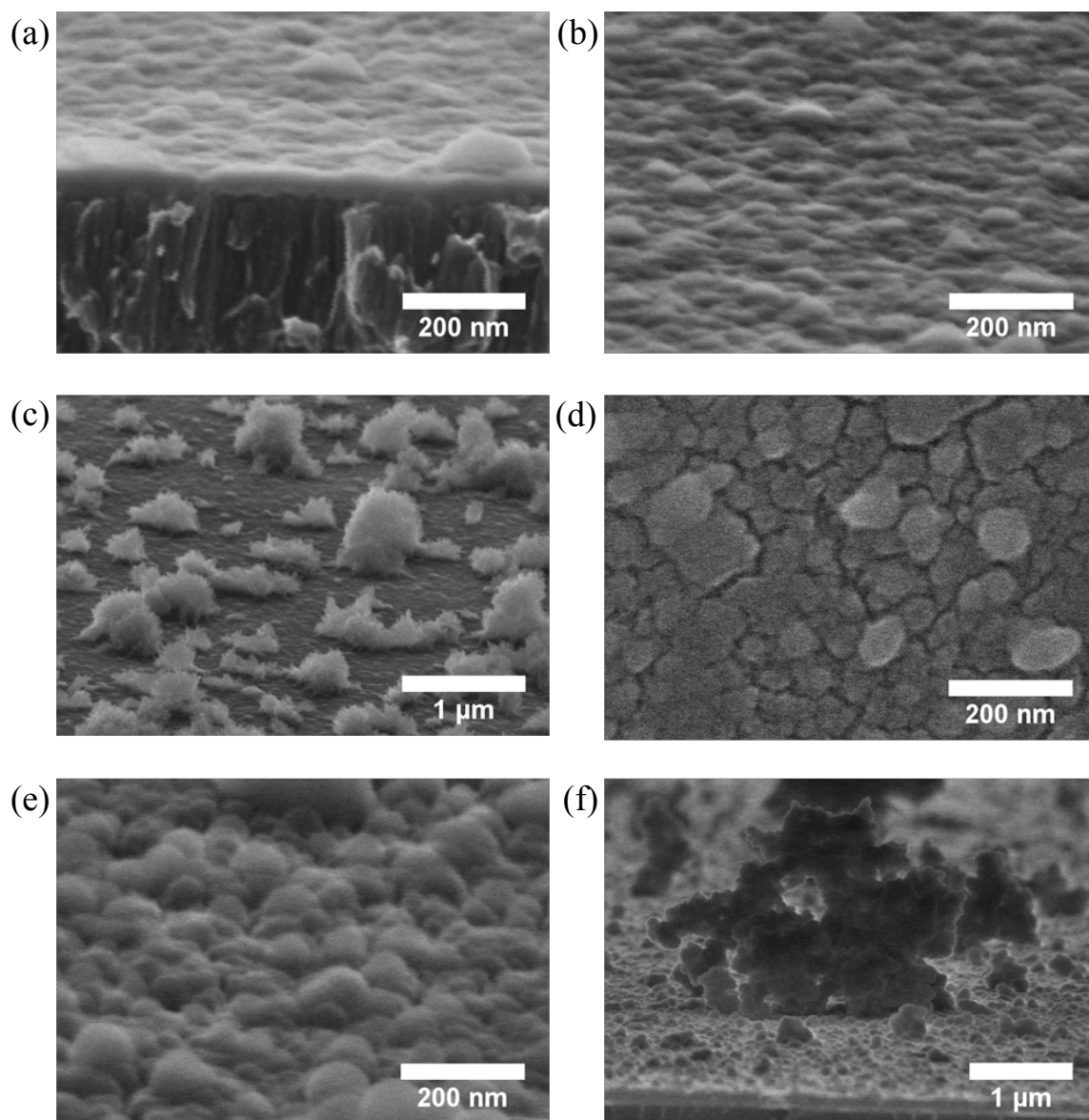


**Fig. 3.16.** SEM images of as-deposited thin films from the doped + acetic electrolyte deposited on thin film nickel on silicon substrates. The sample shown in (a), (b), and (c) is deposited at  $-0.55$  V vs. SCE for 1 hour, with an initial pH of 2.5; the sample shown in (d), (e), and (f) is deposited at  $-0.5$  V vs. SCE for 1 hour, with an initial pH of 5.

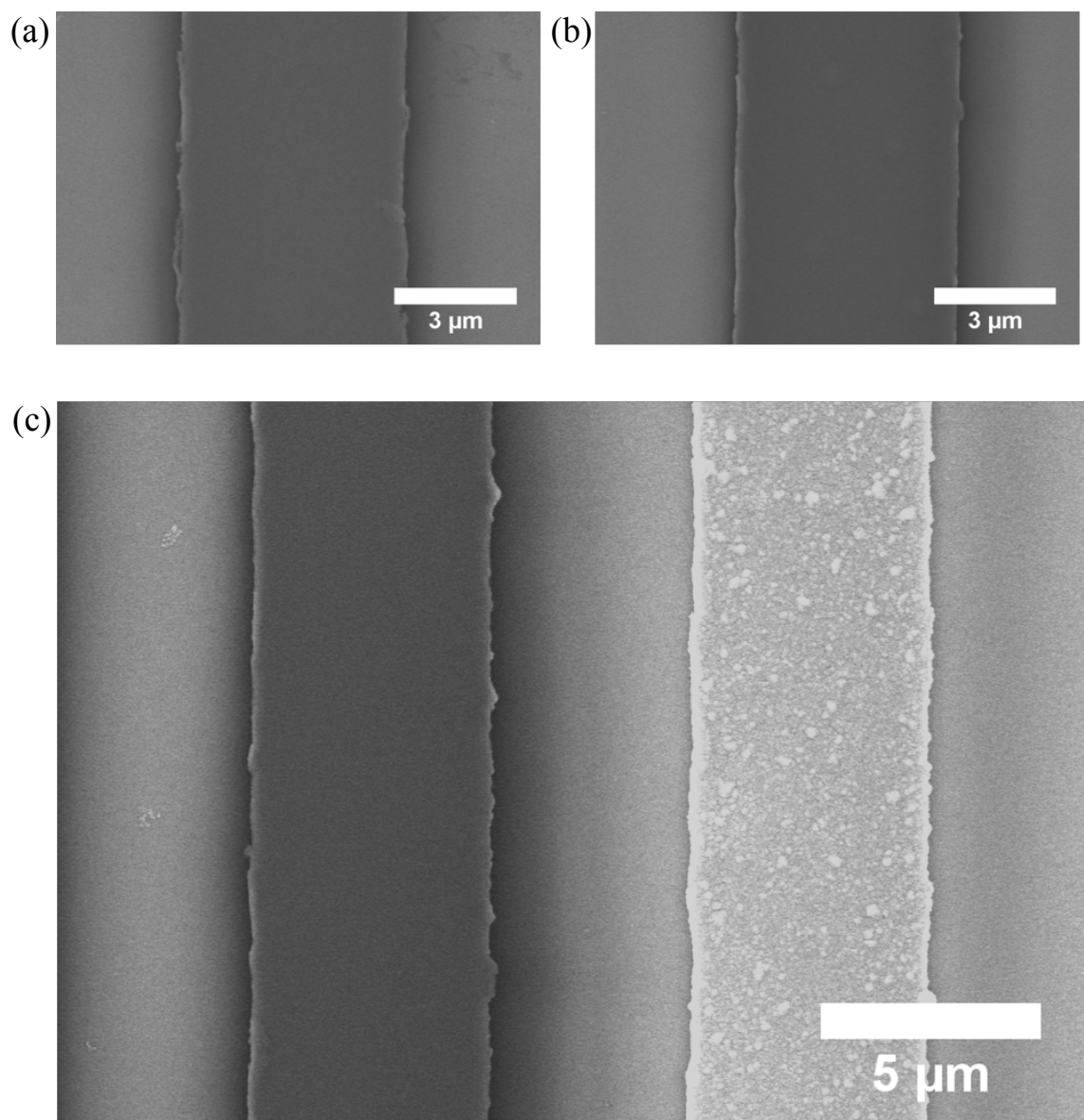


**Fig. 3.17.** Three SEM images taken from the same platinum strip on YSZ sample, with a thin ceria coating deposited from the doped + H<sub>2</sub>O<sub>2</sub> electrolyte at -0.55 V vs. SCE for 0.5 minutes: (a) as-deposited, coated platinum strip before annealing; (b) a coated platinum strip after annealing at 650 °C for 24 hours in 0.1% H<sub>2</sub> in Ar, with no discernable microstructural evolution of the coating or the platinum; (c) different coarsening behavior is observed for coated (c, left) and uncoated (c, right) platinum strips after annealing. Identical results are observed for the doped electrolyte as well.

### 3.4 Discussion

#### 3.4.1 General Deposition Overview

Recall from Section 1.4.2 that the CELD of ceria via electrogeneration of base proceeds in two distinct steps—electrochemical reduction of electrolyte solution species, and subsequent chemical precipitation of cerium species. Note:  $\text{Ce}^{3+/4+}$  herein specifically refers to dissociated aqueous ions, whereas Ce(III/IV) refers to precipitated/solid species of a particular cerium valence state.

During the electrochemical reduction step, either acidic species are consumed or basic species are produced, and both quickly increase the interfacial pH. The primary species that are reduced are dissolved oxygen, hydronium ions, water, nitrate ions, and hydrogen peroxide (if present) [80, 86]. Although not exhaustive, the following list of equations describes their reduction behavior:

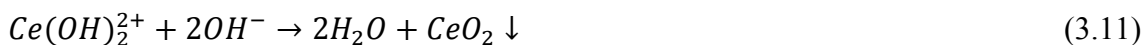


As an applied cathodic potential is made more negative, interfacial pH values measured *in situ* increase to and stabilize at ~10.5 at around -0.4 V vs. SCE, until the potential reaches -1.0 V vs. SCE, at which point the pH jumps upwards of 12 [86]. This corresponds well with calculated interfacial pH values in the range of 10.5 – 10.8 at -0.85 V vs. SCE [82]. Addition of nitrate ions to the electrolyte solution only affect the pH values at potentials more negative than -1.0 V vs. SCE [86], outside of the operational

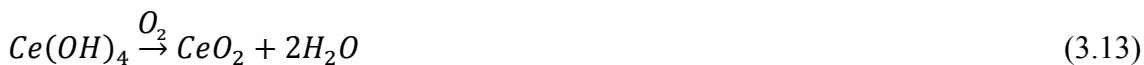
range for this work; therefore, the effect of nitrate ions on the pH can be disregarded.

Note that for all of these reductions, available electrons are required at the surface of the cathode in order for base to continue to be electrogenerated.

Once the electrolyte solution has become sufficiently basic, or, equivalently, enough hydroxide ions have been produced, chemical precipitation begins. There are two precipitation pathways thought to occur. The first is through Ce(III) (Eqn. 3.8), and the second is through Ce(IV) species, but only if H<sub>2</sub>O<sub>2</sub> is present (Eqn. 3.9-3.11):



If Ce(III/IV) hydroxides are the precipitating species, they are readily oxidized to CeO<sub>2</sub> in the presence of O<sub>2</sub>:



Recognizing that naturally aerated electrolyte solutions contain a non-trivial amount of dissolved oxygen, these chemical oxidations can proceed to CeO<sub>2</sub> at any point during the deposition, and definitively occur once the deposit is taken out of the liquid electrolyte and exposed to the ambient air. The previous XRD and Raman results suggest that this oxidation process is fast, even at room temperature. This explains how, even for conditions that should yield strictly Ce(III) precipitation, some Ce(IV) is detected *in situ* via XANES [82].

The Pourbaix diagram from Fig. 3.1. is a helpful aid to understand which cerium species are involved during the chemical precipitation step. As can be seen in the

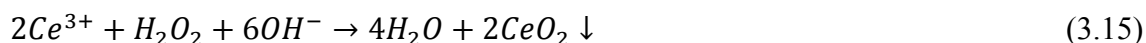
diagram, for most pH values and mild potentials,  $Ce^{3+}$  is the predominant ion in solution. Recall that the initial state of the solution is with no applied potential and at a pH in the range 2.5 – 4. As the state of the system moves to the right of the diagram, meaning that the electrolyte solution is becoming more basic, stability lines are crossed, which specifically indicates which species are involved in the precipitation step.

Consider the case for the additive-free undoped and Sm-doped electrolyte solutions. As a reminder, the black arrow on the right-hand side vertical axis of Fig. 3.1 shows the working cathodic potential for the HSA coatings. As the electrochemical reduction reactions proceed and the interfacial pH increases, it is clearly seen that the  $Ce^{3+}|Ce(OH)_3$  stability line is crossed, described by Eqn. 3.8. Intermediates of the type  $Ce(OH)_x^{+(3-x)}$  exist, where x ranges from 0 to 2, but reported precipitation tests concluded that the kinetics are fast and continuous in progressing from  $Ce^{3+}$  to  $Ce(OH)_3$  [84]. The final pH is around 10.5, at which point  $Ce(OH)_3$  is no longer aqueous, but precipitates out of solution. The gray arrow in Fig. 3.1 indicates the working cathodic potential for thin films in the undoped and Sm-doped electrolyte solutions. Similar to the HSA working potential, the  $Ce^{3+}|Ce(OH)_3$  stability line is crossed, indicating that  $Ce(OH)_3$  is the stable precipitating species for both morphologies in electrolyte solutions where  $H_2O_2$  is not explicitly added.

The addition of hydrogen peroxide to the electrolyte solution greatly influences its chemistry, in particular by chemically inducing the formation of Ce(IV) aqueous species before any potential is applied, according to Eqn. 3.9. This is observed experimentally, manifest by the electrolyte solution appearance changing from transparent to slightly yellow, which is a characteristic color of the  $Ce^{4+}$  valence state. Similarly to the above

discussion,  $Ce^{4+}$  intermediates exist of the type  $Ce(OH)_x^{+(4-x)}$ , where x ranges from 0 to 3, but, compared to  $Ce(OH)_2^{+2}$ , the others are either thermodynamically unfavorable in the pH range above 2.5, or kinetically unfavorable shown by precipitation tests [84-85]. Once the requisite hydroxide ions are produced, Ce(IV) precipitates form according to either Eqn. 3.10 or 3.11. As mentioned previously, the difference between small crystallites of  $xH_2O \cdot CeO_2$  and  $Ce(OH)_4$  is minor, especially considering that the oxidation reaction of  $Ce(OH)_4$  to  $CeO_2$  (Eqn. 3.13) is spontaneous and sufficiently fast, according to the XRD results in Section 3.3.1, which unambiguously show the final crystal structure to be that of cubic fluorite  $CeO_2$ .

One other  $H_2O_2$ -related pathway to precipitation is possible, where  $Ce^{3+}$  ions are directly oxidized to Ce(IV) precipitates, without the  $Ce(OH)_2^{+2}$  intermediate, according to:



Considering the number of species involved in these reactions, however, this scheme seems less kinetically likely than the intermediate-involved pathway proposed above. Either precipitation mechanism involving hydrogen peroxide can be understood in light of the Pourbaix diagram by recognizing that hydrogen peroxide increases the effective solution potential, changing the initial and final potential-pH states of the system [84].

One must also consider the *in situ* production of hydrogen peroxide via the electrochemical reduction of dissolved oxygen through the two-electron pathway (Eqn. 3.2). Consequently, some of the produced Ce(IV) species will have been the result of the  $Ce(OH)_2^{+2}$  path discussed above, even in nominally non- $H_2O_2$  electrolyte solutions.

However, given that the concentration of dissolved oxygen is on the order of  $\mu\text{M}$  [82], the effect on the morphology should be much less than when mM of hydrogen peroxide is explicitly added.

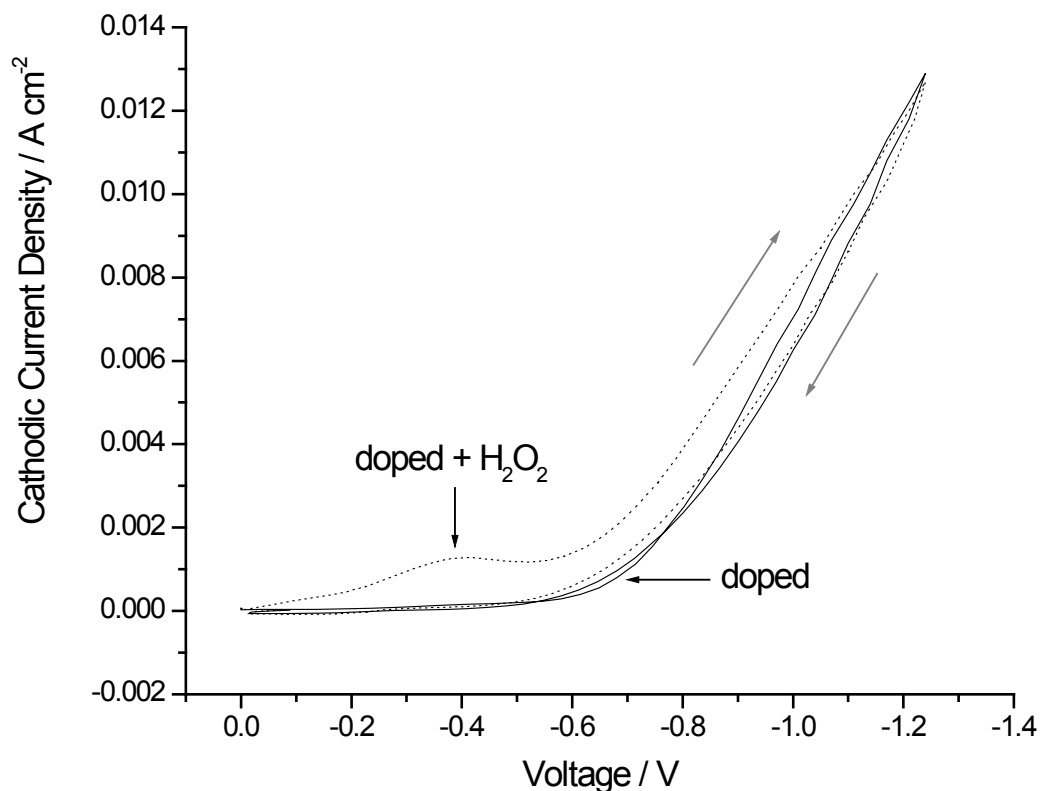


**Fig. 3.18.** CV scans for the doped (solid line) and doped +  $\text{H}_2\text{O}_2$  (dotted line) electrolytes, taken at  $50 \text{ mV s}^{-1}$ . Gray arrows indicate scan direction.

In order to further distinguish between the electrochemistries of the Sm-doped and Sm-doped +  $\text{H}_2\text{O}_2$  electrolyte solutions, their CV scans are shown in Fig. 3.18. The two scans are qualitatively similar to one another except the small peak around  $-0.4 \text{ V}$  vs. SCE in the Sm-doped +  $\text{H}_2\text{O}_2$  case. The shared, large current leg on the more negative potential side of the scan is primarily due to oxygen reduction, hydrogen evolution, and water reduction [86]. The additional peak with  $\text{H}_2\text{O}_2$  could be related to either the

reduction of  $\text{H}_2\text{O}_2$  itself (Eqn. 3.7), or the reduction of Ce(IV) species that had been previously oxidized by  $\text{H}_2\text{O}_2$ . Using  $\text{KNO}_3 + \text{H}_2\text{O}_2$  as a reference electrolyte solution without any cerium species, the resulting CV scan exhibits no additional peak (not shown), indicating that its presence is related to the cerium species. Therefore, the peak's likely origin is an electrochemical reduction of the type:



The hysteresis associated with this peak is related to the deposition that occurs during the more negative section of the scan, which covers the electrode. The fact that there is no additional peak observed in the Sm-doped electrolyte solution CV even after multiple scans reinforces the notion that, although there is some *in situ*  $\text{H}_2\text{O}_2$  production via the reduction of dissolved oxygen, the amount is small enough to not impact the chemistry; otherwise, an additional peak would be observed in the Sm-doped electrolyte solution eventually.

### 3.4.2 The Physical Deposition Picture

A fundamental question remains unanswered. How does deposition of an insulating metal oxide (as  $\text{CeO}_2$  is under these conditions) continue after an initial film is formed? To address this issue, the following argument is presented.

Recall that electrons are needed at the cathode surface to reduce the various available species, producing hydroxide ions. For  $0.8 \text{ mA cm}^{-2}$  at  $-0.8 \text{ V vs. SCE}$  through a  $100 \text{ nm}$  film, an electronic conductivity of  $10^{-8} \Omega^{-1} \text{ cm}^{-1}$  is required. Using the room temperature mobility for electrons in undoped  $\text{CeO}_2$  [94],  $\sim 10^{-8} \text{ cm}^2 \text{ V}^{-1} \text{ s}^{-1}$ , this gives an electron concentration of  $\sim 10^{17} \text{ cm}^{-3}$ . However, using thermodynamic data to calculate

the electron concentration of undoped  $\text{CeO}_2$  at room temperature [32], a value of  $\sim 10^{-26}$   $\text{cm}^{-3}$  is obtained, far below what is needed. Therefore, neither  $\text{CeO}_2$ , nor the non-conducting  $\text{Ce}(\text{OH})_3/\text{Ce}(\text{OH})_4$  are electronically conducting enough to facilitate continual CELD. Consequently, the deposit must remain somewhat porous throughout, constantly allowing molecular access to the metal|electrolyte solution interface, where the requisite electroreductions occur. A 65% dense  $\text{CeO}_2$  thin film is reported on Hastelloy substrates measured by ellipsometry and x-ray reflectivity, although the deposition was anodic [54]. Also, cathodically-produced  $\text{CeO}_2$  nanotubes in the aligned pores of an anodic alumina template showed small cracks and holes by TEM and SEM, particularly in areas furthest from the working electrode [49]. In the case of highly-cracked coatings deposited over lengthy times, there will be even easier access to the metal|electrolyte solution interface—this allows the observed growth up to and even beyond 20  $\mu\text{m}$  thick, although there will be a reasonable thickness limitation before spallation occurs.

Building this physical deposition picture up to the nano-/microscale gives explanation to the clear morphological difference seen in the HSA coatings and thin film microstructures, as well as trends in the Sm-doped and Sm-doped +  $\text{H}_2\text{O}_2$  electrolyte solutions. The former is related to the rate of base electrogeneration, which is dictated by the applied potential—faster rates (more negative potentials) encourage the HSA morphology (Fig. 3.9 and 3.8) and slower rates (less negative potentials) encourage thin film growth (Fig. 3.13 and 3.15). Regardless of applied potential, the Sm-doped electrolyte solution promotes sharper featured growth, whereas the Sm-doped +  $\text{H}_2\text{O}_2$  electrolyte solution generally promotes more spherical, globular growth. This is related to the difference in precipitating species for the two electrolyte solutions— $\text{Ce}(\text{OH})_3$  and

Ce(IV) species, respectively. Hydrogen bonding between as-produced  $\text{Ce}(\text{OH})_3$  molecules is thought to emphasize elongated, needle-like growth, in stark contrast to the spherical growth of the  $\text{CeO}_2$  phase [53, 77, 95]. This could explain the origin of the HSA morphology, and why the Sm-doped +  $\text{H}_2\text{O}_2$  electrolyte solution has a more difficult time producing comparatively fine nanoscale features at standard HSA working potentials. A counter theory for the HSA morphology asserts that hydrogen evolution during the deposition acts as a dynamic template [83]. However, at HSA depositing potentials (-0.7 to -1.0 V vs. SCE), a non-trivial amount of hydrogen evolution is visually apparent for the platinum-based substrates, but none is observed for the nickel-based substrates. This suggests that hydrogen evolution is not the origin of the HSA microstructure, as deposits from both platinum and nickel exhibit the same general features.

### 3.4.3 *Deposition on Non-Conducting Parts of the Substrate*

Up to this point, it has been shown that CELD consistently produces undoped and Sm-doped  $\text{CeO}_2$  in a predictable fashion; that both HSA and thin film morphologies are stable at high temperatures; and that the wide parameter space allows for CELD microstructural tunability. In surveying the fabrication non-negotiables of Section 1.4.1, one remains aloof—maintaining continuous pathways for all mobile species. The oxygen ion pathway is of particular concern for CELD, which no doubt requires an electronically conducting surface, even if it is only one part of a composite metal/metal oxide substrate (like the anti-dot substrates of Chapter 2). In fact, one might be tempted to consider CELD a bottom-up approach, where growth begins from the electronically conducting surface and burgeons outward. This would make forming oxygen ion pathways difficult, as there

would be no inherent means for establishing interfaces between the ceria deposit and the oxide portion of the substrate. Top-down approaches like CVD or PLD are not plagued with such a concern, as their depositions are fairly substrate-material-independent—other issues such as substrate temperature and line-of-sight positioning determine whether deposition occurs. What is demonstrated below, however, is that unambiguous and significant ceria deposition occurs via CELD on non-conducting and conducting parts of composite substrates. This phenomenon can be understood in light of the two-step CELD mechanism, discussed in Sections 3.4.1 and 3.4.2: electrogeneration of base is followed by chemical precipitation.

To assist the above explanation, it is helpful to draw a distinction between the (linguistically similar) cathodic electrodeposition of metals and cathodic electrochemical deposition of oxides. Indeed, classical cathodic electrodeposition of metals on conducting substrates gives misleading insight into the CELD process described in this manuscript. In that scheme, a positive metal cation in solution combines with available electrons on the depositing surface, i.e., the charge-transfer step, reduces its valence to zero, and becomes solid as a consequence (see Fig. 3.3). Because the deposited metal coating is itself electronically conducting, this process can continue indefinitely, as electrons are able to travel to the newly formed deposit|electrolyte solution interface. Once reduced, the adsorbed metal atom is not typically mobile on a micron scale, and therefore does not reposition itself to nearby non-conducting surfaces. In contrast, the charge-transfer step in the CELD of oxides is separate from the deposition step; in fact, the species reduced in the charge-transfer step are themselves distinct from the metal cation species (compare Eqns. 3.1-3.7 and 3.8-3.11). Therefore, there is no restriction to the depositing surface in

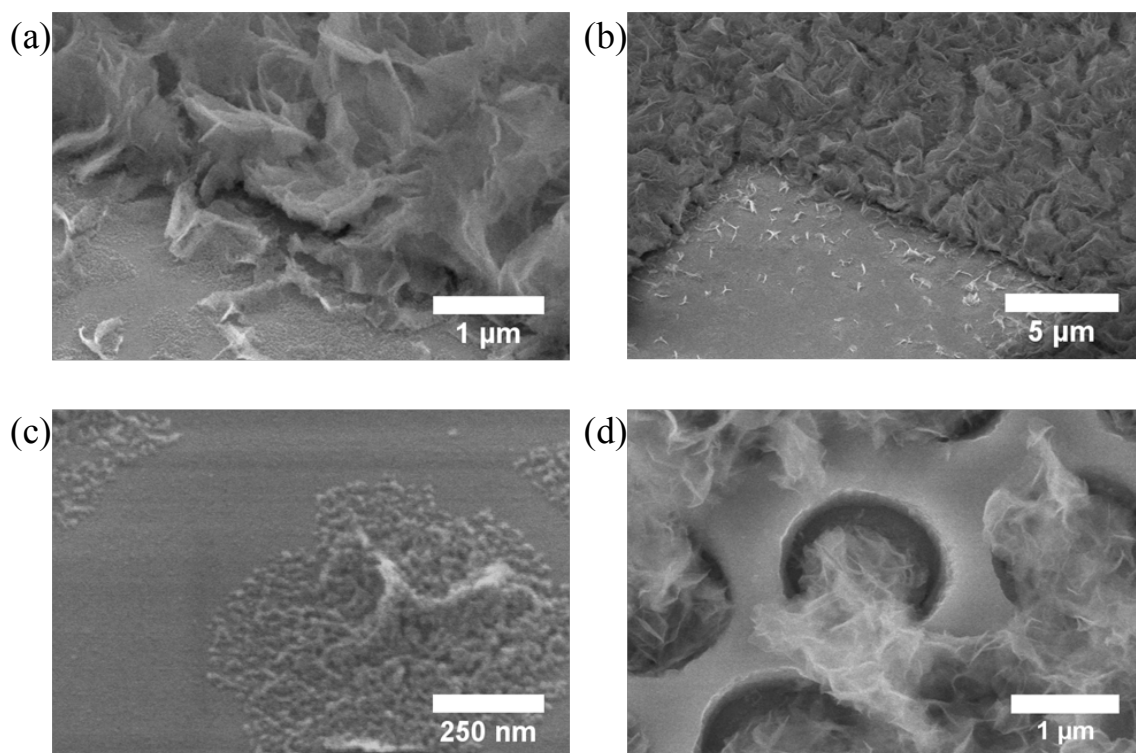


**Fig. 3.19.** SEM images of as-deposited HSA CELD ceria growth on exposed YSZ regions. (a) and (b) show the coated platinum regions in the top right of the images, as well as evidence of deposition on the YSZ regions to the bottom left of the images. (c) shows a highly magnified view of a disconnected ceria deposit surrounded by the extremely smooth YSZ surface. (d) shows deposition proceeding distinctly from the exposed YSZ region inside a pore of the nickel anti-dot network. All depositions are performed at  $0.8 \text{ mA cm}^{-2}$  for 5 minutes in either the undoped (a-c) or doped (d) electrolytes.

CELD like there is in metal electrodeposition. On that note, there is strong evidence that preference is initially given to the oxide component of a composite substrate. Beyond the visual evidence given in this chapter, the strong electrochemical activity characteristics covered in Chapter 4 alleviate any lingering concerns regarding continuous mobile species' pathways.

To reference the specific composite substrates used here, the ceria coating is not restricted to the platinum strips or the nickel anti-dot networks, but can also form on the adjacent, non-conducting YSZ surfaces. Fig. 3.19a and b show a magnified and zoomed-out view, respectively, of a HSA coating deposited on a platinum strip/YSZ substrate,

where the platinum region is toward the top-right and the exposed YSZ is toward the bottom left in both images. Deposition is clearly observed on areas that are adjacent to, but not in direct contact with, the electronically conducting platinum, even as far away as 10  $\mu\text{m}$ . It should be stressed that YSZ is completely electronically insulating at room temperature, so no pathway for electrons exists in these regions. A highly magnified view from the same sample shows an entirely disconnected island of ceria deposited on the exposed YSZ surface (Fig. 3.19c), which definitively debunks the notion that growth initiates on the metal surface and then proceeds outward to the YSZ regions. Fig. 3.19d shows deposit growth distinctly proceeding from the pores of the nickel anti-dot substrate, again, where the YSZ is exposed to the electrolyte solution.

Both the HSA and thin film morphologies can be deposited on the YSZ surface. Fig. 3.20 shows cascading images of a YSZ surface exhibiting clear, ubiquitous thin film deposition. The roughness seen up close in Fig. 3.20a, b, and c is not the original YSZ surface, as the single-crystal substrates are received highly polished to sub-nanometer roughness, as measured by AFM (not shown). It should be mentioned that the sample imaged in Fig. 3.20 was deposited at  $0.8 \text{ mA cm}^{-2}$ , which is typically associated with the HSA microstructure, but the cerium concentration in the undoped electrolyte solution was 0.01 M, below the usual 0.05 M. This explains the planar growth. Fig. 3.21 shows the HSA microstructure effectively grown on the YSZ spacing in between platinum strips, with practically no distinction between the coating's surface features over the platinum

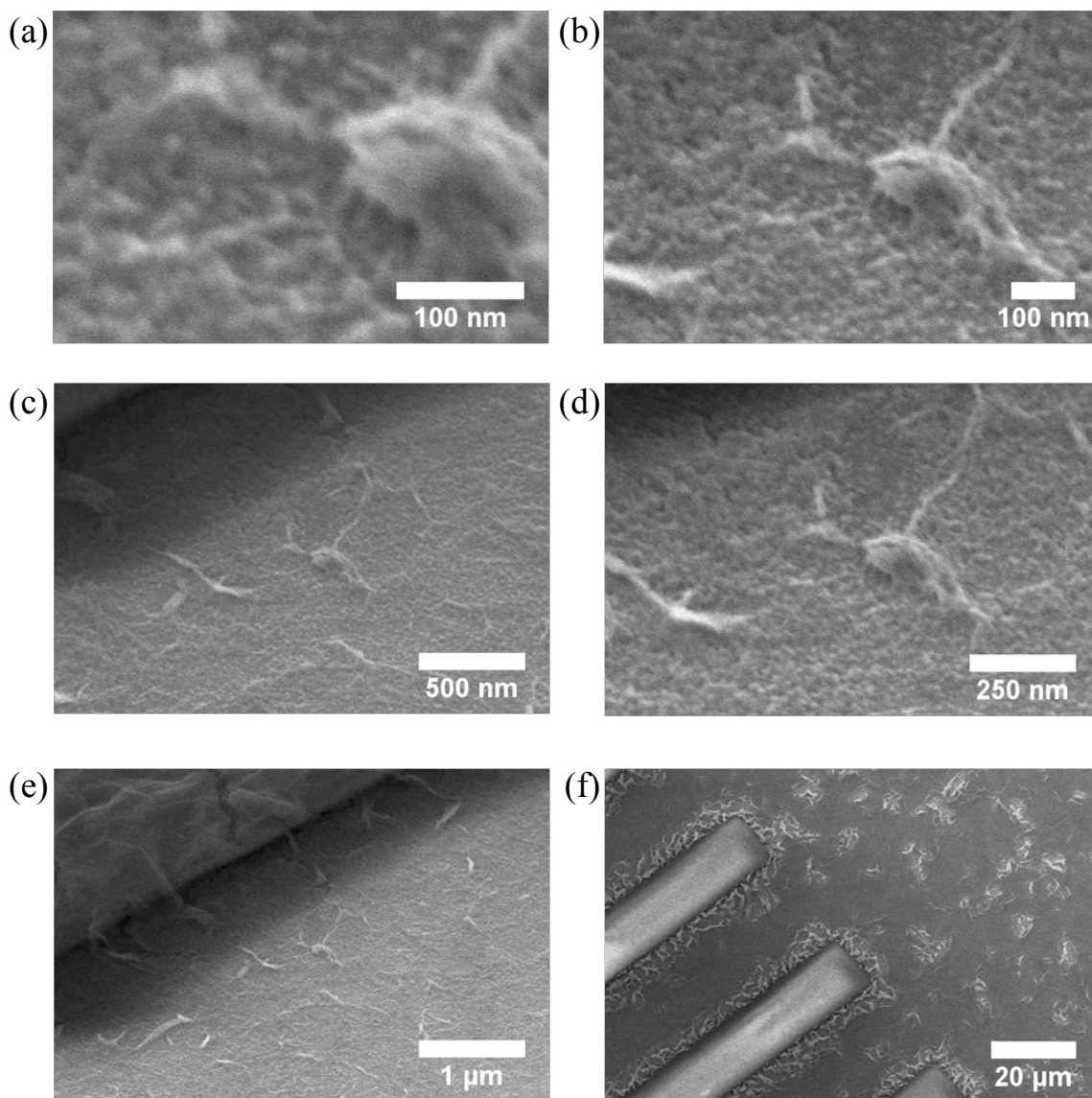


**Fig. 3.20.** SEM images from a single sample exhibiting as-deposited planar CELD ceria growth on a YSZ/platinum strip substrate. Deposition was performed with the undoped electrolyte, but with a lower (0.01 M) cerium nitrate concentration, and at  $0.8 \text{ mA cm}^{-2}$  for 5 minutes. Although this current density is typically associated with HSA structures, the lower cerium concentration leads to planar growth in this case. The flat ceria deposit on the YSZ regions appears to extend microns away from the platinum strips.

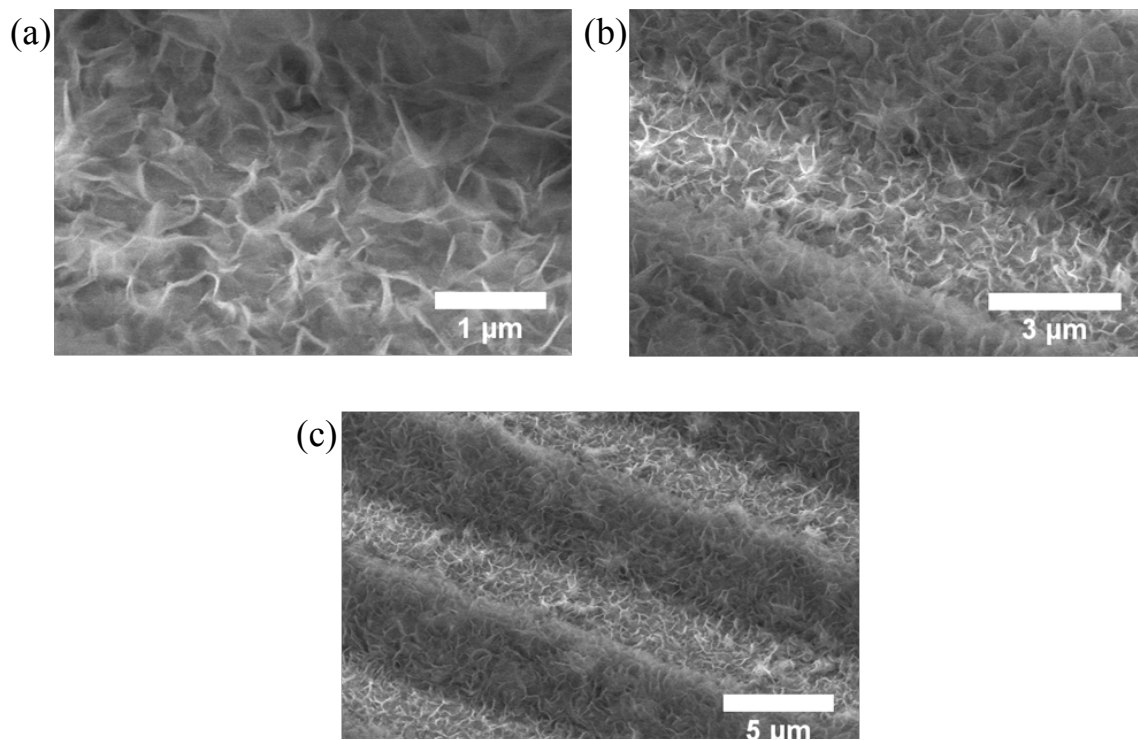


**Fig. 3.21.** SEM images from a single sample exhibiting as-deposited HSA CELD ceria growth on a YSZ/platinum strip substrate. Deposition was performed with the doped electrolyte at  $0.8 \text{ mA cm}^{-2}$  for 10 total minutes. Effective HSA growth on the YSZ regions is clearly seen.

and that over the YSZ. Furthermore, Fig. 3.21 shows quality connectivity between the deposit grown on the YSZ and that grown on the platinum—this is the crucial feature that ultimately provides oxygen ion pathways from surface reaction sites on the deposit that is located on top of the metal regions. Somewhat surprisingly, the thin films are also able to establish such a linkage, as shown in Figure 3.22.

TEM cross-sectional images from a Sm-doped and annealed HSA sample highlight the expected intersecting nano-sheet and needle-like growth on both metal and YSZ areas (Fig. 3.23a); HRTEM images in Fig. 3.23c and 3.23d show qualitatively similar Pt|CeO<sub>2</sub> and YSZ|CeO<sub>2</sub> interfaces, with no voids or other horribly distortional artifacts visible. This suggests that any porosity that existed as-deposited has been

sufficiently removed by annealing at 650 °C for 2 hours in air, not surprising given the small initial crystallite size [57]. Furthermore, the annealed grain size seen in Fig. 3.23b and the selected-area electron diffraction pattern (see Appendix B) correspond well with the XRD results above.

To have what is shown here in significant spatial deposition of ceria onto the metal-adjacent YSZ surface, with a well-adhered and void-free interface is an all-but-certain requirement for facile oxygen ion migration from the YSZ fuel cell electrolyte solution to the ceria anode surface. Indeed, if the CELD of ceria only coated the metal, or if the YSZ|CeO<sub>2</sub> interface was poor, the conduction pathway for oxygen ions would be either non-existent or highly resistive.

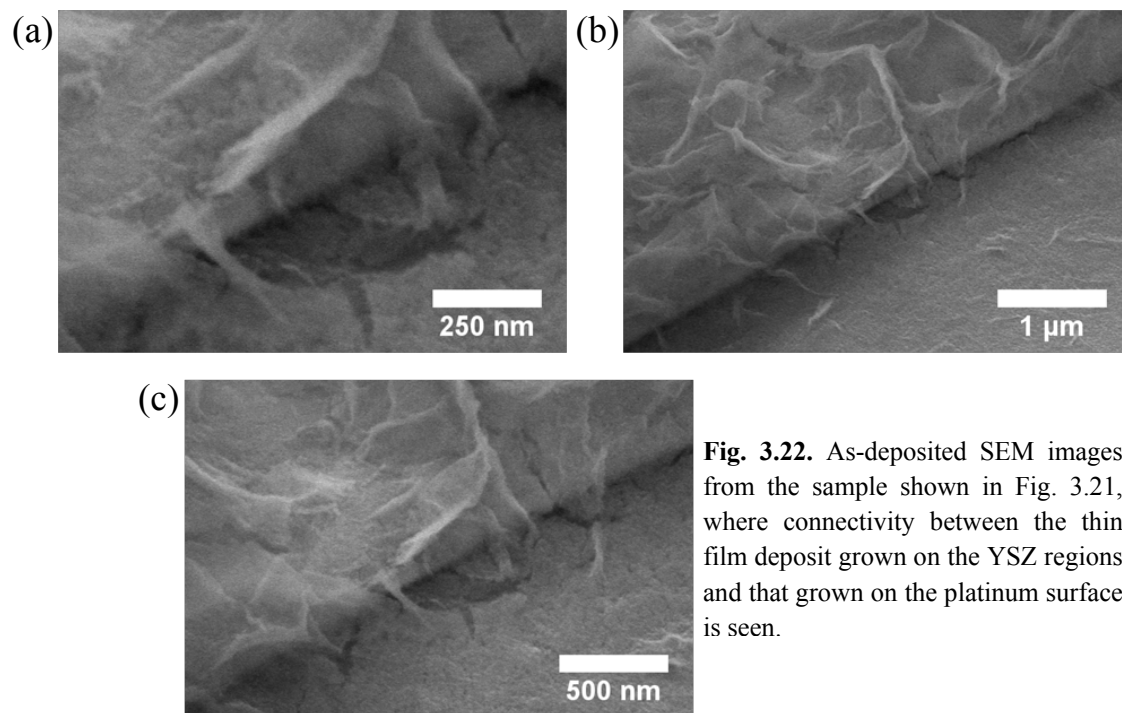


**Fig. 3.22.** As-deposited SEM images from the sample shown in Fig. 3.21, where connectivity between the thin film deposit grown on the YSZ regions and that grown on the platinum surface is seen.

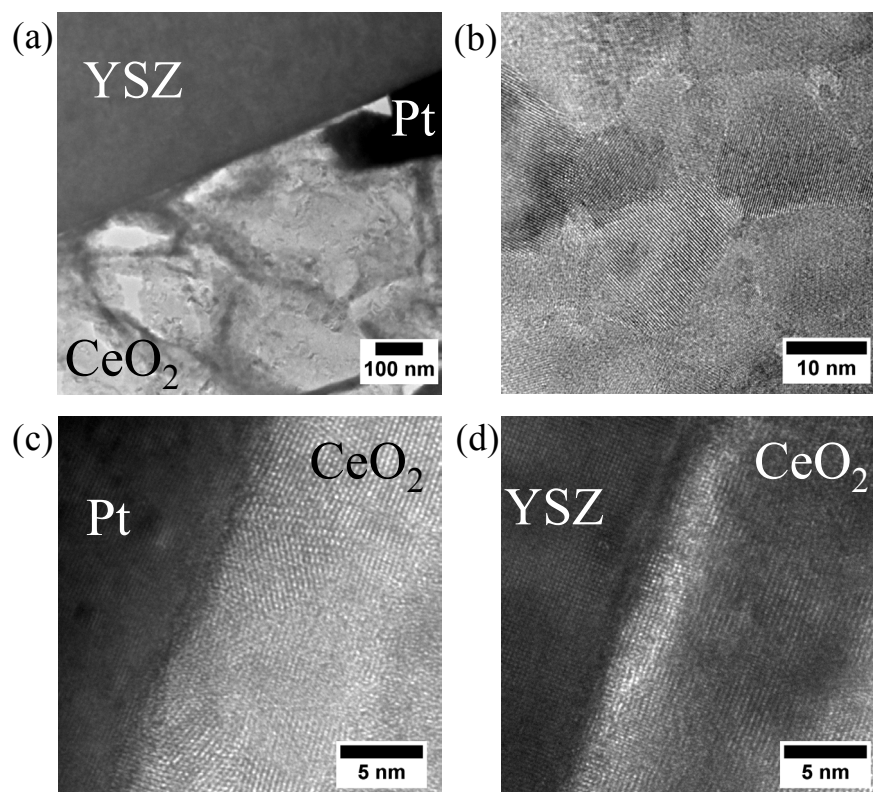


**Fig. 3.23.** TEM images showing definitive deposition on the exposed YSZ areas as a cross-sectional view (a); the polycrystalline nature of the deposit with annealed grain sizes  $\sim 15 - 20$  nm (b); and HRTEM Pt|CeO<sub>2</sub> (c) and YSZ|CeO<sub>2</sub> (d) interfaces. This sample's deposition was performed at  $0.8 \text{ mA cm}^{-2}$  for 10 minutes with the doped electrolyte and annealed at  $650 \text{ }^\circ\text{C}$  for 2 hours in air.

### 3.4.4 HSA and Thin Film Transients

To understand how CELD deposits evolve over time, voltage and current transients of the HSA and thin film morphologies are shown in Fig. 3.24 and 3.25, respectively. For a given electrolyte solution composition and concentration, the steady-state current value depends on the interplay between electrochemical reduction reactions, whose rates collectively give the current density, and any blockages that cover the metal electrode surface, which reduce the number of reduction reaction sites available. These blockages include hydrogen bubbles that persist on the metal surface and any depositing nuclei, as they, too, are electronically insulating.

Fig. 3.24 shows typical voltage transients for the HSA morphology at an applied current density of  $0.8 \text{ mA cm}^{-2}$  on both platinum strip and nickel anti-dot metal network configurations. All of the platinum strip substrates exhibit a double-plateau voltage response. Using the chronological SEM images as guides (Fig. 3.24, I through IV), the first plateau appears to be mostly related to deposition on the YSZ regions. A more negative working potential is required to maintain the constant applied current density once deposition begins to cover the platinum surface (Fig. 3.24, II, III, and IV). Comparing the voltage response of Sm-doped  $5\text{-}5\mu\text{m}$  (Fig. 3.24b) and Sm-doped  $10\text{-}10\mu\text{m}$  (Fig. 3.24c) patterns shows that the platinum pattern sizes do not affect the transients much. There is, however, a significant difference between the undoped electrolyte solution (Fig. 3.24a) and the Sm-doped electrolyte solution (Fig. 3.24b and 3.24c)—the undoped sample has a much shorter dwell time on the first plateau. This suggests that the samarium doping partially inhibits the precipitation kinetics, requiring

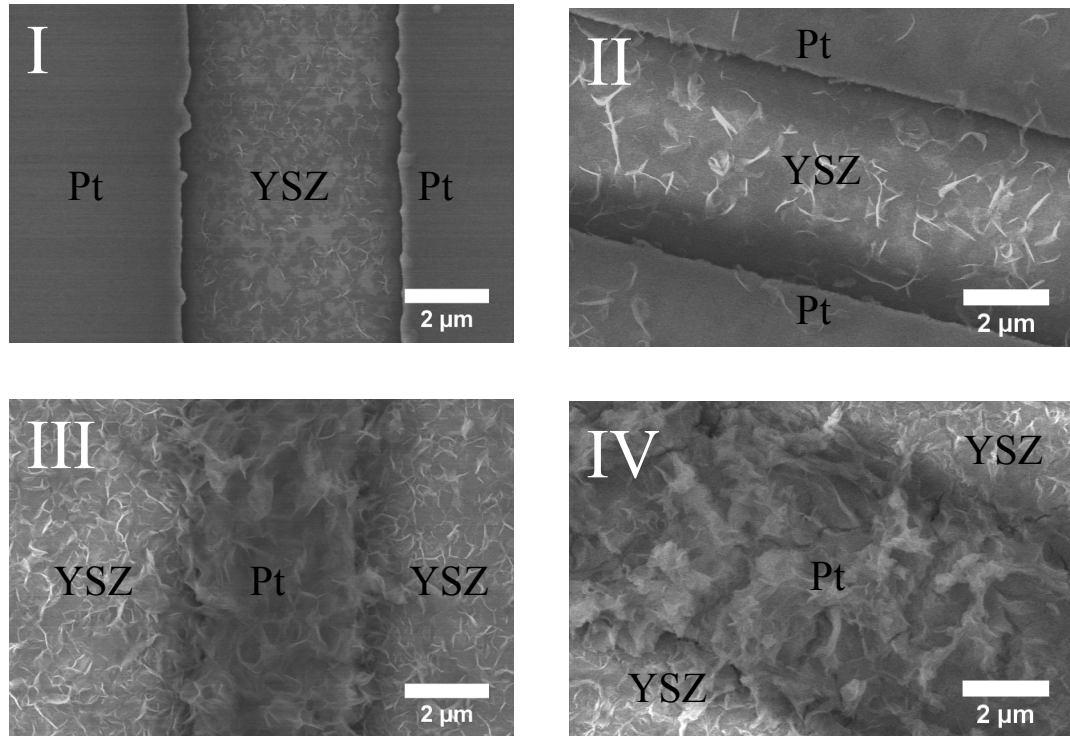
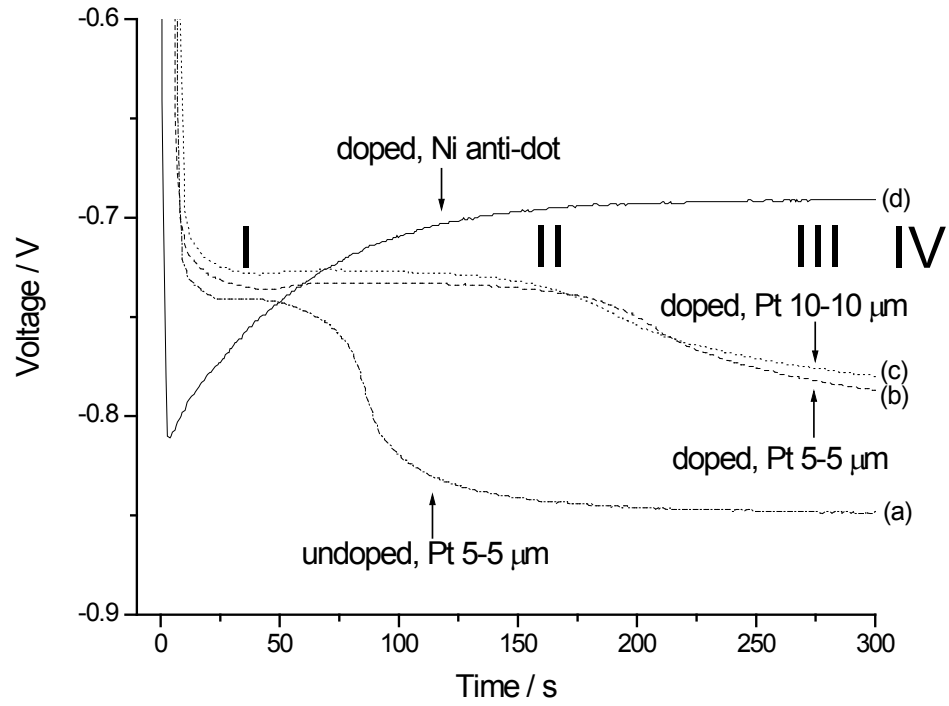


**Fig. 3.24.** HSA voltage transients taken at  $0.8 \text{ mA cm}^{-2}$  for various electrolyte/substrate configurations: (a) undoped, platinum 5-5  $\mu\text{m}$ ; (b) doped, platinum 5-5  $\mu\text{m}$ ; (c) doped, platinum 10-10  $\mu\text{m}$ ; and (d) doped, nickel anti-dot. Also, chronological SEM images of doped, platinum 5-5  $\mu\text{m}$  samples taken at the times indicated by (I, II, III, and IV) on the transient plot.

longer times to deposit on the same YSZ area size. Also, the potential value for the second plateau in the Sm-doped case is less negative than the undoped case, suggesting that the Sm-doped deposit blocks the reduction reactions less, and is, therefore, more porous. Ultimately, ubiquitous deposition occurs on the platinum and YSZ surfaces alike; however, the SEM evidence in Fig. 3.19, 3.23, and 3.24 indicates that the deposit prefers the YSZ to the metal surface initially. Judging from the relative amount of deposit seen to coat the metal after ~5 minutes (Fig. 3.24, IV), it seems that once enough nuclei have formed on the metal surface, continual deposition on those nuclei are preferred to the distant YSZ surface nuclei.

The nickel anti-dot metal network substrate voltage transient has a qualitatively different shape than its platinum strip counterpart. Consider that all HSA working potentials, regardless of the substrate used, are relatively more negative, where both oxygen reduction and hydrogen evolution are major contributors to the current density [86]. However, less hydrogen evolution is observed for nickel-based substrates, meaning that a more negative initial voltage is needed to induce enough ion motion in the liquid electrolyte solution to satisfy the applied current density value. Eventually, the voltage decreases and reaches a steady-state value less negative than that of the platinum strips, probably because there are less hydrogen bubbles blocking reduction reaction sites.

The current transients for the thin film morphologies are shown in Fig. 3.25, again, for platinum strips and nickel anti-dot networks. In this working potential region, oxygen reduction is dominant [86], and can occur via a four-electron pathway (Eqn. 3.1) or a two-electron pathway (Eqn. 3.2). The four-electron pathway has a higher steady-state current than the two-electron pathway [82]. For both Sm-doped and Sm-doped + H<sub>2</sub>O<sub>2</sub>

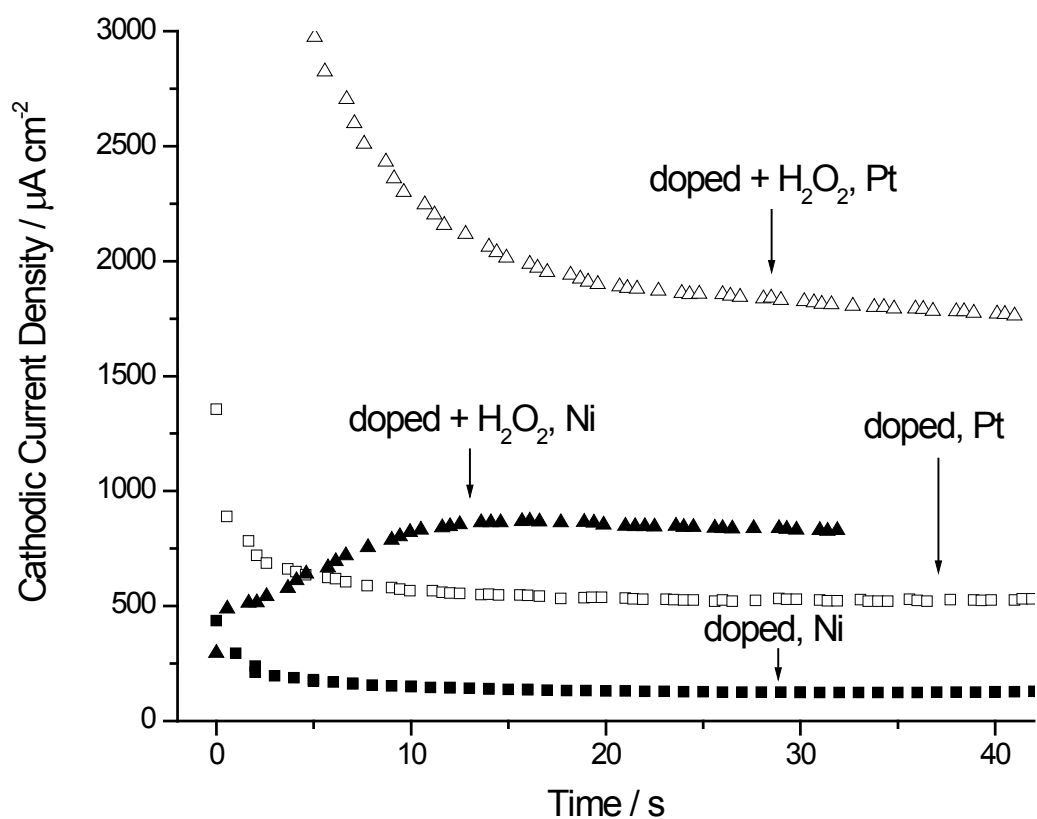


**Fig. 3.25.** Thin film current transients taken at  $-0.55$  V vs. SCE for various substrate/electrolyte configurations. Here, Pt refers to platinum strip networks and Ni refers to nickel anti-dot networks.

electrolyte solutions, the steady state current for platinum substrates is higher than for nickel substrates, possibly indicating a difference in the oxygen reduction pathway for the two metals—platinum follows the four-electron pathway for acidic solutions and then at pH 7 switches to 80% four-electron, 20% two-electron [96]. Comparably definitive literature could not be found for nickel. Other possibilities are that the film is more dense on nickel, or there still is a non-trivial hydrogen evolution-related current for platinum but not nickel, even at these low cathodic potentials.

Higher steady-state current densities are seen in the Sm-doped +  $\text{H}_2\text{O}_2$  electrolyte solution than in the Sm-doped. This can be explained by recalling the Sm-doped +  $\text{H}_2\text{O}_2$

CV scan in Fig. 3.18, where an appreciable current related to the reduction of Ce(IV) intermediates is present. For the Sm-doped and Sm-doped + H<sub>2</sub>O<sub>2</sub> electrolyte solutions, typical thin film deposition rates are roughly 1.6 nm min<sup>-1</sup> and 200 nm min<sup>-1</sup>, respectively. These wildly disparate deposition characteristics should be distinguished from and recognized as unrelated to their current transients; rather, the quickly forming films with H<sub>2</sub>O<sub>2</sub> addition indicate fast kinetics for the  $Ce(OH)_2^{+2}$  route precipitation (Eqn. 3.9 – 3.11), as compared to the Ce(OH)<sub>3</sub> route (Eqn. 3.8).

These time-dependent characteristics underscore the previously discussed notions that unmistakable deposition occurs on the non-conducting YSZ regions, and that the as-deposited coatings must be porous in order for a non-zero steady-state current to exist.

# Chapter 4

## The Electrochemical Activity of CELD Ceria Structures

### 4.1 Introduction, Methods, and Background

#### 4.1.1 *A.C. Impedance Spectroscopy (ACIS) Introduction*

Any good device design philosophy seeks to identify the area(s) of worst performance and address the appropriate issues. In this way, maximum gains can be efficiently accomplished. As fuel cells involve electrochemical reactions and current flow, both inherently rate-related, the primary inhibiting process is referred to as the “rate-limiting step.”

A.C. Impedance Spectroscopy (ACIS) is an invaluable tool for this effort, as it is able to separate relevant processes, such as oxygen ion conduction and electrochemical surface reaction rates, as well as elucidate their associated impedances. Processes are distinguished by probing in the frequency domain, where differing characteristic relaxation frequencies are expected for each process. In brief, a small voltage perturbation is applied to a cell, and the phase-shifted current response is recorded, from which the impedance can be ascertained. A detailed treatment of ACIS as an electrochemical analysis tool can be found in references [94, 97]. For the purposes of this chapter, three basic impedance responses need to be known. As an aid, the complex impedances ( $Z$ ) of a resistor and a capacitor are given below, where  $R$  is resistance,  $C$  is capacitance,  $\omega$  is frequency, and  $j$  is  $\sqrt{-1}$ .

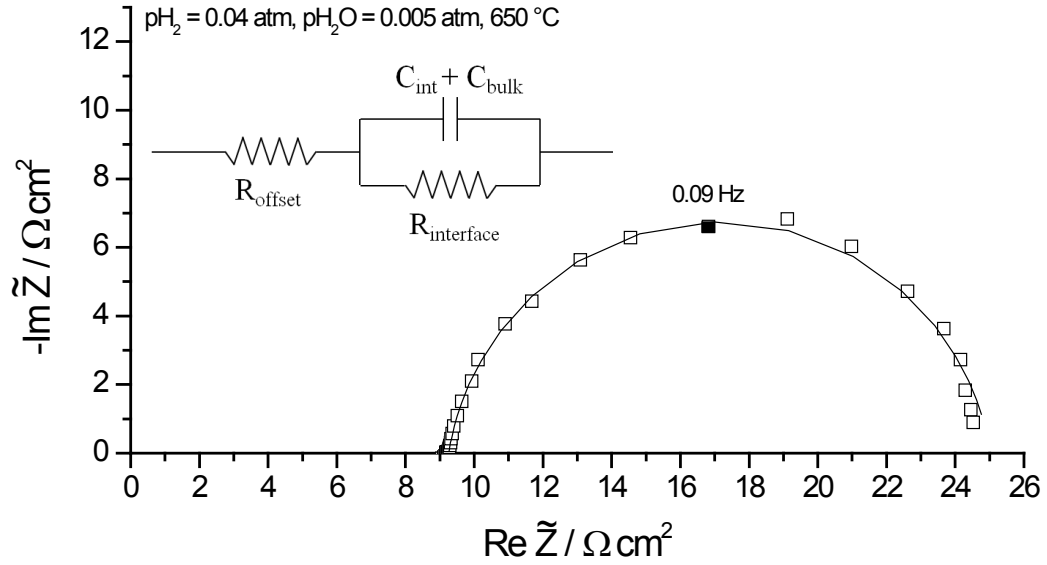


**Fig. 4.1.** A representative Nyquist plot for a PLD film of SDC deposited on single crystal YSZ, on top of which is laid 5-35  $\mu\text{m}$  Pt strip patterns. The equivalent circuit for such a spectra is also given. These data and the equivalent circuit are taken with permission from [1].

$$Z_{\text{resistor}} = R \quad (4.1)$$

$$Z_{\text{capacitor}} = \frac{1}{j\omega C} \quad (4.2)$$

Most often, the complex impedances obtained via ACIS are represented as Nyquist plots, where the positive real component is plotted on the x-axis, and the negative imaginary component is plotted on the y-axis. These plots are parametric with frequency, where data points on the right hand side of the plots are the lower frequencies, and those on the left hand side are higher frequencies. For a purely resistive process, with no associated capacitance (or, with a capacitance that cannot be resolved within experimental limitations), there will be no imaginary component, so the impedance will simply be a point on the x-axis (Eqn. 4.1). For a non-diffusion-related, resistive process with an associated capacitance, a semi-circular, symmetric arc manifests in the Nyquist

plot, owing to the frequency dependence of the capacitive impedance (see Eqn. 4.2). This case is shown in Fig. 4.1 for a YSZ substrate with SDC layers on either side of it, deposited by PLD, and on top of which is a 5-35  $\mu\text{m}$  Pt strip pattern. These data are taken with permission from [1]. Each arc that manifests indicates one resistive process; hence, in Fig. 4.1, there is exactly one process that is probed. The resistance of such a process is easily extracted from the Nyquist representation of the complex impedance—it is simply the breadth, or diameter, of the arc on the real ( $x$ ) axis, or  $\sim 16 \Omega \text{ cm}^2$  for the process in Fig. 4.1. This “ohmic offset” is subtracted for ease of comparison for all subsequent plots. Also note that the arc is offset from the origin—this means that the resistive process is in series with a simple resistor. Its origin is the electronic resistance in the wires connecting the cell to the voltage supply, as well as the ohmic resistance of the oxygen ions in the supporting YSZ substrate. Finally, for a diffusion-related, resistive process, a half tear-drop shaped arc manifests, with a near  $45^\circ$  angled feature at higher frequencies.

Equivalent circuits (with  $R$  and  $C$  elements, among others) are used to represent experimentally measured spectra. As an example, the physically-derived equivalent circuit for the spectra in Fig. 4.1 is shown as an inset. This derivation can be quite complicated, however, these equivalent circuits are not unique, meaning there are essentially an infinite number of equivalent circuits that accurately map to a given measured spectrum. To alleviate (but not eliminate, necessarily) this concern, the work in this chapter employs a physically-derived model to establish the equivalent circuit (see ref [26]).

The strategy used here is to correlate the processes measured via ACIS to the physical geometry of the cell. The reason this is useful is because ACIS probes the most

resistive process for the least resistive serial pathway—this allows the rate-limiting step to be identified. This is done by probing the evolution (or lack, thereof) of ACIS spectra with surrounding atmospheric partial pressure changes and geometric changes. An example of altering the cell's geometry is as follows: if it appears that the rate-limiting process is related to the migration of oxygen ions from point A to point B, then the physical distance from A to B could be doubled, and the impedance response measured again to see if it follows suit. Once a robust correlation is established, systematic architectural changes can be made to maximize electrochemical activity. In addition, the response of the CELD coatings will be compared with that of PLD films deposited on identical substrates.

A quick note on notation is necessary. Electrode impedances (or resistances) that have been normalized by the total deposited area are given as  $\tilde{Z}$  (or  $\tilde{R}$ ), whereas impedances (or resistances) that have been normalized by the projected area of the exposed SDC surface are given as  $\tilde{Z}^*$  (or  $\tilde{R}^*$ ). Accordingly, a resistance value extracted from the Nyquist plots is referred to as an ASR, or area-specific resistance.

#### 4.1.2 *Experimental Approach*

This chapter is concerned with the evaluation of the ceria-based, template-free HSA microstructures discussed in Chapter 3 as a suitable anode candidate, shown schematically in Fig. 4.2d. To do so, symmetric cells are constructed, where identical electrode configurations exist on both sides of a single-crystal YSZ supporting substrate.

The first two porous metal networks mentioned in Chapter 3, namely platinum strips and nickel anti-dot films, are used as conducting substrates during CELD and

current collectors during ACIS probing. Recall that the 3PB, 2PB, and metal/YSZ areas are well-defined for both metal networks. The reader is referred to Chapter 3 for detailed characteristics of these current collectors, as the ones used here are identical.

Three different cell configurations are examined, listed here with increasing complexity.

- *Metal-exposed configuration*: this configuration is the model configuration explored in [1], where a PLD SDC layer is situated underneath Pt patterns. Both the metal network and the PLD SDC under-layer are fractionally parts of the total exposed surface area, as in Fig. 4.2a.
- *Metal-embedded configuration*: PLD/CELD coatings are overlaid onto metal networks on YSZ as in Fig. 4.2b and c. Fig. 4.3 shows SEM images comparing a PLD top-layer (4.3ab) and a CELD top-layer (4.3cd).
- *Metal-sandwich configuration*: first, a dense, 1  $\mu\text{m}$  thick PLD layer is deposited onto a bare YSZ substrate; second, the porous, metal network is laid down as before; and third, PLD/CELD top-layer coatings are overlaid onto both the metal and exposed PLD-SDC, as in Fig. 4.2d and e.

The CELD HSA coatings are deposited with the Sm-doped electrolyte solution and at 0.8  $\text{mA cm}^{-2}$ , as in Chapter 3. The PLD films are deposited at 300 mJ and 5 mtorr  $\text{pO}_2$ , at a substrate temperature of  $\sim 650$  °C. These samples were provided by Dr. William Chueh and Dr. Yong Hao, and the details of the PLD film deposition procedure can be found elsewhere [1, 31].

Once made, the cells are evaluated in a symmetric gas configuration, meaning the same atmospheric conditions (e.g., flow rate, partial pressures) are experienced on both

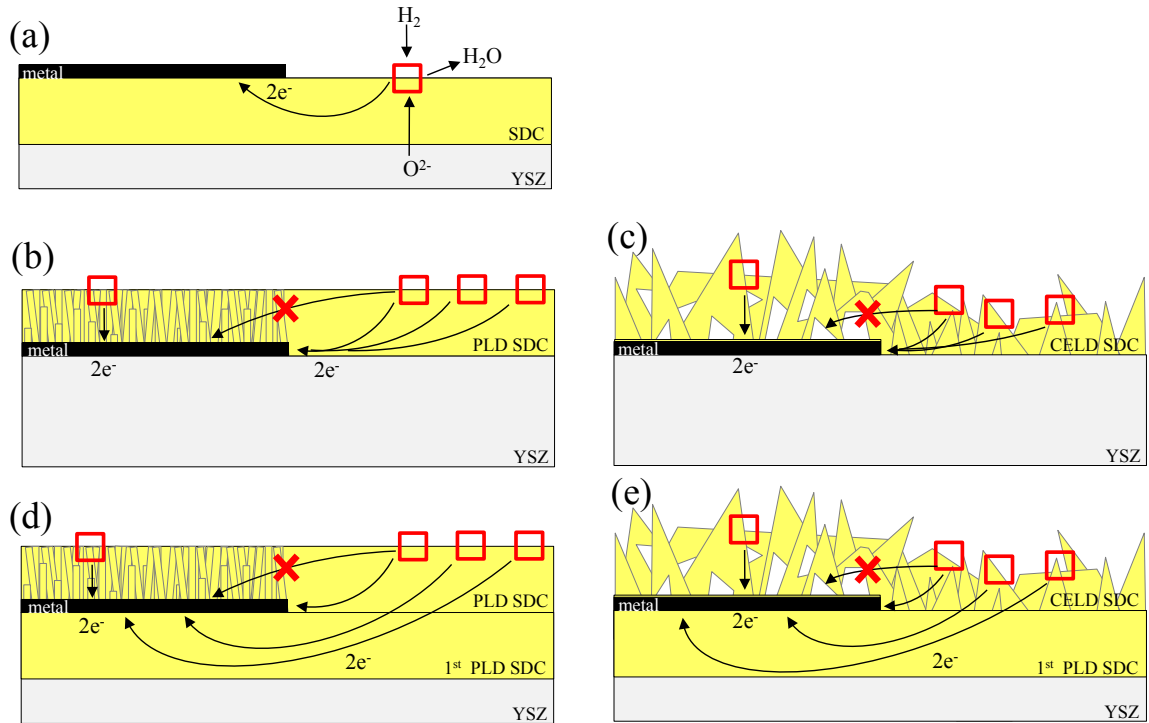


**Fig. 4.2.** Schematics showing surface reaction locations for two-phase boundary (2PB), mixed ionic-electronic conducting substrates (a); PLD (b) and CELD (c) embedding Pt strips; and PLD (d) and CELD (e) sandwich configurations. In (b) and (c) electronic conduction across the deposited layer that lies on top of the metal is inhibited and the field lines are accordingly confined to the nominal 3PB region; in (d) and (e), the same inhibition exists as in (b) and (c), but the field lines are free to readjust themselves to accommodate the newly available underside of the metal. The left column is PLD films, and the right column is CELD coatings. The rows indicate identical configurations.

sides of the YSZ substrate. The primary reason for this is convenience—no sealing is required, and the gas delivery system is simpler.

The electrochemical characterization system consisted of a vertical furnace tube reactor system, through which gas was continually flowed at a total flow rate of ~101 sccm, controlled by MKS PR 400 controllers and MKS mass-flow controllers. Three gas lines were used to achieve specific hydrogen and water partial pressures: a dry, pure hydrogen line; a dry, pure argon line; and a humidified 0.1% hydrogen in argon line. Humidification was achieved by passing the 0.1% H<sub>2</sub> in Ar line through a variable

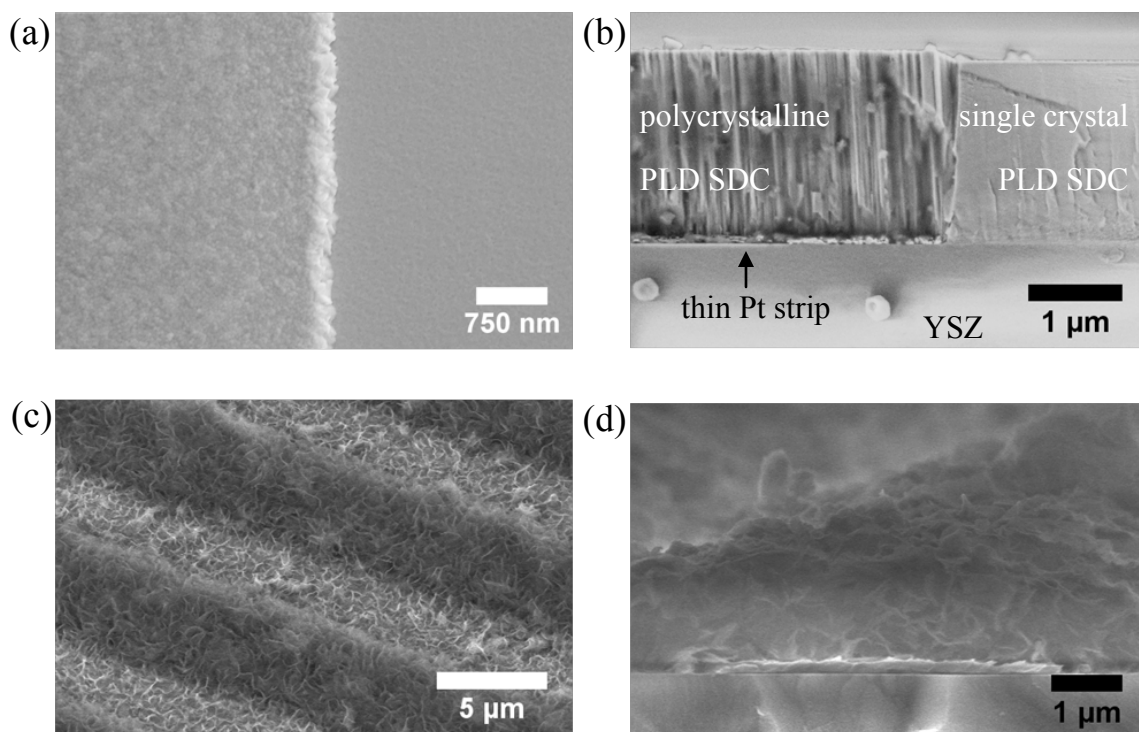


**Fig. 4.3.** SEM images showing PLD top-layer (a and b) and CELD top-layer (c and d) metal-embedded configurations. Depositions are performed at the standard conditions given in the corresponding text.

temperature bubbler. Impedance data were collected using a Solartron 1260A frequency response analyzer at zero bias with a 20 mV perturbation amplitude via an in-house Labview program. Four platinum wires were used to minimize inductance loops. Platinum was chosen for its inertness in oxidative/reductive atmospheres.

#### 4.1.3 *System Precedence*

Previous detailed work has been reported on an analogous, symmetric cell configuration consisting of PLD thin film SDC on YSZ substrates overlaid with lithographically patterned metal current collectors, as in Fig. 4.2a [1, 26, 31-32].

In those experiments, only one semi-circular arc was manifested (see Fig. 4.1), and was unambiguously determined to be related to the SDC|gas interface. This

necessarily means that for this model system, the surface reaction that occurs at the SDC|gas interface is rate-limiting. This simple system is used to provide insight into interpretation of the following data obtained for more complex systems, namely those given schematically in Fig. 4.2.

## **4.2 Arc Identification: PLD Films vs. CELD Coatings**

### *4.2.1 Representative Spectra*

A representative sampling of ACIS spectra taken from metal-embedded cells (Fig. 4.2b and c) under identical conditions is shown in the Nyquist plot of Fig. 4.4. The three cells shown are PLD embedding platinum strips (open circles), CELD embedding platinum strips (open triangles), and CELD embedding a nickel anti-dot film (open squares). Each sample was probed in different gas environments, an example of which is shown for the CELD embedding a nickel anti-dot film in Fig. 4.5. As indicated by the notation, the impedance is normalized by the total deposited area, irrespective of the metal network geometry. Significantly, all spectra of the embedded metal geometry exhibited two similar arcs, even though the SDC deposition techniques are different, and, in the CELD case, different metal networks are used. Recall that frequency is swept from low to high, which is right to left in the Nyquist plots; accordingly, the arc on the right-hand side is referred to as the LF (low frequency) arc, and the arc on the left is the HF (high frequency) arc. From these spectra, it is evident that PLD films have larger LF arcs than the CELD coatings. Also, the HF arc is similarly sized for the PLD/Pt strip and CELD/Pt strip samples, but is slightly smaller for the CELD/Ni anti-dot sample.

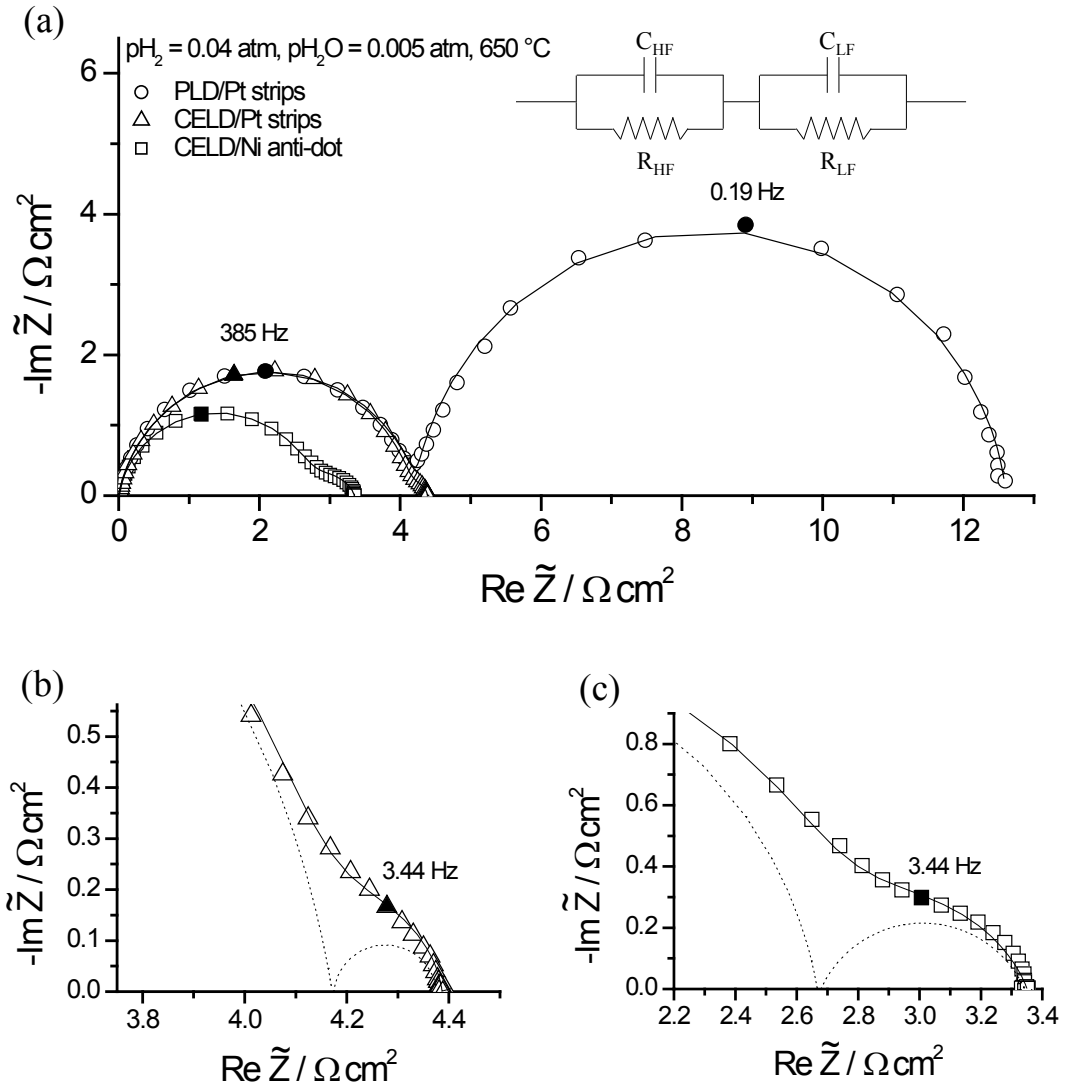


**Fig. 4.4.** (a) Representative Nyquist plots exhibiting the two arc behavior for PLD embedding 5-5  $\mu\text{m}$  Pt strips (open circles), CELD embedding 5-5  $\mu\text{m}$  Pt strips (open triangles), and HSA CELD embedding a Ni anti-dot network with 1.4  $\mu\text{m}$  pores (open squares); (b) a magnified view of the CELD/Pt strips' LF arc; (c) a magnified view of the CELD/Ni anti-dot network's LF arc. Solid lines are the results from the fits to the equivalent circuit shown as an inset in (a); and the dotted lines are simulations of the arcs as a guide to the eyes. The normalization is the entire deposited area for all three cases here.

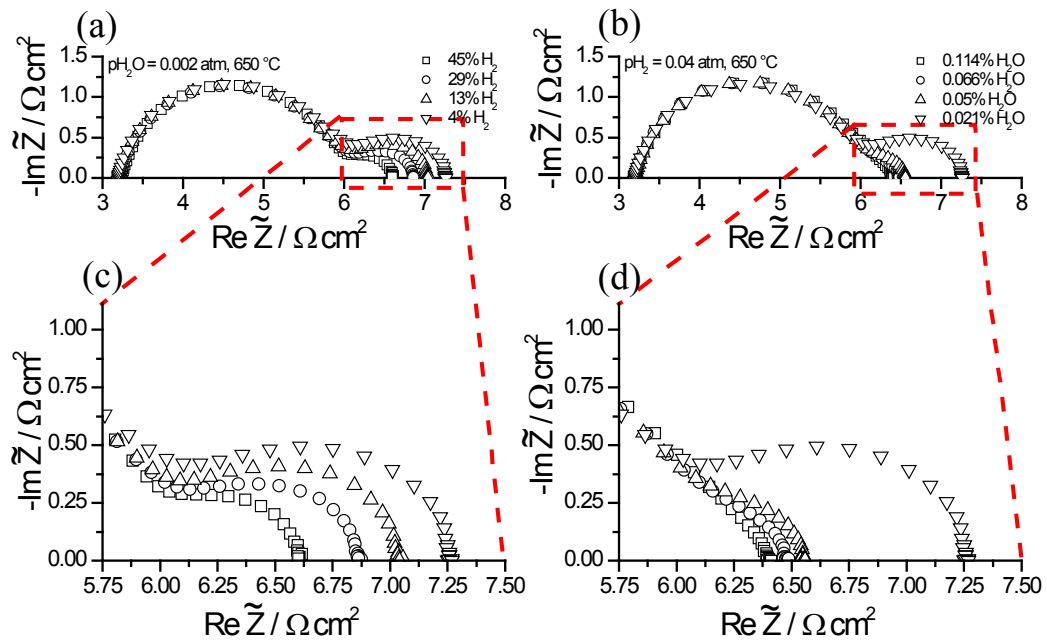


**Fig. 4.5.** Representative hydrogen (a) and water (b) partial pressure dependence of a Ni anti-dot-embedded CELD sample. The anti-dot pores are  $1.4 \mu\text{m}$  and the CELD is deposited at the HSA conditions. The HF arc is relatively static with partial pressure changes, whereas the LF arc strongly depends on the gas atmosphere. The normalization is the entire deposited area. The plots in (c) and (d) are magnified views of the LF arcs in (a) and (b), respectively.

Analogously, a representative sampling of ACIS spectra taken from metal-sandwich cells under identical conditions is shown in the Nyquist plot of Fig. 4.6, again with the resistance normalized by the total deposited area. The two samples shown here are PLD sandwiching platinum strips (c.f. Fig. 4.2d; seen in Fig. 4.6 as open squares), and CELD sandwiching platinum strips (c.f. Fig. 4.2e; seen in Fig. 4.6 as open triangles). Only one arc can be seen for both PLD- and CELD-platinum sandwich samples, which manifests at lower frequencies. Although the sandwich configuration has a more complex fabrication, the response is simpler, so it is considered first in the analysis below.

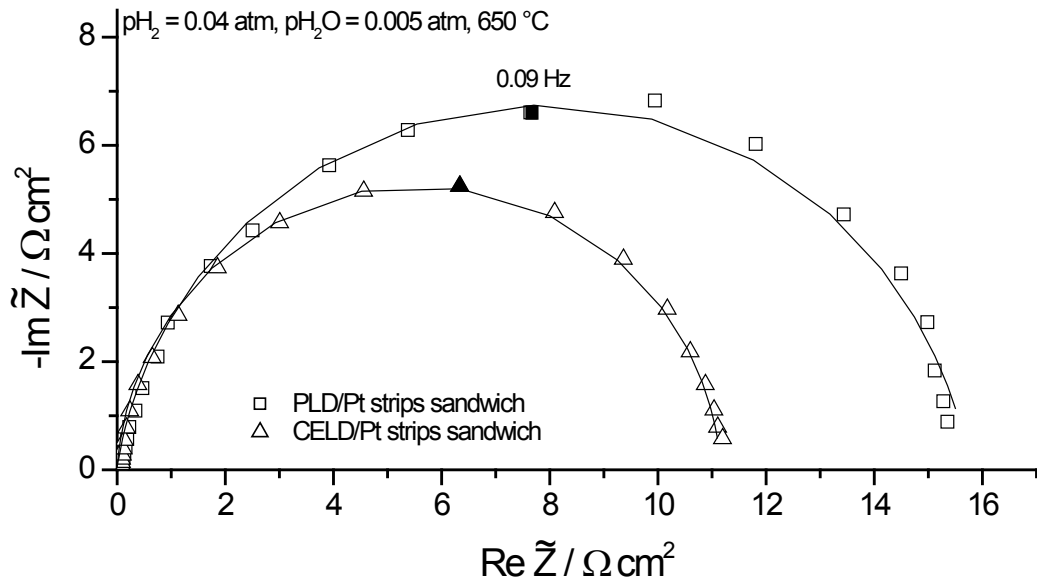


**Fig. 4.6.** Representative Nyquist plot of a PLD/Pt strips sandwich (open squares); and a CELD/Pt strips sandwich (open triangles). In both cases, there is only one arc. Solid lines are the results from the fits to the equivalent circuit from Fig. 4.1. The normalization is the entire deposited area.

#### 4.2.2 Origin of the Single Arc in the Metal-Sandwich Configuration

Recall that the sandwich configuration for both PLD and CELD samples yields a single impedance arc (c.f. Fig. 4.6). Also recall that the model system of a SDC PLD film with Pt strips exposed yields a single arc (c.f. Fig. 4.1). The hydrogen gas dependence of the resistance values from these three samples are compared in Fig. 4.7—namely, the PLD/Pt strips-exposed configuration (black squares), the PLD/Pt strips-sandwich configuration (red circles), and the CELD/Pt strips-sandwich configuration (blue triangles).

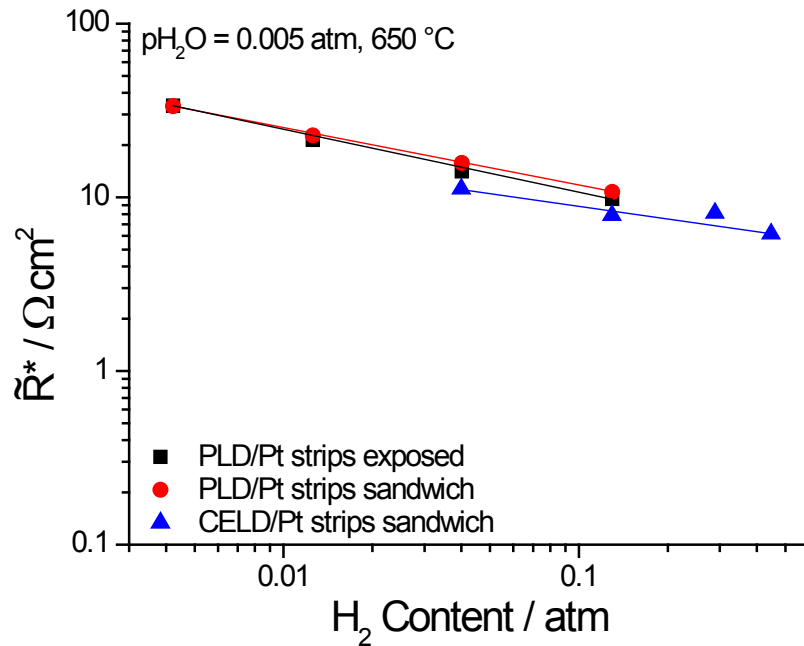


**Fig. 4.7.** Hydrogen partial pressure dependence of the solitary arc resistance values for PLD/Pt strips exposed (black squares), PLD/Pt strips sandwich (red circles), and CELD/Pt strips sandwich (blue triangles) configurations. The normalization is the projected area of the exposed ceria surface. Solid lines are guides to the eyes.

Both the absolute values and gas dependence of the ASRs for each sample are comparable. This strongly suggests that the single arc in the model PLD/Pt strips exposed system is the same as the single arc in the PLD and CELD/Pt strips sandwich configurations. Consequently, it can be concluded that this arc is due to the interface between the SDC surface and the surrounding gas, for each sample compared in Fig. 4.7.

One notable peculiarity remains, however. When CELD is used as the top coating in a platinum-sandwich configuration, the absolute ASR values of the SDC|gas arc do not decrease as would be expected from the higher surface area accessed by the HSA CELD coating. Upon *ex situ* SEM analysis of the CELD/Pt sandwich sample, it can be seen that the CELD coating on the exposed SDC only slightly enhances the surface area, in

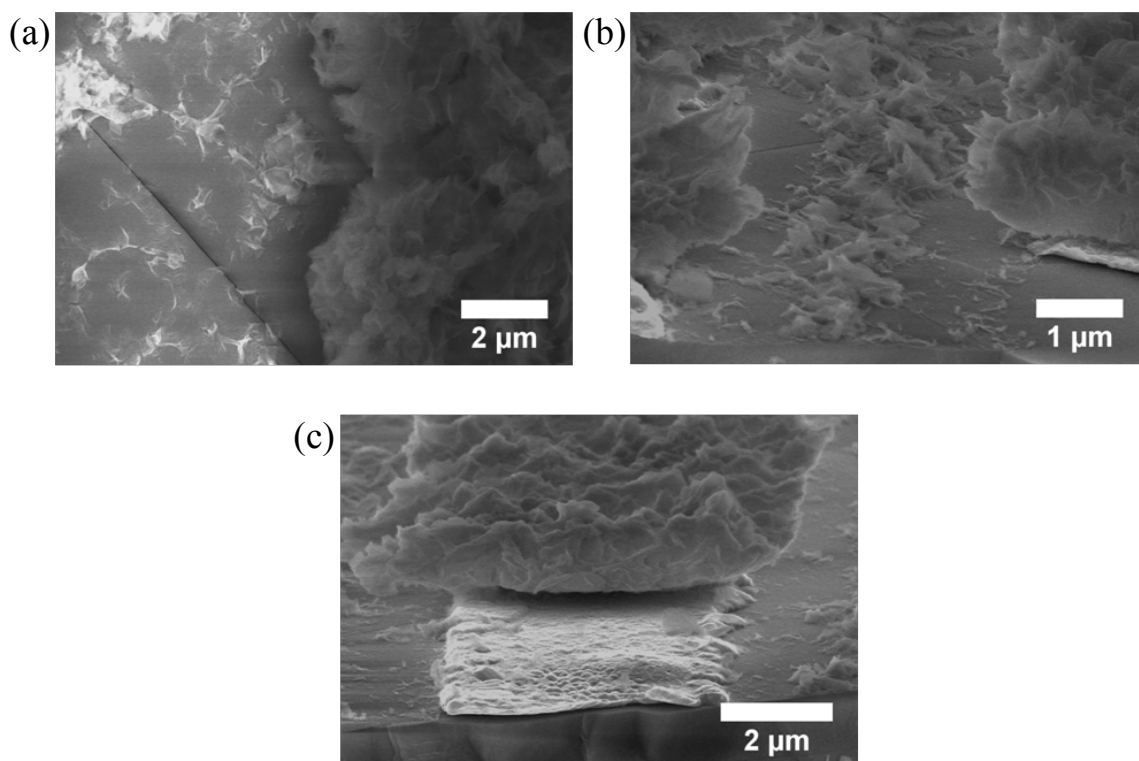


**Fig. 4.8.** SEM images of a CELD/Pt strip-sandwich configuration after testing at 650 °C for ~24 hours: (a) the top-layer CELD does not significantly enhance the surface area over the exposed PLD SDC regions, where some cracking is observed; (b) highly angled view of the phenomena in (a); and (c) the deposit lying on top of the Pt strips appears disconnected from the deposit on the exposed SDC regions, and can be seen here uncovering the Pt strip altogether.

contrast with CELD coatings on YSZ (compare Figure 4.8ab to Figure 4.2cd). Also seen in Figure 4.8, the part of the CELD coating that lies on top of the metal network appears disconnected from the coating on top of the SDC. This is likely due to the volume reduction that inevitably happens when electrochemically deposited oxide material is annealed—this adverse effect is exacerbated for thicker samples like the one shown here. The CELD deposits on Pt/YSZ surfaces also exhibit this behavior, but restricted to a small area in the vicinity of the liquid electrolyte meniscus. A break of this fashion is tantamount to completely nullifying the activity of the SDC above the metal, as no continuous pathway for oxygen ions exists. Furthermore, non-trivial cracking in the first

PLD layer is observed when the second layer is deposited via CELD, but not PLD. This could be due to thin film stresses induced by a slight lattice expansion, arising from the reduction of  $\text{Ce}^{4+}$  to  $\text{Ce}^{3+}$  in the underlying SDC PLD layer during the cathodic electrochemical deposition. These factors undoubtedly affect the measured ASR for CELD/metal-embedded samples.

#### 4.2.3 *Origin of the HF Arc in Embedded Metal Configurations*

Now consider only the HF arc for the metal-embedded configurations shown in Fig. 4.4. Analogously to the previous section, the hydrogen partial pressure dependence of the HF ASR values extracted from the Nyquist plots is shown in Fig. 4.9 for the same three samples from Fig. 4.4—namely, PLD/Pt strips-embedded (black open squares), CELD/Pt strips-embedded (blue open triangles), and CELD/Ni anti-dot-embedded (red open circles) configurations. Note the nearly flat response of the metal-embedded configurations' HF ASRs to changing hydrogen partial pressure. This is true regardless of deposition technique or the metal network underneath. The water dependence is similarly weak (not shown). The apparent lack of partial pressure and fabrication technique dependence of the HF arc suggests a configurational origin, one that is shared between PLD and CELD samples. To further investigate the origin of the HF arc, embedded Pt strip samples of large pattern sizes are analyzed.

Four exotic platinum patterns are utilized to tease out robust dependencies related to the HF arc—50-100  $\mu\text{m}$ , 50-500  $\mu\text{m}$ , 50-900  $\mu\text{m}$ , and 50-1300  $\mu\text{m}$ . When the metal spacing is increased beyond 100  $\mu\text{m}$ , the HF ASR values show appreciable hydrogen/water partial pressure dependence, eventually exhibiting equal but opposite

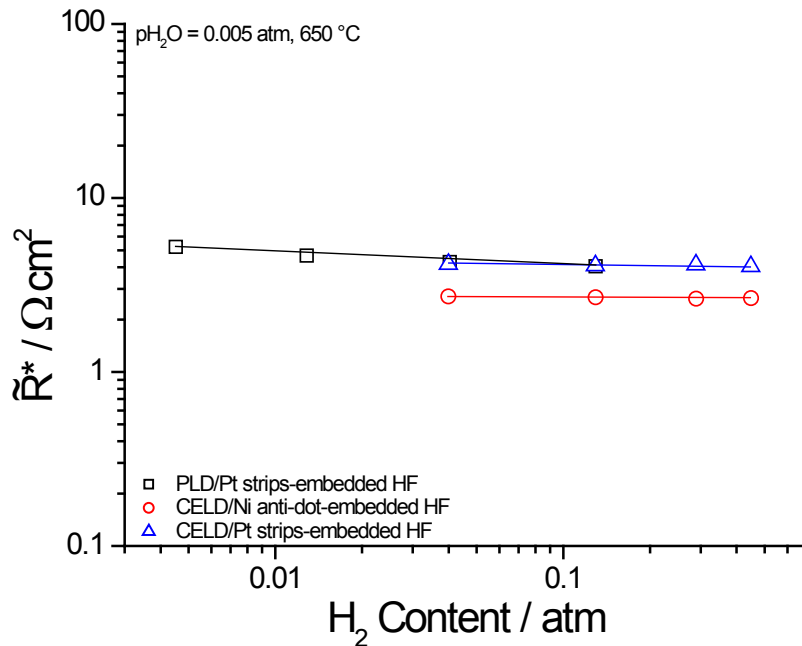


**Fig. 4.9.** Hydrogen partial pressure dependence of the HF arc resistance values for PLD/Pt strips-embedded (black open squares), CELD/Pt strips-embedded (blue open triangles), and CELD/Ni anti-dot-embedded (red open circles) configurations. The normalization is the projected area of the exposed ceria surface. Solid lines are guides to the eyes.

slopes in the log-log plots of Fig. 4.10a and b. This suggests that the HF arc is an electron-related process, as the electronic carrier concentration is oxygen partial pressure dependent [27, 31, 94]. For the same pattern sizes, the ASRs also show a strong relationship to the nominal 3PB length and lateral metal spacing (Fig. 4.10c and d). These dependencies, like the oxygen partial pressure dependence, decrease in intensity as the pattern sizes are made smaller. Also of note is the fact that these HF arcs are decidedly semi-circular, as opposed to half tear-drop shaped, suggesting that neither oxygen ion nor electron diffusion are rate limiting, even on length scales approaching millimeters. These data imply the SDC-metal interface as the origin of the HF arc.

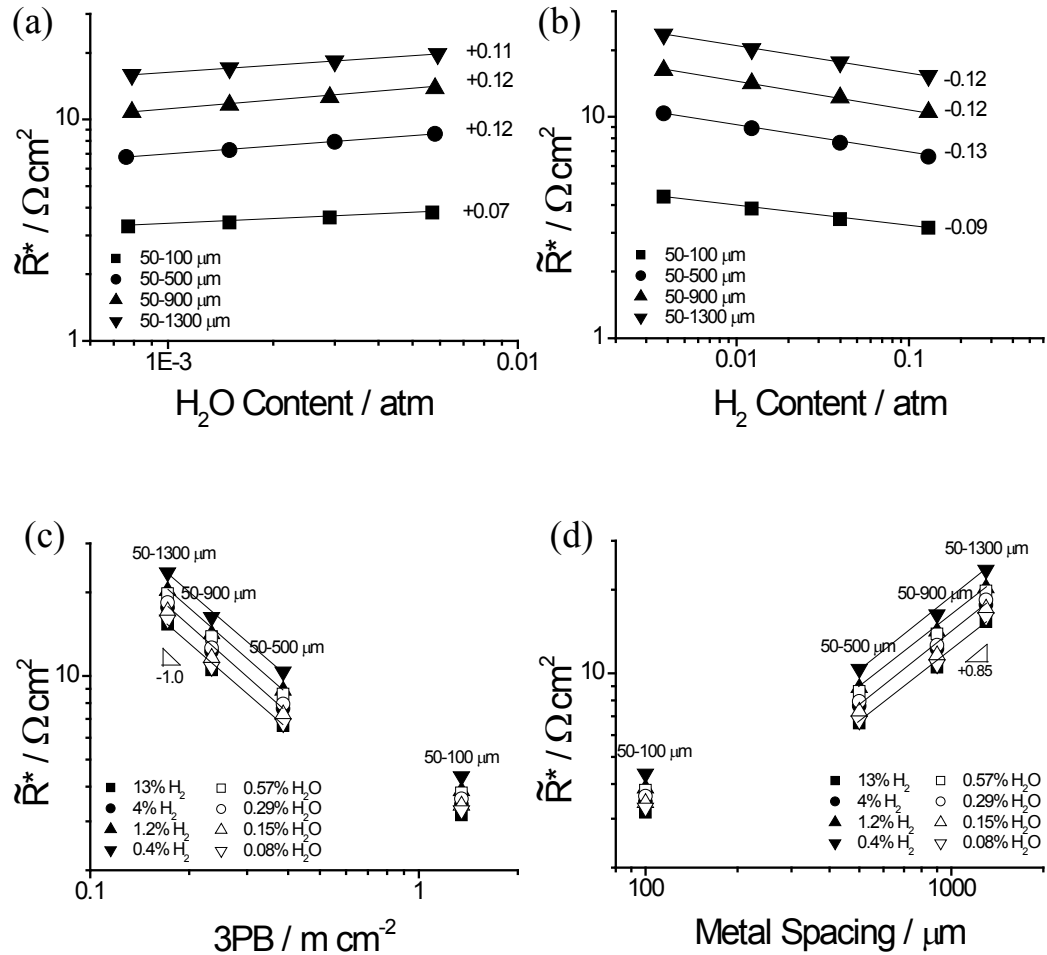


**Fig. 4.10.** HF resistance water (a) and hydrogen (b) partial pressure dependence of PLD embedding Pt strips of large pattern sizes taken at 650 °C; deviation from an explicit oxygen partial pressure dependence can be seen in the smaller patterns. HF resistance three-phase boundary (c) and metal spacing width (d) dependencies are shown for the same samples as in (a) and (b); again, deviation from the strong dependencies can be seen for the smaller pattern sizes. Solid lines are guides to the eyes.

Consider the SEM image in Fig. 4.3b and the corresponding schematic in Fig. 4.2b. SDC deposited via PLD on top of single-crystal YSZ produces epitaxial, single-crystal growth [1, 31]. However, SDC deposited via PLD on top of the platinum strips is polycrystalline and columnar. The columns are oriented perpendicular to the platinum surface, which would cause in-plane electronic migration to be highly resistive. This forces the electron migration paths from a surface reaction site that lies above YSZ, where they are generated, to the nominal 3PB region (see Fig. 4.2b). The coalescence of the field lines to the sides of a 200 nm thick platinum strip manifests as an additional arc at higher frequencies. Electrons that are generated directly above the metal are not restricted in this way, since they only have to travel along the columns' length to access the metal.

CELD samples also exhibit a HF arc, indicating that a similar restriction occurs, albeit for a different reason. Figure 4.11a shows a TEM image of a CELD deposit on top of a platinum surface, which has been annealed at 650 °C for 2 hours in air. Across the entire metal surface, a layer approximately 10 nm thick of dense SDC can be seen. Above this initial layer, sheets and needles of SDC randomly intersect with one another on both the metal and YSZ areas. However, gaseous hydrogen evolution occurs on the metal surface during CELD, making the deposit more porous on the metal than on the YSZ (c.f. Chapter 3). This is schematically shown in Figure 4.2c and confirmed by TEM imaging—a partial view of the inevitable voids above the metal area can be seen in a matrix of SDC in Figure 4.11a. Similar to the PLD case, lateral electronic migration is particularly resistive through the SDC that lies on the metal. An analogous restricting

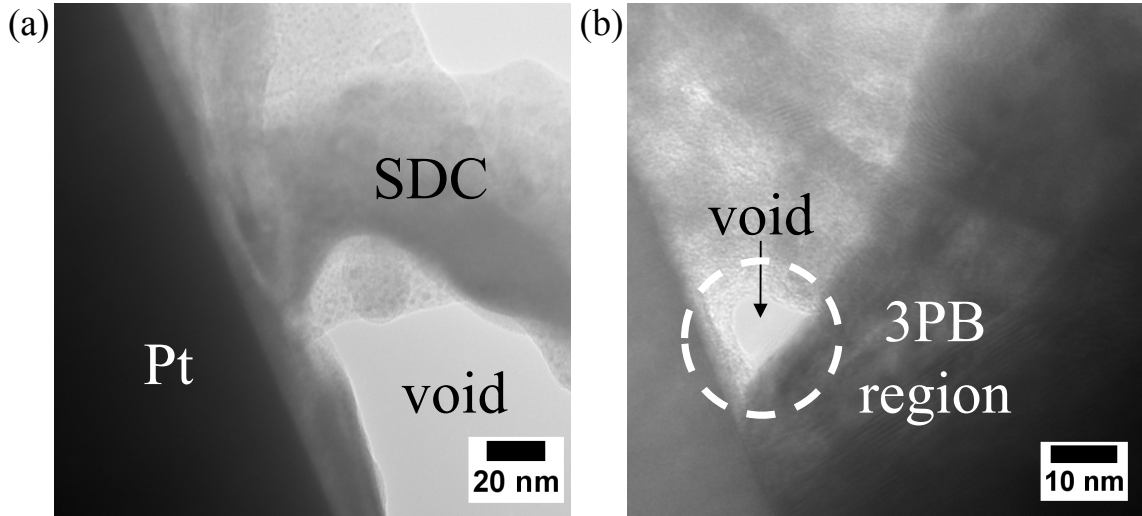


**Fig. 4.11.** TEM images of an annealed (650 °C in ambient air for 2 hours) CELD SDC deposit on a Pt surface, showing the continuous 10 nm thick layer, off of which tortuous nanosheets/needles grow, but with significant voids, particularly above the Pt surface (a) and in the 3PB regions (b). The slight texturing in the SDC deposit is FIB damage incurred during the lift-out process. Images obtained with assistance from Carol Garland, Caltech.

effect occurs for the electronic field lines in the CELD deposits, producing the familiar HF arc. This effect is possibly further exacerbated by an incomplete CELD coating, particularly in the immediate region surrounding the 3PB. Figure 4.9b shows such a void, whose effect would be to reduce the accessible SDC|metal interface even more.

Consistent with this picture, the absolute value difference of the HF ASRs for the CELD/Pt strips-embedded and CELD/Ni anti-dot-embedded samples (see Fig. 4.9) can be explained by their respective metal network thickness difference. The Pt strips are 200 nm thick, whereas the Ni anti-dot network is 400 nm thick.

This electronic pathway restriction theory is confirmed by the metal-sandwich configuration impedance response, namely that the deleterious HF arc disappears and the remaining, lone arc is identical to the single arc of the PLD/Pt strips exposed configuration. The disappearance of the HF arc can be explained as follows. Although the electronic migration through the SDC above the metal areas for both the PLD and CELD

top layers is highly resistive, the presence of a PLD SDC under-layer allows the electronic field lines to be redistributed to the entirety of the underside of the metal, shown schematically in Fig. 4.2d and e.

#### 4.2.4 *Origin of the LF Arc in Embedded Metal Configurations*

Consider now the LF ASRs of the metal-embedded configurations (c.f. Fig. 4.2c and d), whose hydrogen partial pressure dependencies are shown in Fig. 4.12—specifically, the PLD/Pt strips-embedded (black squares), the CELD/Pt strips-embedded (blue triangles), and the CELD/Ni anti-dot-embedded (red circles) configurations are compared. Also included is the data for the single arc in the PLD/Pt strips exposed model system (green upside-down triangles). Comparing the PLD/Pt strips exposed data to the PLD/Pt strips-embedded data, the absolute values and dependencies are almost identical. According to [1], this is within an expected level of variation for the same surface-dominated process. From this comparison, a confident connection can be made between the single arc in metal-exposed configurations and the LF arc in metal-embedded configurations—their origins are from the same surface-dominated, SDC|gas interfacial resistive process.

The context is now complete for understanding the LF arc behavior of CELD/metal-embedded samples. Using Fig. 4.12 as a guide, it can be seen that both the CELD/Pt strips-embedded and CELD/Ni anti-dot-embedded samples exhibit similar hydrogen gas dependencies as the PLD/Pt strips-embedded sample. However, their absolute values are 25 – 50x smaller. Taking the gas dependence similarity to be an indication that the LF arc for the CELD/metal-embedded samples is also surface-related, a simple surface area argument can explain the absolute value difference between these

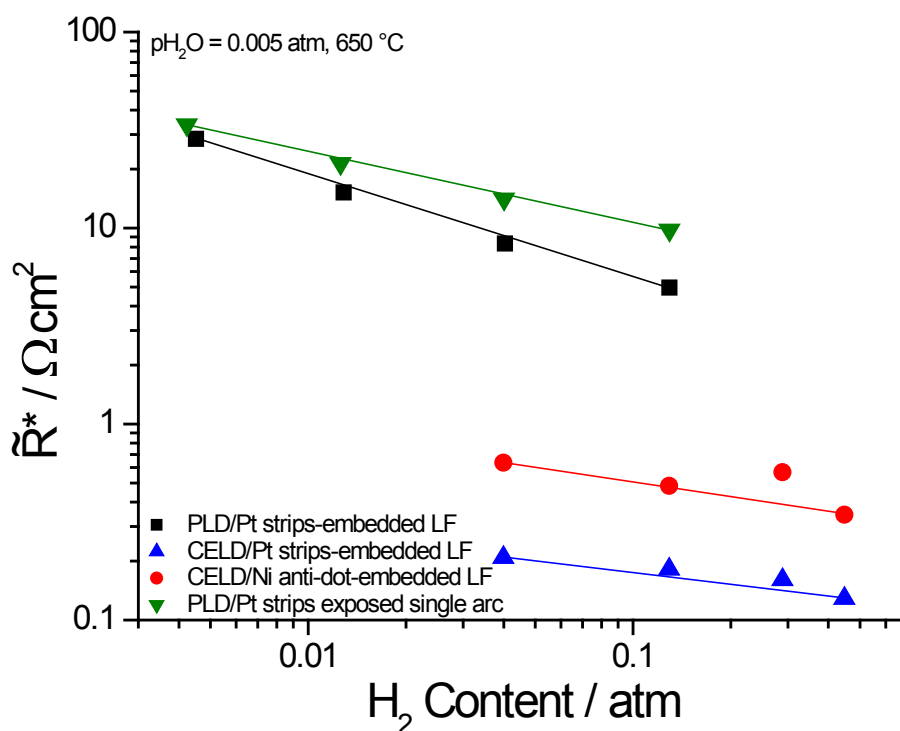


**Fig. 4.12.** Hydrogen partial pressure dependence of the LF arc resistance values for PLD/Pt strips-embedded (black squares), CELD/Pt strips-embedded (blue triangles), and CELD/Ni anti-dot-embedded (red circles) configurations. Also for comparison, the single arc gas dependence for the PLD/Pt strips exposed configuration is shown (green upside-down triangles). The normalization is the projected area of the exposed ceria surface. Solid lines are guides to the eyes.

samples. Indeed, Fig. 4.3a and c show a surface area increase on that order obtained per projected area when using CELD as the top coating. Despite the overall microstructural similarity in the CELD deposits, there is some sample-to-sample surface area variation, which manifests itself as the difference in ASRs between the two CELD samples. These observations establish the LF arc in CELD/metal-embedded configurations to be the SDC|gas interface.

### 4.3 The SDC|Gas Interface Arc: A Closer Look

The following is a brief summary of the results from Section 4.2. It was determined that the single arc that manifested for the metal-sandwich configurations and the LF arc for the metal-embedded configurations are both due to the SDC|gas interface. Hereafter, this arc is referred to as the “SDC|gas interface arc.” This arc is scrutinized in greater detail in this section, with the goal of reducing its associated ASR. Because of the undesirable ASR increase that occurs when utilizing the CELD/metal-sandwich configuration, this section utilizes the CELD/metal-embedded configuration, despite the presence of the HF arc. The SDC|gas interface arc is taken to accurately represent the potential for CELD as a fabrication method for producing highly active electrode structures, and, as such, is the only arc examined from here on out. The rest of the chapter is organized by the metal network that is used.

#### 4.3.1 *Platinum Strips*

Four experimental parameters are varied to ascertain their effect on the SDC|gas interfacial ASR. For each, the gas dependence of the ASR is evaluated, and an attempt to correlate the observed behavior to the deposit geometry via SEM is made. The impedance is normalized by the projected area of the exposed SDC surface.

##### *1. Platinum pattern size effect: 5-5 $\mu\text{m}$ vs. 20-20 $\mu\text{m}$ .*

Undoped HSA ceria is deposited on two platinum pattern sizes, 5-5  $\mu\text{m}$  and 20-20  $\mu\text{m}$ . Their interfacial reaction resistance gas dependencies are shown in Fig. 4.13, where it can be seen that the 5-5  $\mu\text{m}$  pattern ASR absolute values are 2 – 3x smaller than their 20-20

$\mu\text{m}$  counterpart. Examining the SEM images in Fig. 4.14 reveals a stark difference between the total deposition coverage for the two pattern sizes. Both patterns have qualitatively similar deposition on the platinum strip portion of the substrate, but the 20-20  $\mu\text{m}$  pattern only has disconnected, island-like growth on the exposed YSZ portion of the substrate. In contrast, the 5-5  $\mu\text{m}$  pattern has well-connected, HSA growth on seemingly all portions of the substrate, platinum and YSZ alike. Despite the fact that both patterns have nominally 50% platinum and 50% YSZ exposed surfaces, the lack of quality deposition on the YSZ portions lying greater than a few microns away from the base generating metal portions of the substrate causes a decrease in performance. This defines a lateral metal spacing limitation; consequently, only patterns with feature sizes equivalent to (or below, for the nickel anti-dot films) 5-5  $\mu\text{m}$  are subsequently used.

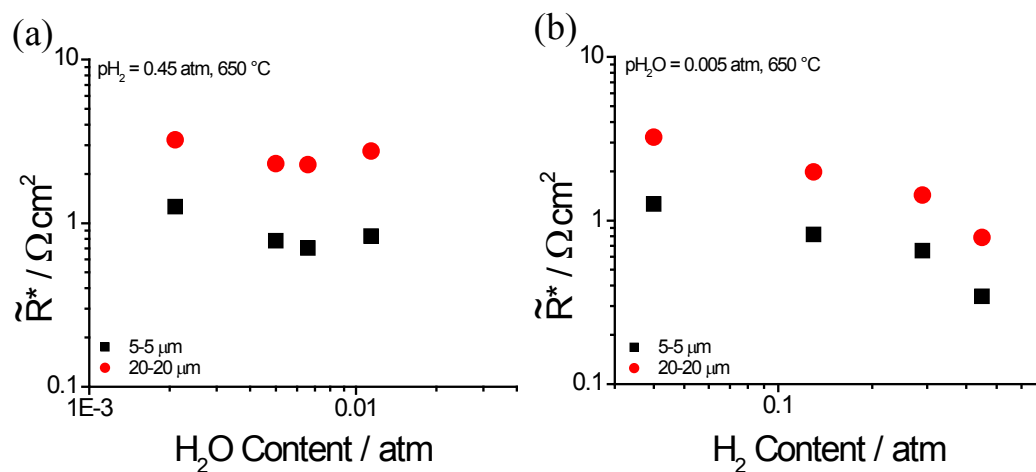


**Fig. 4.13.** Water (a) and hydrogen (b) partial pressure dependencies of the SDC|gas interfacial ASR for 5-5  $\mu\text{m}$  (squares) and 20-20  $\mu\text{m}$  (circles) CELD/Pt strips-embedded samples deposited for 10 minutes with the undoped electrolyte.

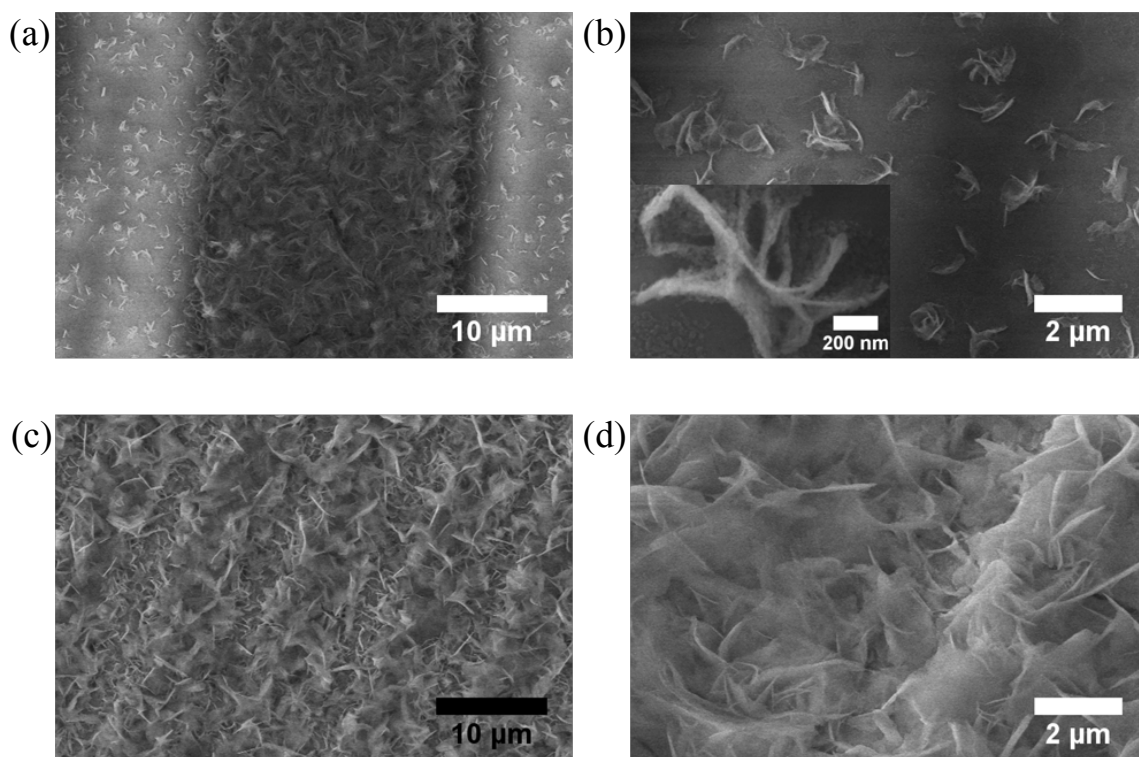


**Fig. 4.14.** SEM images of the samples probed in Figure 4.13: (a) and (b) are top-down views of the 20-20  $\mu\text{m}$  sample; (c) and (d) are angled views of the 5-5  $\mu\text{m}$  sample. The inset in (b) is an isolated HSA ceria growth in the center of a 20  $\mu\text{m}$  wide YSZ region, pictured in low magnification in the rest of (b).

2. *CELD deposition time effect: 5 vs. 10 (vs. 20) min.*

Both CELD undoped and Sm-doped HSA ceria microstructures are evaluated at different deposition times—5 and 10 minutes for the undoped ceria, and 5, 10, and 20 minutes for the Sm-doped ceria.

Figure 4.15 shows the gas dependencies for undoped ceria deposited for 5 and 10 minutes. The only real difference is under water partial pressure change, where the 5 minute sample exhibits a sharper slope. Comparing SEM images for the two samples at equal magnification shows a slight qualitative decrease in apparent surface area for the 10 minute sample (Fig. 4.16). The deposit that lies on top of the platinum strips in the 10 minute sample has less wispy features than that grown on the YSZ surfaces, and as compared to all areas of the deposit grown for 5 minutes. This observation holds true for multiple samples and multiple configurations—prolonged depositions tend to reduce the apparent surface area of the coatings grown on metal surfaces.

Analogously, Figure 4.17 shows the partial pressure dependencies for Sm-doped ceria deposited for 5, 10, and 20 minutes. Similarly to the undoped comparison, the ASRs are essentially the same, although the 10 minute sample performed slightly better in water. The SEM images in Figure 4.18 show a slight deposition coverage increase in going from 5 to 10 minutes of deposition, and the familiar chunky morphology is observed for the 20 minute sample. Recall from Chapter 3 that the deposition rate for Sm-doped ceria is slower than that of undoped ceria. 5 minutes of Sm-doped ceria CELD is not enough to cover the sample with the HSA morphology, hence its higher ASRs as compared to the 10 minute sample. Just like the undoped case, however, chunky coatings over the platinum areas due to prolonged deposition times also increase the ASR.

These results indicate an optimal deposition time—approximately 5 minutes for undoped ceria and approximately 10 minutes for Sm-doped ceria.

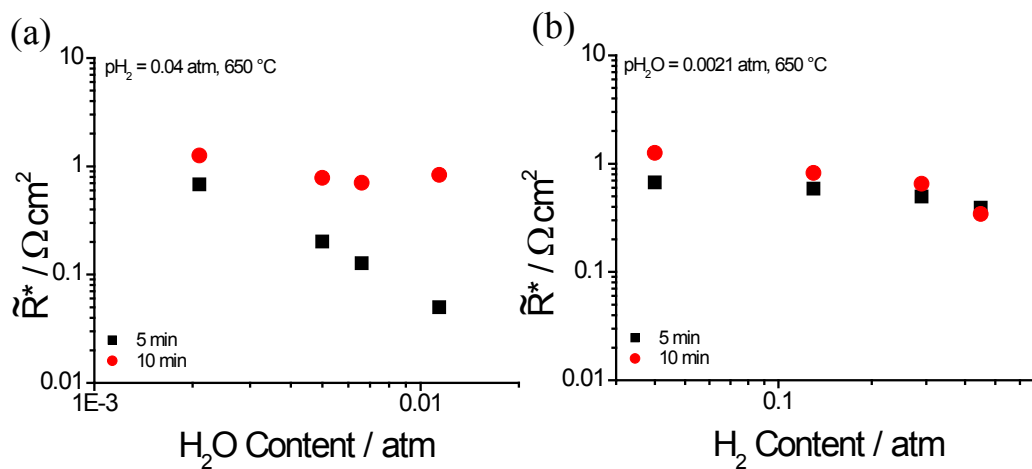


**Fig. 4.15.** Water (a) and hydrogen (b) partial pressure dependencies of the SDC|gas interfacial ASR for 5 minute (squares) and 10 minute (circles) depositions for 5-5  $\mu\text{m}$  CELD/Pt strips-embedded samples with the undoped electrolyte.

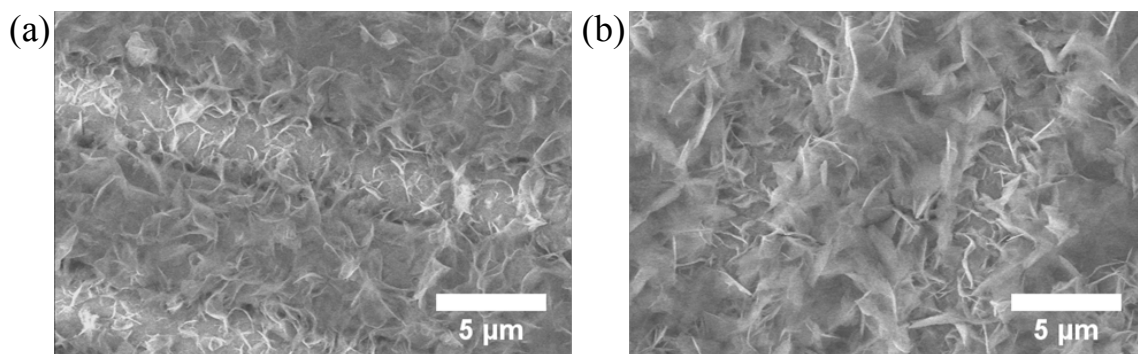


**Fig. 4.16.** SEM images of the undoped samples probed in Fig. 4.15: (a) a 5 minute deposition on a 5-5  $\mu\text{m}$  pattern; (b) a 10 minute deposition on a 5-5  $\mu\text{m}$  pattern.

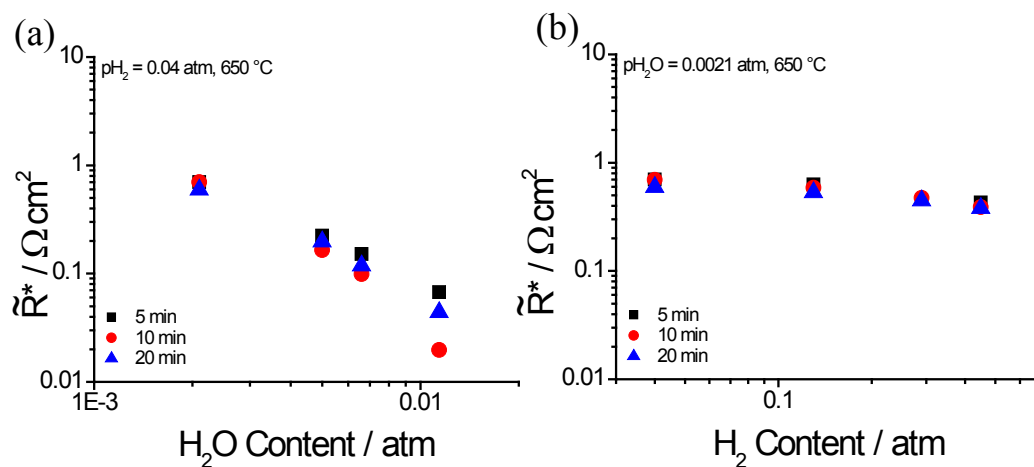


**Fig. 4.17.** Water (a) and hydrogen (b) partial pressure dependencies of the SDC|gas interfacial ASR for 5 minute (squares), 10 minute (circles), and 20 minute (triangles) depositions for 5-5  $\mu\text{m}$  CELD/Pt strips-embedded samples with the doped electrolyte.

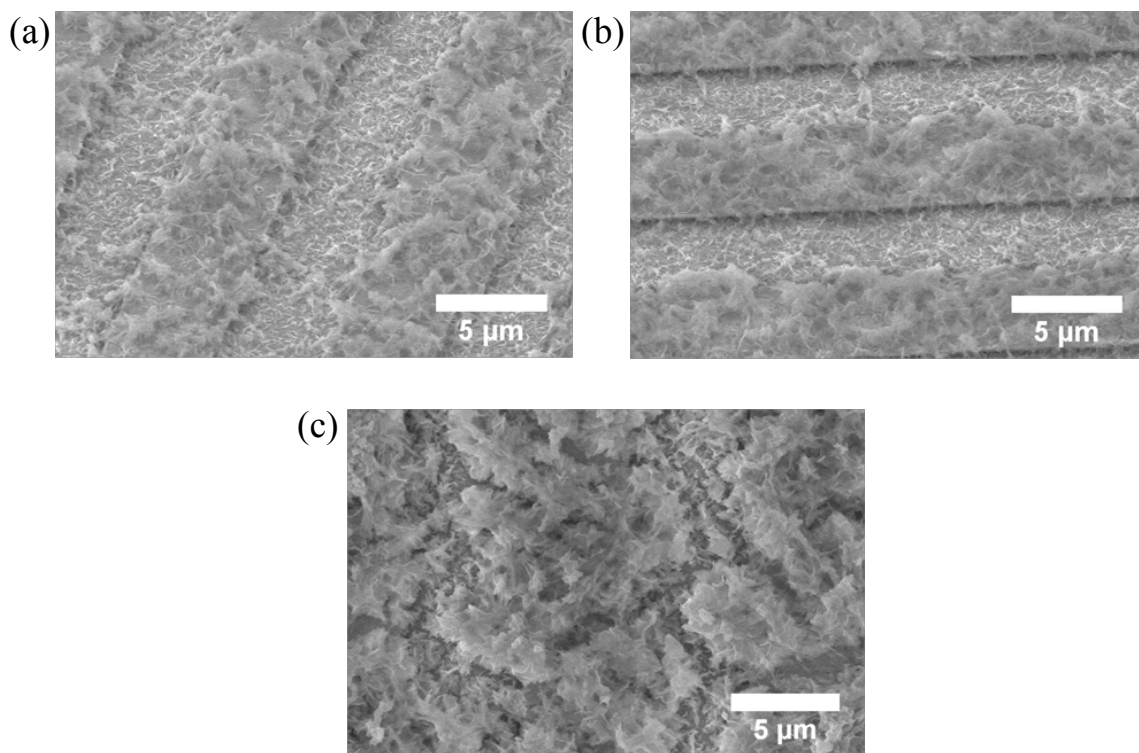


**Fig. 4.18.** SEM images of the doped samples probed in Fig. 4.17: (a) a 5 minute deposition on a 5-5  $\mu\text{m}$  pattern; (b) a 10 minute deposition on a 5-5  $\mu\text{m}$  pattern; and (c) a 20 minute deposition on a 5-5  $\mu\text{m}$  pattern.

### 3. Cation doping effect: undoped vs. Sm-doped ceria.

The doping effect for samples deposited for 5 minutes can be seen in Figure 4.19. There appears to be little to no impact introduced by samarium doping. Considering the similarities in microstructure seen in Figure 4.20, and the short distance charged species must travel, this result is not surprising. Indeed, samarium is not expected to aid the surface reaction kinetics much, and is instead introduced to increase the oxygen vacancy concentration, as in Eqn. 1.5. Conversely, there is a difference in the performance of undoped and Sm-doped samples deposited for 10 minutes, as seen in Figure 4.21, but judging from the SEM images of Figure 4.22, it is likely that this difference is due to slight surface area differences, rather than surface reaction kinetics. Similar to the preceding section, the deposition rate difference between the undoped and Sm-doped samples appears to be the primary culprit here.

Despite the minimal difference for samples deposited for 5 minutes, Sm-doped ceria is preferred over undoped, if for no other reason than compatibility with a Sm-doped ceria electrolyte solution.

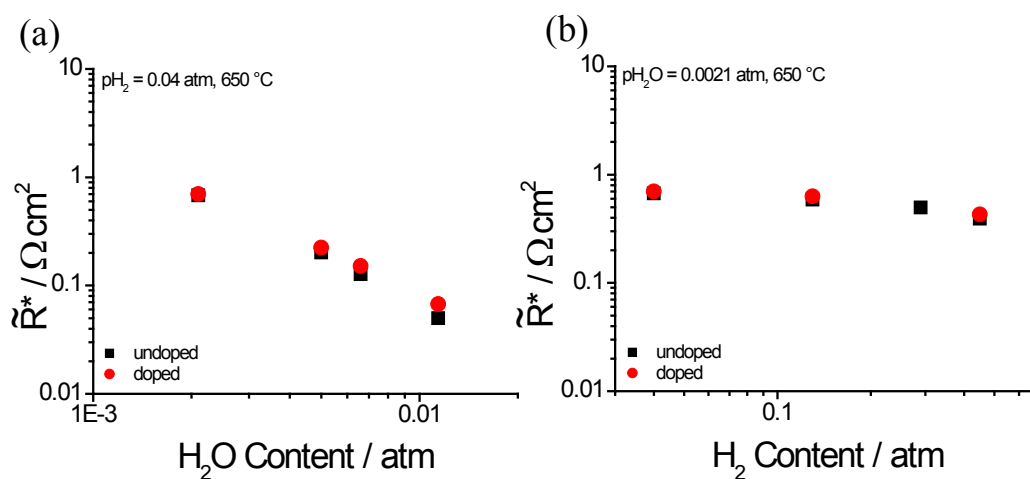


**Fig. 4.19.** Water (a) and hydrogen (b) partial pressure dependencies of the SDC|gas interfacial ASR for undoped (squares) and doped (circles) electrolyte depositions for 5 minutes for 5-5  $\mu\text{m}$  CELD/Pt strips-embedded samples.

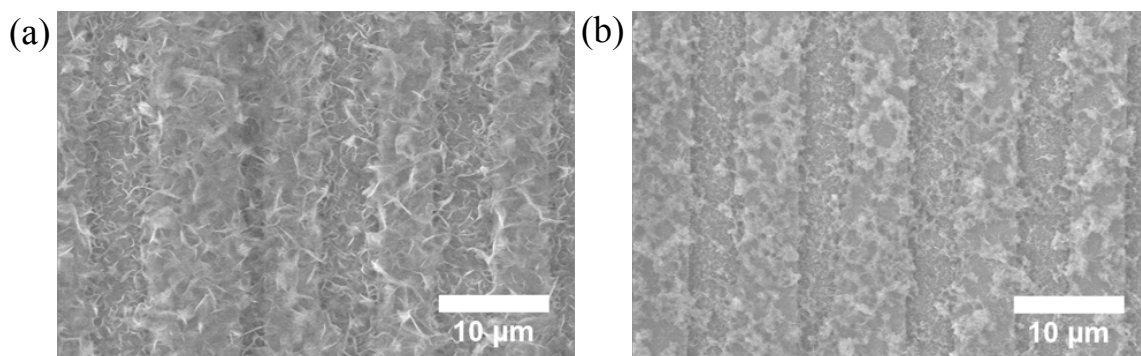


**Fig. 4.20.** SEM images of the 5 minute deposition, 5-5  $\mu\text{m}$  pattern samples probed in Fig. 4.19: (a) with the undoped electrolyte; and (b) with the doped electrolyte.

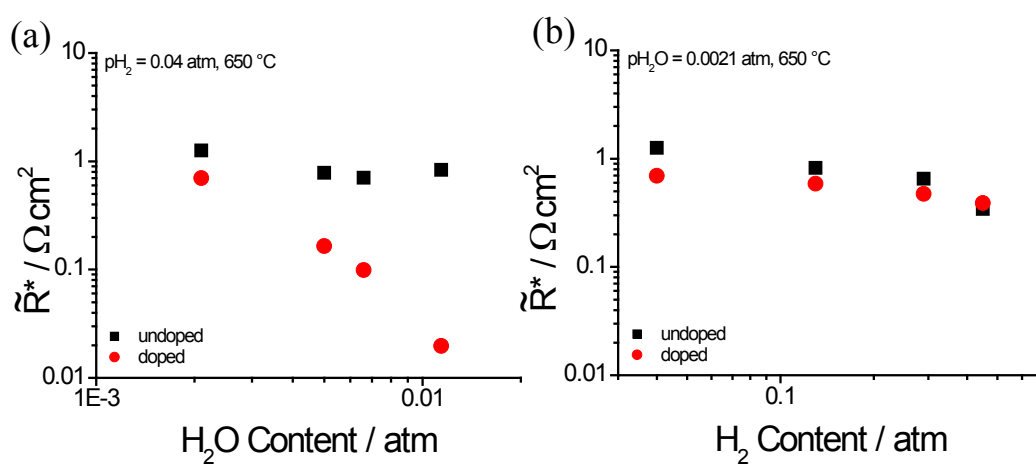


**Fig. 4.21.** Water (a) and hydrogen (b) partial pressure dependencies of the SDC|gas interfacial ASR for undoped (squares) and doped (circles) electrolyte depositions for 10 minutes for 5-5  $\mu\text{m}$  CELD/Pt strips-embedded samples.

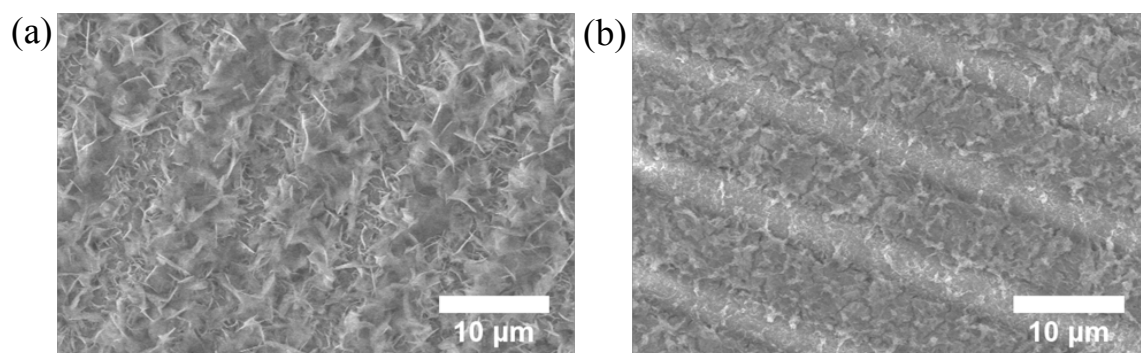


**Fig. 4.22.** SEM images of the 10 minute deposition, 5-5  $\mu\text{m}$  pattern samples probed in Fig. 4.21: (a) with the undoped electrolyte; and (b) with the doped electrolyte.

4. *Consecutive deposition effect: 5 vs. 5+5 minutes.*

Section 3.3.2 outlined the high temperature behavior of the HSA coatings. Therein, undesirable cracking issues were defined, and subsequent depositions were investigated as a possibility to “healing” cracks induced either by the deposition process itself, or a later annealing step. To assess the electrochemical activity impact of consecutive depositions on a single sample, a Sm-doped sample deposited for 5 minutes was subjected to an annealing step at 600 °C for 10 hours. The un-cracked, as-deposited morphology is shown in Fig. 4.24a, and the cracked, as-annealed morphology is shown in Fig. 4.24b. The sample was then probed for the first time via ACIS. Immediately following the testing step, a second 5 minute deposition was performed on the same sample, pictured in Fig. 4.24c. Then, the sample was probed for the second time via ACIS, and is pictured in its final post-second-testing state in Fig. 4.24d.

As can be seen in Figure 4.23, there is practically no change in activity between the 5 and 5+5 minute samples. This is a telling result, indicating that cracking in the HSA morphology is not a significant concern. Fig. 4.24cd exhibits the expected deposition in the former cracks of the sample, yet no impact on the ASR is detected. Although cracking seems intuitively counterproductive, the cracking observed in these samples is on a length scale so as to not prevent the migration of charged species. In fact, in-plane cracking propagated perpendicularly to the length of the platinum strips will not impact movement of charged species in the same perpendicular direction, as is the case for this electrode configuration. If there was significant in-plane cracking along the length of the platinum strips, then there would be an insurmountable barrier for oxygen ions to traverse, in order to access surface reaction sites on top of the metal strips.

From a different perspective, the possibility exists to create even more surface area by consecutive depositions due to concentration on the cracked areas. For this reason, and because it is now known to not have an adverse effect, consecutive depositions are still pursued in practice.

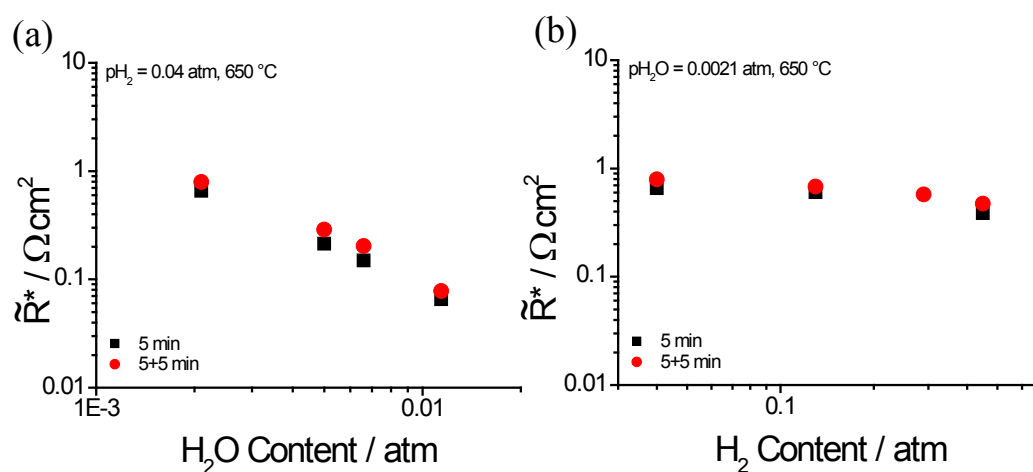


**Fig. 4.23.** Water (a) and hydrogen (b) partial pressure dependencies of the SDC|gas interfacial ASR for a 5-5  $\mu\text{m}$  CELD/Pt strips-embedded sample that underwent two consecutive 5 minute depositions, with a high temperature step in between: the first 5 minute deposition (squares) and the second 5 minute deposition, referred to as 5+5 minute (circles), with the doped electrolyte are shown.

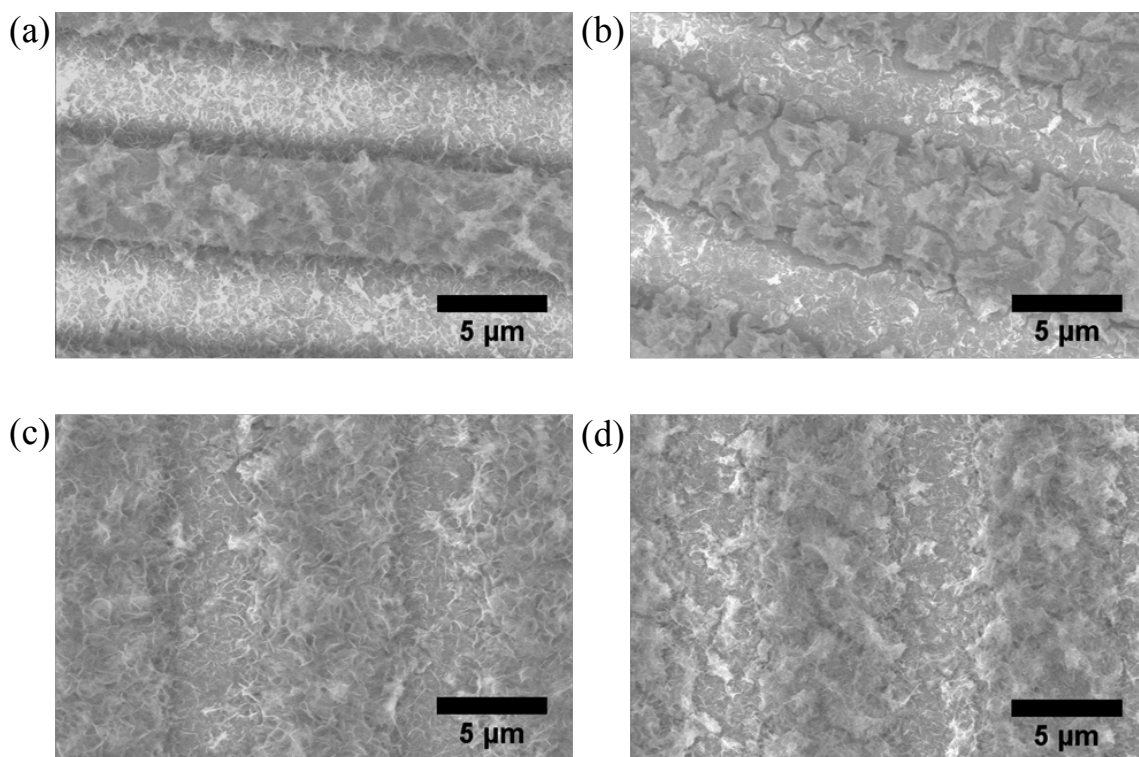


**Fig. 4.24.** Chronological SEM images of the 5-5  $\mu\text{m}$  pattern sample probed in Fig. 4.23: (a) the as-deposited, un-cracked morphology after the first 5 minute deposition; (b) the cracked morphology after annealing at 600  $^{\circ}\text{C}$  for 10 hours in air; (c) the as-deposited morphology after the second 5 minute deposition, healing the cracks; and (d) the cracked morphology post-testing for the second time.

The following is a summary of the insights gained from the above experiments. First, the furthest non-conducting surface distance away from the base electrogenerating metal features should not exceed 3 microns. Prolonged depositions tend to lead to chunky, lower surface area coatings on the metal portions of the substrate. This motivates a reduction in the exposed metal area fraction, but is limited in practice by thermal stability of micro-/nano-sized metal features. 5 minute depositions are preferred for undoped samples, and 10 minute depositions are preferred for Sm-doped samples—the difference is due to the deposition rate influence of cation doping. Sm-doped samples are preferred due to their inherent transport properties, but surface kinetics do not appear to

be impacted at all. Healing cracks by consecutive depositions does not harm the electrode activity, but could lead to a further enhancement of surface area; also, cracking does not appear to be a critical concern in this electrode configuration.

Using the trends with partial pressures, these data can be extrapolated to 97% H<sub>2</sub>, 3% H<sub>2</sub>O, at 650 °C. The best samples give SDC|gas interfacial ASRs in the range 1.3 – 3.7 mΩ cm<sup>2</sup>, far below the state-of-the-art at the time of this writing [24-25].

#### 4.3.2 *Nickel Anti-Dot Films*

Two experimental parameters are investigated for the CELD/Ni anti-dot-embedded configuration, analogous to the treatment of platinum strip samples given above.

##### *1. CELD deposition time effect: 5 vs. 10 vs. 20 + 2.5 minutes.*

The SDC|gas interfacial ASRs of three nickel anti-dot samples are compared in Fig. 4.26, with different deposition times—namely, 5 + 2.5 minutes, 10 + 2.5 minutes, and 20 + 2.5 minutes samples. A 2.5 minute consecutive deposition is used in all three cases. Not much difference can be discerned from the partial pressure dependence plot, although there is a slight ranking under changing p<sub>H<sub>2</sub>O</sub>, with the 10 minute besting the 5 minute and 20 minute samples, in that order. A microstructure investigation revealed some offsetting issues.

All three samples suffer from asymmetric deposition on what should be identical sides of the cell. This is due to an experimental shortcoming. When a sample is dipped into the liquid electrolyte (c.f. Fig. 3.2), one side of the cell is directly facing the counter electrode, whereas the other is facing away from it. The side facing the counter electrode

experiences faster deposition rates than the side facing away. This is shown in Fig. 4.25, where each row of images is a different sample, and the first three images of the first column, i.e., 4.25a, c, and e, represent the side facing away from the counter electrode, and the first three images of the second column, i.e., 4.25b, d, and f, represent the side directly facing the counter electrode. Clear deposition maturity differences can be seen between the two sides of each sample. Longer deposition times develop slat-like growth on top of the original HSA morphology, seen in Fig. 4.25d, f, and h; however, in-between the slats lay ideal HSA morphology (Fig. 4.25g). The 20 minute sample even sees HSA growth on top of the slats, although the slats begin to warp and fold, disconnecting themselves from the underlying layer (Fig. 4.25h).

These features notwithstanding, the critical characteristic that appears to dominate the ultimate performance is overall coverage. The 5 minute sample left innumerable micro-sized regions devoid of the HSA morphology, as in Fig. 4.25a. The 20 minute sample had large areas completely uncovered by any deposit, HSA or not. The 10 minute sample, on the other hand, was the most consistently covered over large and small scales with the desired morphology, and consequently exhibits the best performance. Neither cracking nor slat-growth inhibits performance as much as basic coverage issues.

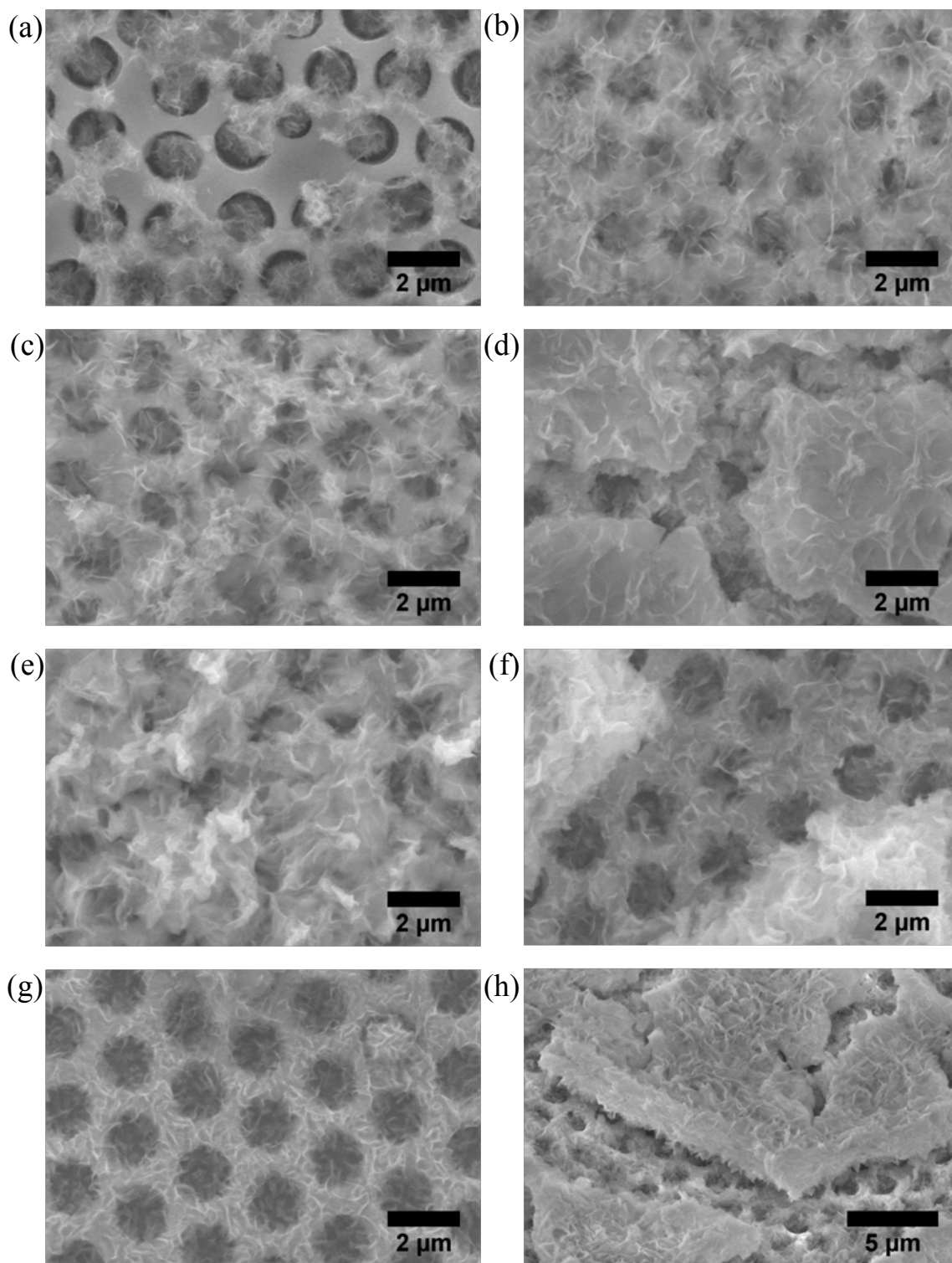


**Fig. 4.25.** SEM images of the doped Ni anti-dot samples probed in Fig. 4.26: the first row is the 5 + 2.5 minute sample, where (a) is taken from the side facing away from the counter electrode and (b) is from the side facing toward it; the second row is the 10 + 2.5 minute sample, where (c) is the side facing away, (d) is the side facing toward; and the third row is the 20 + 2.5 minute sample, where (e) is the side facing away, (f) is the side facing toward. (g) is the morphology lying in between the slats in (d); and (h) shows overgrown slats disconnecting from the substrate from (f).

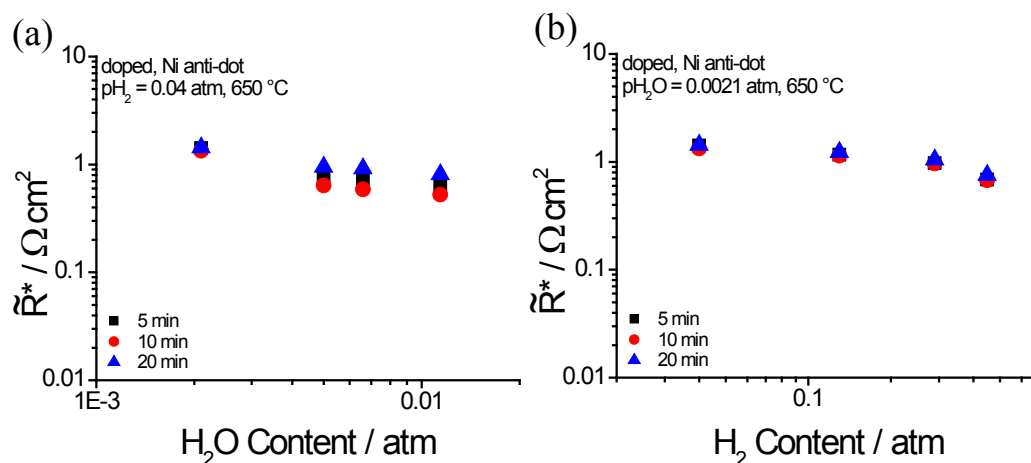


**Fig. 4.26.** Water (a) and hydrogen (b) partial pressure dependencies of the SDC|gas interfacial ASR for CELD/Ni anti-dot-embedded samples deposited with the doped electrolyte for 5 + 2.5 minutes (squares), 10 + 2.5 minutes (circles), and 20 + 2.5 minutes (triangles). The initial PS bead size was  $2 \mu\text{m}$  and etched to  $1.4 \mu\text{m}$ .

## 2. CELD morphology effect: planar vs. HSA(1) and HSA(2).

As discussed in Chapter 3, both HSA and planar film morphologies are possible with CELD ceria. These are compared in Fig. 4.28. There is a clear difference in activity, owing to the surface area difference between HSA samples (see Fig. 4.27ab, HSA(1) and 4.27cd, HSA(2)) and planar samples (see Fig. 4.27ef). Sample-to-sample variability is again seen here in the two HSA samples. This difference appears to correlate well with morphological differences apparent in the SEM images of Fig. 4.27.

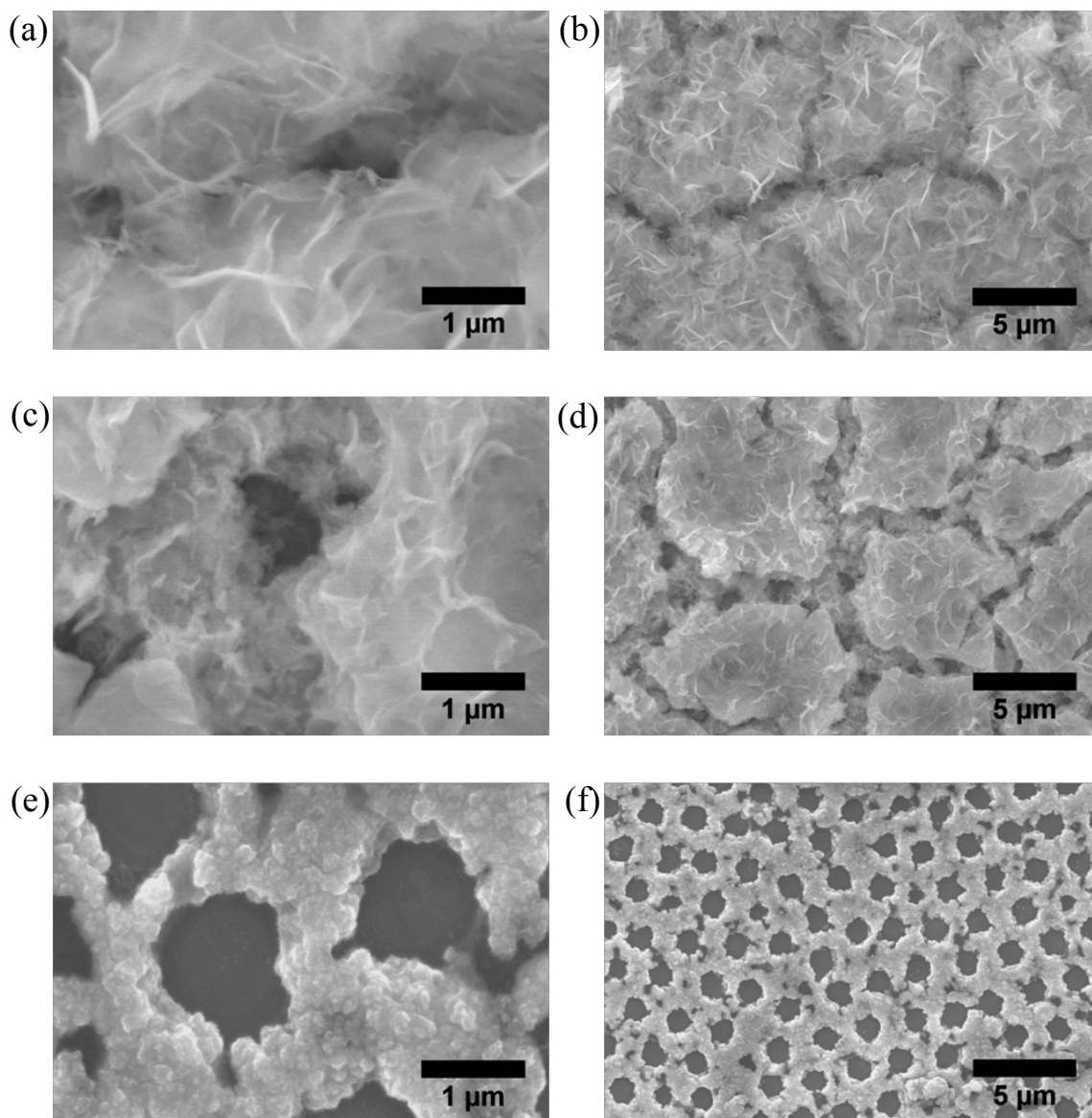


**Fig. 4.27.** Post-testing SEM images of the doped Ni anti-dot samples probed in Fig. 4.28: the first row is HSA(1), deposited for 10 + 2.5 minutes; the second row is HSA(2), deposited for 10 + 2.5 minutes; and the third row is the planar sample, deposited with the doped + H<sub>2</sub>O<sub>2</sub> electrolyte at -0.55 V vs. SCE for 0.5 + 0.5 minutes.

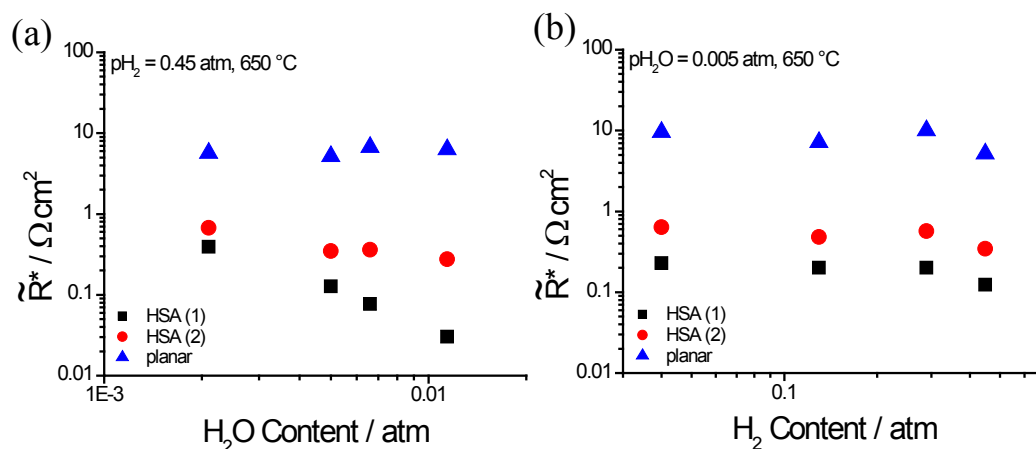


**Fig. 4.28.** Water (a) and hydrogen (b) partial pressure dependencies of the SDC|gas interfacial ASR for CELD/Ni anti-dot-embedded samples deposited with the doped electrolyte for 10 + 2.5 minutes at  $0.8 \text{ mA cm}^{-2}$  (HSA (1), squares), 10 + 2.5 minutes at  $0.8 \text{ mA cm}^{-2}$  (HSA (2), circles), and with the doped +  $\text{H}_2\text{O}_2$  electrolyte for 0.5 + 0.5 minutes at  $-0.55 \text{ V vs. SCE}$  (triangles). The initial PS bead size in each case was  $2 \mu\text{m}$  and etched to  $1.3\text{-}1.4 \mu\text{m}$ .

In summary, consistent HSA coverage is critical, and some sample-to-sample variation exists. The deposition time should be long enough to cover the anti-dot network, but not so long that slat-like growth begins, which effectively covers portions of the enhanced surface area.

Extrapolating the best CELD/Ni anti-dot-embedded configuration data to 97%  $\text{H}_2$ , 3%  $\text{H}_2\text{O}$ , and  $650 \text{ }^\circ\text{C}$ , the best LF ASR is  $6.8 \text{ m}\Omega \text{ cm}^2$ .

It should be stressed that to make use of these promising results, the issues associated with the CELD/metal-sandwich configuration need to be alleviated. The reader should keep in mind that a HF arc still exists for the results presented in the preceding section.

# Chapter 5

## Sundry Specialized CELD

### Microstructures

#### 5.1 Anodic Aluminum Oxide (AAO) Templated Nanowires

Due to their small sizes and potential for controllable features, nanowires/tubes represent an attractive option for increasing the surface area of ceria-based anodes. Templated approaches are currently the most flexible routes to fabricating nanowires/tubes, as only a suitable filling method needs be developed for a particular material composition, be it metallic, semiconducting, or ceramic, and so on. Anodic aluminum oxide (AAO) templates are utilized here for their uniformity and tunability. The AAO template fabrication process is first discussed, and then the CELD of ceria into its pores is investigated.

##### 5.1.1 *AAO Template Formation Mechanism and Background*

Aluminum naturally forms a thin oxide layer at room temperature and ambient atmospheres. Given an extra driving force and a much different environment, this oxide layer can take on a regular porous structure. Specifically, anodically oxidizing aluminum metal in a liquid acidic electrolyte can produce an oxide layer with in-plane, hexagonally arranged and vertically aligned pores (see the schematic in Fig. 5.1 and SEM images in Fig. 5.2). The pores are straight and extend throughout the entire thickness of the oxide, with the exception of a small “barrier layer” lying at the bottom of the pores, at the metal|oxide interface. The geometric ratios of the structural features are primarily

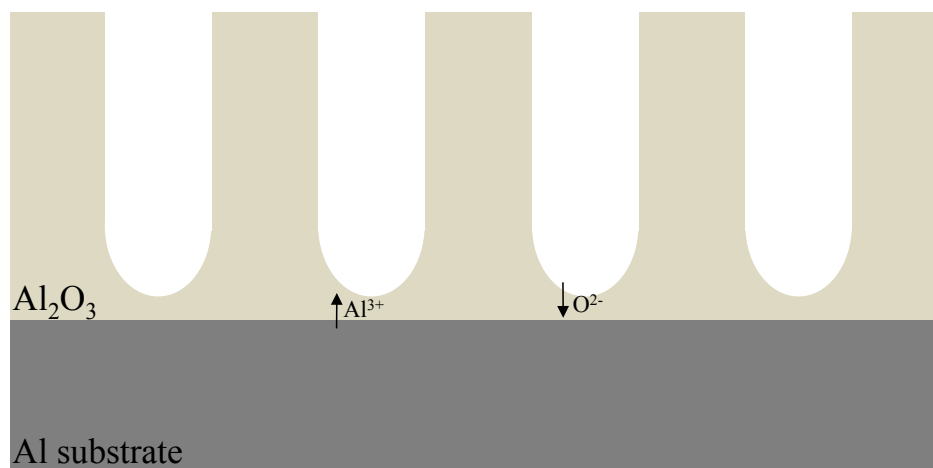


**Fig. 5.1.** A schematic showing a cross-sectional view of the hexagonally arrayed, vertically aligned porous oxide template produced by anodically oxidizing aluminum metal. Aluminum ions generally travel toward the liquid acidic electrolyte and oxygen ions from solution toward the positively biased aluminum metal. An oxide barrier layer exists at the bottom of each pore.

controlled by the applied voltage—the diameter, inter-pore spacing, and even barrier layer thickness all linearly depend on the voltage. In addition, different electrolyte solution compositions provide different feature size ranges and, hence, different operating voltage ranges. The three most common electrolyte solutions in ascending feature size order are sulfuric acid, oxalic acid, and phosphoric acid.

Since the initial investigations began in the 1940's [98-99], attempts have been made to explain the seemingly anomalous behavior of the formation of porous alumina. Recently, a comprehensive picture has been given that adequately explains the formation mechanism and describes the steady-state growth conditions, mainly by uniting the early theories [100-103]. The conclusions presented in the preceding references are summarized below. First, the two governing reactions are given—aluminum ion

generation at the metal|oxide interface, and oxygen ion deposition at the oxide|electrolyte solution interface.



Electric species migration is no doubt happening—the oxide layer continues to thicken and the aluminum metal is consumed as long as a voltage is applied. Although the exact origin of the localized effects that ultimately lead to pore formation is not well-understood, it is now known that compressive stresses at the oxide|electrolyte solution interface induce significant steady-state lateral flow in the oxide, in directions perpendicular to the applied electric field. These stresses appear to come from competitive adsorption of oxygen ions, as in Eqn. 5.2, and anions from the electrolyte solution. The adsorption step highly regulates the current density, as well as impacts the lateral Newtonian flow of the oxide layer, accounting for the extreme dependence of the template geometry on electrolyte solution composition. This also explains why certain acids, such as boric acid, produce dense, planar oxide films under identical conditions as AAO template-producing acidic electrolyte solutions. The viscous flow induced by local stress concentration acts to push oxide material radially away from the pore bottoms, and then up the pore walls, and is ultimately restricted by volume expansion and charge conservation. The cascading effect of the applied voltage on the current density, adsorption rate, local stress formation, and lateral flow of the oxide explains its robust relationship to the geometric feature sizes of the resulting template.

Historically, it has been theorized that the pores were formed simply as a result of the applied voltage leading to local electric field-assisted dissolution of the oxide layer by

Joule (or, resistive) heating. Although this theory alone is unable to explain the invariance of the barrier layer thickness with time, it is a mechanistic factor, as it can lead to inhomogeneity in oxide formation rates for different regions of a single sample [103]. For bulk aluminum samples, Joule heating effects are unnoticeable. However, for thin film aluminum samples, which contain a buried gold or platinum under-electrode, rapid oxide dissolution arising from poor heat conduction of the supporting substrate can expose the gold/platinum to the liquid electrolyte. At operating voltages of 20 – 100 V, this translates into violent gaseous evolution catastrophically destroying the fragile thin film configuration.

#### 5.1.2 *AAO Fabrication Experimental Details*

A two-electrode setup is used, with an HP 6002A DC Power Supply as the voltage source, aluminum metal (exposed surface area 0.5 – 2 cm<sup>2</sup>) as the anode, and a carbon rod cathode, all immersed in an oxalic acid (0.3 – 0.6 M) liquid electrolyte. All anodizations are conducted at 40 V and room temperature. Under these conditions, the as-fabricated pore diameters are 15-25 nm, the inter-pore distance is ~90 nm, and the barrier layer thickness is ~25 nm. To open up the pore diameters, an etching solution of 10 wt % phosphoric acid is used for 10-30 minutes at 30 °C, giving final pore diameters of 40 – 80 nm.

Immediately upon applying a potential, the aluminum is anodically polarized, and aluminum oxide spontaneously and continuously forms until the voltage is turned off. This naturally consumes some depth of the aluminum metal, and for bulk aluminum samples, AAO templates of almost arbitrary thickness can be achieved. The template

thickness naturally depends on the anodization time, with a formation rate of 3 – 4 nm  $\text{sec}^{-1}$ . Free-standing templates can be produced by anodizing for a couple of hours, which gives a template thickness in the tens of microns range. To separate the oxide from the metal, a saturated solution of  $\text{HgCl}_2$  is used to selectively attack the remaining aluminum metal, while the AAO template is undisturbed.

The oxalic acid electrolyte solution does etch the alumina and the aluminum metal during anodization, so a protective quick-drying coating (nail polish) is applied to the meniscus area, as the dissolution activity is greatly enhanced there. In some circumstances without this protective coating, a 0.25 mm thick aluminum foil sample could be entirely etched through, after only a couple hours of anodizing.

Although not a strict requirement for the simple goal of surface area enhancement, an ordered arrangement of pores is desirable, as a more accurate determination of the specific increase in surface area can be calculated. To accomplish this, a two-step anodization process is employed. First, an initial AAO layer is produced at 40 V for 10 minutes. This layer is subsequently removed in a combination of chromic (1.5 wt %) and phosphoric (6 wt %) acid at 60 °C, typically for 1 – 2 hours, depending on the AAO layer thickness. This leaves indentations in the newly-exposed aluminum surface. A second anodization at 40 V is then conducted, which produces the desired ordered arrangement, utilizing the existing indentations as nucleation points. Finally, the pore diameters are etched as before.

Conveniently, there is little variation in the produced structure when forming an AAO template over small or large areas, and there is obvious symbiotic potential for utilizing this liquid, electrochemical technique with other similar methods for ultimately

depositing nanowires, such as the CELDs of Chapter 3. Ultimately, the goal is to grow ceria nanowires onto an existing two-dimensional porous metal network, as in the anti-dot films of Chapter 2. A gradual, graded experimental approach was taken to gather critical criteria for successful AAO template growth in simple systems, before more complex systems were attempted. For the former, 0.25 mm thick bulk aluminum foil is used; for the latter, a thin film of aluminum (0.5 – 2  $\mu\text{m}$ ) is either thermally evaporated or sputtered onto a non-porous thin film of gold/titanium, which itself is thermally evaporated onto a robust substrate such as quartz, silicon, or YSZ. The titanium layer is only 10 nm thick, and is used strictly for adhesion improvement of the gold thin film. Because significant difficulties were encountered with this intermediate system, limited attempts were made to fabricate thin AAO template layers on anti-dot films.

### 5.1.3 *AAO Template Results*

The twice-anodized AAO template process is illustrated in Figure 5.2 for a bulk aluminum foil sample. As can be seen in Fig. 5.2a, the initial pore formation in the first anodization is highly irregular. As the anodization continues, however, a more homogeneous arrangement emerges. The first anodization should be conducted long enough to reach this homogeneous state—10 minutes is sufficient for the conditions given above. Fig. 5.2b shows the result of this evolution, where the first oxide layer has been removed, and a hexagonal configuration of indentations can be seen on the surface of the exposed aluminum metal. The chromic/phosphoric acid mixture used to remove the first anodization layer does not appreciably attack the aluminum over the etching time scales used here. Fig. 5.2cd show the ordered template after the second anodization

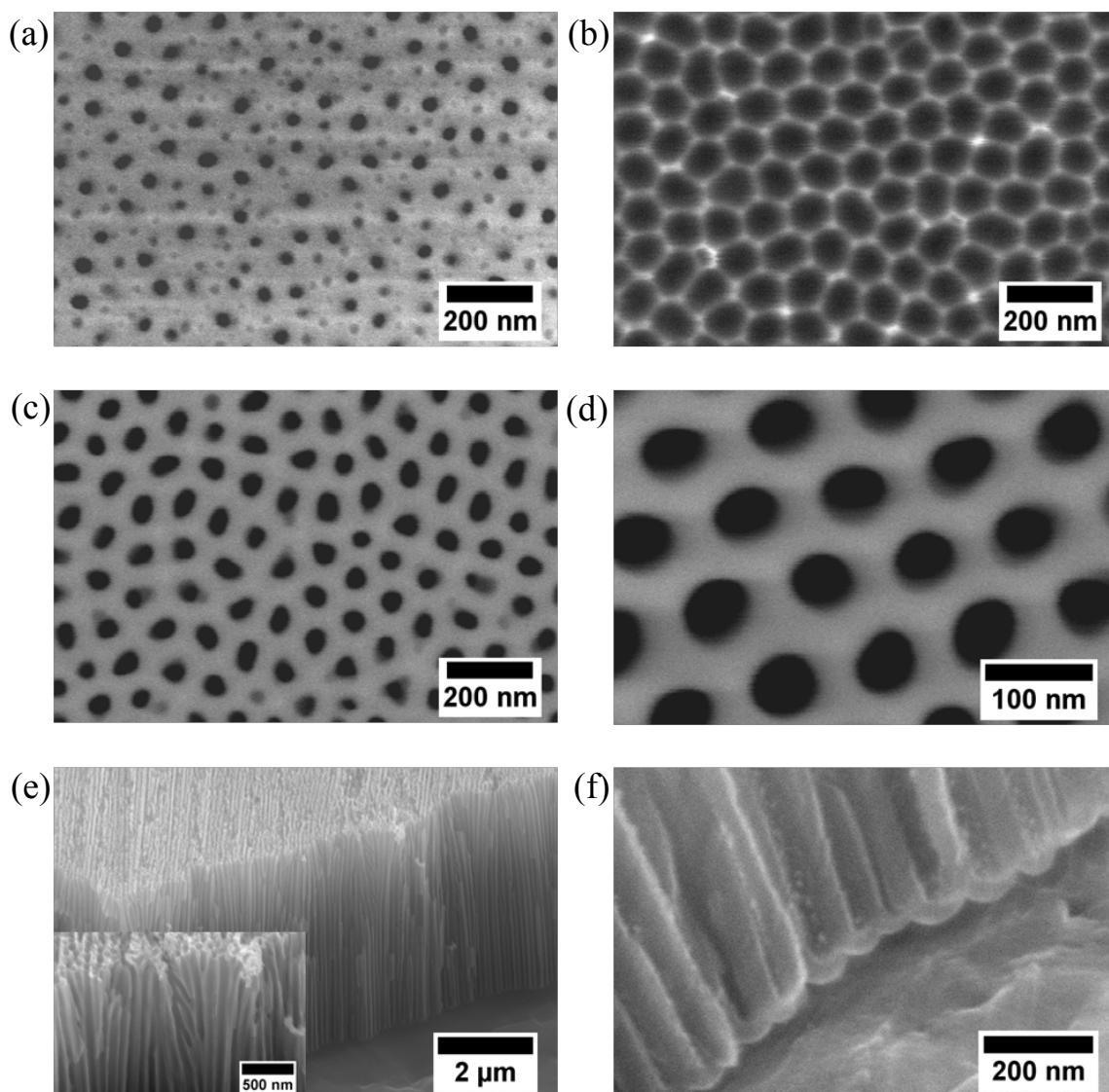


**Fig. 5.2.** SEM images showcasing the two-step anodization procedure (see text for experimental details): (a) a top-down view of the as-fabricated irregular pore growth after the first anodization; (b) after the first anodized oxide layer is removed, periodic depressions can be seen on the newly exposed aluminum metal surface; (c) and (d) top-down views of the second anodization layer after pore opening in phosphoric acid; (e) a cross-sectional view of the pores; and (f) the barrier layers at the bottoms of the pores of the second anodization oxide layer.

and pore etching steps, where the indentation effect from the first anodization can be clearly seen. A cross-sectional view of a thick template is seen in Fig. 5.2e, with an inset displaying some branched pores alongside perfectly aligned ones. Fig. 5.2f shows the unmistakable barrier layer at the bottom of each pore.

No inherent limitation to the thickness of the AAO template was encountered; nonetheless, relatively conservative thicknesses were investigated here, as maintaining contact between as-produced nanowires and the substrate is imagined to be more difficult the larger the aspect ratios are (the aspect ratio is the ratio of the length to the diameter). The other factor affecting the aspect ratio is the pore diameter—a corresponding comparison of different pore diameter etching times is shown in Figure 5.3. This etching

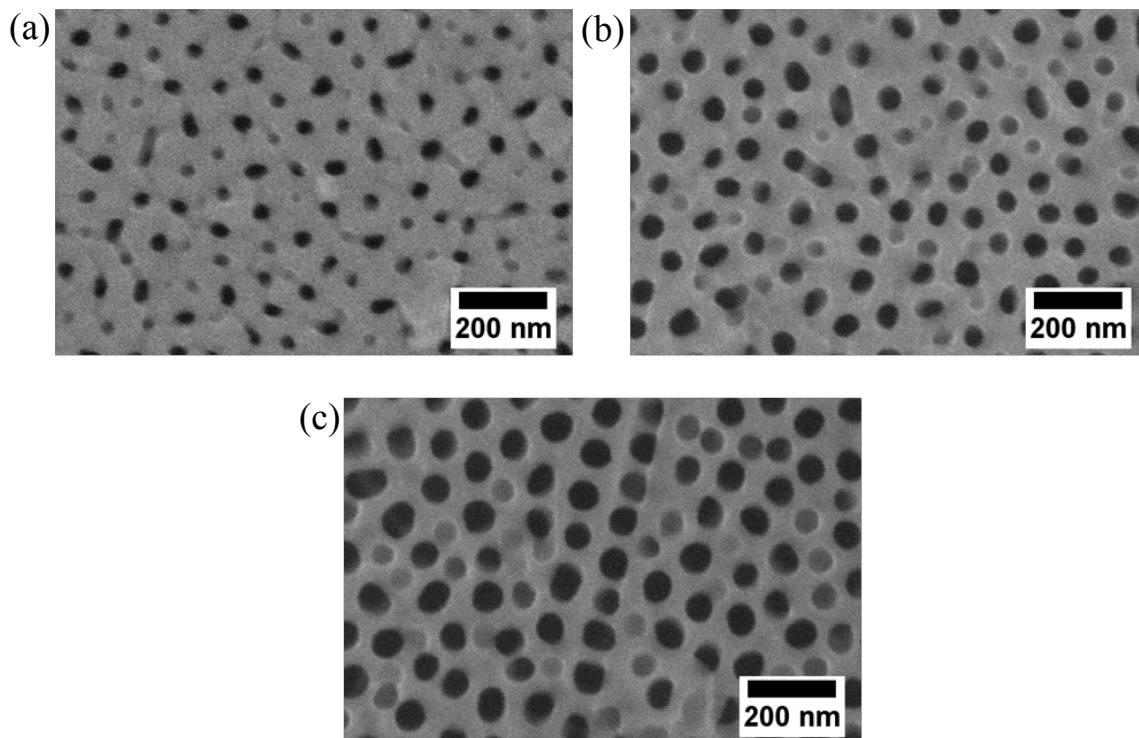


**Fig. 5.3.** SEM images of a twice-anodized template layer with different etching times in 10 wt % phosphoric acid: (a) 10 minutes, (b) 20 minutes, and (c) 30 minutes.

action also removes the barrier layer lying at the bottom of the pores. Without its removal, the barrier layer would cover all of the base electrogeneration sites, preventing the CELD of ceria nanowires.

Similar results to bulk aluminum are shown for sputtered aluminum thin film samples in Figure 5.4. The slight roughness pictured in Fig. 5.4b is a result of the sputtering process, which sometimes deposits large chunks of aluminum, instead of the expected flat and featureless film. The pores can be seen to run right down to the underlying gold surface. Either gold or platinum must be used as the buried electrode, because other non-precious metals would be too easily oxidized, as aluminum is.

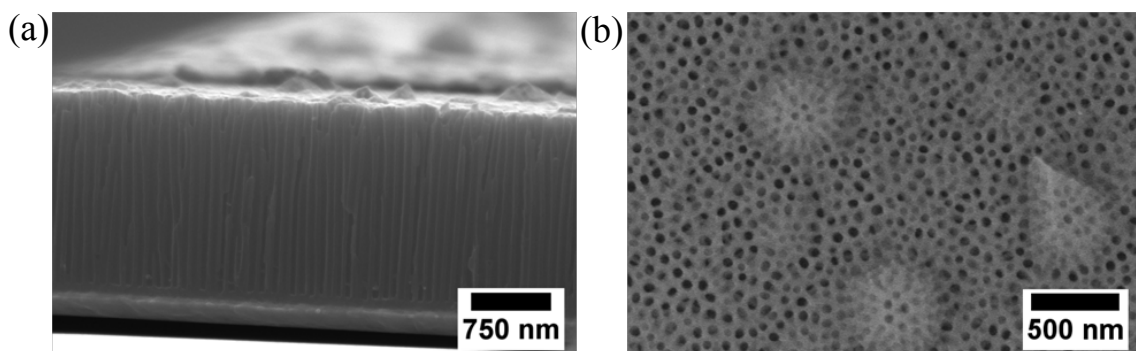


**Fig. 5.4.** SEM images of an AAO template grown from a sputtered aluminum thin film on a gold/titanium buried electrode on a silicon substrate. The pore opening was performed for 20 minutes.

Two prohibitive difficulties were encountered for the aluminum thin film samples. The first is inhomogeneous current densities arising from poor heat dissipation by the supporting substrate, as discussed in Section 5.1.1. Because of this issue, successful thin film AAO template fabrication was less than 1 in 10. Figure 5.5 compares three different quartz substrate thin film samples, with a corresponding current transient taken during each anodization. The first sample contains no buried gold electrode under

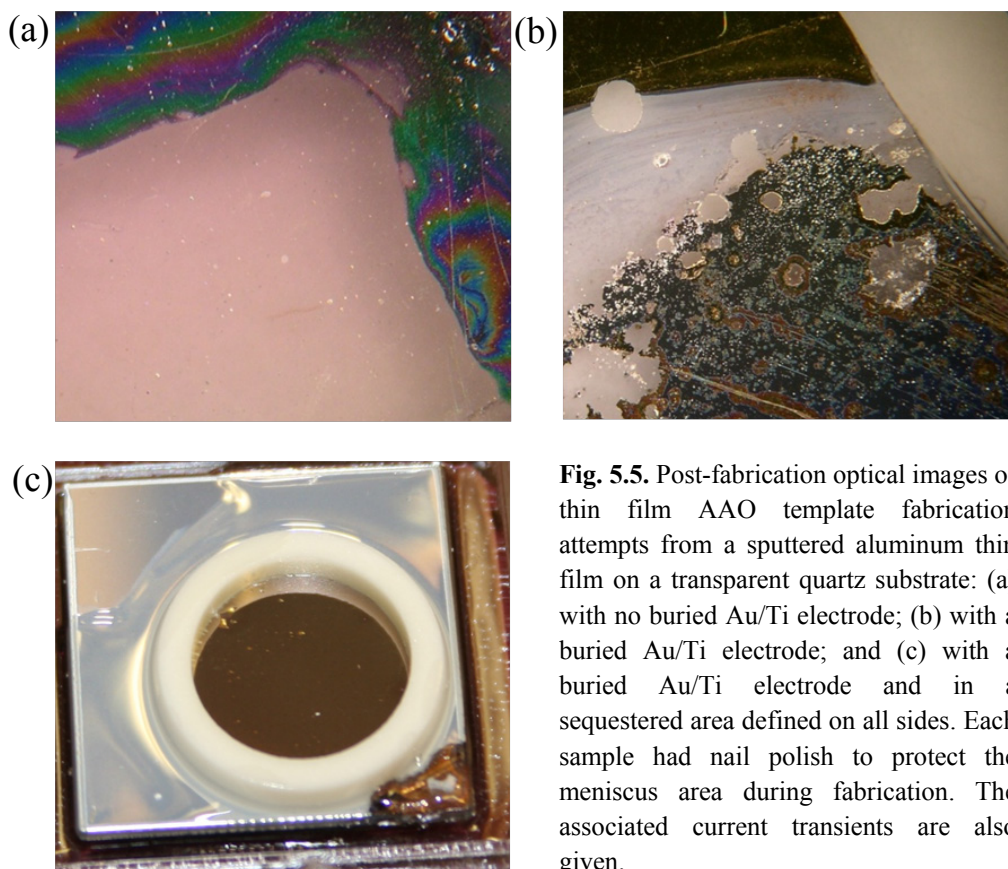
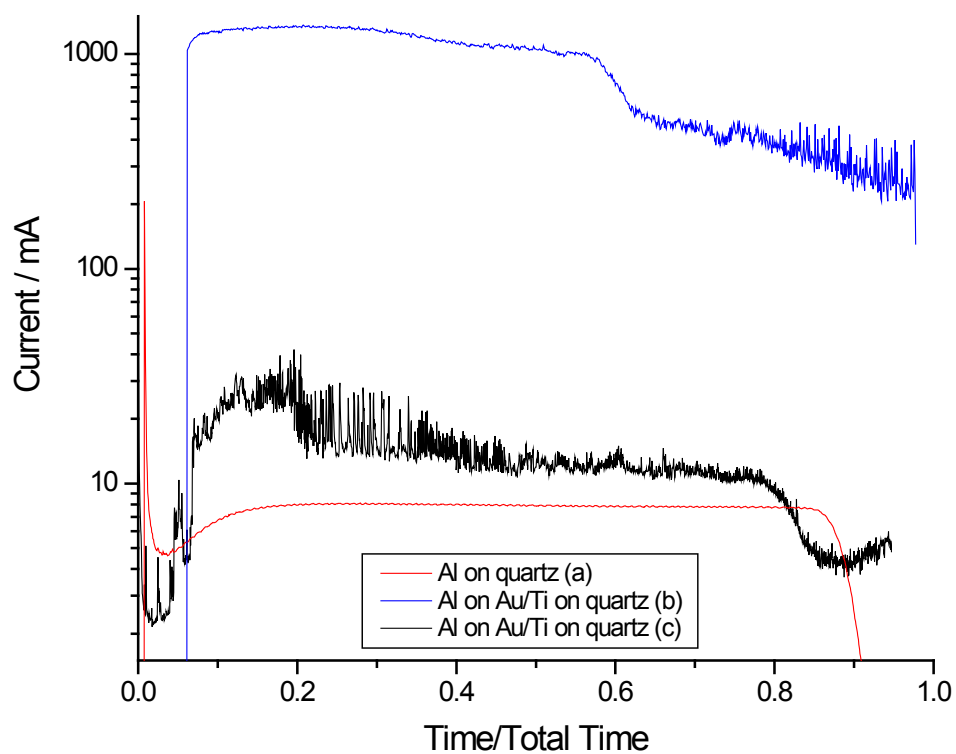


**Fig. 5.5.** Post-fabrication optical images of thin film AAO template fabrication attempts from a sputtered aluminum thin film on a transparent quartz substrate: (a) with no buried Au/Ti electrode; (b) with a buried Au/Ti electrode; and (c) with a buried Au/Ti electrode and in a sequestered area defined on all sides. Each sample had nail polish to protect the meniscus area during fabrication. The associated current transients are also given.

the sputtered aluminum thin film, but still experienced complete oxidation, resulting in the transparent window pictured in the top down view of Fig. 5.5a. Partial oxidation of the aluminum around the border of the sectioned area can be seen manifesting by colorful thin film interference patterns. This sample's current transient is a standard anodization response: after the initial charging current spike, a slight dip in the current is followed by a flat steady-state value, until there is no more aluminum to oxidize and the current drops to zero. In contrast, the sample pictured in Fig. 5.5b contains a buried gold electrode, where violent gaseous evolution can be seen to have ripped apart portions of the film, leaving the gold under-electrode completely exposed in some regions. The corresponding current transient shows orders of magnitude difference in the absolute current values, as well as undesirable spiking. The added current is coming from electrolytic oxidation reactions taking place at exposed gold surfaces. Finally, a successful buried gold electrode sample is shown in Fig. 5.5c, where the sectioned area for anodization is a bronze color, in stark contrast to the protected, un-oxidized aluminum surrounding it. This sample's current transient bears more resemblance to the first, although some variability still exists, largely due to the lower right-hand corner of the sample not being protected enough. Similar to the sample with no buried gold electrode, the current drops significantly when there is no more aluminum to oxidize.

A similar difficulty was reported in ref [103], utilizing a buried gold electrode thin film configuration. To alleviate the problem, the anodization was carried out at  $\sim 5^\circ\text{C}$ , and a pulsed voltage profile was employed, to allow time for any heat intensity to dissipate. An analogous approach could be taken here.

The second issue is related to the barrier layer, shown for a bulk aluminum foil sample in Fig. 5.6a and for a thin film sample in Fig. 5.6b. Note the thickness difference in the barrier layers—the thin film sample has a much thicker barrier layer. Even after etching, this barrier layer does not appear to be completely removed, which precludes subsequent ceria CELD into the pores. This could be related to the non-zero final current value recorded for the sample pictured in Fig. 5.5c. The stray current could be oxidizing some gold metal, producing what appears to be a thicker barrier layer. Nevertheless, this should not be an insolvent issue, as there are many reports of successful nanowire depositions in this configuration, as discussed below.

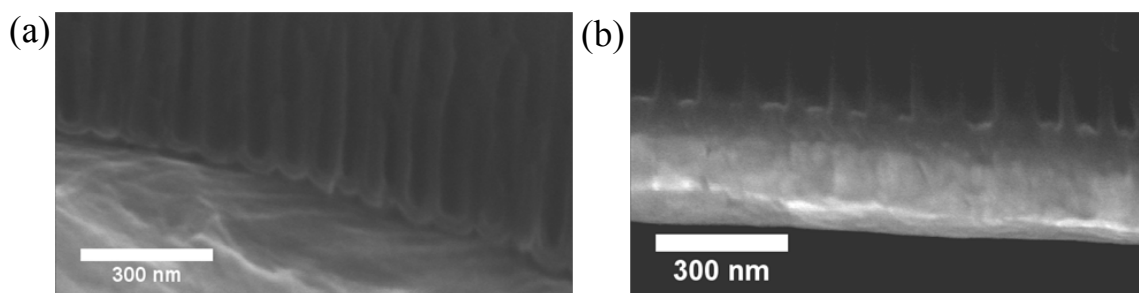


**Fig. 5.6.** SEM images comparing barrier layer thicknesses: (a) ~30 nm from a bulk aluminum foil sample; and (b) ~70 nm from a thin film sputtered aluminum sample.

#### 5.1.4 *Ceria Nanowire Growth*

Aside from ceria [47, 49, 58-59, 81], a wide range of metals and semiconductors have been grown in the pores of AAO templates, from nickel to titania [104-110]. Despite numerous reports of successful electrochemical nanowire deposition into thin film AAO on a conducting substrate, the problems mentioned in the previous section have not been solved here, as of yet. To circumvent those two issues entirely and demonstrate a proof-of-concept, nickel metal was sputter-coated onto one side of a free-standing AAO template (Whatman Anodisc 47) with ~200 nm pore diameters. This template was then attached to a glass slide via conducting copper tape and sealed with nail polish, leaving ~1 cm<sup>2</sup> of an exposed surface. After allowing the electrolyte solution to naturally seep into the AAO pores for ~30 minutes, CELD was performed galvanostatically at 1.6 mA cm<sup>-2</sup>, for 30 minutes. After the deposition was complete, the alumina was etched in stages in 3 M NaOH for 0.5 – 5 minutes. The resulting SEM images are shown in Figure 5.7.

The proportion of pores that are filled with CELD ceria is extremely high—it was difficult to find a pore that is not filled. After etching, the nanowires appear to fall onto each other, clumping up in sections. Although this result is not ideal for pure surface area enhancement, some cross-linking of nanowires could have a beneficial effect for assisting the lateral migration of active species, rather than requiring electrons and oxygen ions to always traverse the length of the nanowire during fuel cell operation.

The entire assembly was also subjected to thermal treatment, to observe the morphological stability of the nanowires. Figure 5.8 shows identically magnified images of the nanowires after annealing at 300 and 500 °C for 5 hours at 5 °C min<sup>-1</sup>, revealing

that there is little to no evolution in the nanowires' structure at these temperatures. This is consistent with the high temperature results from Chapter 3, where much smaller features were shown to be stable up to  $\sim 800$  °C.

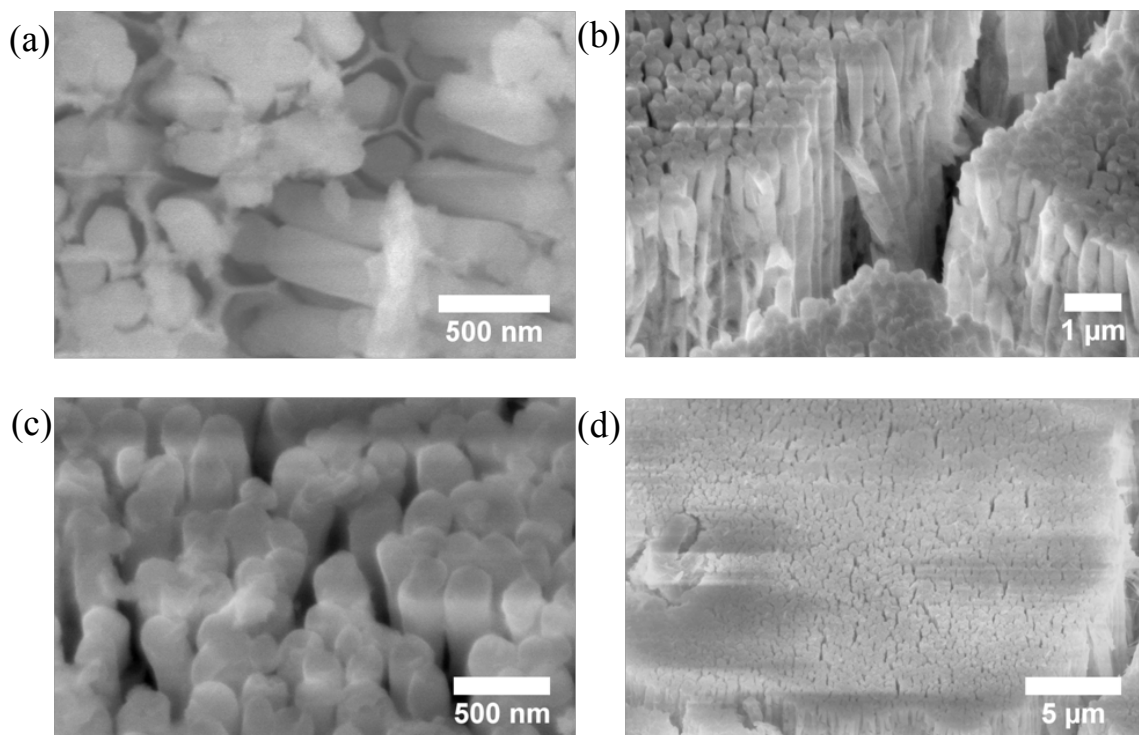


**Fig. 5.7.** SEM images of CELD nanowires grown in the pores of a free-standing AAO template after etching in 3 M NaOH: (a) for 30 seconds and showing a top-down view; and (b-d) for 5 minutes, showing angled views of various magnifications.

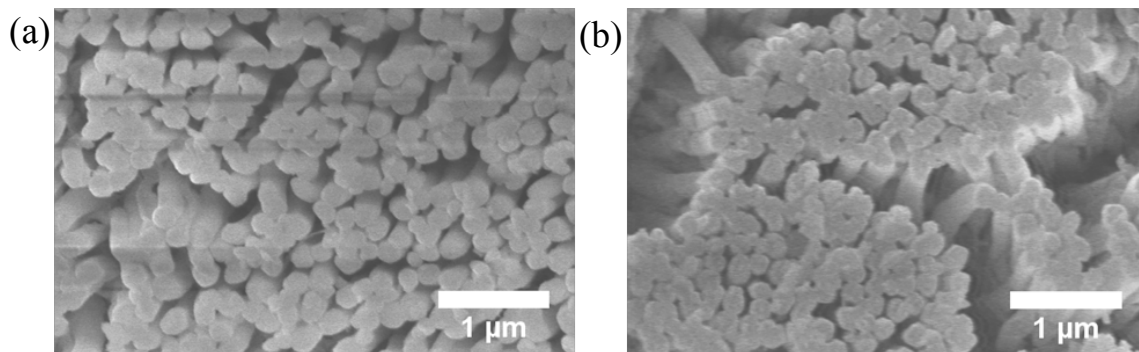


**Fig. 5.8.** SEM images of CELD nanowires grown in the pores of a free-standing AAO template after annealing for 5 hours in air at (a) 300 °C and (b) 500 °C.

## 5.2 Inverse Opals

### 5.2.1 *Inverse Opal Definition and Background*

Nanowires are an effective way to increase surface area, but they are limited to reasonable aspect ratios due to both the ability of the nanowires to stand relatively upright, and the challenges of depositing several microns of aluminum metal that would be required to make AAO templates thick enough to guide such growth. Indeed, the potential electrochemically active space is generally assumed to be on the order of 10 microns perpendicularly away from the electrolyte layer in SOFCs. A large portion of this volume would essentially remain unused in a nanowire-only design.

Another possibility is the inverse opal structure, schematically shown in Fig. 1.5cd. An opal structure is comprised of a three-dimensional close-packing of monodisperse spheres, akin to a micro-sized face-centered cubic structure. An inverse opal is the volume inverse of this close-packed monolith. Typically, one begins with an opal structure, deposits the desired material in the interstices of the opal, and then removes the original opal, leaving a well-defined inverse opal. Spheres with different diameters can be utilized to create a range of three-dimensional surface area enhancement, analogous to the two-dimensional variability shown for anti-dot metal films in Chapter 2 (c.f. Fig. 2.2). Polystyrene (PS) spheres are used here, although both poly(methyl methacrylate) and silica spheres are commonly used.

Any number of fluid based methods can be utilized to fill the interstices of the sacrificial opal structure, from gaseous CVD processes to liquid precursor infiltration techniques [111]. Perhaps the most popular infiltration route for metallic inverse opals is electrodeposition [112-117]; for ceria, most reports utilize techniques based upon

common ceria sol-gel precursors such as alkoxides and chlorides [118-121]. To the author's knowledge, no reports exist at the time of this writing for ceria inverse opal preparation by CELD.

### 5.2.2 *Inverse Opal Fabrication Details*

In keeping with CELD and SOFC configurational requirements, the familiar porous metal networks on YSZ are used as substrates. To establish a PS opal on the substrate,  $\sim 45 \mu\text{L}$  of a 10 wt % PS suspension is drop-cast onto a metal network/YSZ substrate and allowed to naturally dry for  $\sim 1$  hour. Although this produces a randomly arranged opal, ordering is not crucial for surface area enhancement, just as with the CELD ceria nanowires of Section 5.1. After the water from the PS suspension is completely evaporated away, the resulting PS opal adheres nicely to the substrate. The entire assembly is then immersed into an undoped liquid electrolyte in the same CELD system used for the depositions of Chapter 3. Before the depositing potential is applied,  $\sim 30$  minutes is given to allow the electrolyte solution to adequately infiltrate all interstices of the opal, and afterwards ceria is electrochemically deposited as before for 10-30 minutes. The PS spheres are initially removed by extensive water washing post-deposition, and can be completely removed by immersion in a toluene solution for 30 minutes, or thermal treatment at  $\sim 400$  °C.

### 5.2.3 *Inverse Opal Results*

Figure 5.9 shows ceria inverse opal structures grown by CELD on platinum strip/YSZ (Fig. 5.9a-c) and nickel anti-dot/YSZ substrates (Fig. 5.9d) with HSA deposition conditions, i.e.,  $0.8 \text{ mA cm}^{-2}$  with the undoped electrolyte solution. An advantage of

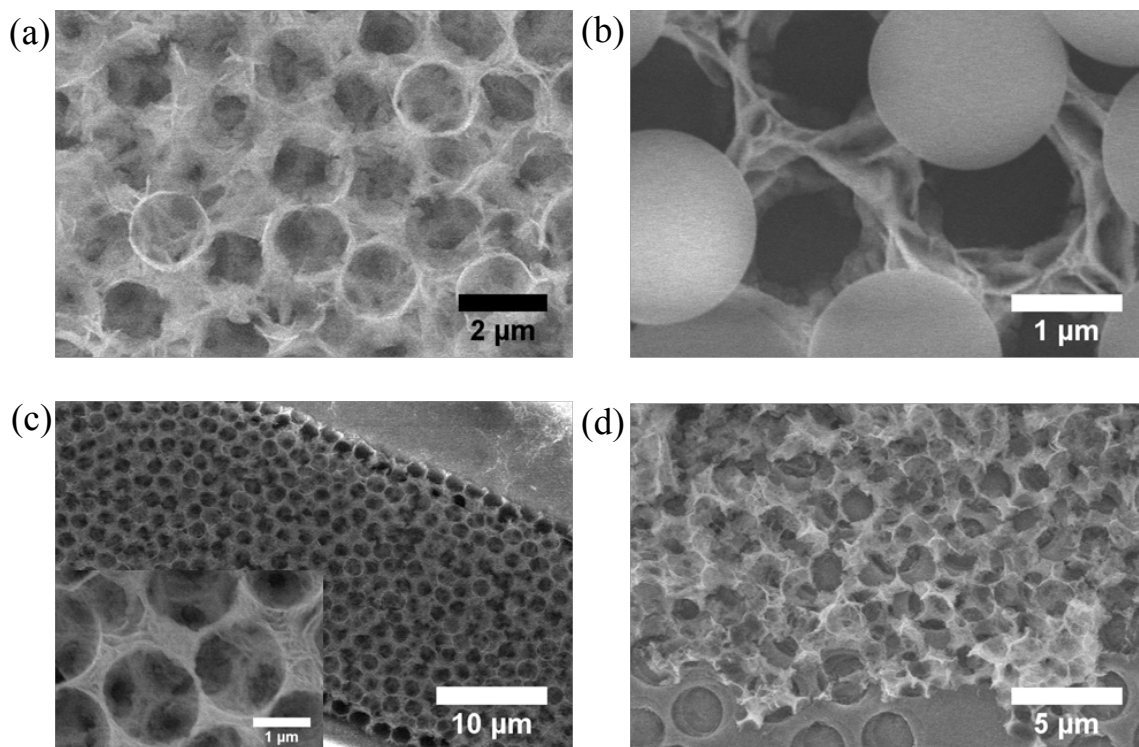


**Fig. 5.9.** SEM images of CELD inverse opal structures grown at  $0.8 \text{ mA cm}^{-2}$  with the undoped electrolyte on (a-c) a 20-20  $\mu\text{m}$  YSZ/Pt strip sample for 10 minutes and (d) on a YSZ/Ni anti-dot substrate for 30 minutes. Immersion in a toluene solution for 30 minutes removed all PS spheres.

depositing at the standard HSA potentials is nano-sized surface area enhancement in addition to the micron-sized templated pores. The familiar nano-sheet/needle features can be seen embedded in the inverse opal walls in Fig. 5.9b and the inset of 5.9c. A 10 minute deposition produced 1-2 inverse opal layers for the platinum strip sample, and a 30 minute deposition produced 3-4 layers for the nickel anti-dot sample.

Two adhesion-related difficulties require further investigation. One, the PS opal consistently sticks to the substrate if unperturbed; however, when immersing the substrate/opal assembly into the CELD electrolyte solution, some of the opal becomes detached. The result is non-templated deposition, as in Fig. 5.10a. Two, the adhesion of

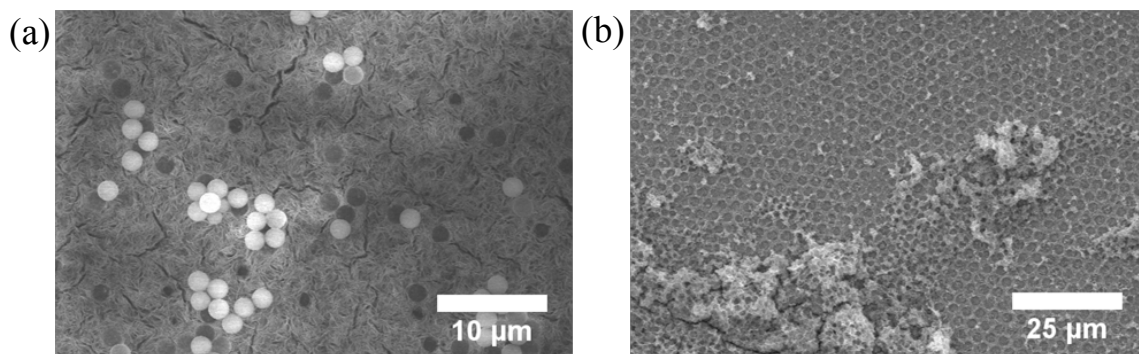


**Fig. 5.10.** SEM images of difficulties encountered with the CELD inverse opal structures from Fig. 5.9: (a) the PS opal structure can be accidentally removed when dipped into the liquid CELD electrolyte, and no inverse opal results; and (b) few contact points between the CELD inverse opal and the substrate can lead to spallation.

the ceria inverse opal to the substrate can be weak due to limited points of contact resulting from the template action of the PS spheres. Fig. 5.10b shows such a situation, where some of the inverse opal structure on a nickel anti-dot substrate spalled during the relatively gentle post-deposition water washing step. As is the case with the nanowire challenges posed in Section 5.1, these problems are solvable.

### 5.3 Oxidation Protection Coatings

Because of its ability to conformally coat irregularly shaped metallic substrates, CELD of ceria has been previously investigated as a corrosion inhibitor [46, 53-56]. Specifically relevant to SOFC fabrication techniques, ceria coatings on metal substrates that protect against unwanted oxidation are investigated below.

#### 5.3.1 *Experimental Details*

A nickel anti-dot film with initial and final PS diameters of 2  $\mu\text{m}$  and 1  $\mu\text{m}$ , respectively, was deposited onto one side of a YSZ single crystal, as before (c.f. Chapter 2). This

substrate was vertically dipped halfway into a Sm-doped ceria CELD electrolyte solution, and a potential was applied at -0.525 V vs. SCE for 1 hour. A thin film of ceria coated half of the cell, whereas the other half still had the nickel anti-dot film exposed. This sample was placed into a PLD system, where a 1 – 2  $\mu\text{m}$  ceria film was deposited onto both its coated and uncoated areas. The PLD operated with a background oxygen partial pressure of 5 mtorr and at a substrate temperature of  $\sim 650$  °C. SEM images are used to evaluate the oxidative state for the coated and uncoated regions.

### 5.3.2 Results

The CELD coated nickel anti-dot film before the PLD deposition is shown in Fig. 5.11a. Smooth and relatively crack-free, the deposition is nearly conformal, even over the occasional trapped PS sphere. The PLD deposition over the coated region appears similarly smooth, as in Fig. 5.11b, although there are more faceted features characteristic of crystalline ceria. Of particular note is the flatness of the area lying directly above the nickel anti-dot film. The cross section of the coated region is also shown in Fig. 5.11c. The border area between the CELD coated and uncoated regions after the PLD deposition is shown in Fig. 5.11c. There is a clear difference between the two, where the coated region is flat, like the original morphology, and the uncoated region has volume-expanded, noticeable by the smaller pore diameter. This volume expansion is from the nickel metal oxidizing to NiO during PLD operation.

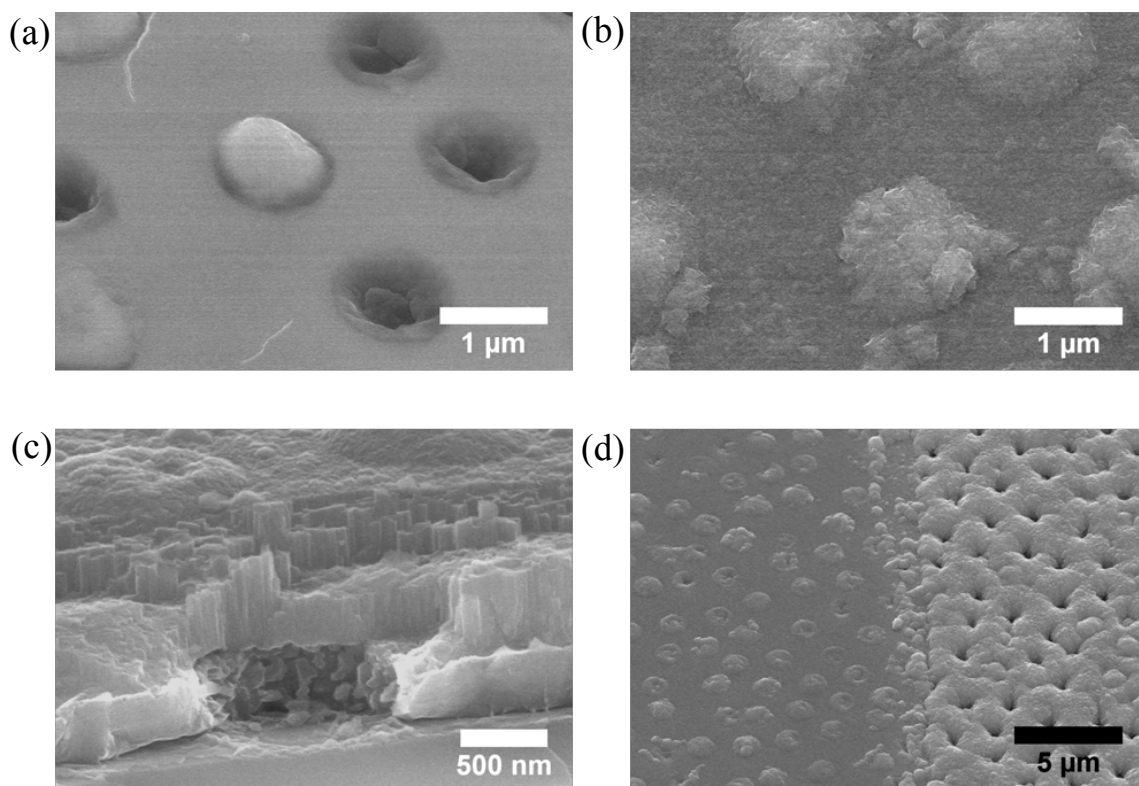


**Fig. 5.11.** SEM images of a thin film CELD ceria coating on a YSZ/Ni anti-dot substrate: (a) as-deposited; (b) the subsequent PLD top coating on the region that was previously coated by CELD ceria; (c) a cross-sectional view of the YSZ substrate/Ni anti-dot layer/CELD ceria layer/ PLD top coating layer; and (d) the PLD top coating showing the border between the previously coated region (left) and the uncoated region (right).

From these results, it can be concluded that the CELD ceria layer effectively prevents significant oxidation of the nickel metal. CELD could be used to treat metallic substrates before they are subjected to high temperature oxidizing conditions commonly used in SOFC fabrication techniques.

#### 5.4 CELD Ceria Grown Directly on MIEC SOFC Cathode Substrates

In contrast to their anode counterparts, SOFC cathodes are commonly comprised of porous MIEC monoliths, typically with perovskite-based crystal structures. Two such MIEC materials are  $\text{Ba}_{0.5}\text{Sr}_{0.5}\text{Co}_{0.8}\text{Fe}_{0.2}\text{O}_{3-\delta}$  (BSCF) and  $\text{SrCo}_{1-x}\text{Nb}_x\text{O}_{3-\delta}$  (SCN) [19, 122].

The mixed conduction is dominated by p-type electronic conduction in both material systems, and both exhibit non-trivial conductivity at room temperature and ambient pressure. This last characteristic, in particular, opens wide the possibility of utilizing BSCF and SCN as conducting substrates in a variety of configurations for CELD ceria. Most tantalizing is the possibility to make an entire cathode-electrolyte-anode SOFC assembly, beginning with the cathode. One can imagine depositing a thin film of ceria by CELD onto a self-supported, porous BSCF substrate, where densification of the ceria thin film could allow it to perform as the electrolyte in a SOFC. The top surface of this newly formed ceria electrolyte could then act as the substrate for subsequent anode fabrication, like the model electrodes from Chapters 2 and 3. This fuel cell fabrication scheme has the advantages of combining processing techniques that are naturally integrated with one another, as well as not requiring the characteristic high processing temperatures associated with more classical approaches.

Accordingly, the CELD of ceria onto BSCF substrates is investigated, with analogous (but not shown) results for SCN substrates.

#### 5.4.1 *Substrate Preparation Details*

Dense and porous BSCF substrates were prepared for CELD studies. A standard powder process is employed for both, with a pore former used for the latter. BSCF powders are prepared by a nitrate-based sol-gel method, which utilizes EDTA and citric acid as complexing agents. The mixing bath is kept at temperatures around 80 °C, which induces gelation. The resulting sticky gel is heat treated at ~250 °C to remove residual organics. The blackened powders are then fully calcined at 950 °C to produce the desired pure

perovskite crystal phase. For dense substrates, this calcined powder is crushed by hand with a mortar and pestle, pressed into a pellet isostatically at 350 MPa, and then ultimately sintered at  $\sim 1050$  °C. For porous substrates, the calcined powder is mixed in a 60:40 volumetric ratio with  $\text{Cs}_2\text{SO}_4$ , which acts as a pore former and is later removed by water immersion, and the two powders are crushed together in the mortar and pestle to ensure adequate mixing. This powder mixture is also isostatically pressed into a pellet, but sintered at  $\sim 800$  °C, owing to the low melting temperature of the cesium sulfate salt ( $\sim 1000$  °C). The resulting pore sizes are on the order of a few microns.

The dense substrates are polished, using up to an 800 grit abrasive paper, and can be simply immersed into the CELD electrolyte solution as before. However, to encourage bridging of the pores by a thin ceria CELD layer and to discourage deposition inside the pores, the porous BSCF substrates are mounted to a glass slide by conducting copper tape, and infiltrated by viscous nail polish. The spontaneous capillary forces are sufficient for full infiltration of the pores. After the polish has hardened, the top surface is gradually planarized by 800 grit abrasive paper, and ultimately smoothed by  $2\ \mu\text{m}$  abrasive cloth (Scientific Instrument Services micro mesh cloth, 12000 grit). The result is a nanometer-scale smooth surface, with seamless interfaces between the nail polish-filled pores and the surrounding BSCF matrix, as in Fig. 5.12. Electrical contact with the external power supply is made via the underlying copper tape, a portion of which extends out from underneath the pellet. All conducting surfaces except the desired smoothed BSCF one are insulated from deposition by nail polish.

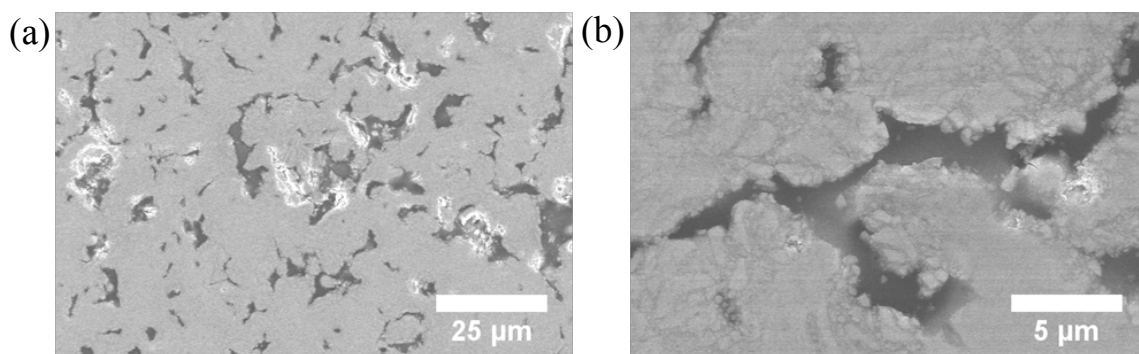


**Fig. 5.12.** SEM images of a porous BSCF substrate that has been infiltrated by viscous nail polish, which has since hardened. These images are taken after planarization by abrasive cloth. The isolated, dark regions are the hardened nail polish, surrounded by the lighter regions of sintered BSCF.

#### 5.4.2 CELD Results and Discussion

Figure 5.13 shows successful undoped ceria HSA deposition at  $1.5 \text{ mA cm}^{-2}$  for 5 minutes onto a dense BSCF substrate. The CELD undoped electrolyte solution used for this sample is slightly altered from the familiar composition—0.1M cerium nitrate with 0.1 M  $\text{H}_2\text{O}_2$ . The voltage response was abnormal in that it reached values of  $-2.2 \text{ V vs. SCE}$ , which is much more negative than on regular metallic substrates. Highly uniform and slightly cracked, the familiar nano-needle/sheet growth can be seen. Fig. 5.13c and d reveal a cross-sectional piece of the deposit that was upended during subsequent handling of the sample. The 5 minute deposition produced a multiple-microns-thick coating on the BSCF, likely due to the high current density. The porous nature of the HSA deposit is clearly visualized in these images.

Deposition onto the porous BSCF substrate assembly is shown in Figure 5.14. Fig. 5.14a shows the sample immediately following deposition, with the nail polish still inside the BSCF pores. Fig. 5.14b-d show the sample after the nail polish has been

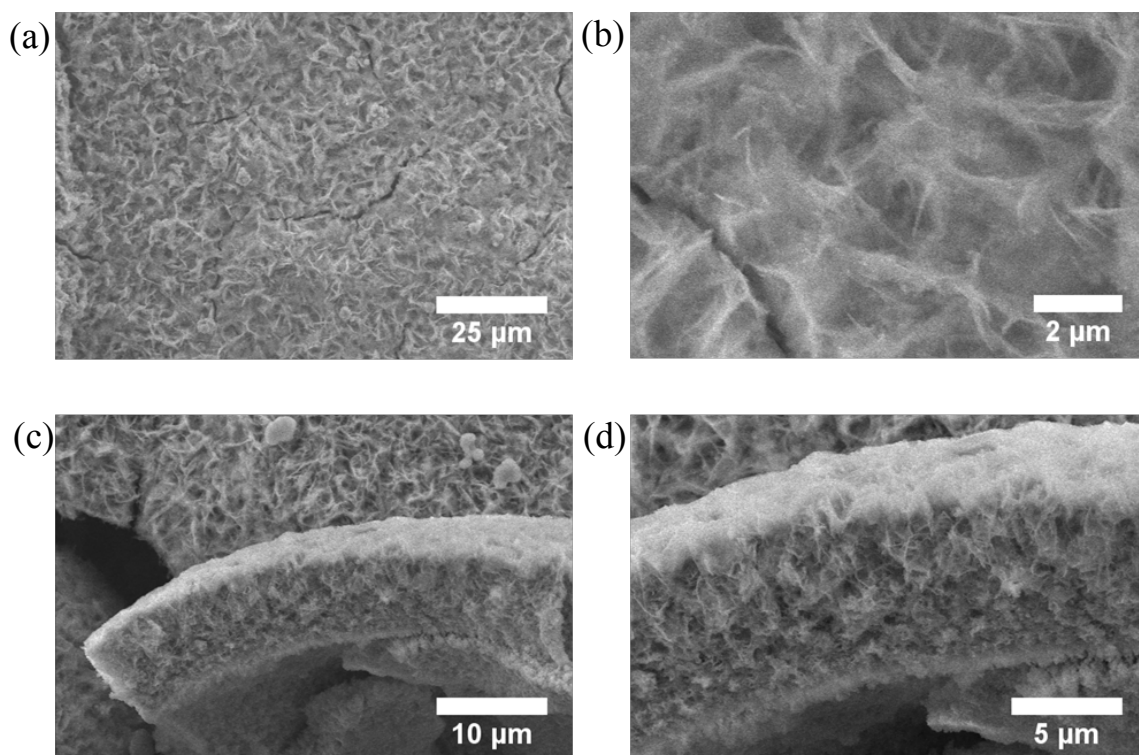


**Fig. 5.13.** As-deposited SEM images of undoped CELD ceria grown on a dense BSCF substrate at  $1.5 \text{ mA cm}^{-2}$  for 5 minutes, with a slightly more concentrated (0.1 M cerium nitrate) electrolyte with 0.1 M  $\text{H}_2\text{O}_2$ : (a) and (b) are top-down views; and (c) and (d) show an upended cross-section.

removed by acetone washing. Some of the smaller pores are successfully bridged by the thin ceria deposit, but as many of the BSCF pores are greater than  $1 \mu\text{m}$ , they remain open and, therefore, gas permeable. This deposition is using the standard Sm-doped electrolyte solution with no hydrogen peroxide additive. Curiously, the applied voltage is only  $-0.5 \text{ V vs. SCE}$ , which should produce a thin, planar film, a la the results obtained in Chapter 3. Furthermore, at a deposition time of only 1 minute without hydrogen peroxide, it is surprising that there is a discernable coating at all, much less one with the HSA microstructure.

To investigate this peculiarity, CV scans for nickel and BSCF substrates in the standard Sm-doped ceria electrolyte solution at  $50 \text{ mV s}^{-1}$  are compared in Figure 5.15.

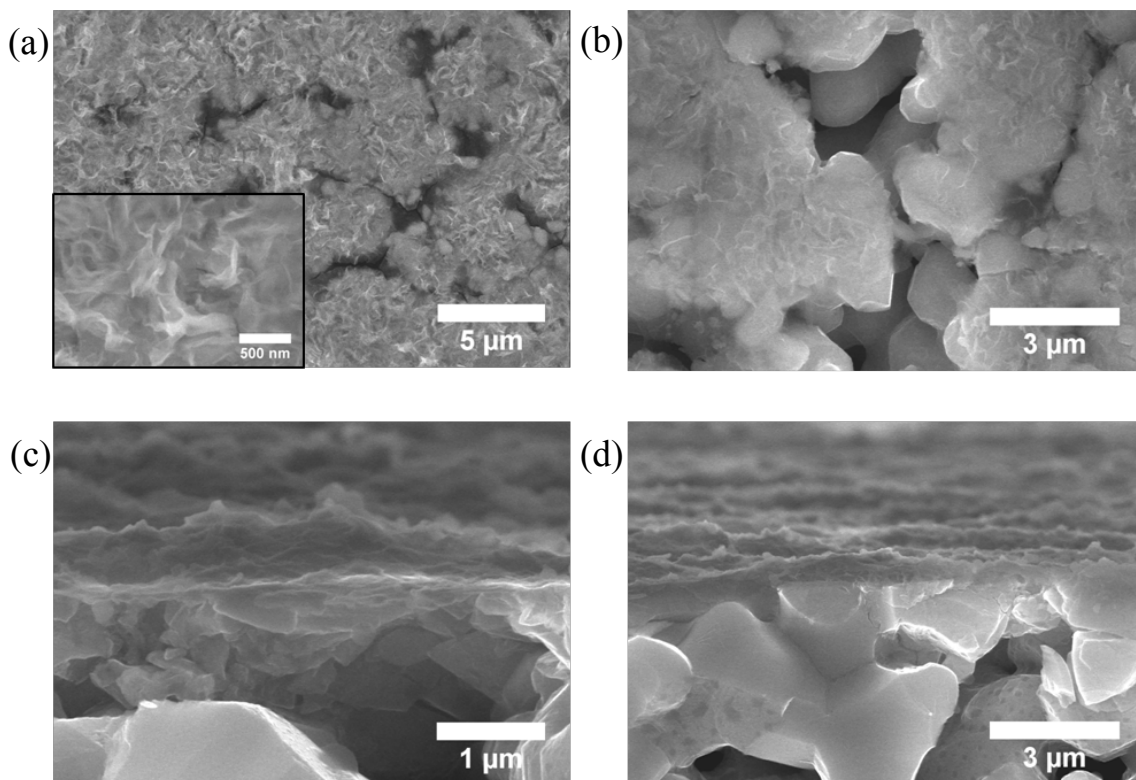


**Fig. 5.14.** SEM images of doped CELD ceria grown on a porous BSCF substrate at  $-0.5$  V vs. SCE for 1 minute: (a) the as-deposited morphology with the nail polish still intact, and a closer view in the inset; (b) same as in (a), but with the nail polish removed; and (c) and (d) cross-sectional images showing some bridging of larger pores.

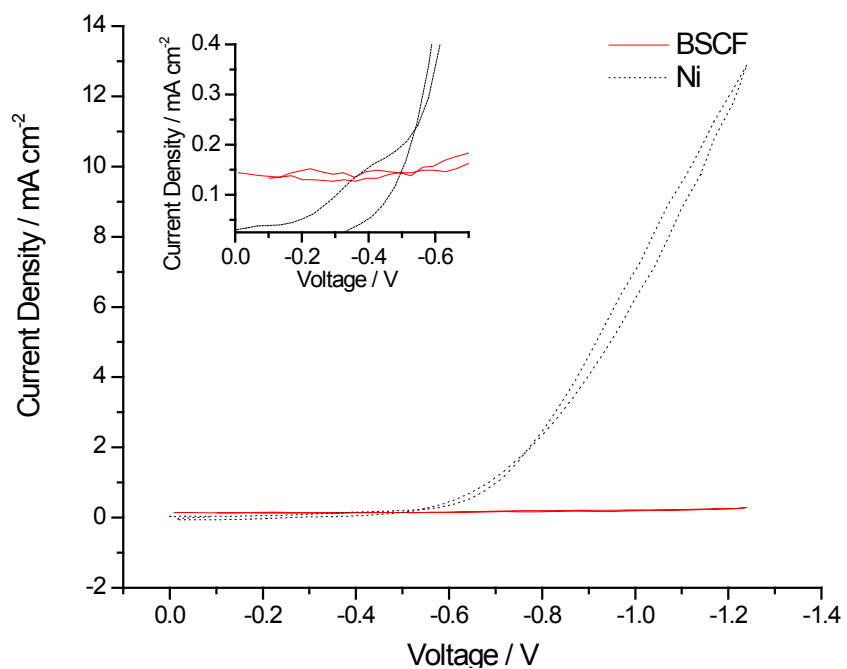


**Fig. 5.15.** CV scans for nickel and BSCF substrates in the standard doped electrolyte, with a scanning rate of  $50$  mV  $s^{-1}$ . Inset is a magnified view for the less negative potential range.

As previously discussed, the large current leg for the nickel substrate corresponds to the reduction of dissolved molecular oxygen and hydrogen gas evolution. As is clearly seen, BSCF does not exhibit such currents at the same voltages. However, BSCF does have a non-zero current at less negative voltages, significantly higher than the nickel substrate, shown in the inset of Fig. 5.15. With such a non-zero current, deposition should be able to occur at these lower voltages.

Indeed, Fig. 5.16a and c show top-down SEM images of films deposited in the Sm-doped ceria electrolyte solution for 30 seconds on porous BSCF at  $-0.2$  V vs. SCE and no applied potential, respectively. When these porous BSCF substrates are removed from the CELD electrolyte solution, a distinctive deep blue/purple film appears, confirming deposition. Close inspection of the images in Figure 5.16 reveal slight cracks or tears in the thin films, even on top of nail polish-filled BSCF pores. After removing the nail polish by acetone washing and annealing at  $700$  °C for 10 hours under ambient air, some of the bridged areas are maintained, while others are punctured, as in Fig. 5.16b. There appears to be a simple correlation between the BSCF pore size and the ability of CELD coatings to bridge the pore. In an effort to boost the bridging capability of these thin films, eleven 30 second-long, subsequent depositions are performed at  $-0.65$  V vs. SCE in the Sm-doped ceria electrolyte solution onto porous BSCF. The as-deposited results are shown in Fig. 5.16d, where some evidence of multiple depositions can be seen by layered tearing in certain areas. This effort does not sufficiently strengthen the deposited film, however, and the nail polish removal step introduced significant holes in the ceria film, as before.

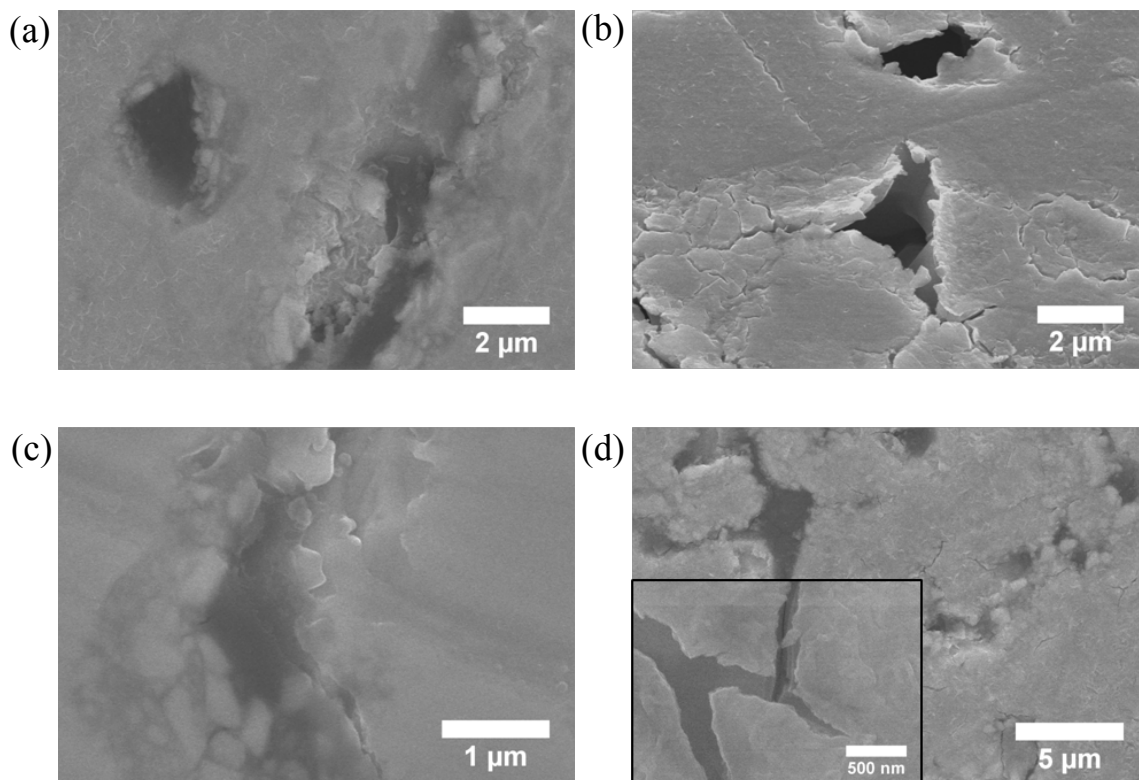
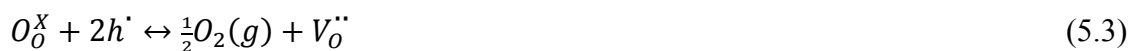


**Fig. 5.16.** SEM images of thin films of CELD ceria grown onto porous BSCF with the doped electrolyte: (a) and (b) at  $-0.2$  V vs. SCE for 30 seconds, (a) as-deposited with the nail polish still intact (dark regions) and (b) after nail polish removal and annealing at  $700$  °C for 10 hours in air; (c) at no applied potential for 30 seconds, shown as-deposited; and (d) after eleven 30 second-long consecutive depositions at  $-0.65$  V vs. SCE, shown as-deposited. The inset in (d) shows layered tearing, confirming multiple depositions.

A plausible explanation for this anomalous behavior is the oxygen electroreduction action of BSCF. The oxygen vacancy defect chemistry for an electron hole/oxygen ion MIEC can be depicted by the following equation:



As the temperature increases, BSCF thermodynamically loses lattice oxygen to the atmosphere; as the temperature decreases, the opposite occurs—BSCF incorporates oxygen from its surroundings into its lattice. However, around room temperature, the kinetics of such incorporation are slow, meaning BSCF that has experienced any high temperatures will be essentially meta-stable at low temperatures seen later in time. This

incorporation reaction could be catalyzed when the BSCF is immersed into a CELD electrolyte solution, and connected to an electronic circuit. Noticing that the non-zero current in the BSCF CV of Fig. 5.15 is cathodic, the direction of current flow is consistent with what would be induced by Eqn. 5.3. However, this explanation offers no insight into why or how ceria is deposited. If it is assumed that the available oxygen vacancies on the surface of BSCF are isolated, i.e. it is unlikely that two vacancies are directly adjacent to each other in the crystal lattice, then only one oxygen atom would be incorporated at a time. For molecular oxygen, this would leave another atom available to aqueous hydrogen ions roaming in the acidic environment to produce a hydroxide ion. Then, the precipitation of cerium species could continue, as before.

There is also scant evidence of BSCF substrates catalyzing anomalous ceria structural growth. Microstructures reminiscent of the so-called nanosheaves of ref [123] and feathery, self-assembling fractal scaffoldings are found near the meniscus area of the sample from Figure 5.13. Some representative structures are pictured in Figure 5.17.

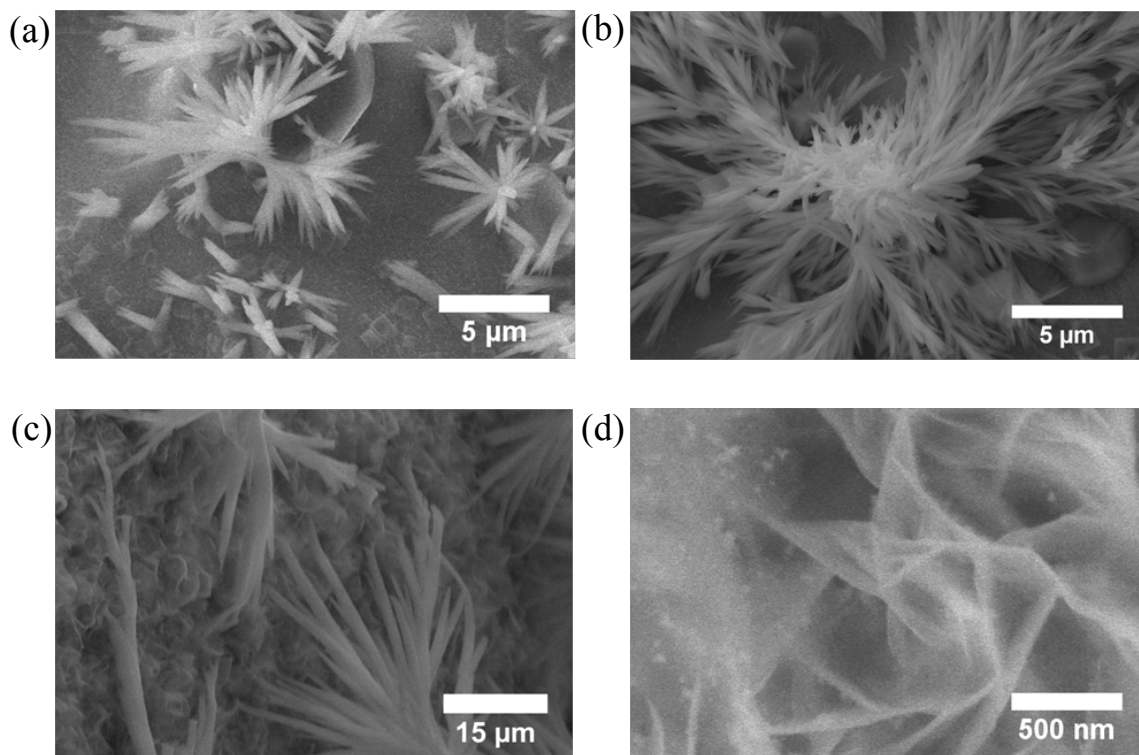


**Fig. 5.17.** SEM images of various structures deposited near the meniscus area for the sample from Fig. 5.13.

## Chapter 6

# Summary and Conclusions

Two fabrication techniques were investigated as they pertain to the assembly of advanced solid oxide fuel cells.

Polymer sphere lithography has been utilized to create two-dimensional metallic networks on fuel cell electrolyte materials. Although the fabrication process involves somewhat imprecise, random elements, the experimental variation from the expected geometries is extremely small. Under fuel cell operating conditions, the structures, and hence, the 3PB and 2PB area fraction values, exhibit remarkable high temperature stability. These well-defined and well-behaved electrode structures access a wide range of 3PB regimes, lending themselves to future mechanistic studies on electrolyte-electrode material systems, as well as providing a strong experimentally correlated basis for computational modeling. Beyond mechanistic studies, these anti-dot structures have served as platforms for fabrication of three-dimensional electrodes.

The cathodic electrochemical deposition of undoped and Sm-doped ceria has been developed in templated and template-free configurations to produce a variety of tunable anode microstructures. The strictly chemical nature of the deposition step allows these electronically insulating coatings to deposit onto non-conducting areas of substrates, insofar as they are close enough to an exposed metal surface. The end result is ubiquitous CeO<sub>2</sub> coatings on thin, porous metallic networks overlaid onto YSZ/porous metal substrates, with quality metal|CeO<sub>2</sub> and YSZ|CeO<sub>2</sub> interfaces, which are morphologically

stable at high temperatures and reducing atmospheres. Deposition was also definitively shown to occur on two MIEC, fuel cell cathode materials—BSCF and SCN.

To probe the activity of CELD Sm-doped ceria anodes, detailed, morphologically-driven ACIS analyses were conducted, revealing two co-dominant, resistive processes for metal network embedded configurations. The LF arc was determined to be surface-related; the HF arc was determined to be configurationally related, in particular to the resistance of electron migration through the SDC deposit on top of the metal regions, and the resulting restriction of the field lines to the nominal 3PB region. The LF arc was therefore taken to represent the true measure of surface activity for CELD ceria. The lowest extrapolated ASR values for this arc were shown to be in the range of 1.3 – 6.8  $\text{m}\Omega \text{ cm}^2$  at 650 °C in 97%  $\text{H}_2$  and 3%  $\text{H}_2\text{O}$ .

## Appendix A

# ImageJ Analysis Details

The following describes the analytical approach to identifying and characterizing the pores of the anti-dot networks using the ImageJ software described in Chapter 2. The process is briefly illustrated in Fig. A.1. First, an as-taken grayscale SEM image is imported into ImageJ (Fig. A.1a); then, the data bar region is cropped and the rest of the image is converted into a true black-and-white image (Fig. A.1b). The ImageJ user can define a grayscale threshold cutoff value, above which the associated pixels are converted to purely black, and below which the pixels are converted to purely white. Consequently, the ideal SEM image to be analyzed is one where there is significant grayscale contrast between the circular pores exposing the electrolyte surface, and the metal network lying on top. Secondary electron imaging mode was chosen owing to its inherent contrast associated with topographical features (recall that the metal network is 200-400 nm thick). Back-scattered mode, which provides elemental materials contrast, added anywhere from 5-15% areal error due to pore shading; and in-lens mode, known for its high contrast imaging ability, was found to provide inconsistencies related to charging effects from the non-conducting YSZ. Care was taken to provide qualitatively consistent contrast in the SEM images across the entirety of the substrate, to ensure accurate and uniform threshold application.

The resulting image (Fig.A.1b) is now a mixture of connected and disconnected black objects, which ImageJ can identify automatically. Problems arise, however, due to dark pixels that are not pore-related. The smaller dark objects can be automatically removed, and the image consequently cleaned up, as in Fig. A.1c. However, the messy,

larger unwanted dark objects remain—these are originally void areas left uncovered during the PS deposition process and result in planar metal regions after the thermal evaporation step. Fortunately, these areas are never circular, so a “circularity” filter can be applied when identifying objects. This filter is applied between Fig. A.1c and d. ImageJ defines a circularity of 1 to be a perfect circle, and 0 to be a straight line. In this way, fractal objects like these metal regions can be removed from the counting. Fig. A.1d is the final pictorial output of the ImageJ process, and shows which objects have been identified. Pore area (2PB), perimeter (3PB), and total pore coverage are all automatically enumerated. Depending on the pore size to be evaluated, different magnification was necessary to ensure accuracy—it was found that no more than 1500 pores could be evaluated from one image and retain acceptable levels of accuracy.

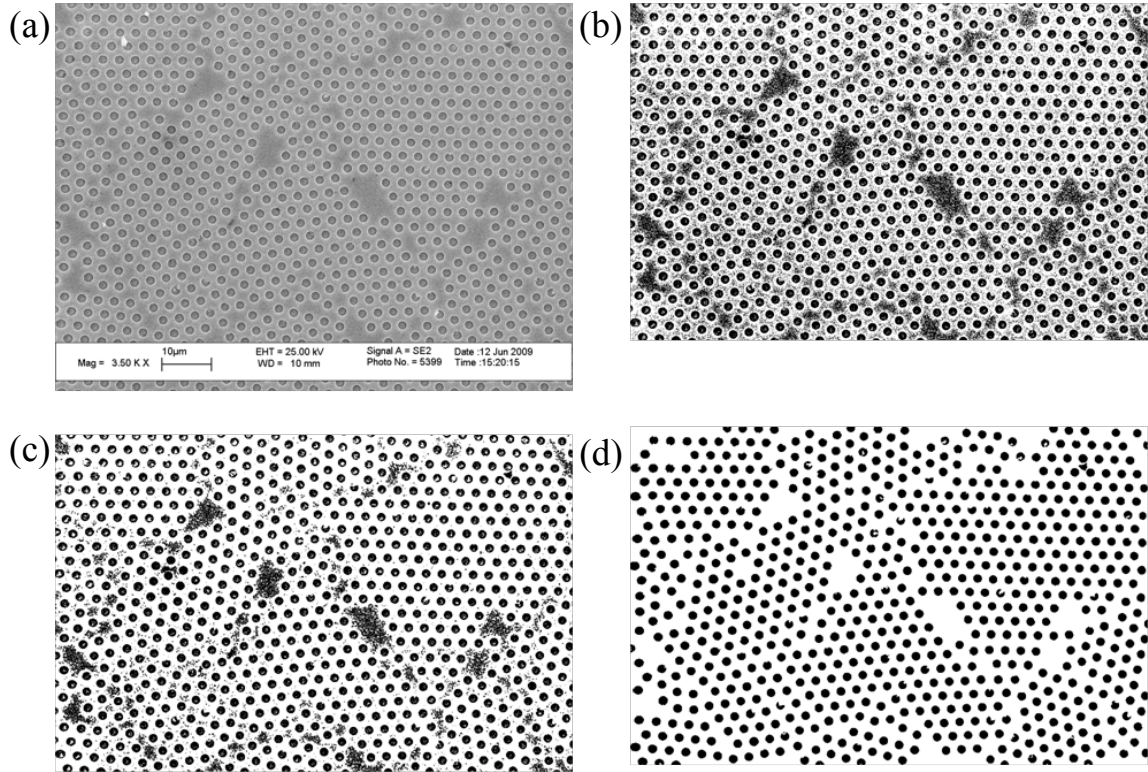


**Fig A.1.** The ImageJ image analysis process: (a) an as-taken SEM image; (b) cropping and conversion to black-and-white; (c) image clean-up; and (d) final image identifying the pores.

## Appendix B

# Additional Images

### B.1 Additional CELD Images

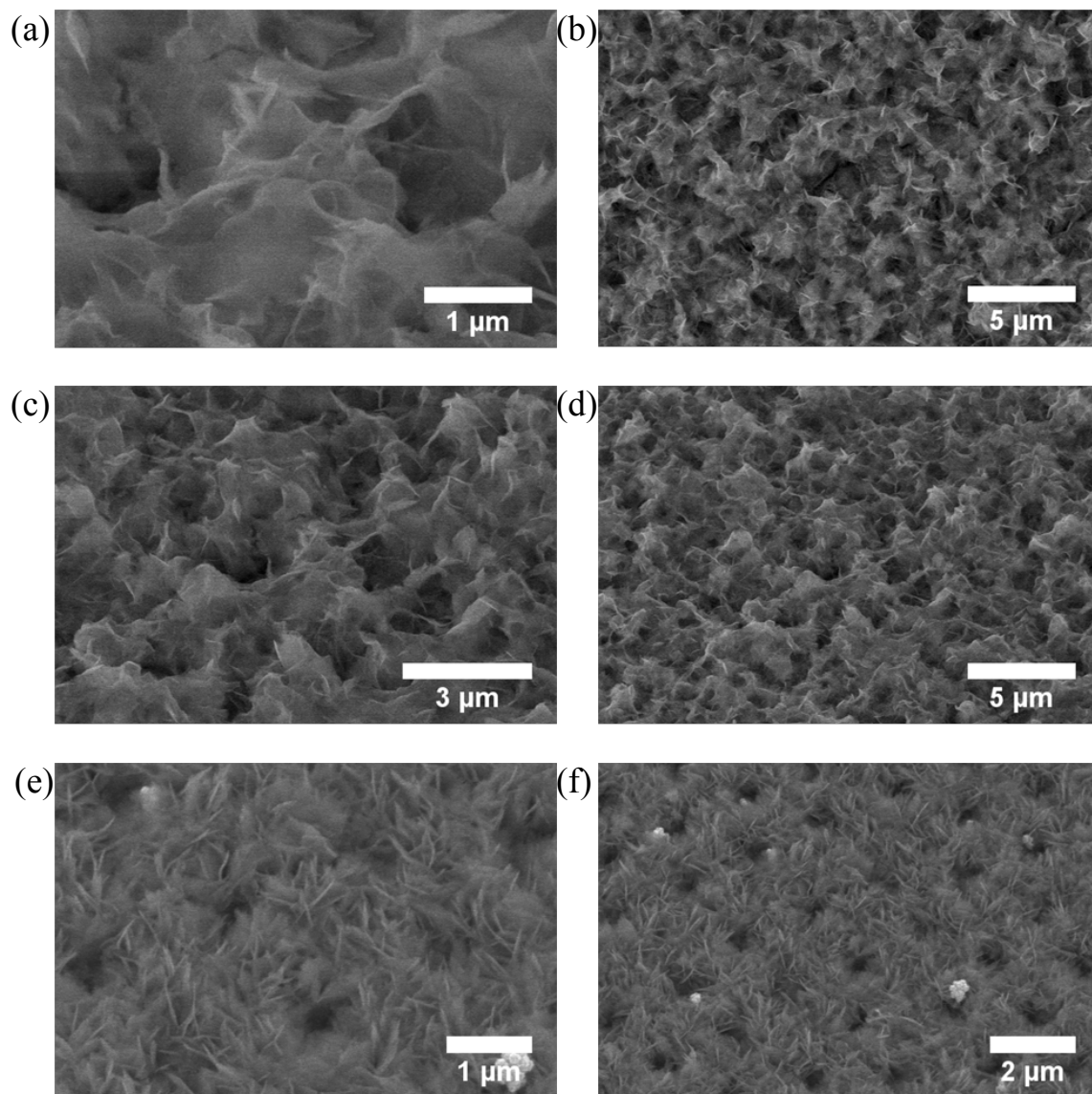


**Fig. B.1.** Angled ( $45^\circ$ ) SEM images of the HSA microstructure deposited at  $0.8 \text{ mA cm}^{-2}$  with a  $0.05 \text{ M}$  doped electrolyte for 5 minutes (a through d); and a  $0.1 \text{ M}$  undoped electrolyte for 5 minutes (e and f).

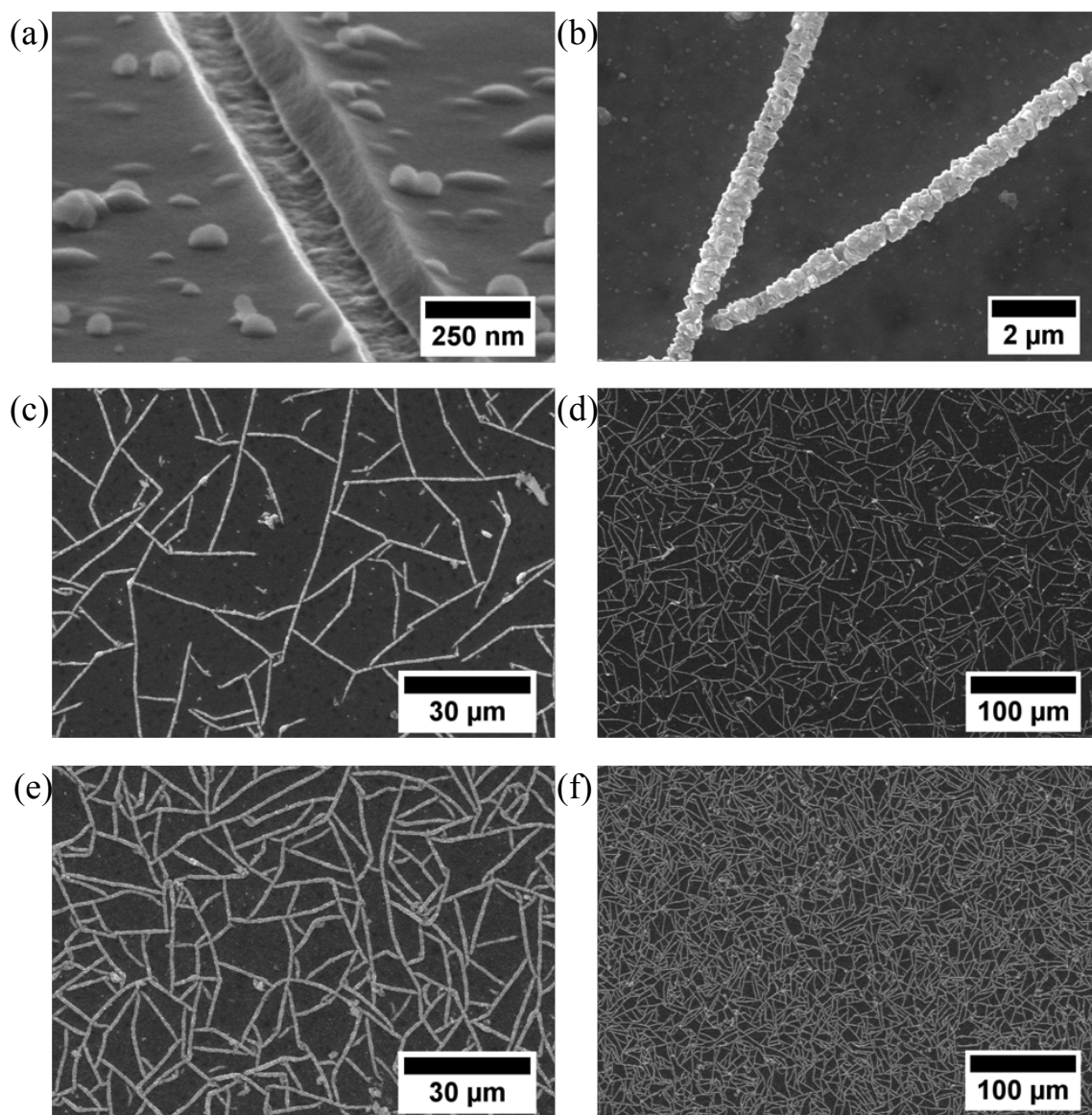


**Fig. B.2.** SEM images of CELD thin films of ceria deposited at  $-0.55$  V vs. SCE with the doped  $+ \text{H}_2\text{O}_2$  electrolyte on thin films of Ni on silicon substrates for different times: (a) – (d) 5 minutes; (e) and (f) 10 minutes. (a) shows an as-deposited crack that forms for thicknesses greater than 300 nm ceria films. (b) – (f) are images taken after annealing in an Ar atmosphere at  $600$  °C for 10 hours. The white strips are crack areas that originally formed as-deposited as in (a), but the exposed Ni metal has oxidized to NiO and volume-expanded out of the crack. The higher degree of cracking for the thicker film in (e) and (f) is easily visualized.

The following TEM images are taken from the same sample shown in Fig. 3.24. (a) is a bright-field image, and (b) through (d) are corresponding dark-field images taken at different tilting angles to highlight various grain orientations, which consequently appear white. (e) is the selected-area diffraction pattern, labeled with approximate lattice parameters. (f) is a HRTEM view of the polycrystalline deposit.

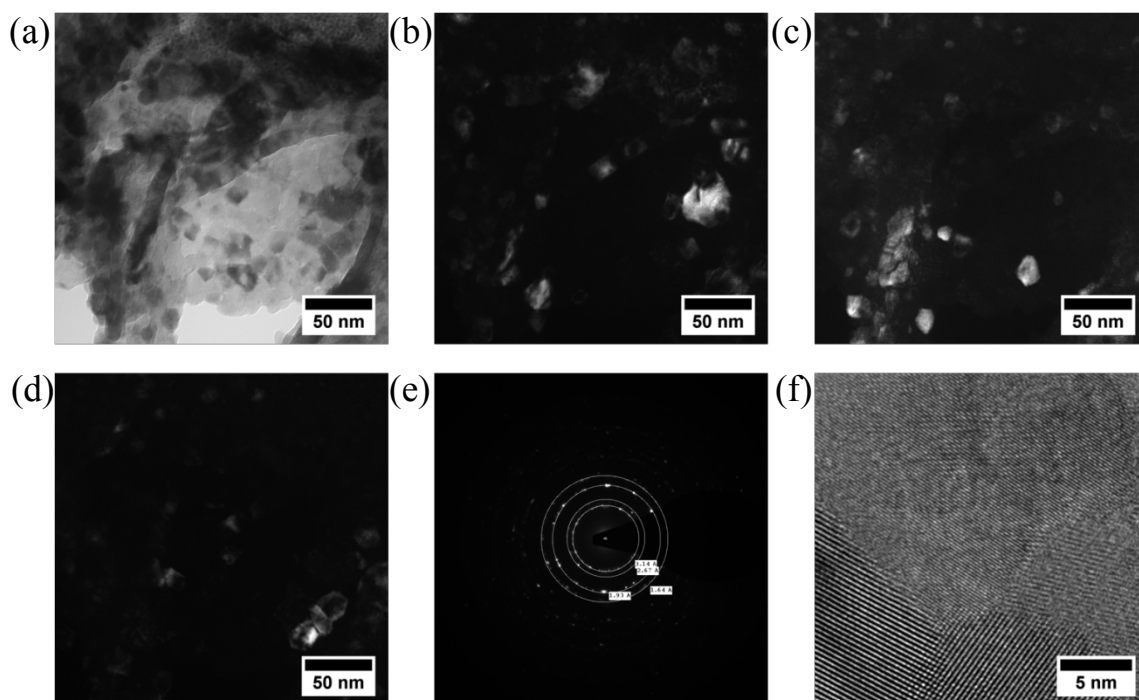
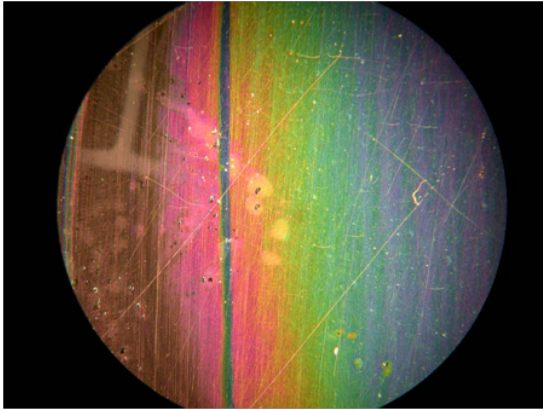


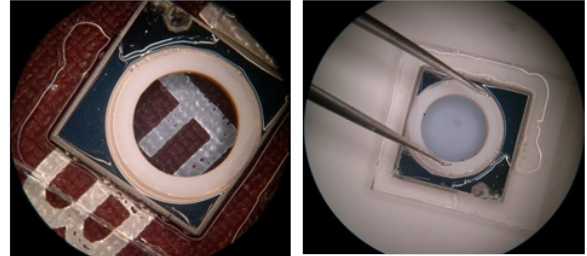
**Fig. B.3.** TEM images taken from the same sample as in Fig. 3.24. See description above.

## B.2 Additional AAO Images

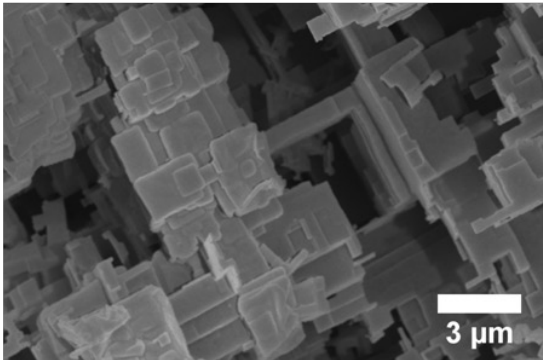
(a)



(b)



(c)



(d)

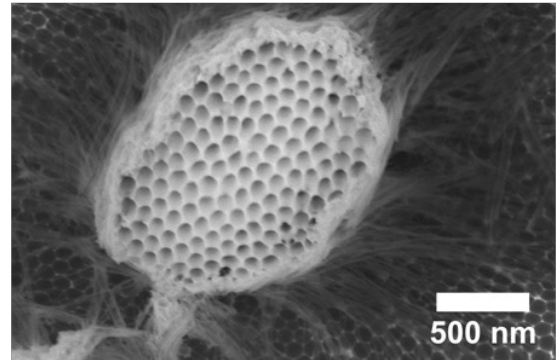


**Fig. B.4.** Various AAO images: (a) optical image of thin film interference patterns resulting from the complete anodic oxidation of sputtered Al on a glass slide; (b) when the sputtered Al is sectioned off, complete anodic oxidation results in a transparent window, seen here on a YSZ single crystal substrate 1 x 1 cm; (c) if Al metal is left in the oxalic acid electrolyte too long, crystallographic etching occurs; and (d) when the AAO template is etched in chromic and phosphoric acid, incomplete template removal results in peculiar structures.

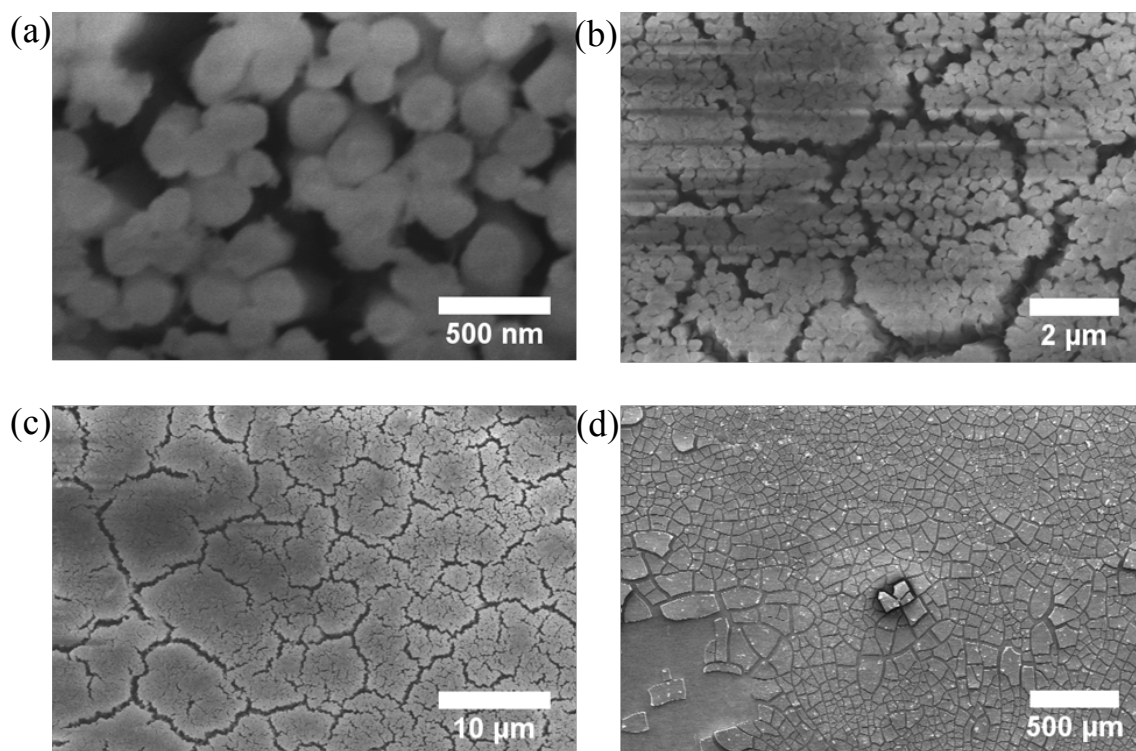


**Fig. B.5.** CELD ceria nanowires from the same sample shown in Fig. 5.7. (a) – (c) are after etching in 3 M NaOH for 2.5 minutes. (d) is as-deposited, showing the scale-like overgrowth of ceria once deposition was complete in the entire pore lengths of the AAO template.

### B.3 Additional Inverse Opal Images

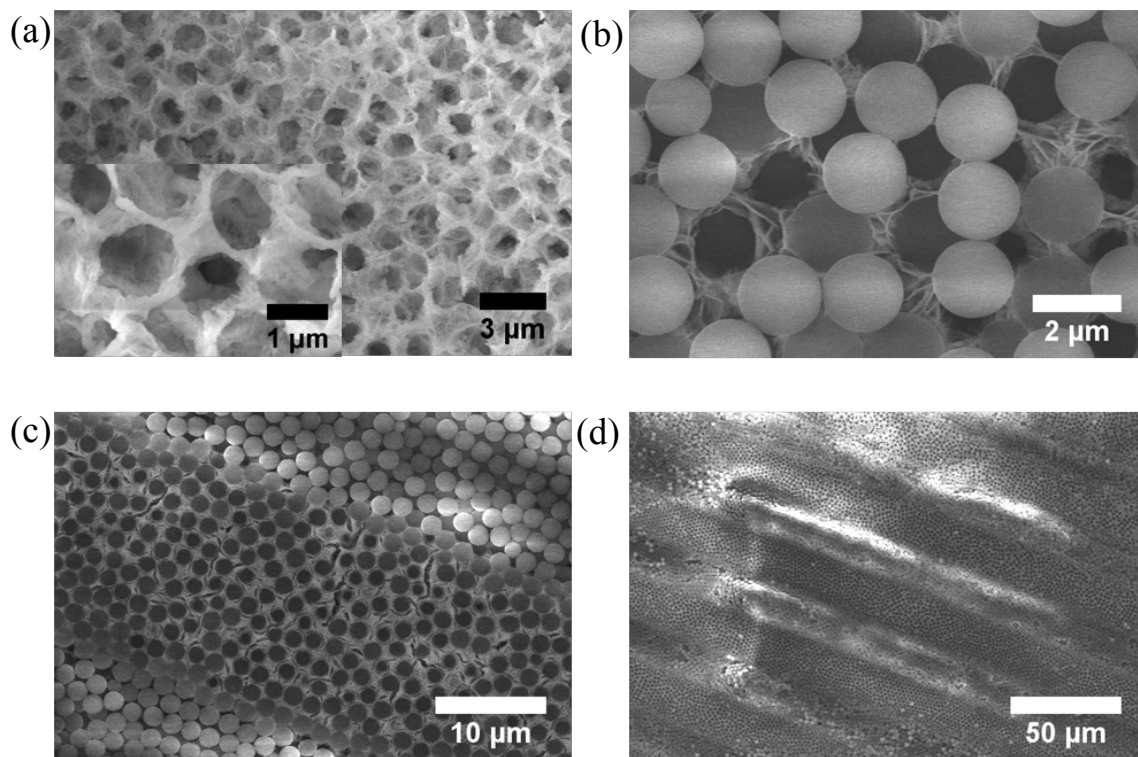


**Fig. B.6.** Various SEM images of inverse opal structures from the same samples as in Fig. 5.9.

### B.4 Additional MIEC Substrate Images

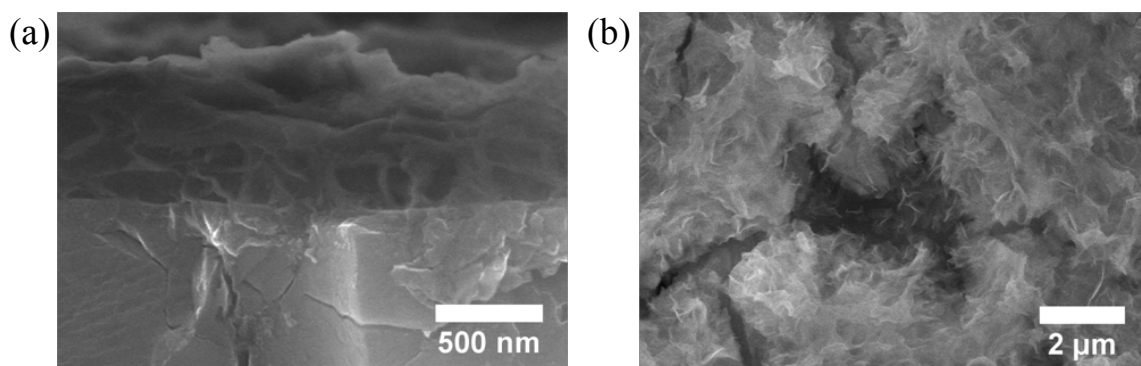


**Fig. B.7.** SEM images of HSA ceria grown on BSCF at  $0.8 \text{ mA cm}^{-2}$  for: (a) 1 minute, showing a good interface between ceria and BSCF; and (b) 5 minutes, showing HSA bridging of a pore in the underlying BSCF filled with nail polish (dark area).

## B.5 Additional Oxidation Protection Coating Images

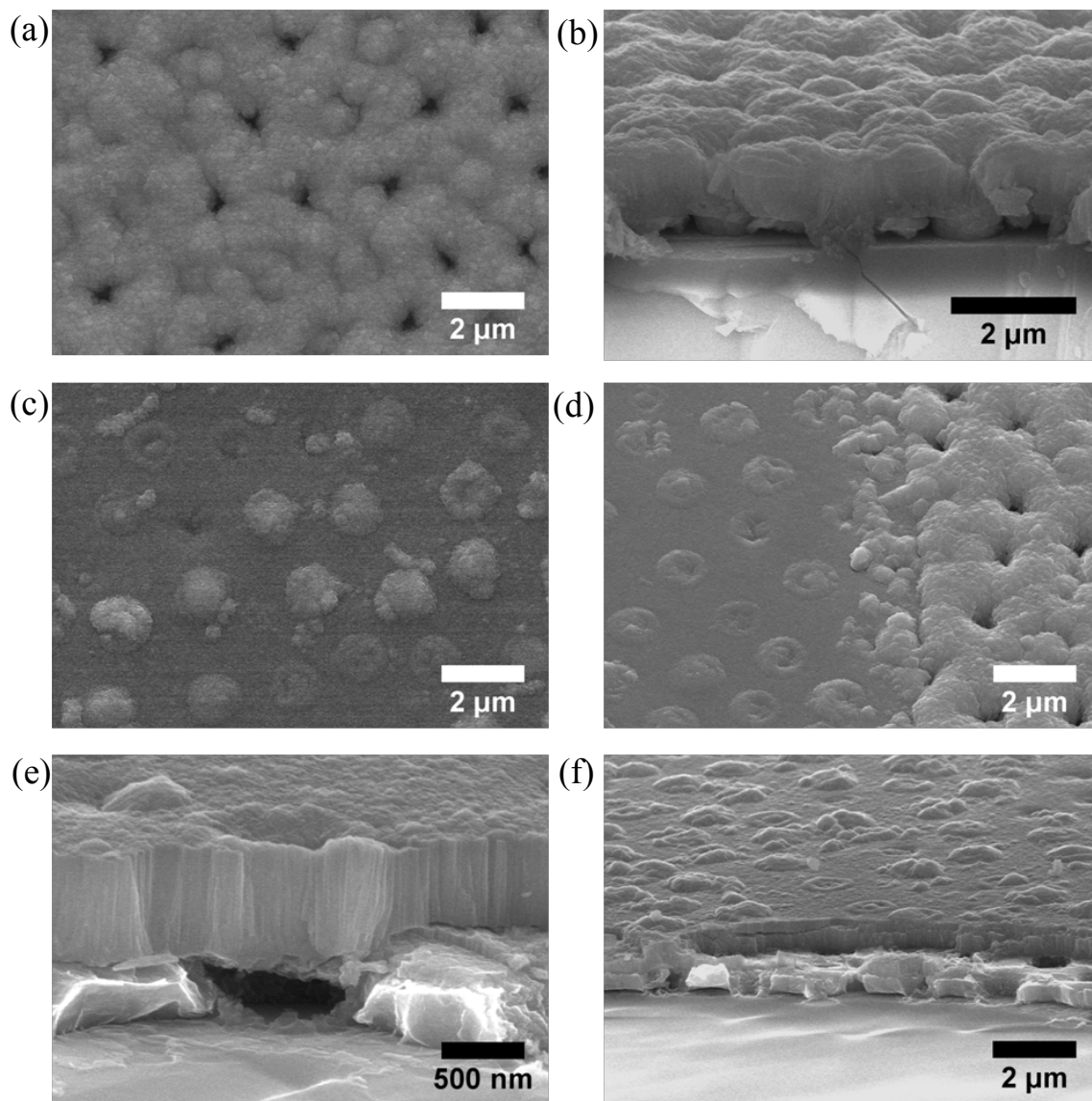


**Fig. B.8.** SEM images of the oxidative protection coating action of CELD ceria, as in Fig. 5.11: (a) and (b) are the Ni anti-dot areas uncovered by CELD; (c) is the area covered by CELD; (d) is the border between the covered and uncovered CELD regions; (e) and (f) are cross-sectional views of the CELD covered regions. All images have a PLD top coating.

# Appendix C

## Alternate SOFC Microstructure Fabrication Routes

### C.1 Solution Impregnation into AAO Templates

A straightforward solution-phase approach to filling the pores of AAO templates was reported in [124]. Briefly, an AAO template is immersed into a 2.5 M cerium nitrate bath for 4 hours, dried at 50 °C for 4 hours, and then thermally treated from 150 – 500 °C to solidify the nanowires/tubes. In an attempt to mimic this approach, an identical cerium nitrate solution was employed with unaided impregnation (Fig. C.1), sonication-assisted impregnation (Fig. C.2), stirring-assisted impregnation (Fig. C.3), and a combination of stirring- and sonication-assisted impregnation (Fig. C.4). The last approach worked best, in terms of filling fraction of the AAO pores. However, any solution-phase route to making nanowires suffers from a common drawback—there is no inherent attachment to an underlying substrate. Attempts were made to thermally sinter nanowires made from these methods to a YSZ underlying substrate while they were still held in place by the surrounding AAO matrix, but thermal treatment of the assembly has the undesirable side-effect of crystallizing the alumina into an un-etchable form. Prolonged treatment in acids, e.g., chromic and phosphoric, and bases, e.g. NaOH, had zero effect, as can be seen in Fig. C.5. Accordingly, this method was abandoned.

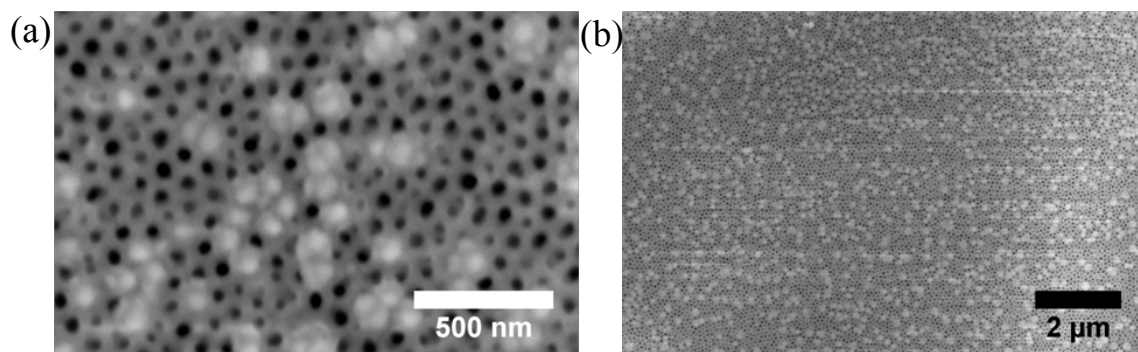


**Fig. C.1.** Ceria nanowires partially filling the pore of an AAO template after unaided solution phase impregnation.

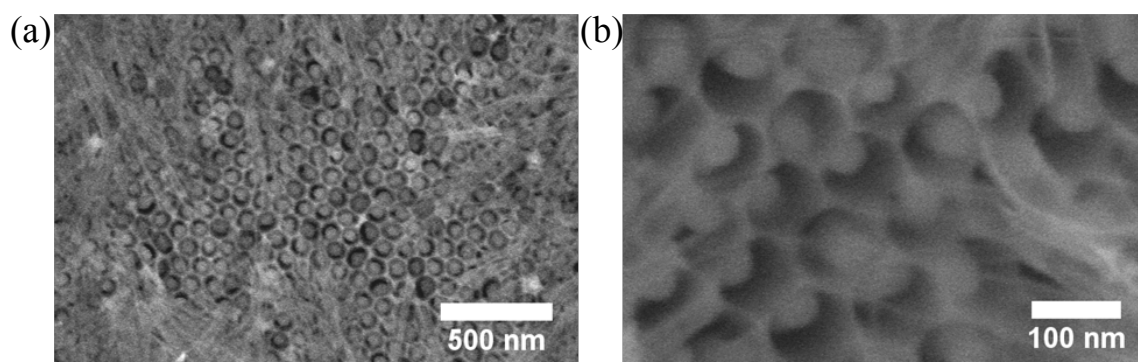


**Fig. C.2.** Ceria nanowires partially filling the pore of an AAO template after sonicated solution phase impregnation.

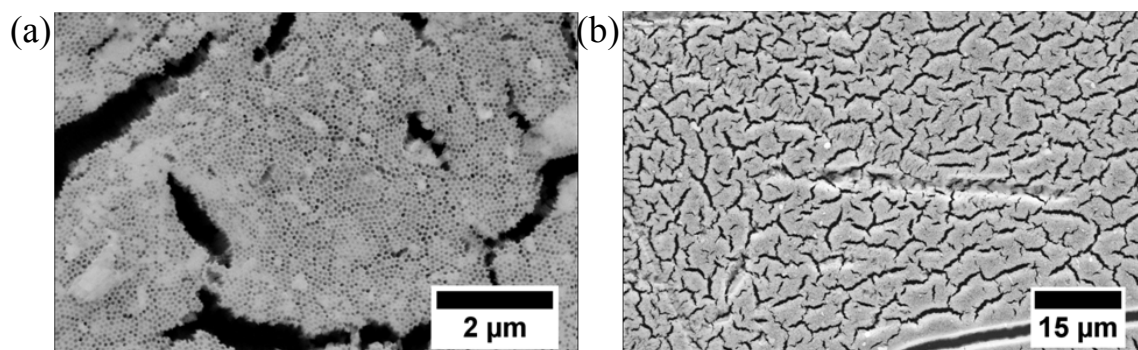


**Fig. C.3.** Ceria nanowires partially filling the pore of an AAO template after stirred solution phase impregnation.

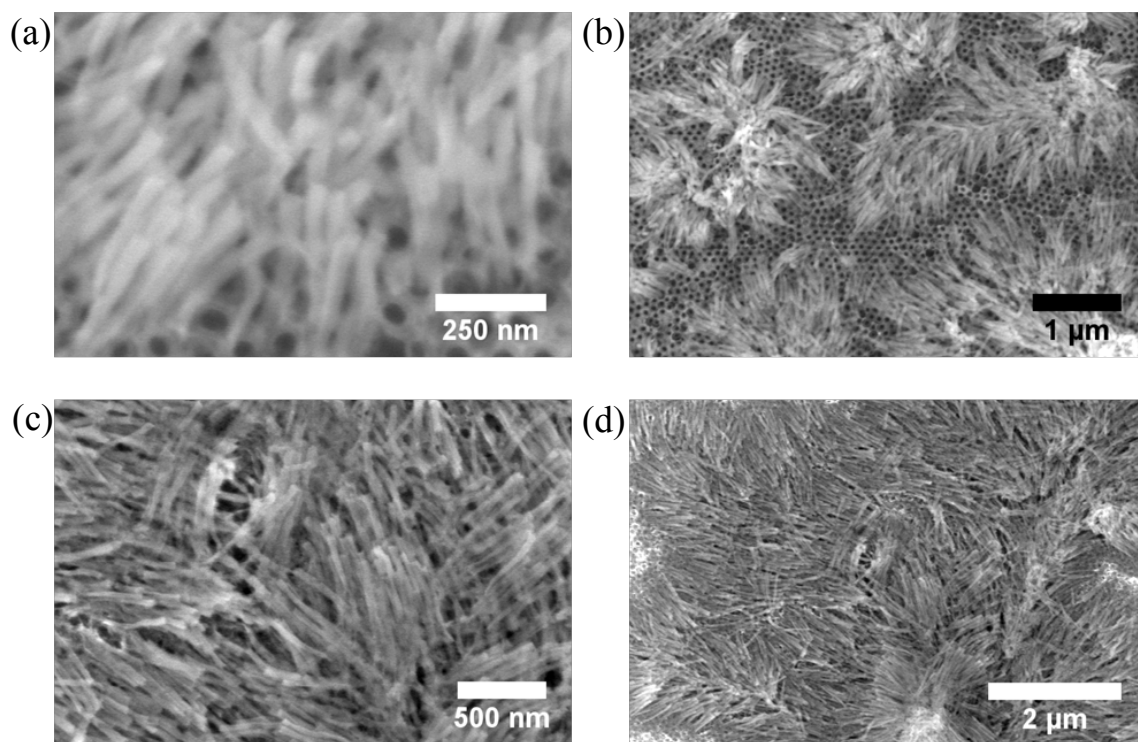


**Fig. C.4.** Ceria nanowires partially filling the pore of an AAO template after sonicated/stirred solution phase impregnation.

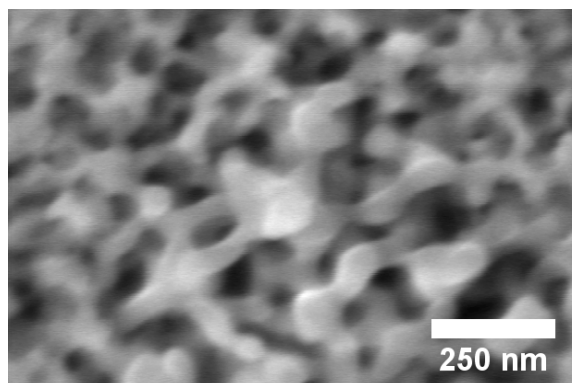


**Fig. C.5.** SEM image of an AAO template after thermal treatment at 1100°C for 5 hours in air, and after unsuccessful, repeated attempts to etch the template in chromic/phosphoric acid mixtures and NaOH.

## C.2 Copper Nanowire Synthesis

It has been known since the 1960's that copper oxide nanowires form spontaneously on the outer surface of the oxide scale during thermal treatment of copper metal at temperatures exceeding 400 °C [125-129]. The aspect ratio and number density can be altered by changing the growth temperature and surrounding atmosphere. This approach works well with bulk copper foil substrates, and also works on copper thin films grown on a supporting substrate. However, the copper metal thin films must be greater than 500 nm in order to produce an appreciable amount of CuO nanowires. The as-produced CuO nanowires can be subsequently reduced in a hydrogen plasma to copper metal [130]. Higher power density plasmas can significantly alter the original CuO morphology, but lower power density plasmas can completely reduce the CuO to Cu without much morphological evolution. Below are selected images from this approach. The combination of copper metal thin film thickness limitations and the inconsistencies of the process lead to its abandonment.

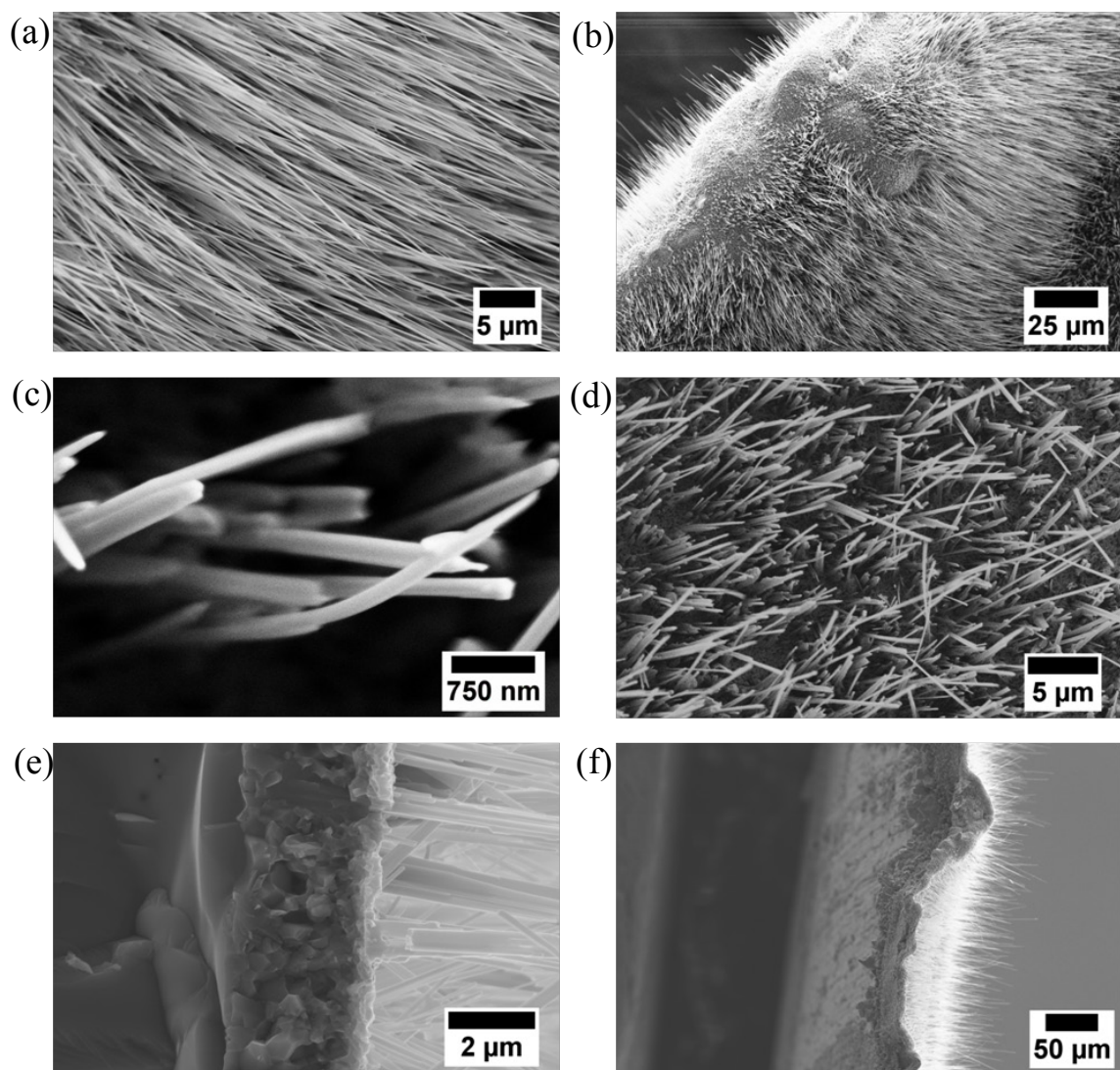


**Fig. C.6.** SEM images of CuO nanowires grown at  $\sim 500$  °C for a couple of hours in ambient air from a 0.25 mm Cu foil.

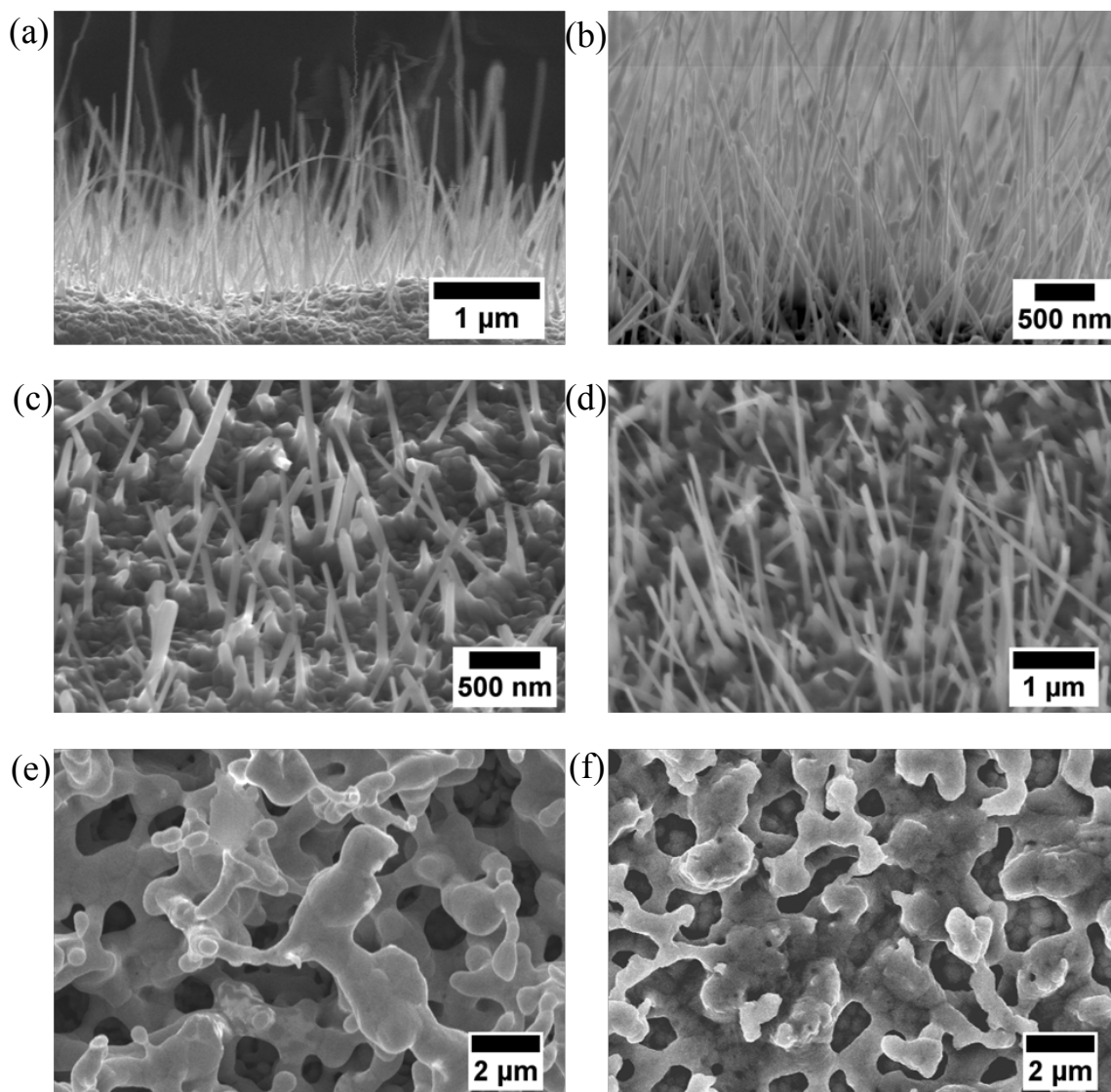


**Fig. C.7.** SEM images of CuO nanowires grown at  $\sim 500$  °C for a couple of hours in ambient air from a thin film of Cu thermally evaporated onto polycrystalline SDC pellets (a) – (d); (e) and (f) show the highly evolved morphology of CuO nanowires to a porous Cu film after they have been reduced in a high power density hydrogen plasma for  $\sim 5$  minutes.

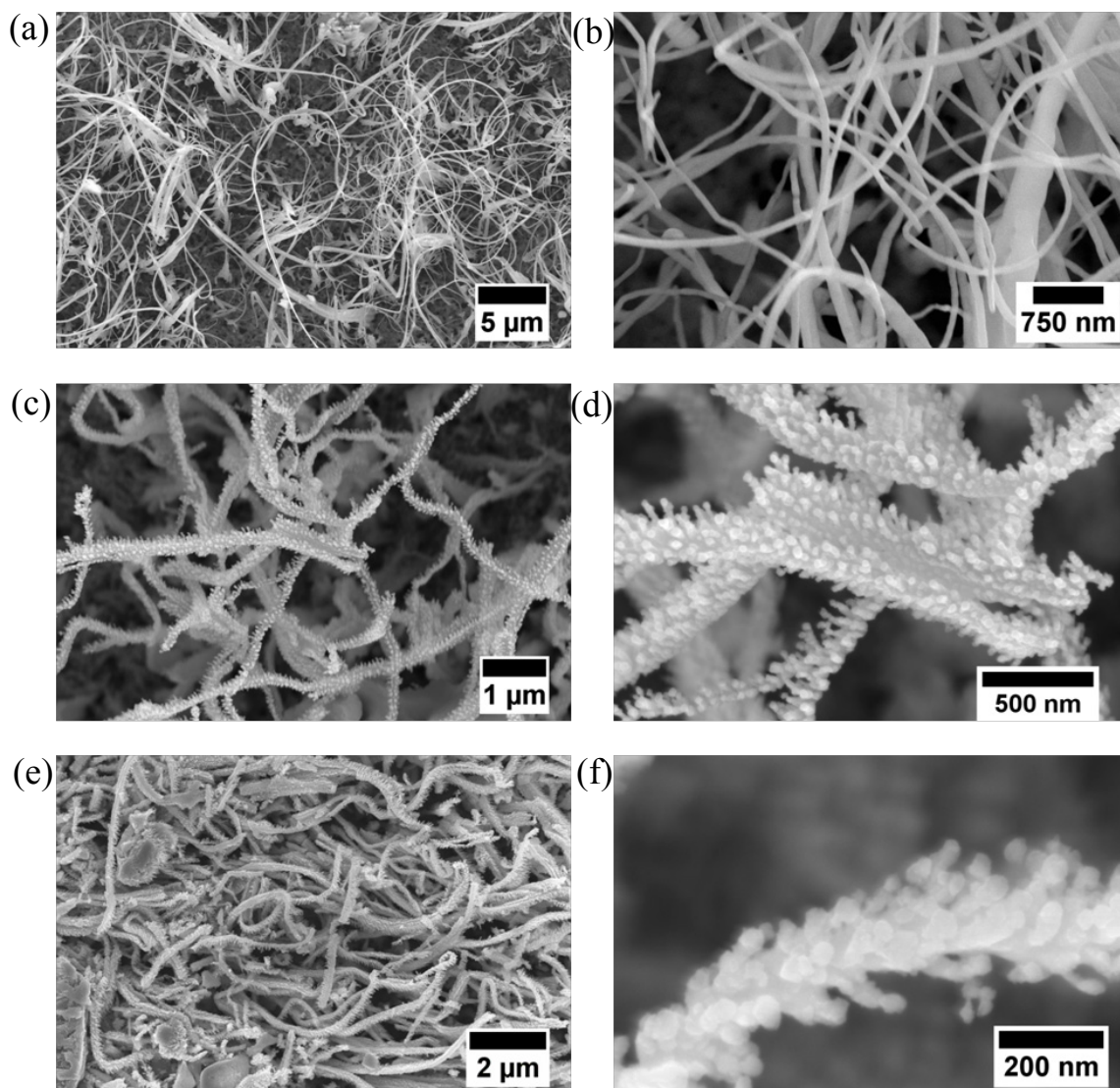


**Fig. C.8.** SEM images of Cu nanowire structures resulting from a moderate power density hydrogen plasma reduction of the CuO nanowires picture in Fig. C.6. (a) and (b) are treated with the plasma for a couple of minutes; (c) – (f) have been treated for greater than 5 minutes, and show some texturing on the nanoscale as a result.

## References

1. Chueh, W.C., *Electrochemical & Thermochemical Behavior of CeO<sub>2</sub>- $\delta$* , in *Materials Science*. 2011, California Institute of Technology.
2. Tarascon, J.M. and M. Armand, *Issues and challenges facing rechargeable lithium batteries*. *Nature*, 2001. **414**(6861): p. 359-367.
3. Zhao, X., et al., *The role of nanomaterials in redox-based supercapacitors for next generation energy storage devices*. *Nanoscale*, 2011. **3**(3): p. 839-855.
4. Zhang, H., G.P. Cao, and Y.S. Yang, *Carbon nanotube arrays and their composites for electrochemical capacitors and lithium-ion batteries*. *Energy & Environmental Science*, 2009. **2**(9): p. 932-943.
5. Carrette, L., K.A. Friedrich, and U. Stimming, *Fuel cells: Principles, types, fuels, and applications*. *Chemphyschem*, 2000. **1**(4): p. 162-193.
6. Ryan O'Hayre, S.-W.C., Whitney Colella, Fritz B. Prinz, *Fuel Cell Fundamentals*. 2006: John Wiley & Sons.
7. Hulteen, J.C. and R.P. Vanduyne, *Nanosphere Lithography - a Materials General Fabrication Process for Periodic Particle Array Surfaces*. *Journal of Vacuum Science & Technology a-Vacuum Surfaces and Films*, 1995. **13**(3): p. 1553-1558.
8. Haynes, C.L. and R.P. Van Duyne, *Nanosphere lithography: A versatile nanofabrication tool for studies of size-dependent nanoparticle optics*. *Journal of Physical Chemistry B*, 2001. **105**(24): p. 5599-5611.
9. Ho, K.C. and J. Jorne, *Electrochemical Impregnation of Nickel-Hydroxide - Flow-through Vs Stagnant Electrodes*. *Journal of the Electrochemical Society*, 1990. **137**(1): p. 149-158.
10. Indira, L. and P.V. Kamath, *Electrogeneration of Base by Cathodic Reduction of Anions - Novel One-Step Route to Unary and Layered Double Hydroxides (Ldhs)*. *Journal of Materials Chemistry*, 1994. **4**(9): p. 1487-1490.
11. Yamazaki, Y., R. Hernandez-Sanchez, and S.M. Haile, *High Total Proton Conductivity in Large-Grained Yttrium-Doped Barium Zirconate*. *Chemistry of Materials*, 2009. **21**(13): p. 2755-2762.

12. Magraso, A., et al., *Development of Proton Conducting SOFCs Based on LaNbO<sub>4</sub> Electrolyte - Status in Norway*. Fuel Cells, 2011. **11**(1): p. 17-25.
13. Tucker, M.C., *Progress in metal-supported solid oxide fuel cells: A review*. Journal of Power Sources, 2010. **195**(15): p. 4570-4582.
14. Haile, S.M., *Fuel cell materials and components*. Acta Materialia, 2003. **51**(19): p. 5981-6000.
15. Eguchi, K., et al., *ELECTRICAL-PROPERTIES OF CERIA-BASED OXIDES AND THEIR APPLICATION TO SOLID OXIDE FUEL-CELLS*. Solid State Ionics, 1992. **52**(1-3): p. 165-172.
16. Tsai, T.P. and S.A. Barnett, *Effect of mixed-conducting interfacial layers on solid oxide fuel cell anode performance*. Journal of the Electrochemical Society, 1998. **145**(5): p. 1696-1701.
17. Steele, B.C.H., *Appraisal of Ce<sub>1-y</sub>Gd<sub>y</sub>O<sub>2-y/2</sub> electrolytes for IT-SOFC operation at 500 degrees C*. Solid State Ionics, 2000. **129**(1-4): p. 95-110.
18. Fleig, J., *Solid oxide fuel cell cathodes: Polarization mechanisms and modeling of the electrochemical performance*. Annual Review of Materials Research, 2003. **33**: p. 361-382.
19. Shao, Z.P. and S.M. Haile, *A high-performance cathode for the next generation of solid-oxide fuel cells*. Nature, 2004. **431**(7005): p. 170-173.
20. Yu, H.C., et al., *Electrochemical characterization and performance evaluation of intermediate temperature solid oxide fuel cell with La<sub>0.75</sub>Sr<sub>0.25</sub>CUO<sub>2.5-delta</sub> cathode*. Journal of Power Sources, 2005. **152**(1): p. 22-26.
21. Pena-Martinez, J., et al., *Performance of XSCoF (X = Ba, La and Sm) and LSCrX' (X' = Mn, Fe and Al) perovskite-structure materials on LSGM electrolyte for IT-SOFC*. Electrochimica Acta, 2007. **52**(9): p. 2950-2958.
22. Zhang, P., et al., *Sr<sub>2</sub>CoMoO<sub>6</sub> anode for solid oxide fuel cell running on H<sub>2</sub> and CH<sub>4</sub> fuels*. Journal of Power Sources, 2011. **196**(4): p. 1738-1743.
23. Tao, S.W. and J.T.S. Irvine, *Synthesis and characterization of (La<sub>0.75</sub>Sr<sub>0.25</sub>)Cr<sub>0.5</sub>Mn<sub>0.5</sub>O<sub>3-delta</sub>, a redox-stable, efficient perovskite anode for SOFCs*. Journal of the Electrochemical Society, 2004. **151**(2): p. A252-A259.

24. Atkinson, A., et al., *Advanced anodes for high-temperature fuel cells*. Nature Materials, 2004. **3**(1): p. 17-27.
25. Jiang, S.P. and S.H. Chan, *A review of anode materials development in solid oxide fuel cells*. Journal of Materials Science, 2004. **39**(14): p. 4405-4439.
26. Ciucci, F., et al., *Surface reaction and transport in mixed conductors with electrochemically-active surfaces: a 2-D numerical study of ceria*. Physical Chemistry Chemical Physics, 2011. **13**(6): p. 2121-2135.
27. Chueh, W.C., W. Lai, and S.M. Haile, *Electrochemical behavior of ceria with selected metal electrodes*. Solid State Ionics, 2008. **179**(21-26): p. 1036-1041.
28. Gross, M.D., J.M. Vohs, and R.J. Gorte, *A strategy for achieving high performance with SOFC ceramic anodes*. Electrochemical and Solid State Letters, 2007. **10**(4): p. B65-B69.
29. Lu, C., et al., *A comparison of Cu-ceria-SDC and Au-ceria-SDC composites for SOFC anodes*, in *Solid Oxide Fuel Cells Viii*, S.C. Singhal and M. Dokiya, Editors. 2003, Electrochemical Society Inc: Pennington. p. 773-780.
30. Marina, O.A., et al., *A solid oxide fuel cell with a gadolinia-doped ceria anode: preparation and performance*. Solid State Ionics, 1999. **123**(1-4): p. 199-208.
31. W.C. Chueh, Y.H., S.M. Haile, *High Electrochemical Activity of the Oxide Phase in Model Ceria-Pt and Ceria-Ni Composite Anode*. Submitted 2011.
32. Chueh, W.C. and S.M. Haile, *Electrochemical studies of capacitance in cerium oxide thin films and its relationship to anionic and electronic defect densities*. Physical Chemistry Chemical Physics, 2009. **11**(37): p. 8144-8148.
33. Wilson, J.R., et al., *Three-dimensional reconstruction of a solid-oxide fuel-cell anode*. Nature Materials, 2006. **5**(7): p. 541-544.
34. Mizusaki, J., et al., *Preparation of Nickel Pattern Electrodes on Ysz and Their Electrochemical Properties in H<sub>2</sub>-H<sub>2</sub>O Atmospheres*. Journal of the Electrochemical Society, 1994. **141**(8): p. 2129-2134.
35. Bieberle, A., L.P. Meier, and L.J. Gauckler, *The electrochemistry of Ni pattern anodes used as solid oxide fuel cell model electrodes*. Journal of the Electrochemical Society, 2001. **148**(6): p. A646-A656.

36. Baumann, F.S., et al., *Quantitative comparison of mixed conducting SOFC cathode materials by means of thin film model electrodes*. Journal of the Electrochemical Society, 2007. **154**(9): p. B931-B941.
37. Bieberle, A. and L.J. Gauckler, *State-space modeling of the anodic SOFC system Ni, H<sub>2</sub>-H<sub>2</sub>O vertical bar YSZ*. Solid State Ionics, 2002. **146**(1-2): p. 23-41.
38. Goodwin, D.G., et al., *Modeling Electrochemical Oxidation of Hydrogen on Ni-YSZ Pattern Anodes*. Journal of the Electrochemical Society, 2009. **156**(9): p. B1004-B1021.
39. Piao, J.H., et al., *A study of process parameters of LSM and LSM-YSZ composite cathode films prepared by screen-printing*. Journal of Power Sources, 2008. **175**(1): p. 288-295.
40. Beckel, D., et al., *Thin films for micro solid oxide fuel cells*. Journal of Power Sources, 2007. **173**(1): p. 325-345.
41. De Jonghe, L.C., C.P. Jacobson, and S.J. Visco, *Supported electrolyte thin film synthesis of solid oxide fuel cells*. Annual Review of Materials Research, 2003. **33**: p. 169-182.
42. Therese, G.H.A. and P.V. Kamath, *Electrochemical synthesis of metal oxides and hydroxides*. Chemistry of Materials, 2000. **12**(5): p. 1195-1204.
43. Zhitomirsky, I., *Cathodic electrodeposition of ceramic and organoceramic materials. Fundamental aspects*. Advances in Colloid and Interface Science, 2002. **97**(1-3): p. 279-317.
44. Bhattacharya, R., et al., *Electrodeposited biaxially textured buffer layer for YBa<sub>2</sub>Cu<sub>3</sub>O<sub>7-δ</sub> (YBCO) superconductor oxide films*. Journal of the Electrochemical Society, 2006. **153**(5): p. C273-C276.
45. Zhitomirsky, I. and A. Petric, *Electrochemical deposition of ceria and doped ceria films*. Ceramics International, 2001. **27**(2): p. 149-155.
46. Kamada, K., N. Enomoto, and J. Hojo, *Optimization of electrochemical synthesis conditions for dense and doped ceria thin films*. Electrochimica Acta, 2009. **54**(27): p. 6996-7000.

47. Bocchetta, P., M. Santamaria, and F. Di Quarto, *Electrosynthesis of Ce-Co mixed oxide nanotubes with high aspect ratio and tunable composition*. *Electrochemical and Solid State Letters*, 2008. **11**(3): p. K27-K30.
48. Zhitomirsky, I. and A. Petric, *Electrolytic and electrophoretic deposition of CeO<sub>2</sub> films*. *Materials Letters*, 1999. **40**(6): p. 263-268.
49. Zhang, C.J., et al., *Heterogeneous films of ordered CeO<sub>2</sub>/Ni concentric nanostructures for fuel cell applications*. *Physical Chemistry Chemical Physics*, 2010. **12**(17): p. 4295-4300.
50. Zivkovic, L., et al., *Effect of samarium addition and annealing on the properties of electrodeposited ceria thin films*. *Thin Solid Films*, 2011. **519**(11): p. 3538-3543.
51. Lair, V., et al., *Synthesis and characterization of cerium oxide by electrochemical methods*. *Physica Status Solidi C - Current Topics in Solid State Physics*, Vol 5, No 11 2008, 2008. **5**(11): p. 3492-3495
- 135.
52. Elbelghiti, H., et al., *Electrodeposition of Ceria on Stainless Steel for SOFC Interconnect Applications*. *Solid Oxide Fuel Cells 10 (Sofc-X)*, Pts 1 and 2, 2007. **7**(1): p. 2391-2397
- 2646.
53. Hamlaoui, Y., et al., *Cathodic electrodeposition of cerium-based oxides on carbon steel from concentrated cerium nitrate solutions Part I. Electrochemical and analytical characterisation*. *Materials Chemistry and Physics*, 2009. **113**(2-3): p. 650-657.
54. Kulp, E.A., et al., *Electrodeposition of nanometer-thick ceria films by oxidation of cerium(III)-acetate*. *Solid State Ionics*, 2007. **178**(11-12): p. 749-757.
55. Li, F.B., R.C. Newman, and G.E. Thompson, *In situ atomic force microscopy studies of electrodeposition mechanism of cerium oxide films: Nucleation and growth out of a gel mass precursor*. *Electrochimica Acta*, 1997. **42**(16): p. 2455-2464.

56. Balasubramanian, M., C.A. Melendres, and A.N. Mansour, *An X-ray absorption study of the local structure of cerium in electrochemically deposited thin films*. Thin Solid Films, 1999. **347**(1-2): p. 178-183.
57. Zhou, Y.C., R.J. Phillips, and J.A. Switzer, *Electrochemical Synthesis and Sintering of Nanocrystalline Cerium(Lv) Oxide Powders*. Journal of the American Ceramic Society, 1995. **78**(4): p. 981-985.
58. Inguanta, R., S. Piazza, and C. Sunseri, *Template electrosynthesis of CeO<sub>2</sub> nanotubes*. Nanotechnology, 2007. **18**(48): p. -.
59. Bocchetta, P., M. Santamaria, and F. Di Quarto, *From ceria nanotubes to nanowires through electrogeneration of base*. Journal of Applied Electrochemistry, 2009. **39**(11): p. 2073-2081.
60. Zhitomirsky, I. and A. Petric, *Electrochemical deposition of yttrium oxide*. Journal of Materials Chemistry, 2000. **10**(5): p. 1215-1218.
61. Wang, A.Q. and T.D. Golden, *Anodic electrodeposition of cerium oxide thin films - I. Formation of crystalline thin films*. Journal of the Electrochemical Society, 2003. **150**(9): p. C616-C620.
62. Golden, T.D. and A.Q. Wang, *Anodic electrodeposition of cerium oxide thin films - II. Mechanism studies*. Journal of the Electrochemical Society, 2003. **150**(9): p. C621-C624.
63. Mahajan, S., et al., *Tuning plasmons on nano-structured substrates for NIR-SERS*. Physical Chemistry Chemical Physics, 2007. **9**(1): p. 104-109.
64. Shiu, J.Y., et al., *Fabrication of tunable superhydrophobic surfaces by nanosphere lithography*. Chemistry of Materials, 2004. **16**(4): p. 561-564.
65. Boneberg, J., et al., *The formation of nano-dot and nano-ring structures in colloidal monolayer lithography*. Langmuir, 1997. **13**(26): p. 7080-7084.
66. Burmeister, F., et al., *Colloid monolayers as versatile lithographic masks*. Langmuir, 1997. **13**(11): p. 2983-2987.
67. Spada, E.R., et al., *Homogeneous growth of antidot structures electrodeposited on Si by nanosphere lithography*. Journal of Applied Physics, 2008. **103**(11): p. -.

68. Haginoya, C., M. Ishibashi, and K. Koike, *Nanostructure array fabrication with a size-controllable natural lithography*. Applied Physics Letters, 1997. **71**(20): p. 2934-2936.
69. Dimitrov, A.S. and K. Nagayama, *Steady-State Unidirectional Convective Assembling of Fine Particles into 2-Dimensional Arrays*. Chemical Physics Letters, 1995. **243**(5-6): p. 462-468.
70. Onoda, G.Y. and E.G. Liniger, *Experimental-Determination of the Random-Parking Limit in 2 Dimensions*. Physical Review A, 1986. **33**(1): p. 715-716.
71. Mihi, A., M. Ocana, and H. Miguez, *Oriented colloidal-crystal thin films by spin-coating microspheres dispersed in volatile media*. Advanced Materials, 2006. **18**(17): p. 2244-+.
72. Dimitrov, A.S. and K. Nagayama, *Continuous convective assembling of fine particles into two-dimensional arrays on solid surfaces*. Langmuir, 1996. **12**(5): p. 1303-1311.
73. Trau, M., D.A. Saville, and I.A. Aksay, *Field-induced layering of colloidal crystals*. Science, 1996. **272**(5262): p. 706-709.
74. Hayward, R.C., D.A. Saville, and I.A. Aksay, *Electrophoretic assembly of colloidal crystals with optically tunable micropatterns*. Nature, 2000. **404**(6773): p. 56-59.
75. Park, S.H., D. Qin, and Y. Xia, *Crystallization of mesoscale particles over large areas*. Advanced Materials, 1998. **10**(13): p. 1028-+.
76. Scientific, T. *NIST Traceable Particle Size Standards*.
77. Hamlaoui, Y., et al., *Cathodic electrodeposition of cerium based oxides on carbon steel from concentrated cerium nitrate. Part II: Influence of electrodeposition parameters and of the addition of PEG*. Materials Chemistry and Physics, 2010. **120**(1): p. 172-180.
78. Arurault, L., B. Daffos, and F.X. Sauvage, *Nanocrystallized ceria-based coatings prepared by electrochemistry on TA6V titanium alloy*. Materials Research Bulletin, 2008. **43**(4): p. 796-805.

79. Zhou, Y.C. and J.A. Switzer, *Growth of cerium(IV) oxide films by the electrochemical generation of base method*. Journal of Alloys and Compounds, 1996. **237**(1-2): p. 1-5.
80. Arurault, L., et al., *Electrochemical preparation of adherent ceria coatings on ferritic stainless steel*. Thin Solid Films, 2004. **466**(1-2): p. 75-80.
81. Bocchetta, P., M. Santamaria, and F. Di Quarto, *Cerium oxyhydroxide nanowire growth via electrogeneration of base in nonaqueous electrolytes*. Electrochemical and Solid State Letters, 2008. **11**(9): p. K93-K97.
82. Aldykiewicz, A.J., A.J. Davenport, and H.S. Isaacs, *Studies of the formation of cerium-rich protective films using x-ray absorption near-edge spectroscopy and rotating disk electrode methods*. Journal of the Electrochemical Society, 1996. **143**(1): p. 147-154.
83. Li, G.R., et al., *Microstructural evolution of CeO<sub>2</sub> from porous structures to clusters of nanosheet arrays assisted by gas bubbles via electrodeposition*. Langmuir, 2008. **24**(8): p. 4254-4259.
84. Hayes, S.A., et al., *The phase stability of cerium species in aqueous systems - I. E-pH diagram for the Ce-HClO<sub>4</sub>-H<sub>2</sub>O system*. Journal of the Electrochemical Society, 2002. **149**(12): p. C623-C630.
85. Yu, P., et al., *The phase stability of cerium species in aqueous systems - II. The Ce(III/IV)-H<sub>2</sub>O-H<sub>2</sub>O<sub>2</sub>/O<sub>2</sub> systems. Equilibrium considerations and pourbaix diagram calculations*. Journal of the Electrochemical Society, 2006. **153**(1): p. C74-C79.
86. Nobial, M., et al., *The nitrate reduction process: A way for increasing interfacial pH*. Journal of Electroanalytical Chemistry, 2007. **600**(1): p. 87-94.
87. Giannuzzi, L.A. and F.A. Stevie, *A review of focused ion beam milling techniques for TEM specimen preparation*. Micron, 1999. **30**(3): p. 197-204.
88. Jennings, A.T., M.J. Burek, and J.R. Greer, *Microstructure versus Size: Mechanical Properties of Electroplated Single Crystalline Cu Nanopillars*. Physical Review Letters, 2010. **104**(13): p. -.

89. Saitzek, S., et al., *Nanostructured ceria: a comparative study from X-ray diffraction, Raman spectroscopy and BET specific surface measurements*. Physica Status Solidi a-Applications and Materials Science, 2008. **205**(7): p. 1534-1539.
90. Weber, W.H., K.C. Hass, and J.R. McBride, *Raman-Study of CeO<sub>2</sub> - 2nd-Order Scattering, Lattice-Dynamics, and Particle-Size Effects*. Physical Review B, 1993. **48**(1): p. 178-185.
91. Kosacki, I., et al., *Raman scattering and lattice defects in nanocrystalline CeO<sub>2</sub> thin films*. Solid State Ionics, 2002. **149**(1-2): p. 99-105.
92. Balasubramanian, M., C.A. Melendres, and A.N. Mansour, *X-ray absorption spectroscopy study of the local structure of heavy metal ions incorporated into electrodeposited nickel oxide films*. Journal of the Electrochemical Society, 1999. **146**(2): p. 607-614.
93. Phok, S. and R.N. Bhattacharya, *Effect of samarium doping on electrodeposited CeO<sub>2</sub> thin film*. Physica Status Solidi a-Applications and Materials Science, 2006. **203**(15): p. 3734-3742.
94. Lai, W. and S.M. Haile, *Impedance spectroscopy as a tool for chemical and electrochemical analysis of mixed conductors: A case study of ceria*. Journal of the American Ceramic Society, 2005. **88**(11): p. 2979-2997.
95. Chang, H.Y. and H.I. Chen, *Morphological evolution for CeO<sub>2</sub> nanoparticles synthesized by precipitation technique*. Journal of Crystal Growth, 2005. **283**(3-4): p. 457-468.
96. Sepa, D.B., M.V. Vojnovic, and A. Damjanovic, *Reaction Intermediates as a Controlling Factor in the Kinetics and Mechanism of Oxygen Reduction at Platinum-Electrodes*. Electrochimica Acta, 1981. **26**(6): p. 781-793.
97. M. E. Orazem, B.T., *Electrochemical Impedance Spectroscopy*. 2008: John Wiley & Sons.
98. Edwards, J.D. and F. Keller, *Formation of Anodic Coatings on Aluminum*. Transactions of The Electrochemical Society, 1941. **79**(1): p. 135-144.
99. Hunter, M.S. and P. Fowle, *Factors Affecting the Formation of Anodic Oxide Coatings*. Journal of the Electrochemical Society, 1954. **101**(10): p. 514-519.

100. Houser, J.E. and K.R. Hebert, *The role of viscous flow of oxide in the growth of self-ordered porous anodic alumina films*. Nature Materials, 2009. **8**(5): p. 415-420.
101. Skeldon, P., et al., *A tracer study of porous anodic alumina*. Electrochemical and Solid State Letters, 2006. **9**(11): p. B47-B51.
102. Garcia-Vergara, S.J., et al., *Compositional evidence for flow in anodic films on aluminum under high electric fields*. Journal of the Electrochemical Society, 2007. **154**(9): p. C540-C545.
103. Matefi-Tempfli, S. and M. Matefi-Tempfli, *Vertically Aligned Nanowires on Flexible Silicone using a Supported Alumina Template prepared by Pulsed Anodization*. Advanced Materials, 2009. **21**(40): p. 4005-+.
104. Fan, Z.Y., et al., *Electrical and photoconductive properties of vertical ZnO nanowires in high density arrays*. Applied Physics Letters, 2006. **89**(21): p. -.
105. Yasui, N., A. Imada, and T. Den, *Electrodeposition of (001) oriented CoPt L1(0) columns into anodic alumina films*. Applied Physics Letters, 2003. **83**(16): p. 3347-3349.
106. Fusil, S., et al., *Nanolithography based contacting method for electrical measurements on single template synthesized nanowires*. Nanotechnology, 2005. **16**(12): p. 2936-2940.
107. Sander, M.S., et al., *Template-assisted fabrication of dense, aligned arrays of titania nanotubes with well-controlled dimensions on substrates*. Advanced Materials, 2004. **16**(22): p. 2052-+.
108. Yang, Y., et al., *Anodic alumina template on Au/Si substrate and preparation of CdS nanowires*. Solid State Communications, 2002. **123**(6-7): p. 279-282.
109. Vlad, A., et al., *Nanowire-decorated microscale metallic electrodes*. Small, 2008. **4**(5): p. 557-560.
110. Chong, M.A.S., et al., *Combinational template-assisted fabrication of hierarchically ordered nanowire arrays on substrates for device applications*. Applied Physics Letters, 2006. **89**(23): p. -.
111. Colvin, V.L., *From opals to optics: Colloidal photonic crystals*. Mrs Bulletin, 2001. **26**(8): p. 637-641.

112. Yu, X.D., et al., *Filling fraction dependent properties of inverse opal metallic photonic crystals*. *Advanced Materials*, 2007. **19**(13): p. 1689-+.
113. Chung, Y.W., et al., *Fabrication of various nickel nanostructures by manipulating the one-step electrodeposition process*. *Journal of the Electrochemical Society*, 2007. **154**(6): p. E77-E83.
114. Bartlett, P.N., T. Dunford, and M.A. Ghanem, *Templated electrochemical deposition of nanostructured macroporous PbO<sub>2</sub>*. *Journal of Materials Chemistry*, 2002. **12**(10): p. 3130-3135.
115. Bartlett, P.N., et al., *Optical properties of nanostructured metal films*. *Faraday Discussions*, 2004. **125**: p. 117-132.
116. Yan, H.W., et al., *Fabrication of 2D and 3D ordered porous ZnO films using 3D opal templates by electrodeposition*. *Electrochemistry Communications*, 2005. **7**(11): p. 1117-1121.
117. Zhu, R., et al., *Controlling the electrodeposition of mesoporous metals for nanoplasmonics*. *Nanoscale*, 2009. **1**(3): p. 355-359.
118. Holland, B.T., et al., *Synthesis of highly ordered, three-dimensional, macroporous structures of amorphous or crystalline inorganic oxides, phosphates, and hybrid composites*. *Chemistry of Materials*, 1999. **11**(3): p. 795-805.
119. Wang, T.W., et al., *Preparation of a large Mesoporous CeO<sub>2</sub> with crystalline walls using PMMA colloidal crystal templates*. *Colloid and Polymer Science*, 2006. **285**(1): p. 1-9.
120. Waterhouse, G.I.N., et al., *Physical and optical properties of inverse opal CeO<sub>2</sub> photonic crystals*. *Chemistry of Materials*, 2008. **20**(3): p. 1183-1190.
121. Zhao, J.P., et al., *Fabrication of three-dimensionally ordered macroporous gadolinia-doped ceria films*. *New Journal of Chemistry*, 2008. **32**(6): p. 1014-1019.
122. Zhou, W., et al., *A novel efficient oxide electrode for electrocatalytic oxygen reduction at 400-600 degrees C*. *Chemical Communications*, 2008(44): p. 5791-5793.
123. Kim, S., et al., *Anomalous Electrical Conductivity of Nanosheaves of CeO<sub>2</sub>*. *Chemistry of Materials*, 2009. **21**(7): p. 1182-1186.

124. Yu, K.L., et al., *Convenient synthesis of CeO<sub>2</sub> nanotubes*. Materials Science and Engineering B-Solid State Materials for Advanced Technology, 2007. **139**(2-3): p. 197-200.
125. Gulbransen, E.A., T.P. Copan, and K.F. Andrew, *Oxidation of Copper between 250-Degrees-C and 450-Degrees-C and the Growth of CuO Whiskers*. Journal of the Electrochemical Society, 1961. **108**(2): p. 119-123.
126. Jiang, X.C., T. Herricks, and Y.N. Xia, *CuO nanowires can be synthesized by heating copper substrates in air*. Nano Letters, 2002. **2**(12): p. 1333-1338.
127. Kumar, A., et al., *The effect of growth parameters on the aspect ratio and number density of CuO nanorods*. Journal of Physics-Condensed Matter, 2004. **16**(47): p. 8531-8543.
128. Zhang, K.L., et al., *Synthesis of large-area and aligned copper oxide nanowires from copper thin film on silicon substrate*. Nanotechnology, 2007. **18**(27): p. -.
129. Chopra, N., B. Hu, and B.J. Hinds, *Selective growth and kinetic study of copper oxide nanowires from patterned thin-film multilayer structures*. Journal of Materials Research, 2007. **22**(10): p. 2691-2699.
130. Qin, Y., T. Staedler, and X. Jiang, *Preparation of aligned Cu nanowires by room-temperature reduction of CuO nanowires in electron cyclotron resonance hydrogen plasma*. Nanotechnology, 2007. **18**(3): p. -.